

Electronic Theses and Dissertations, 2004-2019

2013

Absorptive And Refractive Optical Nonlinearities In Organic Molecules And Semiconductors

Davorin Peceli
University of Central Florida

 Part of the [Electromagnetics and Photonics Commons](#), and the [Optics Commons](#)
Find similar works at: <https://stars.library.ucf.edu/etd>
University of Central Florida Libraries <http://library.ucf.edu>

This Doctoral Dissertation (Open Access) is brought to you for free and open access by STARS. It has been accepted for inclusion in Electronic Theses and Dissertations, 2004-2019 by an authorized administrator of STARS. For more information, please contact STARS@ucf.edu.

STARS Citation

Peceli, Davorin, "Absorptive And Refractive Optical Nonlinearities In Organic Molecules And Semiconductors" (2013). *Electronic Theses and Dissertations, 2004-2019*. 2571.
<https://stars.library.ucf.edu/etd/2571>

**ABSORPTIVE AND REFRACTIVE OPTICAL NONLINEARITIES
IN
ORGANIC MOLECULES AND SEMICONDUCTORS**

by

DAVORIN PECELI
B.S. University of Zagreb, 2003
M.S. University of Central Florida, 2007

A dissertation submitted in partial fulfillment of the requirements
for the degree of Doctor of Philosophy
in CREOL, The College of Optics and Photonics
at the University of Central Florida
Orlando, Florida

Spring Term
2013

Major Professors: Eric W. Van Stryland and David J. Hagan

© 2013 Davorin Peceli

ABSTRACT

The main purpose of this dissertation is to investigate photophysical properties, third order nonlinearity and free carrier absorption and refraction in organic materials and semiconductors. Special emphasis of this dissertation is on characterization techniques of molecules with enhanced intersystem crossing rate and study of different approaches of increasing triplet quantum yield in organic molecules.

Both linear and nonlinear characterization methods are described. Linear spectroscopic characterization includes absorption, fluorescence, quantum yield, anisotropy, and singlet-oxygen generation measurements. Nonlinear characterization, performed by picosecond and femtosecond laser systems (single and double pump-probe and Z-scan measurements), includes measurements of the triplet quantum yields, excited-state absorption, two-photon absorption, nonlinear refraction and singlet and triplet-state lifetimes.

The double pump-probe technique is a variant of the standard pump-probe method but uses two pumps instead of one to create two sets of initial conditions for solving the rate equations allowing a unique determination of singlet- and triplet-state absorption parameters and transition rates. The advantages and limitations of the double pump-probe technique are investigated theoretically and experimentally, and the influences of several experimental parameters on its accuracy are determined. The accuracy with which the double pump-probe technique determines the triplet-state parameters improves when the fraction of the population in the triplet state relative to the ground state is increased. Although increased accuracy is in

principle achievable by increasing the pump fluence in the reverse saturable absorption range, it is shown that the DPP is optimized by working in the saturable absorption regime.

Two different approaches to increase intersystem crossing rates in polymethine-like molecules are presented: traditional heavy atom substitution and molecular levels engineering. Linear and nonlinear optical properties of a series of polymethine dyes with Br- and Se- atoms substitution, and a series of new squaraine molecules, where one or two oxygen atoms in a squaraine bridge are replaced with sulfur atoms, are investigated. A consequence of the oxygen-to-sulfur substitution in squaraines is the inversion of their lowest lying $\pi\pi^*$ and $n\pi^*$ states leading to a significant reduction of singlet-triplet energy difference and opening of an additional intersystem channel of relaxation. Experimental studies show that triplet quantum yields for polymethine dyes with heavy-atom substitutions are small (not more than 10%), while for sulfur-containing squaraines these values reach almost unity. Experimental results are in agreement with density functional theory calculations allowing determination of the energy positions, spin-orbital coupling, and electronic configurations of the lowest electronic transitions.

For three different semiconductors: GaAs, InP and InAsP two photon absorption, nonlinear refraction and free carrier absorption and refraction spectrums are measured using Z-scan technique. Although two photon absorption spectrum agrees with the shape of theoretical prediction, values measured with picosecond system are off by the factor of two. Nonlinear refraction and free carrier nonlinearities are in relatively good agreement with theory. Theoretical values of the third order nonlinearities in GaAs are additionally confirmed with femtosecond Z-scan measurements.

Due to large spectral bandwidth of femtosecond laser, three photon absorption spectrum of GaAs was additionally measured using picosecond Z-scan. Again, spectral shape is in excellent agreement with theory however values of three photon absorption cross sections are larger than theory predicts.

This dissertation is dedicated to my family.

ACKNOWLEDGMENTS

First, I would like to thank my advisors Dr. Eric W. Van Stryland and Dr. David J. Hagan for giving me opportunity to work in their group and learn from them. Their guidance and continuous support during my research time have been invaluable in the development of this dissertation. Although their schedule was very busy they always had enough time for me.

My special thanks go to Dr. Olga Przhonska, who provided me with most of the organic molecules studied in this dissertation, for her countless suggestions and advise. Without her this dissertation would not have been possible. Special thanks also go to Dr. Artëm E. Masunov for his quantum chemical calculation and analysis.

I would also like to thank postdocs who have worked in our group Dr. Scott Webster, Dr. Dmitry Fishman, and Dr. Lazaro Padilha, from whom I learned most of my experimental skill. It was a great pleasure to work with all NLO group members Mattew Reichert, Himansu Pattanaik, Trenton Ensley, Manuel Ferdinandus, Brendan Turnbull, Dr. Honghu Hu and former members Dr. Claudiu Cirloganu, Dr. Gero Nootz and Dr. Peter Olszak.

Thanks to the entire faculty, staff and students at CREOL.

Finally, I would like to thank all my friends and my family for their love and support.

TABLE OF CONTENTS

LIST OF FIGURES	xi
LIST OF TABLES.....	xi
LIST OF ACRONYMS/ABBREVIATIONS	xxii
CHAPTER 1. INTRODUCTION.....	1
1.1 Background and Motivation	1
1.2 Dissertation Outline	4
CHAPTER 2. PHOTOPHYSICS OF ORGANIC MOLECULES	6
2.1 Molecular Orbital Theory	6
2.2 Spin Multiplicity of Singlet and Triplet states - Nature of Excited States.....	9
2.3 Intersystem Crossing and Spin-orbit (SO) Coupling.....	17
2.4 Singlet Oxygen.....	22
2.5 Nonlinear Absorption and Refraction.....	25
CHAPTER 3. LASER SYSTEMS AND EXPERIMENTAL TECHNIQUES	30
3.1 Picosecond Laser	30
3.2 Picosecond OPG/OPA and DFG	32
3.3 Femtosecond Laser System.....	34

3.4 Femtosecond OPG/OPA and DFG	35
3.5 Beam Parameter Calibration	37
3.6 Linear Spectroscopic Techniques	38
3.7 Non-linear Spectroscopic Techniques	43
3.7.1 Pump-probe Method	43
3.7.2 Singlet Depletion Method	51
3.7.3 White-light Continuum Pump-probe Spectroscopy – Measurements of ESA Spectrum	54
3.7.4 Double Pump-probe Method.....	56
3.7.5 Triplet Lifetime Measurements.....	58
3.7.6 Z-scan.....	59
3.7.7 Two-photon Excitation Fluorescence (2PF) Spectroscopy.....	63
CHAPTER 4. OPTIMIZATION OF DOUBLE PUMP-PROBE TECHNIQUE	65
CHAPTER 5. π - CONJUGATED MATERIALS WITH ENHANCED INTERSYSTEM CROSSING RATES	80
5.1. Polymethine-like molecules	80
5.1.1 Linear Experimental Results	85
5.1.2 Nonlinear Experimental Results	87
5.1.3 Quantum-chemical analysis	98

5.2. Axially Dendronised Ruthenium(II) Pthalocyanine and Napthalocyanine	107
5.2.1 Linear optical properties of Ru Pc and Nc.....	109
5.2.2 Nonlinear optical properties of Ru Pc and Nc	110
CHAPTER 6. SEMICONDUCTORS.....	116
6.1 Optical Properties of Semiconductors	116
6.2 Z-scan Measurements of Bound-electronic and Free-carrier Nonlinearities in Semiconductors.....	119
6.3 Three-Photon Absorption in GaAs	131
6.4 Discussion of picosecond results	136
CHAPTER 7. CONCLUSION	143
7.1 Summary.....	143
7.2 Future Work	146
APENDIX A: PICOSECOND Z-SCAN MEASUREMENTS OF α_2 , σ_{FC} , n_2 AND σ_T	148
APENDIX B: PICOSECOND Z-SCAN MEASUREMENTS OF 3PA IN GaAs	161
APENDIX C: COPYRIGHT PERMISSION LETTERS	169
LIST OF REFERENCES	174

LIST OF FIGURES

Figure 2.1. Combination of two identical atoms to form a molecule using atomic wavefunctions to obtain bonding and antibonding molecular orbitals[11].	7
Figure 2.2. Covalent bonds in ethylene [12].	8
Figure 2.3. Vector representation of electron spin.	9
Figure 2.4. Vector representation of singlet and triplet states.	11
Figure 2.5. Five-level model. S_0 , S_1 and S_n are singlet levels, T_1 and T_n are triplet levels. σ 's are cross-sections. τ 's are transition lifetimes. Boxes next to electronic levels show spin orientations of the two electrons with the highest energy[15].	14
Figure 2.6. Operation of H_{SOC} on p_y orbital.	18
Figure 2.7. Visual representation of spin-orbit coupling matrix element for transitions between (a) states of the same orbital configurations and (b) states of different orbital configurations. ...	21
Figure 2.8. Energy of the two lowest excited states of molecular oxygen. Orbital configurations of just the last two electrons are shown. Σ , Δ and Σ are spectroscopic symbols of the ground, first and second excited states respectively.	22
Figure 2.9. Quenching of the photosensitizer's triplet state and production of singlet oxygen. k^Q_T is the quenching rate of T_1 .	24
Figure 2.10. Energy level diagram of a three-level system of only singlet transitions. S_0 , S_1 and S_n are singlet electronic energy levels. σ_{Sij} and τ_{Sij} are cross-sections and lifetimes. τ_{S10} includes both radiative and non-radiative decays.	27

Figure 3.1. Layout of a picosecond laser: A-aperture, BS-beamsplitter, L-lens, M-mirror, PC-pockels cell, QWP-quarter wave plate, R-Nd:YAG rod.....	31
Figure 3.2. Layout of a picosecond OPG/OPA: A-aperture, BS-beamsplitter, L-lens, M-mirror.....	32
Figure 3.3. Tunability range for the picosecond OPG/OPA.....	33
Figure 3.4. Femtosecond laser system layout	34
Figure 3.5. Layout of the regenerative amplifier cavity: L-lens, BS-beamsplitter, PC-pockels cell, FR-Faraday rotator.....	35
Figure 3.6. Layout of the femtosecond OPG/OPA: A-aperture, BS-beamsplitter, L-lens, M-mirror, CL-cylindrical lens, CM-cylindrical mirror, NC-nonlinear crystal, DG-diffraction grating, GP-fused silica plate, TD-time delay, PR-polarization rotator.	36
Figure 3.7. Beam profile at 532 nm (second harmonic of Nd:YAG laser taken with WinCam D CCD camera (a), Autocorrelation measurement ($\tau_{\text{HW}1/e} = 11\text{ps}$) and (c) Knife edge scan ($w_0 = 50\ \mu\text{m}$).....	37
Figure 3.8. Singlet oxygen luminescence spectrum.....	41
Figure 3.9. Linear absorption of dye SD-S 7508 in toluene before and after experiment.	42
Figure 3.10. Schematic of a pump-probe experiment.....	43
Figure 3.11. Energy level diagram of a five-level system of singlet and triplet transitions. S_0, S_1 and S_n are singlet while T_1 and T_m are triplet electronic energy levels. σ_{ij} and τ_{ij} are cross-sections and lifetimes pertaining to the particular singlet and triplet transitions, respectively. As indicated by the circles, τ_{S10} and τ_{T10} include both radiative and non-radiative decays.....	45
Figure 3.12 Numerical models of pump-probe dynamic (a) for molecules with $\phi_T=0$ and (b) for molecules with $\phi_T > 0$	48

Figure 3.13. (a) Molecular structures and molar absorptivity spectra of SiNc in toluene. (b) Pump-probe experimental results and theoretical fitting for SiNc: (a) $T_L = 0.94$, $F = 100 \text{ mJ/cm}^2$ ($E = 15 \text{ }\mu\text{J}$, $w_0 = 95 \text{ }\mu\text{m}$). Pumping wavelength is 532 nm; $\sigma_{S1n} = 32 \times 10^{-18} \text{ cm}^2$; $\tau_S = 1.5 \text{ ns}$; ... 51

Figure 3.14. Singlet depletion measurement for (a) SiNc at 770nm, $T_L = 0.7$ and $F = 11 \text{ mJ/cm}^2$ ($E = 1 \text{ }\mu\text{J}$, $w_0 = 75 \text{ }\mu\text{m}$) and (b) SD-SO 7517, $T_L = 0.8$ and $F_I = 0.5 \text{ mJ/cm}^2$ ($E = 0.5 \text{ }\mu\text{J}$, $w_0 = 250 \text{ }\mu\text{m}$)..... 53

Figure 3.15 White light continuum pump-probe setup..... 55

Figure 3.16. Schematic of the double pump-probe experiment..... 57

Figure 3.17 Triplet state lifetime measurement of SD-SO 7517 in ACN. Pump: $\lambda = 660 \text{ nm}$, $\tau_{\text{HW}1/e} = 7 \text{ ps}$. CW probe $\lambda = 660 \text{ nm}$ 58

Figure 3.18. Z-scan experimental setup..... 59

Figure 3.19.(a) Z-scan open aperture measurements for ZeSe at 532nm: $E = 200 \text{ nJ}$, $\tau_{\text{HW}1/e} = 11 \text{ ps}$, $w_0 = 16 \text{ }\mu\text{m}$ and (b) closed aperture measurements for CS_2 : $E = 180 \text{ nJ}$, $\tau_{\text{HW}1/e} = 11 \text{ ps}$, $w_0 = 16 \text{ }\mu\text{m}$ 60

Figure 3.20. Z-scan open aperture measurements for SD-O 2405 in toluene at 460 nm in 1mm cell for several different energies: $\tau_{\text{HW}1/e} = 8 \text{ ps}$, $w_0 = 16 \text{ }\mu\text{m}$, $T(\text{lin}) = 0.92$, $\sigma_{\text{S01}} = 1.5 \times 10^{-18} \text{ cm}^2$, $\tau_{\text{S10}} = 2.5 \text{ ns}$ 61

Figure 3.21. (a) Femtosecond open aperture Z-scan measurements for SD-S 7508 in toluene at 550 nm in a 1mm cell for several different energies: $\tau_{\text{HW}1/e} = 140 \text{ fs}$, $w_0 = 16.7 \text{ }\mu\text{m}$, $T(\text{lin}) = 0.86$, $\sigma_{\text{S01}} = 4.8 \times 10^{-18} \text{ cm}^2$, $\tau_{\text{S10}} = 4.5 \text{ ps}$. (b) Picosecond open aperture Z-scan measurements for SD-S 7508 in toluene at 550 nm: $\tau_{\text{HW}1/e} = 8 \text{ ps}$, $w_0 = 16 \text{ }\mu\text{m}$, $T(\text{lin}) = 0.93$, $\sigma_{\text{S01}} = 4.8 \times 10^{-18} \text{ cm}^2$, $\sigma_{\text{S1n}} = 62 \times 10^{-18} \text{ cm}^2$, $\tau_{\text{S10}} = 4.5 \text{ ps}$, $\tau_{\text{S1n}} = 20 \text{ fs}$ and $\Phi_T = 0.98$ 62

Figure 3.22. Schematics of the two photon fluorescence experimental setup 63

Figure 4.1. (a) and (b) Numerical simulation of DPP dynamics shown as normalized transmittance vs. time delay between pump and probe pulses for SiNc at 532 nm with parameters for different ϕ_T and σ_{T1m} . Using $\kappa = +22 \times 10^{-18} \text{ cm}^2$, $\sigma_{S0I} = 2.8 \times 10^{-18} \text{ cm}^2$, and $\sigma_{S1n} = 32 \times 10^{-18} \text{ cm}^2$, (a) $T_L = 0.6$ ($C = 2 \text{ mM}$) with an input fluence of $F = 13 \text{ mJ/cm}^2$ in each pump and (b) $T_L = 0.95$ ($C = 0.3 \text{ mM}$) with an input fluence of $F = 190 \text{ mJ/cm}^2$ in each pump. (c) and (d) Population dynamics for the ground (N_0), first excited singlet (N_{S1}) and triplet (N_{T1}) states using $\phi_T = 0.2$ and $\sigma_{T1m} = 1.2 \times 10^{-16} \text{ cm}^2$ for the two cases of DPP simulation in (a) and (b), respectively. 67

Figure 4.2. Solutions of rate equations (1) and (2): (a) Plot of normalized transmittance vs. delay between pump and probe pulses for the DPP in SiNc indicating changes in transmittance $T_2^{(i)}$ with time as defined in Eq. 5. ΔT_2 is the difference between $T_2^{(b)}$ and $T_2^{(a)}$. The inset shows the expanded region in transmittance between $T_2^{(b)}$ and $T_2^{(a)}$. (b) $|\Delta T_2 / \Delta \phi_T|$ vs. input fluence at a concentration of $C = 0.37 \text{ mM}$, (c) $\Delta T_2 / \Delta \phi_T$ vs. N_{TOT} with $F = 190 \text{ mJ/cm}^2$ in each pump, and (d) $\Delta T_2 / \Delta \phi_T$ vs. the difference in cross sections $\sigma_{T1m} - \sigma_{S0I}$ at $C = 0.37 \text{ mM}$ and $F = 190 \text{ mJ/cm}^2$ in each pump. 69

Figure 4.3. The DPP setup for picosecond measurements. Here all wavelengths are the same. Line colors are used to distinguish separate pulses for clarity..... 74

Figure 4.4. Experimental results and theoretical fitting for SiNc: (a) $C = 2.1 \text{ mM}$ ($T_L = 0.7$) and $F = 11 \text{ mJ/cm}^2$ ($E = 1 \text{ }\mu\text{J}$, $w_0 = 75 \text{ }\mu\text{m}$) in each pump; (b) $C = 0.36 \text{ mM}$ ($T_L = 0.94$), $F = 100 \text{ mJ/cm}^2$ ($E = 15 \text{ }\mu\text{J}$, $w_0 = 95 \text{ }\mu\text{m}$) in each pump. Pumping wavelength is 532 nm; $\sigma_{S1n} = 32 \times 10^{-18} \text{ cm}^2$; $\tau_S = 1.5 \text{ ns}$; (c) Experimental results and theoretical fitting for SiNc at 770 nm; $C = 15 \text{ }\mu\text{M}$

($T_L = 0.3$), $F = 0.84 \text{ mJ/cm}^2$ ($E = 0.7 \text{ }\mu\text{J}$, $w_0 = 230 \text{ }\mu\text{m}$) in the first and $F = 0.92 \text{ mJ/cm}^2$ ($E = 0.7 \text{ }\mu\text{J}$, $w_0 = 220 \text{ }\mu\text{m}$) in the second pump; $\sigma_{SIn} = (4.0 \pm 0.2) \times 10^{-16} \text{ cm}^2$; $\tau_S = 1.5 \text{ ns}$; and (d) population dynamics for case (c). The inset in Figure 4.4 a shows three curves that fit the data within the experimental errors indicating low accuracy under these experimental conditions. ... 76

Figure 4.5 DPP experimental results and theoretical fitting for SD 7517: Pump wavelength at (1) 640 nm (red fit); $\sigma_{S0I} = 5.1 \times 10^{-16} \text{ cm}^2$; $\sigma_{SIn} = (2.8 \pm 0.2) \times 10^{-16} \text{ cm}^2$; $C = 6.8 \text{ }\mu\text{M}$ ($T_L = 0.8$); $F = 0.32 \text{ mJ/cm}^2$ ($E = 0.1 \text{ }\mu\text{J}$, $w_0 = 140 \text{ }\mu\text{m}$) in the first and $F = 0.52 \text{ mJ/cm}^2$ ($E = 0.1 \text{ }\mu\text{J}$, $w_0 = 110 \text{ }\mu\text{m}$) in the second pump; and pump wavelength at (2) 660 nm (blue-dash fit); $\sigma_{S0I} = 12.1 \times 10^{-16} \text{ cm}^2$; $\sigma_{SIn} = (5.8 \pm 0.2) \times 10^{-16} \text{ cm}^2$, and $C = 3 \text{ }\mu\text{M}$ ($T_L = 0.8$); $F_1 = 0.5 \text{ mJ/cm}^2$ ($E = 0.5 \text{ }\mu\text{J}$, $w_0 = 250 \text{ }\mu\text{m}$) in the first and $F_2 = 0.55 \text{ mJ/cm}^2$ ($E = 0.5 \text{ }\mu\text{J}$, $w_0 = 240 \text{ }\mu\text{m}$) in the second pump. In both cases $\tau_S = 1.4 \text{ ns}$ 79

Figure 5.1. General structure of PD molecule; n is length of conjugated chain and R_i is terminal group. 80

Figure 5.2 General structure of SD molecule; electron acceptor C_4O_2 at the center of the chain and R_i is terminal group. 81

Figure 5.3 Molecular structures, absorption (solid lines 1, 2), fluorescence (dashed lines 1', 2') and anisotropy (1'', 2'') for: (a) PD 2350 (1, 1', and 1'') and PD 2929 (2, 2', and 2''); (b) PD 1852 (1, 1', and 1'') and PD 2972 (2, 2', and 2''); (c) PD 4216 in ACN (1). Absorption and fluorescence spectra are measured in ethanol; anisotropy spectra are measured in glycerol. No fluorescence was detected for PD 4216. 83

Figure 5.4 Molecular structures, absorption (solid lines 1, 2), fluorescence (dashed lines 1', 2') and anisotropy (1'', 2'') for: (a) SD-O 2405 (1, 1', and 1'') and SD-S 7508 (1) in toluene; (b) SD-

O 2053 (1, 1', and 1'') and SD-SO 7517 (2, 2', and 2'') in DCM; (c) SD-O 2577 (1, 1', and 1'') in ethanol and SD-S 7504 (2, 2', and 2'') in toluene; (d) SD-O 2243 (1, 1', and 1'') in DCM and SD-S 7507 (2, 2', and 2'') in toluene. All anisotropy spectra are measured in pTHF. No fluorescence was detected for SD-S 7508..... 84

Figure 5.5 (b) Single pump-probe measurements for SD-O 2577 in DCM at 532 nm (linear transmittance 0.7, pump fluence 3.8 mJ/cm^2 , $\sigma_{SOI} = 8.8 \times 10^{-18} \text{ cm}^2$, $\sigma_{SIn} = 1.3 \times 10^{-16} \text{ cm}^2$, $\tau_S = 0.9 \text{ ns}$); (c) DPP measurements for SD-S 7504 in toluene at 670 nm (linear transmittance 0.75, fluence in each pump 0.33 mJ/cm^2 , $\sigma_{SOI} = 5.2 \times 10^{-16} \text{ cm}^2$, $\sigma_{SIn} = (2.6 \pm 0.5) \times 10^{-16} \text{ cm}^2$, $\sigma_{TIn} = (2.5 \pm 0.5) \times 10^{-16} \text{ cm}^2$, $\tau_S = (0.50 \pm 0.05) \text{ ns}$)..... 89

Figure 5.6 Linear absorption (1), S - S (2) and T - T (3) ESA absorption spectra for (a) SD-O 2053; (b) SD-SO 7517; (c) SD-O 2405. Decay kinetics for (d) SD-O 2053 at 532 nm (pump fluence 2.6 mJ/cm^2 , $\sigma_{SOI} = 33 \times 10^{-18} \text{ cm}^2$, $\sigma_{SIn} = 0.9 \times 10^{-16} \text{ cm}^2$, $\tau_S = 2.5 \text{ ns}$); (e) SD-SO 7517 at 570 nm (pump fluence 0.5 mJ/cm^2 , $\sigma_{SOI} = 23 \times 10^{-18} \text{ cm}^2$, $\sigma_{SIn} = 1.3 \times 10^{-16} \text{ cm}^2$, $\sigma_{TIn} = 2.5 \times 10^{-16} \text{ cm}^2$, $\tau_S = 1.5 \text{ ns}$) (f) SD-O 2405 at 532 nm (pump fluence 1 mJ/cm^2 , $\sigma_{SOI} = 9.2 \times 10^{-18} \text{ cm}^2$, $\sigma_{SIn} = 1.3 \times 10^{-16} \text{ cm}^2$, $\tau_S = 2.2 \text{ ns}$);. SD-O 2053 and SD-SO 7517 are measured in ACN, and SD-O 2405 is measured in toluene..... 91

Figure 5.7 Linear absorption (1), S - S (2) and T - T (3) ESA absorption spectra (a) and decay kinetics (b) at 480 nm (pump fluence 0.5 mJ/cm^2 , $\sigma_{SOI} = 90 \times 10^{-18} \text{ cm}^2$, $\sigma_{SIn} = 1 \times 10^{-16} \text{ cm}^2$, $\tau_S = 4.5 \text{ ps}$) (1) and 570 nm (pump fluence 0.5 mJ/cm^2 , $\sigma_{SOI} = 6.5 \times 10^{-18} \text{ cm}^2$, $\sigma_{TIn} = 0.5 \times 10^{-16} \text{ cm}^2$, $\tau_S = 4.5 \text{ ps}$) (2) for SD-S 7508 in toluene..... 92

Figure 5.8 Triplet lifetime measurements for SD-S 7517 in (a) toluene and in (b) ACN. Shorter decays (1) correspond to air-saturated solutions, while longer decays (2) correspond to solutions with oxygen removed..... 94

Figure 5.9 Normalized one-photon absorption (1, 2), excitation anisotropy (1', 2'), and two-photon absorption spectra (1'', 2'') for SD-O 2053 (1, 1', 1'') and SD-S 7517 (2, 2', 2''). The two-photon excitation wavelengths and absorption cross sections are shown on the top and right axes, correspondingly. 2PA data shown by solid red circles for SD-S 7517 and solid blue circles for SD-O 2053 are obtained by open-aperture Z-scans. 2PA data shown by blue open circles for SD-O 2053 correspond to 2PF measurements. All spectra are measured in ACN, except excitation anisotropy in pTHF. 96

Figure 5.10 Isosurfaces of the essential Kohn-Sham orbitals in in XY and XZ planes for PD 1852..... 102

Figure 5.11 Molecular schematic of SD-S 7508 showing two perpendicular chromophores, one between nitrogen atoms (blue) and the second between sulfur atoms (yellow). Table presents isosurfaces of Kohn-Sham orbitals in XY and XZ planes for SD-S 7508..... 105

Figure 5.12 Molecular structures, absorption (solid lines) and fluorescence (dashed lines) for: (a) RuPc-G3; (b) RuNc-G3. Absorption and fluorescence spectra are both measured in toluene.. 108

Figure 5.13 (a) DPP and fitting results for RuNc-G3 at a pump of 710 nm ($\sigma_{sol} = 6.6 \times 10^{-16}$ cm²), $C = 12$ μ M ($T_L = 0.6$), $F = 3.4$ mJ/cm² ($E = 0.7$ μ J, $w_0 = 115$ μ m) in each pump. The values obtained are: $\phi_T = (0.97 \pm 0.01)$, $\sigma_{S1n} = (3.5 \pm 0.1) \times 10^{-16}$ cm², $\sigma_{T1m} = (3.4 \pm 0.1) \times 10^{-16}$ cm², and $\tau_S = 5.3$ ps. Inset: greater temporal resolution scan showing S₁ dynamics for the first pump pulse

only. (b) DPP population dynamics for the ground, first excited singlet and triplet states for RuNc-G3 for the conditions in (a).	111
Figure 5.14 Linear absorption (1), S - S (2) and T - T (3) ESA absorption spectra for (a) RuPc-G3 and (b) RuNc-G3. Decay kinetics for (c) RuPc-G3 at 570 nm (pump fluence 2.6 mJ/cm^2 , $\sigma_{S01} = 33 \times 10^{-18} \text{ cm}^2$, $\sigma_{S1n} = 0.9 \times 10^{-16} \text{ cm}^2$, $\tau_S = 2.5 \text{ ns}$); (d) RuNc-G3 at 520 nm (pump fluence 0.5 mJ/cm^2 , $\sigma_{S01} = 23 \times 10^{-18} \text{ cm}^2$, $\sigma_{S1n} = 1.3 \times 10^{-16} \text{ cm}^2$, $\sigma_{T1n} = 2.5 \times 10^{-16} \text{ cm}^2$, $\tau_S = 1.5 \text{ ns}$).....	113
Figure 5.15 Triplet lifetime measurements for RuNc-G3 in toluene. Shorter decays (1) correspond to air-saturated solutions, while longer decays (2) correspond to solutions with oxygen removed.	114
Figure 6.1. Band structure of GaAs with four bands: the electron (e) band, the heavy-hole (hh) band, the light-hole (lh) band and split-off hole (so) band.	118
Figure 6.2 Linear spectrum of GaAs, InP and InGaAs.....	119
Figure 6.3 Pulse width of picosecond OPG/A.....	123
Figure 6.4 (a) Picosecond Z-scan results measured for 2PA in GaAs (black circles) compared to the theory (red solid line) and the same theory scaled by a factor of 2.5 (blue solid line) and (b) free carrier absorption results for GaAs.....	124
Figure 6.5 (a) Picosecond Z-scan results measured for 2PA in InP (black circles) compared to the theory (red solid line) and the same theory scaled by a factor of 2 (blue solid line) and (b) free-carrier absorption results for InP.....	124
Figure 6.6 (a) Picosecond Z-scan results measured for 2PA in InAsP (black circles) compared to the theory (red solid line) and the same theory scaled by a factor of 2 (blue solid line) and (b) free carrier absorption results for InAsP	125

Figure 6.7 (a) n_2 results for GaAs measured with picosecond (blue circles) and femtosecond (green circles) pulses compared to the theory (red solid line) and (b) σ_r spectrum of GaAs.	126
Figure 6.8 (a) n_2 results for InP measured with picosecond (blue circles) pulses compared to the theory (red solid line) and (b) σ_r spectrum of GaAs.	126
Figure 6.9 (a) n_2 results for InAsP measured with picosecond (blue circles) pulses compared to the theory (red solid line) and (b) σ_r spectrum of InAsP.	127
Figure 6.10 CA/OA for picosecond Z-scans of InP at 1100nm. All curves are fit with the same value of $n_2 = -80 \times 10^{-5} \text{ cm}^2/\text{GW}$ indicating no influence of free-carrier refraction.....	128
Figure 6.11 (a) CA/OA for picosecond Z-scans of InP at 1300nm fit with a third-order n_2 . (b) Plot of $\Delta n/I_0$ versus I_0 . Intercept gives $n_2 = -39 \times 10^{-5} \text{ cm}^2/\text{GW}$	129
Figure 6.12 CA/OA for picosecond Z-scans of InP at 1300nm fit with full code:.....	129
Figure 6.13 CA/OA for picosecond Z- scan of InP at 1750nm fit with full code:	130
Figure 6.14 Pulse width of femtosecond OPG/A.....	131
Figure 6.15 Femtosecond Z-scan results measured for 3PA in GaAs [blue squares] compared to the four-band theory (black solid line) and the same theory scaled by a factor of 2.5 (red solid line).	132
Figure 6.16 Pulse width of picosecond pulses using DFG.	133
Figure 6.17 (a) Picosecond Z-scan of GaAs at 2300nm - fit with a pure α_3 and.....	134
Figure 6.18 Z-scan of GaAs at 2300nm - fit with the full code: $\alpha_3 = 0.52 \text{ cm}^3/\text{GW}^2$, $\sigma_{\text{FC}} = 1.2 \times 10^{-16} \text{ cm}^2$	134
Figure 6.19 Picosecond Z-scan results for 3PA in GaAs (blue squares) compared to the four-band theory (black solid line) and the same theory scaled by a factor of 7 (green solid line)....	135

Figure 6.20 FCA of GaAs: (a) experimental results, (b) calculated contributions to FCA from holes and excited electrons.	136
Figure 6.21 Setup 1: Autocorrelation setup using KDP crystal.	137
Figure 6.22 Autoceorrelation signal of ps idler using KDP crystal fit with a single Gaussian pulse (blue line) and double Gaussian pulse (red line).	138
Figure 6.23 Setup2: Autocorrelation setup using 2PA on GaAs detector.	139
Figure 6.24 Autoceorrelation signal at 1000nm measured on the same day with Setup 1(a) and Setup 2 (b).	140
Figure 6.25 Pulse spectrum at 1000nm.	141
Figure 6.26 (a) Autocorrelation and (b) Z-scan of GaAs using 1064nm from the laser itself....	142

LIST OF TABLES

Table 1. Photophysical parameters of SD-O, SD-SO and SD-S dyes: $\lambda^{\max}_{\text{Abs}}$ and $\lambda^{\max}_{\text{Fl}}$ are the peak absorption and fluorescence wavelengths; ϵ^{\max} is the peak extinction coefficients; Φ_F is fluorescence quantum yield; τ_S is lifetime of lowest singlet excited state; Φ_T and Φ_Δ are triplet and singlet oxygen generation quantum yields, respectively; and τ_{T10} is the lifetime of lowest triplet excited state. Two components in τ_{T10} (last column) correspond to double exponential decays observed in toluene. Solvent abbreviations: ethanol (EtOH), toluene (TOL), acetonitrile (ACN) and dichloromethane (DCM). 97

Table 2. Excitation energies (E_{TD} , eV), leading singlet and triplet configurations, and oscillator strengths (Osc.) predicted with TD-B3LYP/6-31G*/PCM, singlet excitation energies predicted with FD-B3LYP/6-31G*/PCM (E_{FD} , eV), and SOC matrix elements between dominant configurations of each triplet and the lowest singlet S_1 , calculated at the planar optimized S_1 geometry, and out-of-plane distorted S_1 geometry. 106

Table 3. Photophysical parameters of RuPc-G3 and RuNc-G3: $\lambda^{\max}_{\text{Abs}}$ and $\lambda^{\max}_{\text{Fl}}$ are the peak absorption and fluorescence wavelengths; ϵ^{\max} is the peak extinction coefficients; Φ_F is fluorescence quantum yield; τ_S is lifetime of lowest singlet excited state; Φ_T is triplet quantum yield, respectively; and τ_{T10} is the lifetime of lowest triplet excited state..... 115

Table 4. Sample properties of GaAs, InP and InGaAs: bandgap energy, E_g , linear index of refraction, n_0 , and sample thickness, L 120

LIST OF ACRONYMS/ABBREVIATIONS

<u>Acronym/Unit</u>	<u>Description</u>
1PA	One-Photon Absorption
1PF	One-Photon Fluorescence
2PA	Two-Photon Absorption
2PF	Two-Photon Absorption Induced Fluorescence
ACN	Acetonitrile
AOS	All Optical Switching
BLA	Bond Length Alternation
cm	centimeter
CS ₂	Carbon Disulfide
CW	Continuous Wave
D	Debye (unit of dipole moment, equal to 3.33×10^{-30} C·m)
DCM	Dichloromethane
DFG	Difference Frequency Generation
ESA	Excited-State Absorption

eV	electron volt (1.6×10^{-19} V)
fs	femtosecond
FWHM	Full-Width-of-Half-Maximum
GM	Goppert-Mayer
GW	Gigawatt
HOMO	Highest Occupied Molecular Orbital
HW1/e	Half-Width-1/e
ISC	Inter-system Crossing
ISRE	Intermediate State Resonance Enhancement
kHz	Kilohertz
LUMO	Lowest Unoccupied Molecular Orbital
mJ	millijoule
μ J	microJoule
μ m	micrometer
MO	Molecular Orbital
NIR	Near-Infrared

nJ	nanoJoule
nm	nanometer
NLO	Nonlinear Optics
NLA	Nonlinear Absorption
NLR	Nonlinear Refraction
ns	nanosecond
OD	Optical Density
OKE	Optical Kerr Effect
OPG/OPA	optical parametric generator / amplifier
O-SD	Oxygen Squaraine
PD	Polymethine Dye
PMT	Photomultiplier tube
ps	picosecond
THF	Tetrahydrofuran
SHG	Second Harmonic Generation
SD-S	Oxygen-Squaraine

SD-S	Sulfur-Squaraine
SD-SO	Sulfur-Oxygen-Squaraine
UV	Ultra Violet
WLC	White-Light Continuum

CHAPTER 1. INTRODUCTION

1.1 Background and Motivation

For a high intensity field the process of light - matter interaction becomes nonlinear. Materials exhibiting strong nonlinear absorption are of interest for applications including power limiting devices, optical switching, 3D microscopic imaging etc. Since their properties are relatively easily tailored through molecular engineering, organic materials are excellent candidates for nonlinear optical applications. Nonlinear Optics (NLO) is the branch of optics that deals with the interaction of intense light radiation with matter. The NLO response of atomic oscillators due to interaction with high intensity fields is no longer linearly proportional to the field of the incoming light wave. The medium's response in the presence of an electric field is described with the electric polarization, \mathbf{P} . \mathbf{P} can be expanded into a power series of the electric field, \mathbf{E} :

$$\mathbf{P} = \epsilon_0 (\chi^{(1)} \mathbf{E} + \chi^{(2)} \mathbf{E}^2 + \chi^{(3)} \mathbf{E}^3 + \dots) = \mathbf{P}^{(1)} + \mathbf{P}^{(2)} + \mathbf{P}^{(3)} + \dots \quad (1.1)$$

where $\chi^{(n)}$ represent the n-th order optical susceptibility. Linear phenomena (index of refraction and absorption coefficient of a material) are described by the first term in the expansion. The second term, $\chi^{(2)}$, represent nonlinear effects such as second harmonic generation, sum and difference frequency generation, optical rectification, linear electro optic effect and parametric emission. The third term in the expansion, given by $\chi^{(3)}$, is responsible for effects like 3rd harmonic generation, nonlinear refraction, two-photon absorption (2PA), stimulated Raman and Brillouin scattering, four-wave mixing, and self or cross phase modulation. All $\chi^{(3)}$ terms are dependent on the irradiance (energy per unit area per unit time) of incident pulse. In media with

inversion symmetry all even-order elements are zero and only odd terms should be considered. Although, two photon absorption (2PA) was first theoretical predicted by Göppert-Mayer [1] in 1931, experimental studies of nonlinear optical effects weren't possible until Maiman's demonstration of the first laser in 1960 [2]. The beginning of the field is considered the observation of second-harmonic generation by Franken et. al. in 1961 [3].

Organic materials are excellent candidates for nonlinear optical applications. Their main advantage lies in a fact that their optical properties can be easily tailored by molecular structure engineering. Molecular photophysics is a field of science concerned with physical processes induced upon interaction of light with organic molecules. It involves processes where a molecule absorbs a photon but does not undergo any chemical changes. Although the first photophysical reactions were observed from about 1850 to 1920 they were not properly understood until the advent of quantum mechanics. Development of important theories and experimental research started from 1950 with the availability of new spectroscopic and analytical techniques.

When the incident fluence is high enough, excited states in a molecule can become significantly populated. If the life-time of the excited state is not too short compared to the incident temporal pulsewidth of a pulse, electrons in the excited state may experience additional absorption that promotes it to a higher-lying excited state before it relaxes to the ground state. This cumulative type of nonlinearity is called Excited State Absorption (ESA). When the absorption cross-section of the excited state is smaller than the ground state absorption cross-section nonlinear process is called saturable absorption (SA) and the transmission of the system increases with increase of incident radiation. When the absorption cross-section of the excited state is larger than the ground state absorption cross-section, the nonlinear process is called

reverse saturable absorption (RSA). In the RSA case the system will be less transmissive with an increase of the incident radiation.

Lewis et al. were first to publish their experimental observation of SA in 1941 [2]. At that time the process of optical bleaching was explained as equilibrium between absorption and stimulated emission. However, a full understanding of ESA came with the work of Giuliano and Hess in 1967 [4]. They used a 5-level model to explain that optical bleaching in organic dyes is a process of exciting the ground-state population of molecules to higher states with smaller absorption cross sections. From 1960 SA materials were used for temporal pulse-width compression of lasers through mode locking [5] and Q-switching [6]. On the other hand, greater interest in RSA didn't start before 1984, when Harter et al. [7] showed that RSA materials can be used for designing power regulation devices.

Besides the above mentioned applications, molecules with large Intersystem Crossing (ISC) rates from singlet to triplet excited states are also desirable for photodynamic therapy (PDT), phosphorescent and organic light-emitting diodes. Accurate determination of the triplet state parameters such as triplet quantum yield, ϕ_T , triplet-triplet (T-T) absorption cross section, σ_T , and lifetime of triplet state, τ_T , is of great importance for all these applications.

Semiconductors are another excellent candidates for nonlinear optical applications. Semiconductors are materials with crystalline structure. The band structure of semiconductors, described with continuous energy bands separated by an energy gap, gives rise to their unique linear and nonlinear optical properties. The energy band gap, E_g , in semiconductors is usually less than 1-3 eV. In equilibrium, bands in electronic ground state semiconductors are bands are filled up to the Fermi level. In intrinsic semiconductors the Fermi level lies in between the

valence and conduction bands. The highest band below the Fermi level is called the valence band, and the bands above the Fermi level are called conduction bands. In intrinsic semiconductors Fermi level lies in between valence and conduction band. Large magnitude of nonlinear absorption and refraction in semiconductors is of a great interest for passive optical limiting [8].

1.2 Dissertation Outline

Chapter 2. consists of general information regarding photophysics of organic molecules with emphasis on intersystem crossing and spin-orbit coupling. Description of laser systems used in this work together with linear and nonlinear experimental methods commonly used for characterization of organic materials and semiconductors is presented in Chapter 3. Chapter 4. discusses Double Pump Probe technique for determination of triplet quantum yield in organic molecules. Advantages and limitations of the Double Pump Probe technique are investigated theoretically and experimentally, and the influence of several experimental parameters on its accuracy is determined. Chapter 5. is dedicated to description of optical characterization of two different group of organic molecules. First group consists of linear conjugated molecules with two different approaches to increase intersystem crossing: polymethine dyes with heavy atom substitution, and a series of new squaraine molecules, where one or two oxygen atoms in a squaraine bridge are replaced with sulfur atoms. Second group contain cyclic conjugated molecules; Pthalocyanine and Naphthalocyanine with Ruthenium substitution as central atom and axially substituted pyridine rings at the focal point of third-generation Fréchet-type G3 dendrons.

Chapter 6. is dedicated to measurements of bound electronic and free carrier nonlinearities in a direct gap semiconductors with zinblende structure. Chapter 7. presents conclusion of this work and discuss the future directions.

CHAPTER 2. PHOTOPHYSICS OF ORGANIC MOLECULES

2.1 Molecular Orbital Theory

The structure of every molecular electronic state and its change upon interaction with light is best described with a particular molecular orbital (MO) electron configuration. MO's are formed as a linear combination of constituent valence shell atomic orbitals while inner ("core") electrons which are tightly bound remaining in their original atomic orbitals [9].

Since wave functions can interfere constructively and destructively, linear combination of atomic orbitals lead to formation of bonding MOs with high electron probability between the nuclei and anti-bonding MOs with zero electron probability between nuclei, with bonding orbitals having lower energy than anti-bonding orbitals (Figure 2.1a).

Five different types of MO's are important from the standpoint of organic photophysics: sigma-bonding (σ), sigma anti-bonding (σ^*), pi-bonding (π), pi-anti-bonding (π^*) and non-bonding (n)[10]. Sigma orbitals (Figure 2.1b) are formed as a combination of 1s and 2p one-electron atomic orbitals. π (Figure. 2.1c) and n orbitals are results of overlapping of atomic 2p orbitals. Non-bonding orbitals, n , are not involved in actual bonding with very little electron probability concentration between molecules. While n orbital lie in the plane of the molecule π and π^* orbital are perpendicular to the plane of the molecule.

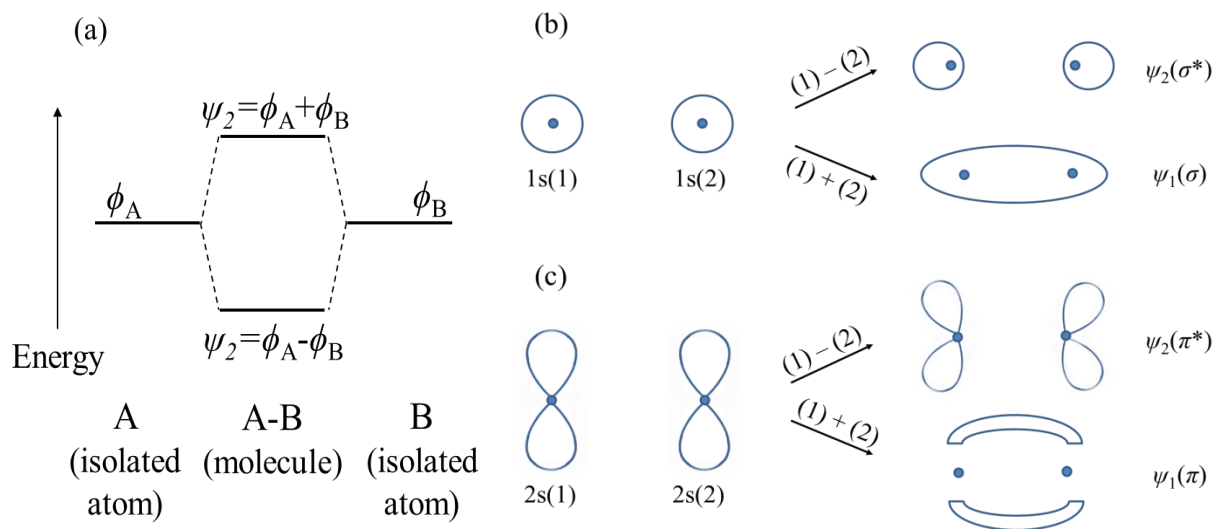


Figure 2.1. Combination of two identical atoms to form a molecule using atomic wavefunctions to obtain bonding and antibonding molecular orbitals[11].

In the ground state, electrons are filling orbitals in a molecule according to the Pauli “exclusion” principle, i.e. two identical electrons cannot occupy the same state, and according to the Aufbau principle (or “building up” principle) electrons occupy orbitals in order of increasing energy. Molecular electronic states are described using only two electrons in the highest MO, since the “core” electrons do not participate in photophysical processes.

Organic materials, based on the type of bonding, are divided into saturated and conjugated compounds. Saturated compounds contain only a single bond formed by the axial overlap of two σ electrons [12]. Electrons in a σ bond are confined very tightly and can be only excited only with a high frequency light. Main absorption peak of saturated compounds lies usually somewhere in deep UV spectral range.

Conjugated compounds contain at least one double or triple bond. Double bonds, in addition to σ bond, include π electron bond, while triple bonds include one σ bond and two π

electron bonds. Simple example of conjugated molecule is shown in Figure 2.2. In ethylene molecule carbon and two hydrogen atoms lie in plane defined by σ bonds (green line) while two p orbitals, included in π bond (red line), are perpendicular to that plane.

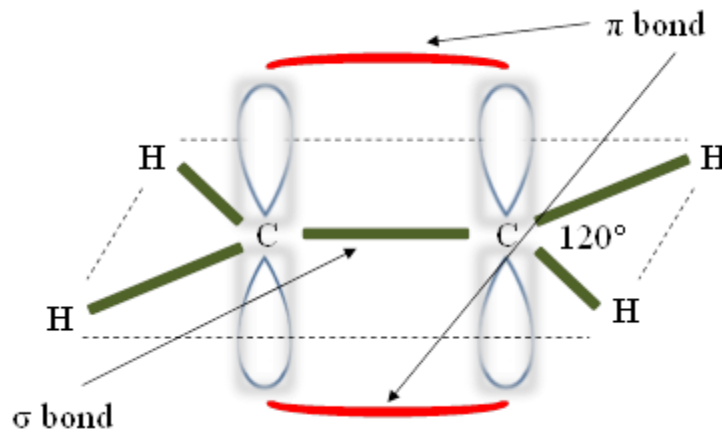


Figure 2.2. Covalent bonds in ethylene [12]

π electrons are weakly bounded and similar to free electrons in semiconductors, are delocalized and spread out through the whole molecule. Electron delocalization leads to strong polarizability and a large transition moment that increases both the linear and nonlinear optical responses. π -conjugated compounds absorb light in the visible and near infrared part of spectrum. For a material with conjugated chain length L and number of π electrons N , the longest wavelength of the absorption, in the first approximation, is given by [13]:

$$\lambda_{\max} = \frac{8mc}{n} \frac{L^2}{N+1} \quad (2.1)$$

where m is an electron mass, c is speed of light and h - Planck constant. From (2.1), it is evident that λ_{\max} depends only on L and N . Changing conjugation length L of molecule, will result in

tuning the main absorption peak to the desired wavelength. In this work only π -conjugated materials will be considered.

2.2 Spin Multiplicity of Singlet and Triplet states - Nature of Excited States

Every electron is characterized by its inherent angular momentum, i.e., spin. The electron spin quantum number, s , can possess only two values: $+1/2$ - for spin-up (\uparrow) and $-1/2$ for spin-down (\downarrow). Although spin is completely a quantum phenomenon, it is common in photophysics to represent the electron spin as a vector, see Figure 2.3.

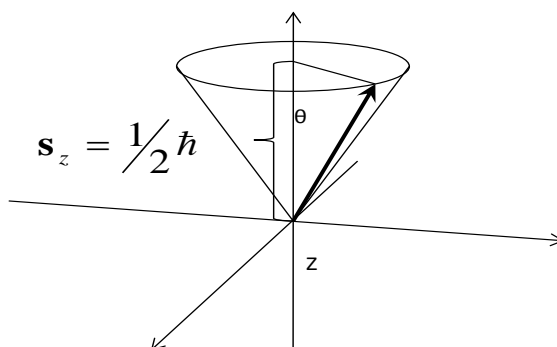


Figure 2.3. Vector representation of electron spin

According to the uncertainty principle, only one component of \mathbf{s} can be experimentally measured. Usually the measured spin component is along the arbitrary z-axis, s_z [11].

Pauli principle states that in every molecular orbital there can be only two electrons with paired spins. The total spin quantum number, S , of a filled orbital is defined as the sum of the spins of the two electrons. If two electrons are paired, their total spin is equal to zero. The spin multiplicity for a given orbital is defined as $M = 2 \cdot S + 1$. States, where two spins are paired ($S =$

0), has a multiplicity $M=1$, and it is called singlet state, since there is only one possible spin projection value $M_S = 0$ (2.2).

After excitation, one of the electrons is promoted to a higher orbital. Since the two electrons are not in the same orbital, it is not required that the spins be paired. Electrons in the excited states can change their spin orientations, so that the spins of both electrons become parallel. In that case, the total spin of the system is equal to one and the multiplicity is $M=3$. This is so called (triplet state with three different spin projection values $M_S = -1, 0, 1$ (2.2). In a magnetic field triplet states splits into three different energy levels [14]. Radiationless transitions which includes a flip of spin between two electronic states of different multiplicity is called intersystem crossing (ISC). The total spin wave function, $|S, M_S\rangle$, of a two electron system is given by:

$$\begin{aligned}
 |0,0\rangle &= \frac{1}{\sqrt{2}}(\uparrow\downarrow - \downarrow\uparrow) & M_S = 0 & & S = 0 \text{ (singlet)} \\
 \\
 \left. \begin{aligned}
 |1,1\rangle &= \uparrow\uparrow & M_S = 1 \\
 |1,0\rangle &= \frac{1}{\sqrt{2}}(\uparrow\downarrow + \downarrow\uparrow) & M_S = 0 \\
 |1,-1\rangle &= \downarrow\downarrow & M_S = -1
 \end{aligned} \right\} & S = 1 \text{ (triplet)}
 \end{aligned} \tag{2.2}$$

A vector representation of singlet and triplet states is shown in Figure 2.4.

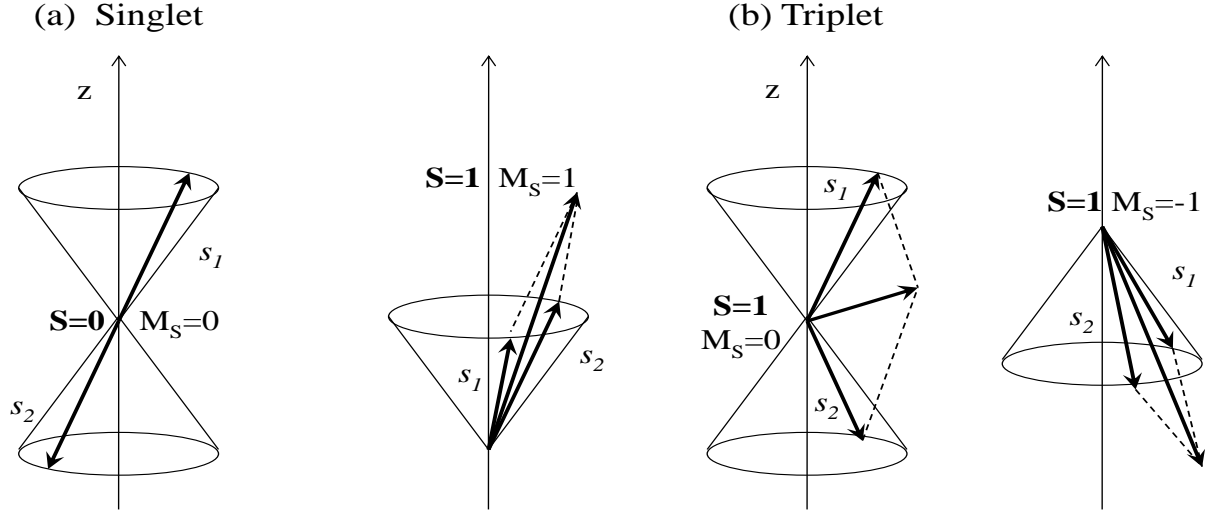


Figure 2.4. Vector representation of singlet and triplet states.

The energy level of a triplet state is in general lower than the energy level of a singlet state of the same orbital configuration. Due to the Pauli principle, two electrons with the same spin orientation can't occupy the same region of space, i.e., electrons with the same spin avoid each other. As a result, the electronic repulsion between two electrons gets smaller lowering the energy of the state [10, 15]. Thus, in general a state with larger total spin makes the system more stable. This is a consequence of Hund's rule [16], which states that for a given electron configuration, the term with maximum multiplicity has the lowest energy.

The energy difference between triplet and singlet states is given by [17]

$$\Delta E_{ST} = E(S_1) - E(T_1) = 2K, \quad (2.3)$$

where K is an exchange integral, a quantum correction to the Coulomb electron-electron repulsion. For two states, upper (u) and lower (l) and two electrons, 1 and 2, K_{ij} is defined as

$$K_{ul} = \iint \psi_u(1)\psi_l(1) \left(\frac{e^2}{r_1 - r_2} \right) \psi_u(2)\psi_l(2) dr_1 dr_2. \quad (2.4)$$

Since K has a positive value, the triplet state always has a lower energy than the singlet state. It is obvious that K is proportional to the spatial orbital overlap integral $\int \psi_i \psi_j d\tau$ [15, 18] where $\int d\tau$ denotes integral over space. As an example, the overlap between n and π^* orbitals is small compared to the overlap between π and π^* orbitals, and consequently, that energy difference between singlet and triplet states for an (n, π^*) orbital configuration will be smaller than for a (π, π^*) configuration.

2.3 Absorption of Light in Organic Molecules

The physical consequence of the absorption or emission of light by organic molecule is the transition of an electron between molecular levels of different energies. The energy difference between two states, E_{12} , is equal to the energy of the absorbed or emitted photon:

$$E_{12} = h\nu = h \frac{c}{\lambda} \quad (2.5)$$

where h is Planck's constant, ν is the frequency, c the speed of light and λ the wavelength. In the most cases, the longest wavelength of absorption corresponds to promotion of an electron from the highest occupied molecular orbital (HOMO) to the lowest unoccupied molecular orbital (LUMO).

Electron properties in molecules are described with the molecular electronic wave function Ψ . $|\Psi|^2 d\tau$ represents the probability of finding the electron in the volume element $d\tau$. Due to The Born-Oppenheimer approximation, electronic and nuclear motion in molecules can be treated separately. At the same time, since magnetic and electric interactions are weak, each electronic motion can be separated into a space component (motion of electrons in orbital) and a spin component. This approximation allows us to write the molecular wave function as:

$$\Psi \sim \phi_e \chi S \quad , \quad (2.6)$$

where ϕ_e is the electronic orbital component of the wave function, χ is the nuclear (vibration) component of the wave function and S is the spin component of the wave function.

The transition rate constant between two states, according to the time-dependent theory, is given by Fermi's Golden rule:

$$k = \frac{2\pi}{\hbar} |V_{fi}|^2 \rho(E_{fi}) \quad , \quad (2.7)$$

where $\rho(E_{fi})$ is the Frank-Condon weighted density of states that ensures energy conservation and is inversely proportional to the energy difference between states ΔE . $V_{fi} = \left| \langle \psi_f | \hat{H} | \psi_i \rangle \right|$ is the electronic matrix element of coupling initial and final states which gives the selection rules for transitions. \hat{H} is the perturbation Hamiltonian. Using the Born-Oppenheimer approximation, V can be separated into the product of an electronic orbital part $\langle \phi_f | \hat{H} | \phi_i \rangle$ representing the orbital overlap of states, the spin part $\langle S_f | S_i \rangle$ and nuclear vibrational part $\langle \chi_f | \chi_i \rangle$ called the Franck-Condon (FC) factor representing the vibrational overlap.

Jablonski diagram. Various intramolecular processes initiated by absorption of light are usually illustrated by the state energy diagram referred to as the Jablonski diagram (Figure 2.5) [15]. S_0 represents the singlet ground state, i.e., the state in which the molecule has the minimum electronic energy. S_1 is the lowest energy excited singlet state and T_1 the lowest triplet state. S_2 and T_2 are higher lying singlet and triplet states. Associated with every electronic state there is a manifold of dense vibrational states.

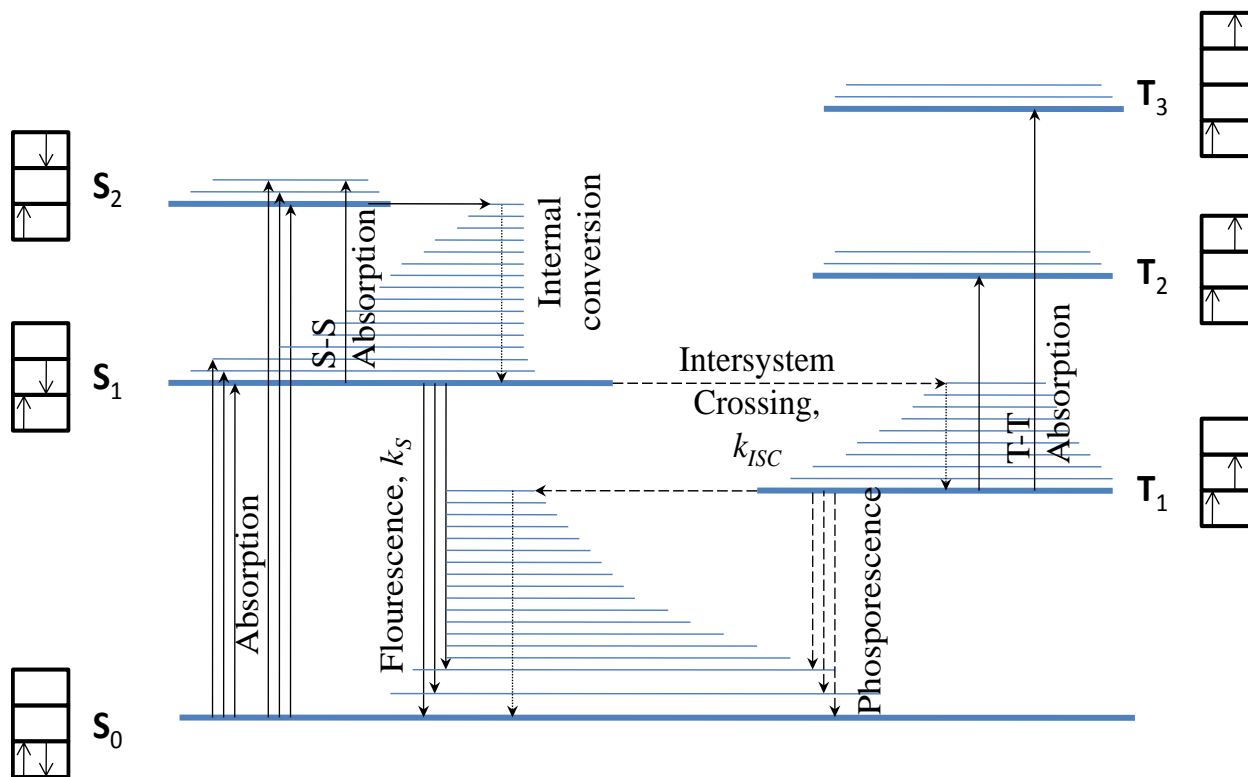


Figure 2.5. Five-level model. S_0 , S_1 and S_n are singlet levels, T_1 and T_n are triplet levels. σ 's are cross-sections. τ 's are transition lifetimes. Boxes next to electronic levels show spin orientations of the two electrons with the highest energy[15].

In Figure 2.5 are shown both radiative and non-radiative processes:

1. "Allowed" singlet-singlet absorption ($S_0 + h\nu \rightarrow S_1$).
2. "Allowed" singlet-singlet emission, called fluorescence ($S_1 + h\nu \rightarrow S_0$).
3. "Allowed" singlet-singlet nonradiative transition called internal conversion (IC) ($S_1 \rightarrow S_0 + \text{heat}$).
4. "Forbidden" transitions between states of different spin, ISC ($S_1 \rightarrow T_1 + \text{heat}$).
5. "Forbidden" triplet-singlet emission, called phosphorescence ($T_1 + h\nu \rightarrow S_0$).

6. “Forbidden” triplet-singlet nonradiative transition ($T_1 \rightarrow S_0 + \text{heat}$).
7. “Allowed” transitions between states of the same spin, ($S_n \rightarrow S_1 + h\nu$ and $T_n \rightarrow T_1 + h\nu$).

Internal conversion (IC) is nonradiative relaxational transition from higher to lower excited state. Difference in energy between higher excited states above S_1 is typically much smaller than between states S_0 and S_1 which leads to larger vibrational overlap between higher excited states.

Fluorescence is emission of light from the molecule after absorption of electromagnetic radiation. Since vibronic overlap between states depends on energy difference, upon excitation to some higher singlet state, S_n , molecule rapidly (sub picosecond time scale) relaxes through nonradiative process called Internal Conversion (IC) to state S_1 . Due to large energy difference and small vibrational overlap between states S_0 and S_1 , lifetime of state S_1 is relatively long so that the radiative fluorescence is most probable channel of depopulation. This is basis of Kasha’s rule [19, 20]: independent of the method of excitation, photon emission from a level of a given multiplicity (singlet or triplet) always occurs from the lowest level of a given multiplicity (although there are some exceptions for materials with a large energy gap between excited states, like in azulene [21, 22]). Fluorescence quantum yield (ϕ_F) is defined as the number of the emitting molecules divided by the number of absorbed photons.

Phosphorescence is emission of light from triplet state, process similar to fluorescence, however on much longer timescale. Since the lifetime of the lowest singlet state, S_1 , is usually the longest among the singlet states, independent of the way of excitation, singlet-triplet transitions usually have the highest probability to occur from level S_1 . Triplet quantum yield (ϕ_T) is defined as the fraction of molecules that make nonradiative transitions from the singlet to triplet state directly or through some intermediate state.

Types of Transitions and Excited States. Electronic transitions between different orbitals give rise to different types of excited states [23, 24]. When an electron is promoted from n to π^* orbital, the transition is then $(n \rightarrow \pi^*)$ and the state is symbolized as (n, π^*) . In the same way, a transition from π to π^* and the state is symbolized as (π, π^*) . Due to the small spatial overlap between n and π^* orbitals, (n, π^*) is partially forbidden and usually of smaller intensity than (π, π^*) state. Both (n, π^*) and (π, π^*) can be singlet or triplet states. Another important transition from the standpoint of molecular photophysics is charge transfer (CT) transitions. CT transitions are common transitions in electron-donor and electron-acceptor complexes that correspond to the transfer of an electron from the donor to the acceptor induced by absorption of light. The CT transition band is in general broad and structureless.

Relative position of excited states depends on both structural and environmental factors. In carbonyl compounds the $n \rightarrow \pi^*$ transition is usually one having the lowest energy, resulting in (n, π^*) as a first excited state. In molecules like a polymethine, a high degree of conjugation lowers the energy difference between π and π^* orbitals and significantly shifts the (π, π^*) state to longer wavelengths, establishing (π, π^*) as a first excited state. Increase of the solvent polarity usually shifts $(n \rightarrow \pi^*)$ transition band to shorter wavelengths and $(\pi \rightarrow \pi^*)$ band to longer wavelengths.

2.3 Intersystem Crossing and Spin-orbit (SO) Coupling

Transitions that include a change of spin are forbidden due to the selection rules ($\Delta s = 0$)[25]. For two possible spin states s_1 and s_2 , spin overlap integral $\int s_1 s_2 d\tau_s$ for a given transition is 1 if $s_1 = s_2$ (spin wave functions are normalized) or 0 if $s_1 \neq s_2$. $\int d\tau_s$ represents integral over spin space. However, this selection rule can be broken under certain internal or external perturbations (described below), which will cause mixing of pure singlet and triplet states allowing transition between states of different spin multiplicity. In that case pure spin state (singlet and triplet) loses its meaning and singlet state possesses a certain degree of triplet character and vice versa.

Perturbations responsible for mixing of pure singlet and triplet states are described with the spin-orbit coupling operator. The spin-orbit interaction is based on the magnetic interaction between the magnetic angular momentum (μ_L) due to the electron's orbital angular momentum (L) and the internal magnetic angular momentum (μ_S) due to an electron spin magnetic moment (S). The electron's orbital motion generates a magnetic torque that changes the orientation of the electron's spin magnetic moment. As a result of this interaction neither orbital nor spin angular momentum are individually conserved anymore. However the spin-orbit coupling provides conservation of total angular momentum, $\hat{j} = \hat{l} + \hat{s}$ by coupling a change in spin with a compensating orbital jump. In that case the change in spin angular momentum is exactly balanced by a change in the orbital angular momentum. As an example, the result of an H_{SOC} operation on a p_y orbital would be an orbital rotation and its conversion into a p_x orbital (Figure 2.6).

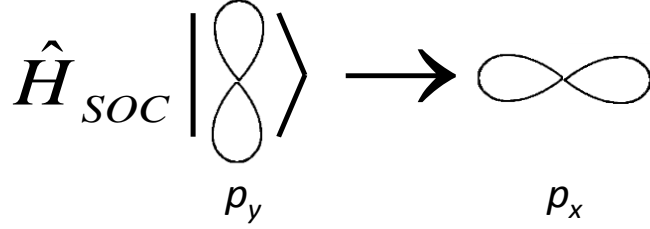


Figure 2.6. Operation of H_{SOC} on p_y orbital

The Hamiltonian of the spin-orbit interaction [26] for a single electron in a central potential field is given by:

$$\hat{H}_{SOC} = \frac{Ze^2}{4\pi\epsilon_0 2m^2c^2} \frac{1}{r^3} \mathbf{S} \cdot \mathbf{L} \quad , \quad (2.8)$$

or shorter by:

$$\hat{H}_{SOC} = \xi(r)(\mathbf{S} \cdot \mathbf{L}) \quad , \quad (2.9)$$

where $\xi(r) = \frac{Ze^2}{4\pi\epsilon_0 2m^2c^2} \frac{1}{r^3}$ is a term which depends on the field of the nucleus and is called the spin-orbit coupling factor. $\mathbf{S} \cdot \mathbf{L}$ is the spin orbit coupling operator.

For a two electron system:

$$\hat{H}_{SOC} = \xi_1 \hat{l}_1 \cdot \hat{s}_1 + \xi_2 \hat{l}_2 \cdot \hat{s}_2 = \frac{1}{2} (\xi_1 \hat{l}_1 + \xi_2 \hat{l}_2) (s_1 + s_2) + \frac{1}{2} (\xi_1 \hat{l}_1 - \xi_2 \hat{l}_2) (s_1 - s_2). \quad (2.10)$$

The second part of Equation 2.10 is responsible for mixing states of different multiplicity.

If we let it act on a pure singlet state $|0,0\rangle$:

$$\begin{aligned}
(s_{z1} - s_{z2})|0,0\rangle &= (s_{z1} - s_{z2}) \frac{1}{\sqrt{2}} (\uparrow\downarrow - \downarrow\uparrow) \\
&= \frac{1}{\sqrt{2}} \frac{\hbar}{2} (\uparrow\downarrow + \uparrow\downarrow + \downarrow\uparrow + \downarrow\uparrow) = \hbar \frac{1}{\sqrt{2}} (\uparrow\downarrow + \downarrow\uparrow) = \hbar|1,0\rangle
\end{aligned} \tag{2.11}$$

resulting in a pure triplet state $|1,0\rangle$.

The energy (E), or strength of the spin orbit coupling for a single electron in a central potential field of nuclear charge + Ze is given as a matrix element:

$$E_{SOC} = \hbar^2 \langle R(r)_{nl} | H_{SO} | R(r)_{nl} \rangle \quad , \tag{2.12}$$

where $R(r)_{nl}$ is a hydrogen wavefunction,

$$E_{SOC} = \frac{e^2 \hbar^2}{4m^2 c^2 a_0^2} \frac{Z^4 [j(j+1) - l(l+1) - 3/4]}{n^3 (l+1)(l+1/2)l} \quad . \tag{2.13}$$

The dependence on Z^4 indicates that with an increase of the atomic number of the central atom, the effective spin-orbit coupling and inter-system crossing rates from singlet to triplet will also increase. This effect is well-known as the “heavy atom” effect [15, 27] (usually atoms with $Z > 10$ are considered heavy [10]). Evidently, to maximize effect of Z electron’s orbit should approach the nuclei as close as possible making the SO coupling a localized effect.

According to Equation 2.6, the intersystem crossing rate, k_{ISC} , is expressed with Fermi's Golden rule for radiationless transitions as [28]:

$$k_{ISC} = \frac{2\pi}{\hbar} \rho \langle \psi(S) | H_{SOC} | \psi(T) \rangle^2 \quad , \tag{2.14}$$

where $\langle \psi(S) | H_{SOC} | \psi(T) \rangle$ is the spin-orbit coupling (SOC) matrix element with corresponding SOC Hamiltonian, H_{SOC} , and again ρ is the Franck–Condon weighted density of states representing energy conservation, this time depending inversely on the singlet-triplet energy splitting, ΔE_{ST} . Obviously, the transition probability gets larger with a decrease of the energy gap. This is the so called Energy gap law [29]. The Franck-Condon density of states ρ at room temperature (T) can be evaluated in the form of a Boltzmann distributed population as [30, 31]:

$$\rho = \frac{1}{\sqrt{4\pi\lambda_M RT}} \exp\left[-\frac{(\Delta E_{ST} + \lambda_M)^2}{4\lambda_M k_B T}\right], \quad (2.15)$$

where λ_M is the Marcus reorganization energy which includes both intramolecular and solvent-induced relaxations and k_B is the Boltzmann constant. As seen from Equations 2.13 and 2.15, the two main parameters contributing to the intersystem crossing rate k_{ST} are the nuclear charge Z, and ΔE_{ST} .

Selection Rules for Intersystem crossing. For the transition matrix elements in (2.14) to be significant it is important that the initial and final orbitals have some degree of overlap. Since operation of H_{SOC} on any orbital is its rotation it is obvious that k_{ISC} will be very small for transitions between states with the same orbital configurations. A visual representation [11] of spin-orbit coupling matrix element is shown in Figure 2.7.

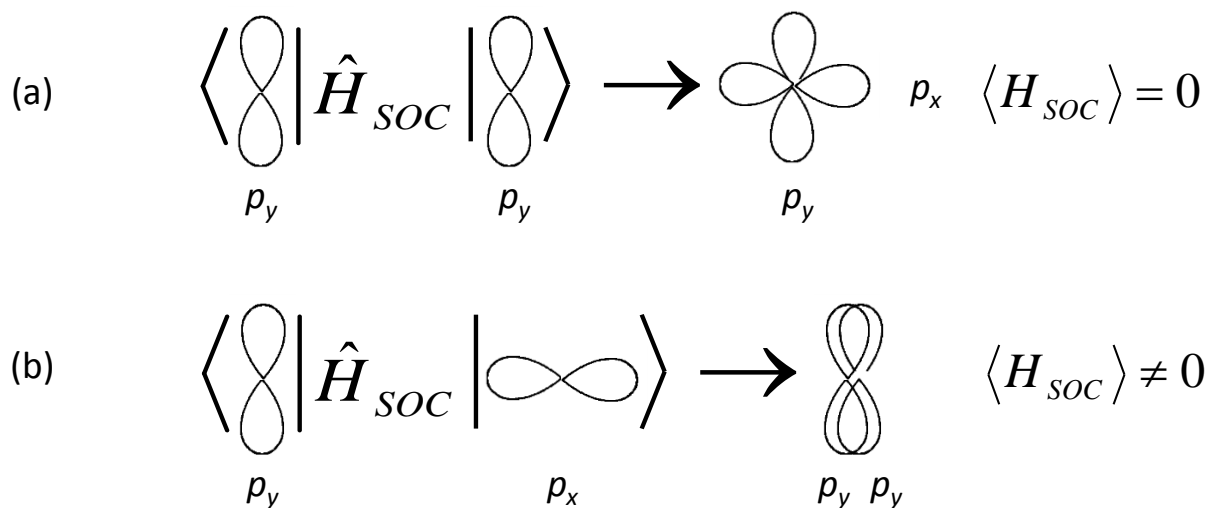
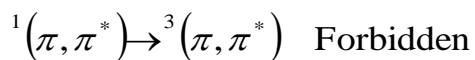
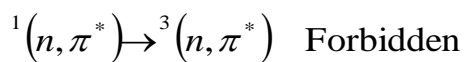
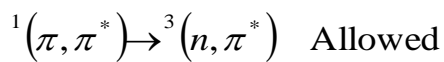
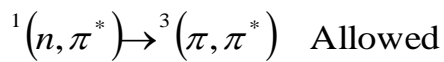


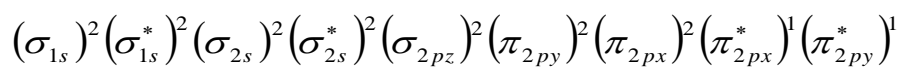
Figure 2.7. Visual representation of spin-orbit coupling matrix element for transitions between (a) states of the same orbital configurations and (b) states of different orbital configurations.

For molecules that have low lying excited states of different spatial configurations relatively close in energy, for example (n, π^*) and (π, π^*) states, the previous considerations are the basis for the so called El-Sayed selection rules for ISC [32]:



2.4 Singlet Oxygen

Molecular oxygen is one of the few compounds (oxygen, methylene, nitrene etc.) with a triplet ground state ($^3\text{O}_2$) and first singlet excited state ($^1\text{O}_2$) which is opposite to that of most organic molecules. The explanation for such an interesting property lies in the particular electronic configuration of oxygen's ground state [23]. A total of 16 electrons are placed in the available orbitals according to the Aufbau and Hund rules:



The last two electrons occupy two degenerate π^* orbitals. According to Hund's rule the lowest energy configuration for this system will be with both spins parallel.

Molecular oxygen has two relatively low lying singlet excited states shown in Figure 2.8.

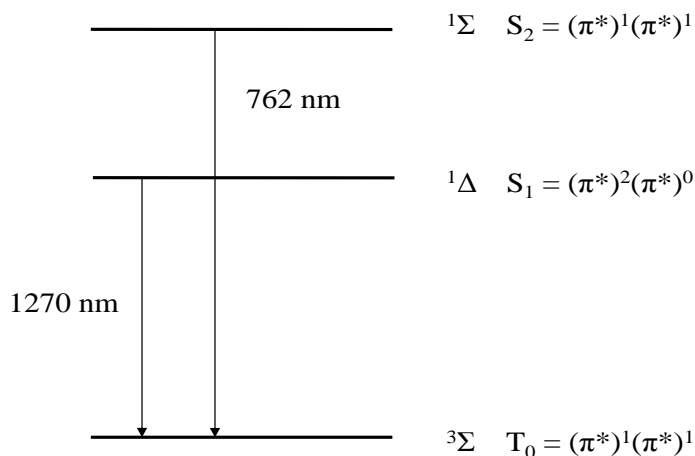


Figure 2.8. Energy of the two lowest excited states of molecular oxygen. Orbital configurations of just the last two electrons are shown. Σ , Δ and Σ are spectroscopic symbols of the ground, first and second excited states respectively.

Due to the specific chemical reactivity, singlet oxygen can be used for many applications such as water disinfection and purification, organic synthesis and specifically for photodynamic therapy (PDT) of cancer. PDT treatment combines drug delivery by a molecular sensitizer upon illumination of an appropriate wavelength (typically within the therapeutic window of 600-1000nm) to create the $^1\text{O}_2$, which destroys abnormal cells.

Because of the different spin multiplicity of the ground and first singlet excited state direct excitation of molecular oxygen is not a very efficient process. The most common method of producing $^1\text{O}_2$ is through photosensitization [33]. Photosensitization is a process where an organic molecule, called the sensitizer, is excited by one- or two- photons, to a higher singlet excited state. For centrosymmetric molecules, states populated by one-photon and two-photon absorption will be, in general, different due to the selection rules. As already mentioned, since the lifetime of the lowest singlet state, S_1 , is usually the longest, independently of the method of excitation, ISC will happen in most cases from the lowest singlet state, S_1 . The population of the triplet state can be quenched by molecular oxygen in the ground state (triplet-triplet annihilation) through two possible channels: energy transfer (Type one) or charge transfer (Type two). An outcome of the triplet-triplet annihilation is oxygen in the singlet excited state $^1\text{O}_2$ ($^1\Delta_g$) and the photosensitizer in the ground singlet state [34]. A graphical description of the photosensitization process is shown in Figure 2.9. Obviously, production of singlet oxygen will highly depend on the ISC rate of the photosensitizer. The quantum yield of singlet oxygen generation (ϕ_Δ) represents the number of moles of singlet oxygen formed per mole of photons absorbed [11]. Generation of singlet oxygen upon one-photon excitation of a molecular sensitizer has been extensively studied over the past decades [35, 36]. Recent interest in PDT has shifted toward

development of two-photon absorbing sensitizers which allows longer wavelengths of excitation, a deeper length of light penetration through tissue with less scattering and higher spatial resolution[37, 38].

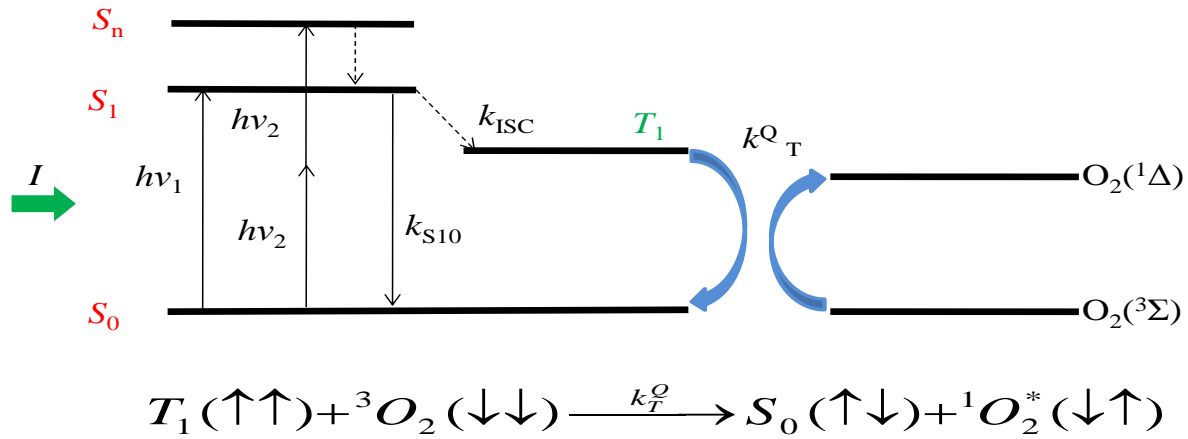


Figure 2.9. Quenching of the photosensitizer's triplet state and production of singlet oxygen. k_T^Q is the quenching rate of T_1 .

In addition to the previously described method, singlet oxygen can also be produced by quenching of the state S_1 . As opposed to the triplet-triplet annihilation process quenching of the S_1 state results in the sensitizer being in the first excited triplet state and oxygen in the excited singlet state. Quenching of both states S_1 and T_1 at the same time would give a maximum value of $\phi_\Delta = 2$. However, the main requirement for quenching of state S_1 is that ΔE_{ST} be larger than the difference between ground and first excited state energies of molecular oxygen. Since all materials in this work have much smaller values of ΔE_{ST} , photosensitization of state S_1 will be ignored.

2.5 Nonlinear Absorption and Refraction

Here we are considering a media with inversion symmetry where all even-order susceptibility tensor elements are zero. For a monochromatic beam with frequency ω , wavevector $k = n_0\omega/c$, amplitude A , and phase Φ that travels in the z direction

$$E = Ae^{i\Phi}e^{i(kz-\omega t)} \quad , \quad (2.16)$$

irradiance is defined as

$$I = \frac{n_0 c \epsilon_0}{2} A^2 \quad (2.17)$$

where ϵ_0 is the permittivity of free space. Applying Maxwell's equations to equation (2.16) for a nonlinear medium with polarization response given by (1.1) using the thin sample and slowly varying envelope approximations, we can obtain equations for the change of irradiance and total phase inside the medium [39]:

$$\frac{dI}{dz} = -\alpha I \quad , \quad (2.18)$$

$$\frac{d\Phi}{dz} = nk_0 \quad . \quad (2.19)$$

α , total absorption coefficient and n , total refractive index are given by:

$$\alpha = \alpha_0 + \alpha_{NL} \quad (2.20)$$

$$n = n_0 + n_{NL} \quad (2.21)$$

where α_0 and α_{NL} are linear and nonlinear absorption coefficients and n_0 and n_{NL} are linear and nonlinear refractive indexes respectively. Change of phase only due to the nonlinear effects:

$$\frac{d(\Delta\Phi)}{dz} = n_{NL}k_0 \quad (2.22)$$

Both α_{NL} and n_{NL} depend on the input electric field. Taking into account only third order term in equation (1.1) nonlinear absorption and refraction are given by relations:

$$\alpha_{NL} = \alpha_2 I \quad (2.23)$$

$$n_{NL} = n_2 I \quad (2.24)$$

Equation (2.23) represents 2PA while equation (2.24) represents the nonlinear optical Kerr effect. 2PA coefficient α_2 and the nonlinear refractive index n_2 are related to the complex susceptibility $\chi^{(3)}$ through expressions [39]:

$$\alpha_2 = \frac{3k_0}{2n_0^2 c \epsilon_0} \text{Im}(\chi^{(3)}(\omega; \omega, -\omega, \omega)) \quad , \quad (2.25)$$

$$n_2 = \frac{3}{4n_0^2 c \epsilon_0} \text{Re}(\chi^{(3)}(\omega; \omega, -\omega, \omega)) \quad . \quad (2.26)$$

The 2PA cross section, δ_{2PA} , is used to describe the 2PA properties of individual molecule. δ_{2PA} , is given in units of $1 \times 10^{-50} \text{ cm}^4 \text{ photon}^{-1} \text{ molecule}^{-1}$ or ‘‘Goppert-Mayer’’ (GM). In SI units δ_{2PA} is defined as

$$\delta_{2PA}(\omega) = \frac{3h\omega^2}{2n_0^2 c^2 \epsilon_0 N} \text{Im}(\chi^3(-\omega; \omega, -\omega, \omega)) \quad . \quad (2.20)$$

As already mentioned, the multitude of energy levels in organic compounds allows successive transitions between different states, giving rise to ESA. Being dependent on fluence rather than intensity, ESA belongs to the class of so called slow or cumulative nonlinearities.

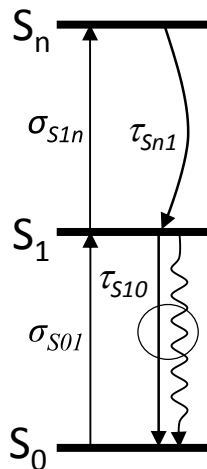


Figure 2.10. Energy level diagram of a three-level system of only singlet transitions. S_0 , S_1 and S_n are singlet electronic energy levels. σ_{Sij} and τ_{Sij} are cross-sections and lifetimes. τ_{S10} includes both radiative and non-radiative decays.

When a laser pulse is incident on a material it will first excite part of population from the ground state to the first excited state. If lifetime of the first excited state is not too short compared to pulse time width, the remaining photons from the pulse can additionally excite part of the first excited state population to a higher excited state. The propagation equation for the beam intensity in the case of ESA, taking into consideration only the simplified all singlet 3-level model (Figure 2.10.), is given by relation 2.21.

$$\frac{dI(z)}{dz} = -\sigma_{S0I}N_0I - \sigma_{S1n}N_{S1}I \quad (2.21)$$

In Equation 2.21 σ_{S01} is the ground state absorption cross section, σ_{S1n} is the excited state absorption cross section and N_{S1} is the population of the first excited state.

Change in the phase due to ESA is given by

$$\frac{d(\Delta\Phi)}{dz} = \sigma_{r,S1} N_{S1} \quad (2.22)$$

where $\sigma_{r,S1}$ is the excited state refraction cross section.

ESA vs. 2PA For simplicity we ignore depletion of the ground state so that $N_0(t) \cong N_0$ at all times along with population of the higher excited states due to sub picosecond relaxation time to the first excited state. The rate equation for the first excited state is;

$$\frac{dN_{S1}}{dt} = \frac{\sigma_{S01} N_0}{\hbar\omega} I \quad (2.22)$$

$$N_{S1}(t) = \frac{\sigma_{S01}}{\hbar\omega} \int_{-\infty}^t I(t') dt' \quad (2.23)$$

$$\frac{dI(t')}{dz} = -\sigma_{S01} N_0 I(t') - \sigma_{S1n} I(t') \frac{\sigma_{S01}}{\hbar\omega} \int_{-\infty}^t I(t') dt' \quad (2.24)$$

Integrating equation (2.23) over time and taking $\int_{-\infty}^{\infty} I(t) dt = F$, where F is the fluence we

obtain;

$$\frac{dF(z)}{dz} = -\sigma_{S01} N_0 F(z) - \frac{\sigma_{S01} \sigma_{S1n}}{\hbar\omega} \int_{-\infty}^{\infty} I(t) \left[\int_{-\infty}^t I(t') dt' \right] dt \quad (2.25)$$

Integrating equation (2.24) by parts yields;

$$\frac{dF(z)}{dz} = -\sigma_{s01} N_0 F(z) - \frac{\sigma_{s01} \sigma_{s1n}}{\hbar \omega} \frac{1}{2} F^2(z) , \quad (2.26)$$

or

$$\frac{dF(z)}{dz} = -\alpha_1 F(z) - \alpha_2^{\text{eff}} F^2(z) . \quad (2.27)$$

This equation is similar to equation (2.17); however, this is not a $\chi^{(3)}$ process but rather a $\chi^{(1)} \cdot \chi^{(1)}$ process.

CHAPTER 3. LASER SYSTEMS AND EXPERIMENTAL TECHNIQUES

All nonlinear experiments in this work are done with picosecond (pulse width $\tau_{\text{HW1/e}} \sim 15$ ps) and femtosecond (pulse width $\tau_{\text{HW1/e}} \sim 100$ fs) laser systems.

3.1 Picosecond Laser

The light source for the picosecond experiments was an EKSPLA PL-2143 Nd:YAG laser operating at 1064 nm with a 10 Hz repetition rate. This laser system produces pulses with duration around 15 ps (HW1/eM) of energy ~ 100 mJ. The laser schematic is given in Figure 3.1. The main cavity consists of mirrors M1 and M5, both with transmittance 99%. The oscillating optical field builds up by pumping a Nd:YAG rod R1 with a flashlamp. Modelocking is achieved passively by saturable absorption (solution of modelocking dye in ethanol) and actively by Pockels cell PC1. The pulse travels back and forth in the cavity ~ 200 times ($2\mu\text{s}$). Through dynamic and fixed losses the amplitude of the pulse is kept at a constant and relatively low level to avoid energy depletion of the Nd:YAG rod. Pulse amplitude and stability is controlled by a negative feedback loop.

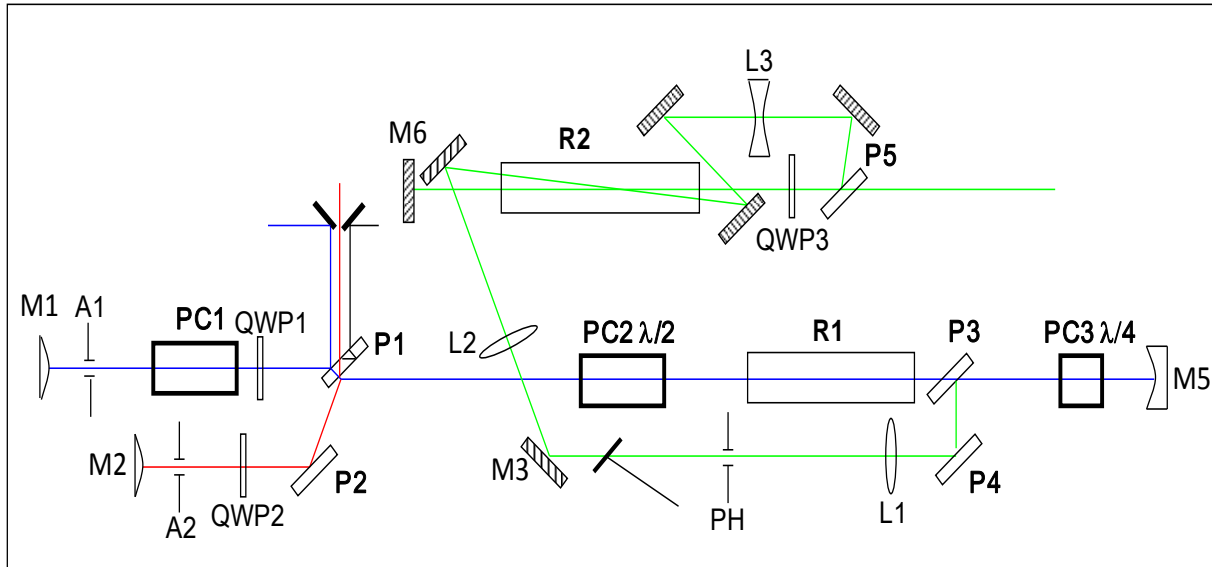


Figure 3.1. Layout of a picosecond laser: A-aperture, BS-beamsplitter, L-lens, M-mirror, PC-pockels cell, QWP-quarter wave plate, R-Nd:YAG rod

After formation of a stable pulse in the master oscillator. Pockels cell PC2 and polarizer P1 switch the pulse to a regenerative oscillator consisting of mirrors M2, M5 and rod R1. In the regenerative amplifier the pulse is amplified to $\sim 500\mu\text{J}$. After achieving peak power, the pulse is directed to the power amplifier by Pockels cell PC3 and polarizer P5.

Just before the amplifier the pulse goes through a spatial filter to remove all other modes except TEM_{00} . The pulse then travels through the pumped amplifier rod three times and reaches its maximum energy of $\sim 100\text{ mJ}$.

The picosecond OPG/A schematic is given in Figure 3.2. At the entrance of the OPG/A, the 355nm beam is split with beam splitter BS1 into two beams, one with 15% of the total energy and one with 85%. The weak portion of the beam is transformed with a small aperture into a flat top beam and then focused into a Lithium triborate (LiB_3O_5 - LBO) crystal. Mirror M9 reflects the beam back for one more pass through the crystal. This beam is used as a seed beam of parametric fluorescence for the amplification process. After reflection from a grating and passing through another spatial filter, the seed is recombined with a strong 355nm pulse and amplified in two passes through an LBO crystal. The output wavelength of the signal or idler is selected with a set of band-pass filters. The wavelength range of the system is from 420nm to 2.3 μm with a small gap between 680 nm and 740 nm (Figure 3.3a.).

In addition, this system is capable of producing mid-IR wavelengths through the difference frequency generation, DFG, process using a AgGaS_2 crystal. The tuning range for the DFG process using AgGaS_2 crystal is from 2.3 μm to 11.5 μm (Figure 3.3b.).

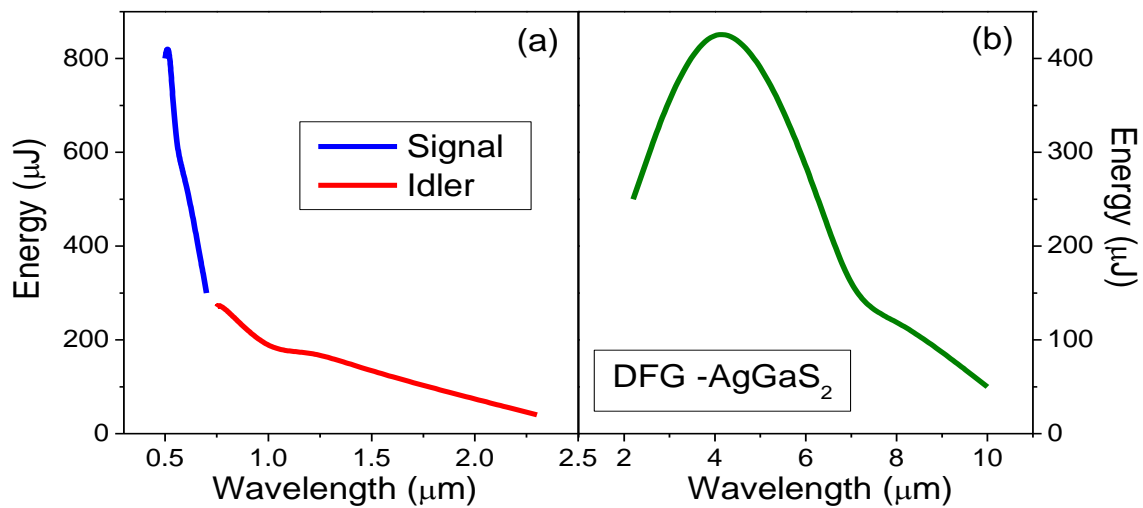


Figure 3.3. Tunability range for the picosecond OPG/OPA.

3.3 Femtosecond Laser System

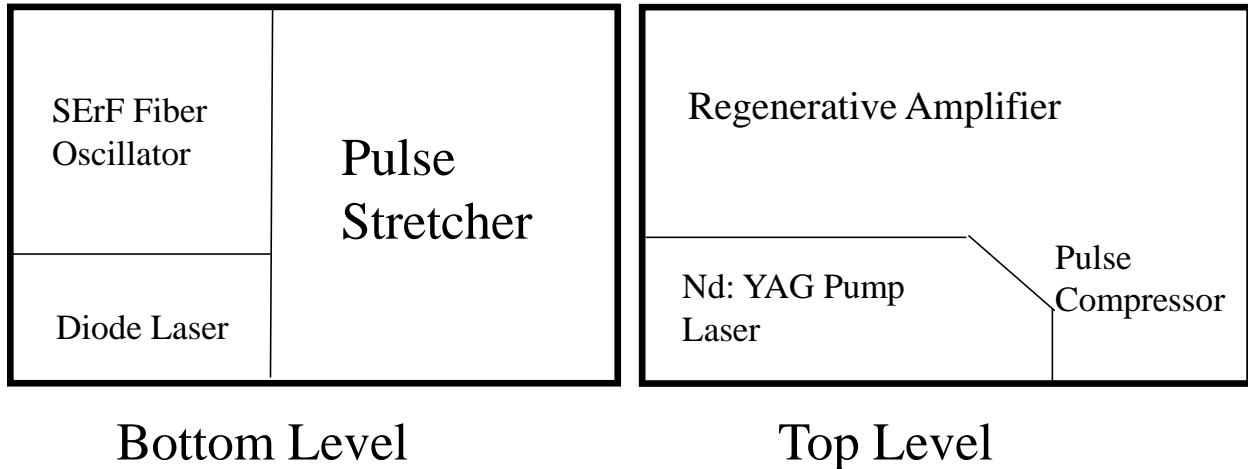


Figure 3.4. Femtosecond laser system layout

The femtosecond laser used in this work is a Clark CPA-2210 system operating at 775 nm with a repetition rate of 1kHz and a pulsewidth of ~100 fs (HW1/eM), producing ~1.6mJ pulses. The bandwidth of the laser is ~7 nm (FWHM). The system layout (bi-level design) is shown in Figure 3.4.

The seed beam in the Ti:Sapphire regenerative amplifier cavity is a 775 nm beam at a 27 MHz repetition rate. This seed is the second harmonic of a 1550 nm Erbium doped fiber ring laser pumped by a solid-state fiber-coupled diode laser operating at 980nm. The seed pulse is first stretched to ~200 ps by a multi-pass reflecting diffraction grating and then switched to a regenerative amplifier (Figure 3.5.) by a Pockels cell. The gain medium of the regenerative amplifier is pumped by 532nm, ~200ns pulse at 1 KHz Q-switched frequency doubled Nd:YAG laser. The pulse is amplified in the Ti:Sapphire cavity with tens of passes until the mJ energy level is reached and then switched out with a Pockels cell. The pulse is finally compressed using a

multi-pass transmission grating. The process in which the pulse is first stretched, then amplified and in the end compressed again is called Chirped Pulse Amplification (CPA). The CPA approach allows large amplification levels without damaging the gain medium.

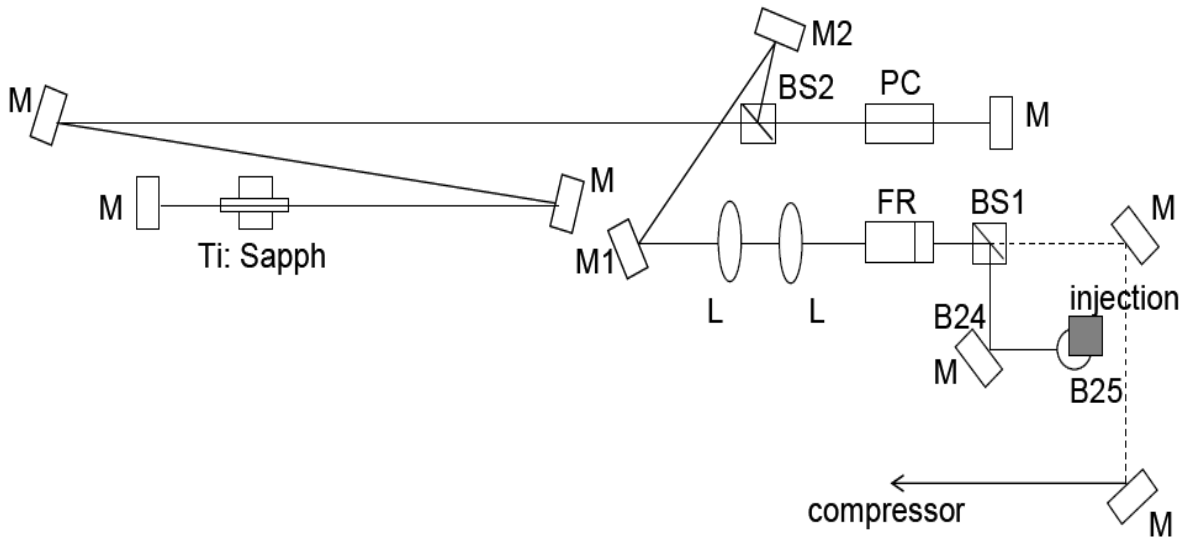


Figure 3.5. Layout of the regenerative amplifier cavity: L-lens, BS-beamsplitter, PC-pockels cell, FR-Faraday rotator.

3.4 Femtosecond OPG/OPA and DFG

The output of the Clark CPA-2110 laser is used to pump an OPG/A, Traveling-wave Optical Parametric Amplifier of Superfluorescence (TOPAS C) produced by Light Conversion, Ltd. The pump beam is first divided into three beams with two beamsplitters. The first pump beam is used for generation of a broad band superfluorescence signal (SFL) inside a Barium Borate- β -BaB₂O₄ (BBO) crystal. The SFL serves as the seed for the next two steps of

amplification where the beam is again overlapped with the other two pumps. The wavelength is selected by reflection from a grating after a fourth pass through the BBO and by rotation of the crystal in the phase-match plane. Additional wavelength selection is obtained through second and fourth harmonic generation and sum- and difference-generation of the signal and idler by motorized mixer crystals on the outside of the OPG/A. The layout of the femtosecond OPG/OPA is shown on Figure 3.6.

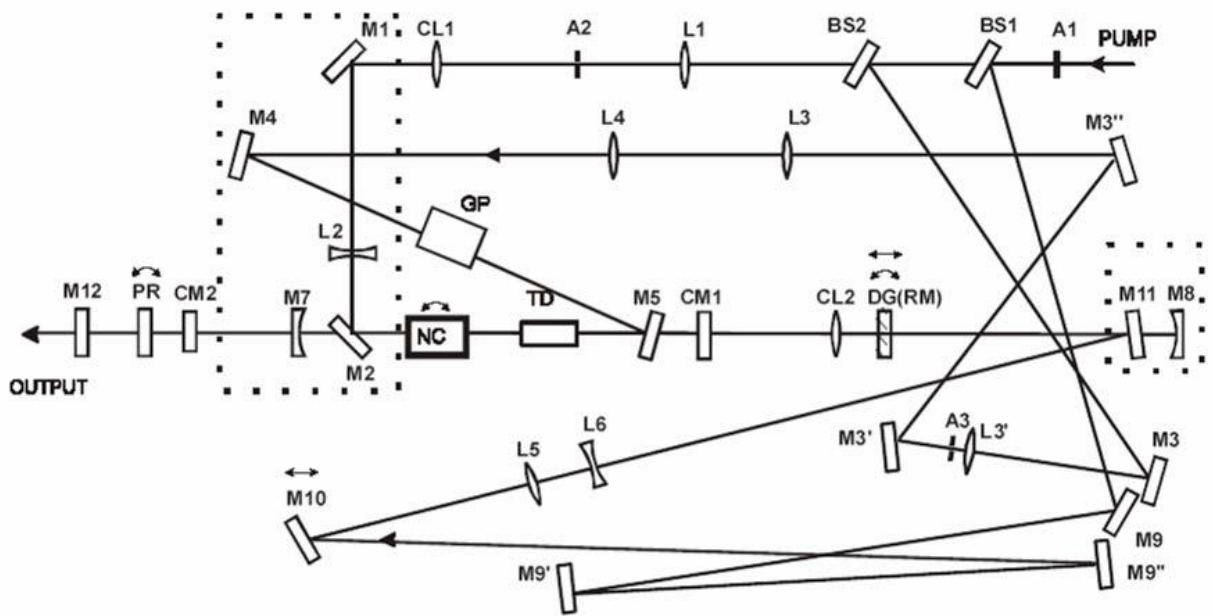


Figure 3.6. Layout of the femtosecond OPG/OPA: A-aperture, BS-beamsplitter, L-lens, M-mirror, CL-cylindrical lens, CM-cylindrical mirror, NC-nonlinear crystal, DG-diffraction grating, GP-fused silica plate, TD-time delay, PR-polarization rotator.

3.5 Beam Parameter Calibration

Accurate determination of nonlinear optical parameters using pump-probe and Z-scan requires accurate knowledge of laser beam parameters; energy, temporal pulse width and beam waist. The temporal pulse width is usually measured by second order autocorrelation while the beam waist is measured by knife edge scans.

In the case of Z-scan, the multiple knife edge scans are performed by scanning the beam in the direction perpendicular to the beam from one side of the focus to the other. This allows determination of the minimum beam waist at the focus and also gives a determination of the M^2 parameter which gives information on the beam quality. On the other hand, pump-probe requirements for determination of the beam waist are not so strict. The pump-probe requires only an exact determination of the beam spot-size at the position of sample.

Examples of spatial beam profiles, autocorrelation measurements and knife edge scans are shown in Figure 3.7.

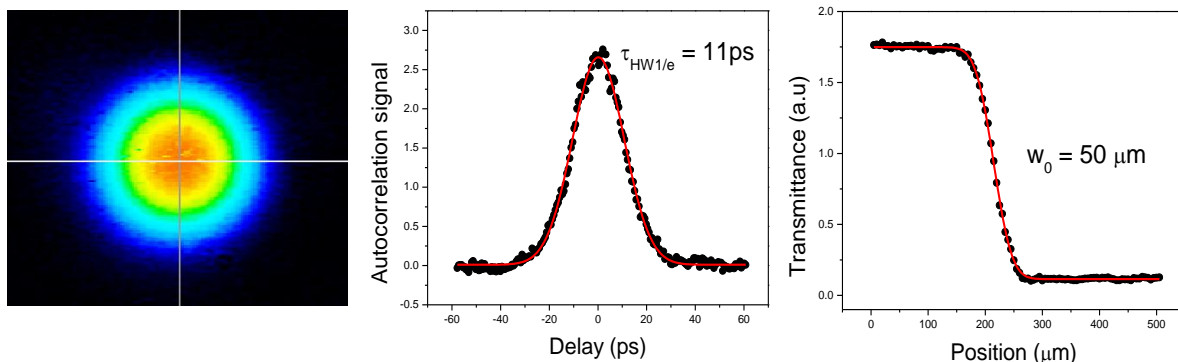


Figure 3.7. Beam profile at 532 nm (second harmonic of Nd:YAG laser taken with WinCam D CCD camera (a), Autocorrelation measurement ($\tau_{HW1/e} = 11 \text{ ps}$) and (c) Knife edge scan ($w_0 = 50 \mu\text{m}$).

3.6 Linear Spectroscopic Techniques

Measurements of the linear properties of organic molecules include one-photon absorption (1PA) spectra, one-photon fluorescence spectra, fluorescence quantum yield (ϕ_F) and one-photon excitation fluorescence anisotropy spectra.

The 1PA spectrum and absorption optical density (OD) were measured with a Cary-500 UV-Vis-NIR (170nm to 3300nm) spectrophotometer. The molar extinction coefficient (ε) can be determined from OD from the relation:

$$\varepsilon = -\frac{OD}{C \cdot L} \quad (3.1)$$

where C is the concentration in molarity ($M = \text{mol/liter}$), and L is the sample length in cm.

For all nonlinear measurements in this work, of great importance is a very accurate determination of the ground state absorption cross section (σ_{S01}) at the wavelength where the measurements are performed. σ_{S01} and ε are connected through the simple relation:

$$\sigma_{S01} = 1000 \ln(10) \frac{\varepsilon}{N_A} = 3.82 \cdot 10^{-21} \varepsilon \quad , \quad (3.2)$$

where N_A is Avogadro's number.

Fluorescence spectra are measured with a PTI QuantaMaster spectrofluorimeter with a nitrogen cooled (77 K) Hamamatsu R5509-73 photomultiplier using 10 mm optical quartz cells. All fluorescence spectra have to be corrected for the spectral responsivity of the detection system. ϕ_F is measured using the standard method of comparison with a standard dye Cresyl Violet perchlorate. Cresyl Violet perchlorate has a fluorescence quantum yield, $\phi_F = 0.54$, an absorption peak at 594 nm and fluorescence peak at 620 nm [40].

From spectroscopic measurements, we can estimate the fluorescence lifetime $\tau_S = \eta \tau_N$. τ_N which is the natural lifetime and can be calculated from the Strickler-Berg equation [41]:

$$\frac{1}{\tau_N} = 2.88 \times 10^{-9} n^2 \varepsilon^{\max} \left[\frac{\int F(\nu) d\nu \times \int \frac{\varepsilon(\nu)}{\nu} d\nu}{\int \frac{F(\nu)}{\nu^3} d\nu} \right], \quad (3.3)$$

where n is the refractive index of the solvent, ε^{\max} is the molar absorbance at the peak of the absorption band, and $F(\nu)$ and $\varepsilon(\nu)$ are the normalized fluorescence and absorption spectra.

The spectral positions of the optical transitions and relative orientation of the transition dipole moments can be determined with one-photon excitation anisotropy measurements [19]. For these measurements, to reduce depolarization effects caused by rotational reorientation, the sample is prepared in the viscous solvent poly-tetrahydrofuran (pTHF). To avoid reabsorption of the fluorescence the concentration of the sample should be relatively low ($C \sim 1 \mu\text{M}$).

For a given excitation wavelength, λ , the anisotropy value, r , can be calculated from the equation;

$$r(\lambda) = \frac{I_{\parallel}(\lambda) - I_{\perp}(\lambda)}{I_{\parallel}(\lambda) + 2I_{\perp}(\lambda)}, \quad (3.4)$$

where $I_{\parallel}(\lambda)$ and $I_{\perp}(\lambda)$ are the intensities of the fluorescence signal, usually measured near the fluorescence maximum. $I_{\parallel}(\lambda)$ is polarized parallel while $I_{\perp}(\lambda)$ is perpendicular to the polarization of the excitation light. Anisotropy value ranges from 0.4 to -0.2, depending on relative orientation between absorption and emission dipole moments. Values near 0.4 in the excitation anisotropy spectrum indicate a small angle between the absorption and emission transition dipoles, suggesting allowed one-photon absorption (1PA) transitions; while valleys

indicate large angles between these two dipoles, suggesting forbidden 1PA transitions, such as transitions between states of the same symmetry. Valleys in the anisotropy spectra could indicate the positions of allowed 2PA transitions. Quantum-chemical calculations together with analysis of the anisotropy spectra allow determination of the position of 1PA forbidden transitions, such as transitions between states of the same symmetry, indicating possible transition energies of the final electronic states in the 2PA spectra. This information cannot be obtained from linear absorption measurements.

The same approach is used to measure the quantum yield of singlet oxygen generation, (ϕ_{Δ}). The singlet oxygen, $^1\text{O}_2$, luminescence at ≈ 1270 nm is measured at room temperature using a PTI QuantaMaster spectrofluorometer with a nitrogen cooled Hamamatsu R5509-73 photomultiplier tube detector. The principle of determination of the $^1\text{O}_2$ generation quantum yield is the same as the one used for the determination of ϕ_F . In this case, the dye used as a reference is Acridine in ACN with known $\phi_{\Delta} = 0.82$ [42]. A typical plot of the singlet oxygen luminescence is shown on Figure 3.8.

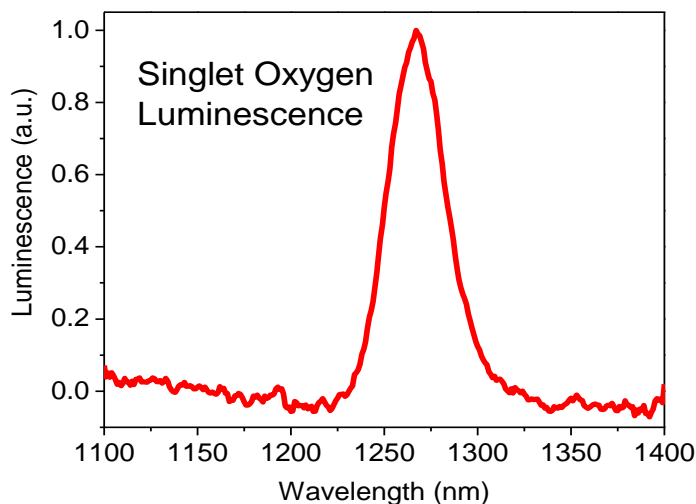


Figure 3.8. Singlet oxygen luminescence spectrum.

Photochemical stability of the dye was determined by monitoring the linear absorption spectra. A change greater than 10% (that of the photodamaged area under the spectrum divided by the initial, undamaged area under the spectrum) in linear absorption is signature of poor photochemical stability of dye. The linear absorption spectrum should be measured before and after every experiment. An example of a typical photochemical decomposition of a dye, SD-S 7508, caused with a fluence of $\sim 190 \text{ mJ/cm}^2$ illumination is shown in Figure 3.9. 20% change in the linear absorption spectrum of this dye indicates special care should be taken during experimental procedure. Usually a flow cell is used to exchange the solution in the focal volume with undamaged dye solution.

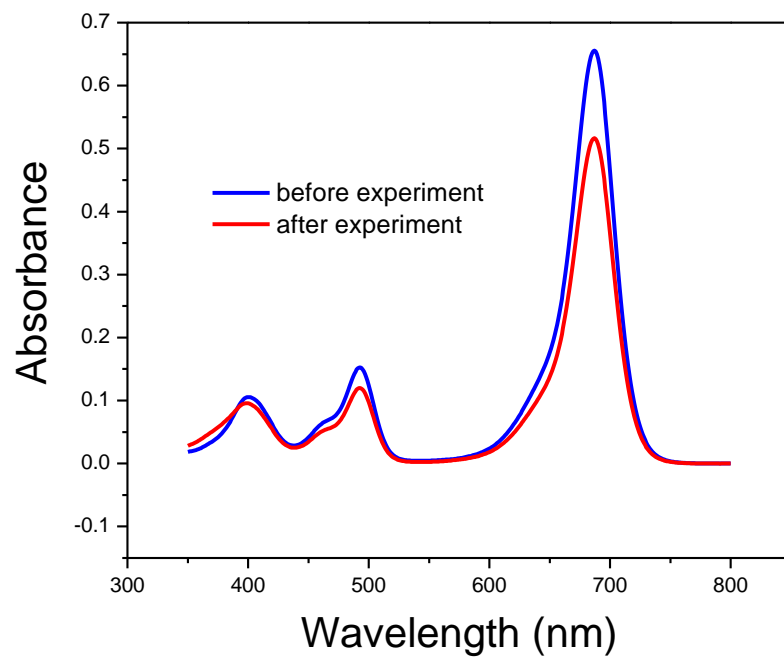


Figure 3.9. Linear absorption of dye SD-S 7508 in toluene before and after experiment.

3.7 Non-linear Spectroscopic Techniques

3.7.1 Pump-probe Method

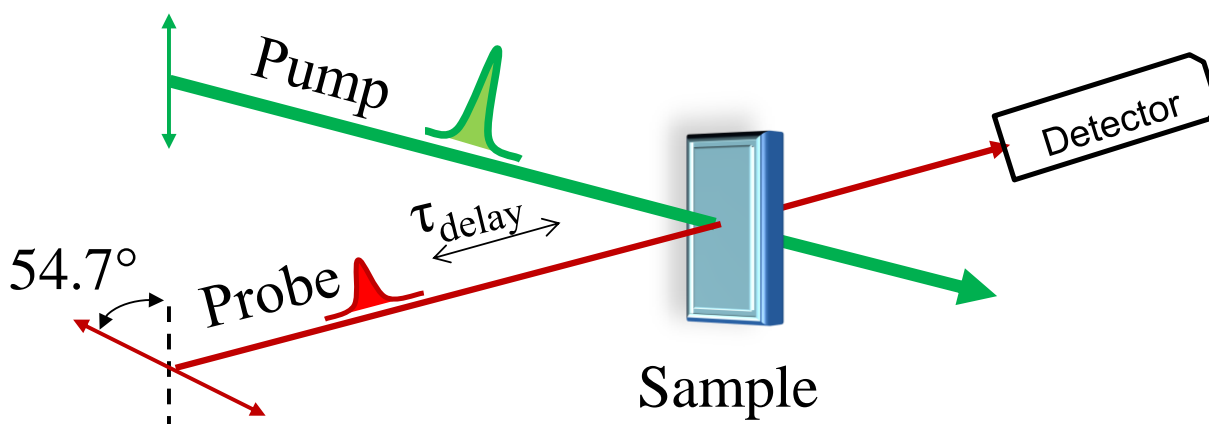


Figure 3.10. Schematic of a pump-probe experiment.

Pump-probe is a standard experimental method in nonlinear optics for characterizing organic molecules. The basic idea is to use two pulses; strong pump pulse and weak probe pulse (usually, probe pulse is delayed in time with respect to the pump pulse). The wavelength of the two pulses can be the same (degenerate pump-probe) or different (non-degenerate pump-probe) depending on the experiment requirements. The pump excites population in the molecule from the ground state to some higher singlet excited state S_n . Redistribution of population in the system results in optical nonlinearity. By monitoring the transmittance of the probe with various time delays it is possible to obtain information about the population dynamics as a function of time and to determine the mechanisms that govern the nonlinear processes.

In all pump-probe experiments in this work the polarization angle of the probe is set at 54.7° (the “magic angle”) with respect to the polarization of the pump to avoid pump induced

orientational diffusional effects [19, 43]. The “Magic angle” is the 3-dimensional analog of 45° in 2-dimensions and it comes from the average value of $\cos^2(\theta) = 1/3$. All pump-probe experiments were performed in 1 mm optical quartz cells.

The standard five-level energy diagram (simplified Jablonski diagram shown in Figure 2.5) describing light absorption and emission of organic molecules with singlet-singlet (SS) and triplet-triplet (TT) transitions and their relaxation processes is presented in Figure. 3.11. As already mentioned, there are several competing processes to depopulate the S_1 state which include: (1) radiative (fluorescence) and non-radiative decay (internal conversion) into the singlet ground state (S_0) with lifetime τ_{S10} ; (2) excitation to the higher-lying singlet states (S_n) by sequential absorption of another photon; and (3) ISC leading to population of a triplet state with lifetime τ_{ISC} . The rate of depopulation of the singlet excited state ($k_S = 1/\tau_S$) is equal to the fluorescence decay rate ($k_{S10} = 1/\tau_{S10}$) plus the intersystem crossing rate, ISC ($k_{ISC} = 1/\tau_{ISC}$); i.e., $k_S = k_F + k_{ISC} = 1/\tau_S = 1/\tau_{S10} + 1/\tau_{ISC}$.

The decay from T_1 to S_0 can also follow a non-radiative or radiative (phosphorescent) pathway; however, the lifetime of the T_1 state is long (usually 10^{-8} to 10^2 s) due to the spin-forbidden nature of a triplet-singlet transition so in most cases it can be ignored in a description of the excited state dynamics.

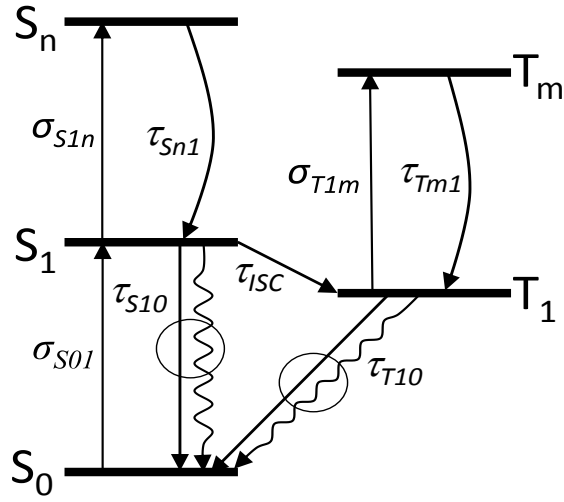


Figure 3.11. Energy level diagram of a five-level system of singlet and triplet transitions. S_0 , S_1 and S_n are singlet while T_1 and T_m are triplet electronic energy levels. σ_{ij} and τ_{ij} are cross-sections and lifetimes pertaining to the particular singlet and triplet transitions, respectively. As indicated by the circles, τ_{S10} and τ_{T10} include both radiative and non-radiative decays.

The propagation and rate equations for the full five-level system are described in Equations (3.5) and (3.6):

$$\frac{dI}{dz} = -\sigma_{S0I}N_{S0}I - \sigma_{S1n}N_{S1}I - \sigma_{T1m}N_{T1}I, \quad (3.5)$$

$$\begin{aligned} \frac{dN_{S0}}{dt} &= -\frac{\sigma_{0I}N_{S0}I}{\hbar\omega} + \frac{N_{S1}}{\tau_{S10}} + \frac{N_{T1}}{\tau_{T10}} \\ \frac{dN_{S1}}{dt} &= \frac{\sigma_{0I}N_{S0}I}{\hbar\omega} - \frac{N_{S1}}{\tau_{S10}} - \frac{\sigma_{S1n}N_{S1}I}{\hbar\omega} + \frac{N_{Sn}}{\tau_{Snl}} - \frac{N_{S1}}{\tau_{ISC}} \\ \frac{dN_{Sn}}{dt} &= \frac{\sigma_{S1n}N_{S1}I}{\hbar\omega} - \frac{N_{Sn}}{\tau_{Snl}}, \\ \frac{dN_{T1}}{dt} &= -\frac{\sigma_{T1m}N_{T1}I}{\hbar\omega} + \frac{N_{Tm}}{\tau_{Tm1}} + \frac{N_{S1}}{\tau_{ISC}} - \frac{N_{T1}}{\tau_{T10}} \\ \frac{dN_{Tm}}{dt} &= \frac{\sigma_{T1m}N_{T1}I}{\hbar\omega} - \frac{N_{Tm}}{\tau_{Tm1}} \end{aligned}, \quad (3.6)$$

where I is the irradiance, z is the depth in the sample; N_{S0} , N_{S1} , N_{Sn} , N_{T1} , N_{Tm} are populations in the singlet, S_0 , S_1 , and S_n and triplet, T_1 and T_m states, respectively. τ_{S10} and τ_{T10} are the fluorescence and phosphorescence lifetimes (both including radiative and nonradiative decays). The total population, $N_{TOT} = N_{S0} + N_{S1} + N_{Sn} + N_{T1} + N_{Tm}$, is conserved at all times and it is determined from the linear Beer-Lambert's law:

$$T_L = \exp(-\alpha_0 L) , \quad (3.7)$$

where $\alpha_0 = \sigma_{S01} N_{TOT}$ is the linear absorption coefficient and L is the sample length.

The triplet quantum yield, ϕ_T , is defined as:

$$\phi_T = \frac{\tau_S}{\tau_{ISC}} = \frac{\tau_{S10}}{\tau_{S10} + \tau_{ISC}} . \quad (3.9-31)$$

Since the lifetimes τ_{Sn1} and τ_{Tm1} are usually short (sub-picosecond), modeling of ESA dynamics for the measurements done with picosecond pulses allows neglecting the populations of the higher singlet (S_n) and triplet (T_n) states. However, this assumption is not always valid for the femtosecond measurements.

With excitation pulses shorter than ~ 10 ns and pulse repetition rates less than 10's of kHz, the rate of the triplet-state depopulation, $1/\tau_{T10}$, is also neglected in modeling in both picosecond and femtosecond experiments.

The transmittance of the probe for optically thin materials is calculated from the propagation equation (3.5). Numerical models for two cases of pump-probe dynamics are shown in Figure 3.12. In both cases at zero delay, pump and probe pulses are overlapped in time and space and the probe sees the maximum portion of ground state population excited to the first

excited singlet state. When the lifetime of the singlet excited state is longer than the temporal pulse width, the molecule can absorb additional photons promoting the electron to some higher excited state. The initial change in transmittance at zero delay between pump and probe, ΔT_0 , allows determination of the singlet-singlet excited state absorption cross section, σ_{S1n} . A decrease of transmittance at zero delay is an indication of RSA ($\sigma_{S1n} > \sigma_{S0I}$) while an increase is an indication of SA ($\sigma_{S1n} < \sigma_{S0I}$). The first singlet excited state population can move to the ground state or first triplet state. As the delay between pump and probe is increased, the probe sees a different population distribution between energy levels. If $\phi_T \approx 0$, the population of T_1 will be small and the transmittance of the probe will recover to its initial value (Figure 3.12a). In the case where $\phi_T > 0$, one portion of population from the S_1 state will move to the state T_1 and the transmittance will reach some constant value (compared to the lifetime of the singlet state, the triplet state lifetime, τ_p , can be taken as infinite). Again, the triplet state cross-section, σ_{T1n} , can be larger or smaller than the ground state cross-section σ_{0I} leading to RSA or SA from the triplet state. To detect triplet state population, the delay of the probe with respect to the pump needs to be at least two times longer than the singlet state lifetime. The change in transmittance due to absorption of the triplet-state population is represented by ΔT_I (Figure 3.12 b).

To mathematically describe the physical processes presented in Figure 3.11, the propagation and rate equations (3.5 and 3.6) are utilized together with initial conditions:

$$N_0(0) = N_{TOT} \quad N_{S1}(0), N_{Sn}(0), N_{T1}(0), N_{Tm}(0) = 0 \quad (3.8)$$

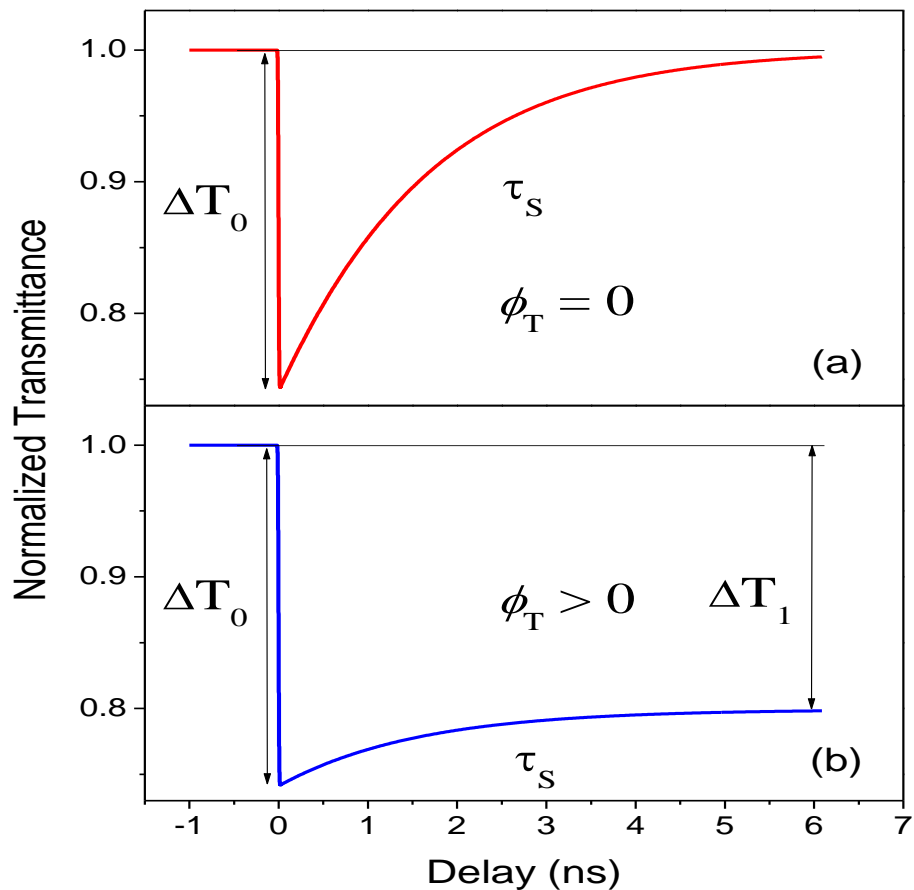


Figure 3.12 Numerical models of pump-probe dynamic (a) for molecules with $\phi_T=0$ and (b) for molecules with $\phi_T > 0$.

The total population, N_{TOT} , is conserved:

$$N_{TOT} = N_{S0}(t) + N_{S1}(t) + N_{T1}(t) \quad (3.9)$$

where N_{S0} , N_{S1} and N_{T1} are the ground-state, singlet excited state and triplet populations respectively. If the singlet-state lifetime, τ_S , is much longer than the pulse duration (“fast

absorber”, $\tau_{\text{pulse}} \ll \tau_{\text{ISC}}, \tau_S$), decay of population from S_1 can be ignored during the pulse. Also, since the lifetimes of higher excited states are usually in the sub-picosecond regime, changes in the population of S_1 due to ESA during the pump can be neglected.

The population dynamics can be described with simple rate equations having exponential solutions:

$$\frac{dN_{S_1}(t)}{dt} = -k_S \cdot N_{S_1}(t) \quad (3.10)$$

$$\frac{dN_{T_1}(t)}{dt} = k_{\text{ISC}} \cdot N_{S_1}(t) \quad (3.11)$$

$$\frac{dN_{S_0}(t)}{dt} = k_{S_{10}} \cdot N_{S_1}(t) \quad (3.12)$$

The first equation can be solved exactly to give,

$$N_{S_1}(t) = N_{S_1}(0) \exp(-k_{S_{01}} \cdot t) \quad (3.13)$$

From (S4) with $k_{\text{ISC}}/k_S = \phi_T$:

$$\begin{aligned} N_T(t) - N_T(0) &= +k_{\text{ISC}} \cdot \int_0^t N_{S_1}(0) \cdot e^{-k_S \cdot t} dt \Rightarrow \\ N_T(t) &= \frac{k_{\text{ISC}}}{k_S} \cdot N_{S_1}(0) \cdot (1 - e^{-k_S \cdot t}) = \phi_T \cdot N_{S_1}(0) \cdot (1 - e^{-k_S \cdot t}) \quad (3.14) \end{aligned}$$

Similarly, from (3.12) the population of the ground state after the pump ($k_S = k_{S_{10}} + k_{\text{ISC}}$) is:

$$N_{S_0}(t) = N_{S_0}(0) + \frac{k_{S_{10}}}{k_S} \cdot N_{S_1}(0) \cdot (1 - e^{-k_S \cdot t}) = N_{S_0}(0) + (1 - \phi_T) \cdot N_{S_1}(0) \cdot (1 - e^{-k_S \cdot t}) \quad (3.15)$$

The probe transmittance due to population redistribution is then given by:

$$\begin{aligned}
T_1(t) &= \exp(-\sigma_{S01} \cdot L \cdot N_{S0}(t) - \sigma_{S1n} \cdot L \cdot N_{S1}(t) - \sigma_{T1m} \cdot L \cdot N_{T1}(t)) \\
&= \exp \left[\begin{array}{l} -\sigma_{S01} \cdot L \cdot N_{S0}(0) - \sigma_{S01} \cdot L \cdot (1 - \phi_T) \cdot N_{S1}(0) - \\ \sigma_{T1n} \cdot L \cdot \phi_T \cdot N_{S1}(0) + (\sigma_{S01} \cdot (1 - \phi_T) + \sigma_{T1m} \cdot \phi_T - \sigma_{S1n}) \cdot L \cdot N_{S1}(0) \cdot \exp(-k_S \cdot t) \end{array} \right] \quad (3.16)
\end{aligned}$$

with $T_L = \exp[-\sigma_{S01} \cdot L \cdot \{N_{S0}(0) + N_{S1}(0)\}] = \exp(-\sigma_{S01} \cdot L \cdot N_{TOT})$. From equation

(3.16) with $\Delta T_1(t) = T_1(t)/T_L$:

$$\Delta T_1(t) = \exp \left[\begin{array}{l} \sigma_{S01} \cdot L \cdot \phi_T \cdot N_{S1}(0) - \sigma_{T1n} \cdot L \cdot \phi_T \cdot N_{S1}(0) \\ + (\sigma_{S01} \cdot (1 - \phi_T) + \sigma_{T1m} \cdot \phi_T - \sigma_{S1n}) \cdot L \cdot N_{S1}(0) \cdot \exp(-k_S \cdot t) \end{array} \right] , \quad (3.17)$$

where $\Delta T_1(t) = T_1(t)/T_L$ is the normalized transmittance.

At delays longer than the singlet decay time, τ_S , the change in transmittance, $\Delta T_1(\infty)$, can be taken as constant due to the long lifetime of the triplet state. Therefore,

$$\Delta T_1(\infty) = \exp[\sigma_{S01} \cdot L \cdot \phi_T \cdot N_{S1}(0) - \sigma_{T1n} \cdot L \cdot \phi_T \cdot N_{S1}(0)] = \text{constant} \quad (3.18)$$

$$\phi_T \cdot (\sigma_{T1m} - \sigma_{S01}) = \text{constant} = \kappa \quad . \quad (3.19)$$

The silicon naphthalocyanine derivative (SiNc) is a well-known triplet absorber and a photochemically very stable compound (molecular structure and molar absorptivity spectrum in toluene are shown in Figure 3.13a.). Results of pump-probe experiments at 532nm measured with picosecond pulses for SiNc are shown in Figure 3.13b.

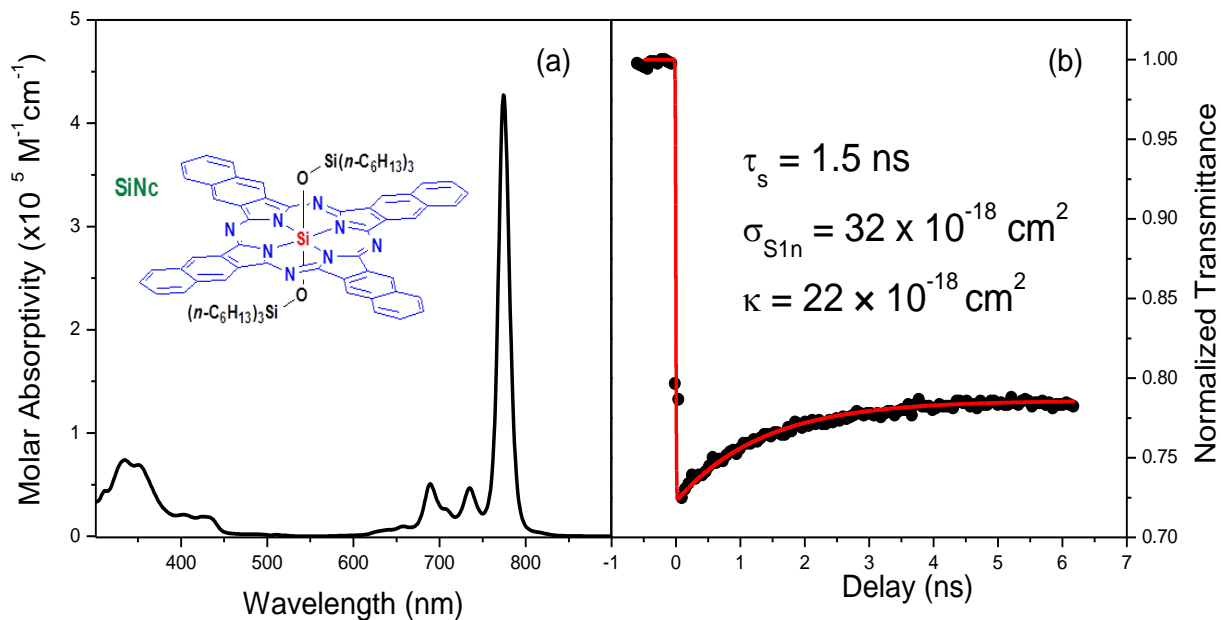


Figure 3.13. (a) Molecular structures and molar absorptivity spectra of SiNc in toluene. (b) Pump-probe experimental results and theoretical fitting for SiNc: (a) $T_L = 0.94$, $F = 100 \text{ mJ/cm}^2$ ($E = 15 \text{ } \mu\text{J}$, $w_0 = 95 \text{ } \mu\text{m}$). Pumping wavelength is 532 nm ; $\sigma_{S1n} = 32 \times 10^{-18} \text{ cm}^2$; $\tau_S = 1.5 \text{ ns}$;

3.7.2 Singlet Depletion Method

A commonly used method of ϕ_T determination is the so called ‘‘Singlet Depletion’’ or ‘‘Ground State Recovery’’ technique [44, 45]. This method is basically a pump-probe experiment, usually using a single pump pulse and a weak probe at the same wavelength, in a spectral region where there is strong saturable absorption. It is based on the assumption that both σ_{S1n} and σ_{T1n} can be neglected. If these conditions are fulfilled, this method can yield accurate results for ϕ_T . The method also works very well if σ_{S1n} and σ_{T1n} are approximately equal.

Absorption ($\Delta\alpha$) of the probe is defined as:

$$\Delta\alpha = \ln(\Delta T) . \quad (3.20)$$

From equation (3.17):

$$\Delta\alpha = \left(\begin{array}{l} \sigma_{S01} \cdot L \cdot \phi_T \cdot N_{S1}(0) - \sigma_{T1n} \cdot L \cdot \phi_T \cdot N_{S1}(0) \\ + (\sigma_{S01} \cdot (1 - \phi_T) + \sigma_{T1n} \cdot \phi_T - \sigma_{S1n}) \cdot L \cdot N_{S1}(0) \cdot e^{-k_{tot} \cdot t} \end{array} \right) , \quad (3.21)$$

so

$$\Delta\alpha = a_2 + a_1 \cdot e^{-k_{tot} \cdot t} . \quad (3.22)$$

$\Delta\alpha$ is the single exponential decay with amplitudes a_1 and a_2 given by :

$$a_2 = (\sigma_{S01} \cdot -\sigma_{T1n}) \cdot \phi_T \cdot L \cdot N_{S1}(0) \dots\dots\dots (3.23)$$

$$\begin{aligned} a_1 &= (\sigma_{S01} - \sigma_{S1n} - (\sigma_{S01} - \sigma_{T1n}) \cdot \phi_T) \cdot L \cdot N_{S1}(0) \\ &= (\sigma_{S01} - \sigma_{S1n}) \cdot L \cdot N_{S1}(0) - a_2 \end{aligned} . \quad (3.24)$$

From (3.23) and (3.24) we have:

$$\frac{a_2}{(\sigma_{S01} \cdot -\sigma_{T1n}) \cdot \phi_T} = \frac{a_1 + a_2}{(\sigma_{S01} - \sigma_{S1n})} , \quad (3.25)$$

so ϕ_T is equal to

$$\phi_T = \frac{a_2}{a_1 + a_2} \left(\frac{1 - \sigma_{S1n} / \sigma_{S01}}{1 - \sigma_{T1n} / \sigma_{S01}} \right) , \quad (3.26)$$

for $\sigma_{S01} \gg \sigma_{S1n}, \sigma_{T1n}$ or $\sigma_{S1n} \approx \sigma_{T1n}$:

$$\phi_T = \frac{a_2}{a_1 + a_2} = \frac{\Delta\alpha(\infty)}{\Delta\alpha(0)} . \quad (3.27)$$

As seen from Equation (47), ϕ_T can be determined only from amplitudes obtained from the singlet depletion curve without knowing the ESA cross sections. However, the method's main limitation lies in the fact that it might not always be possible to find a region where $\sigma_{S01} \gg \sigma_{S1n}, \sigma_{T1n}$ or $\sigma_{S1n} \approx \sigma_{T1n}$.

Singlet depletion experimental results measured with picosecond pulses for SiNc at 770nm and SD-SO 7517 (details about these compounds will be given in chapter 5.) measured at 660nm are shown in Figure 3.14.

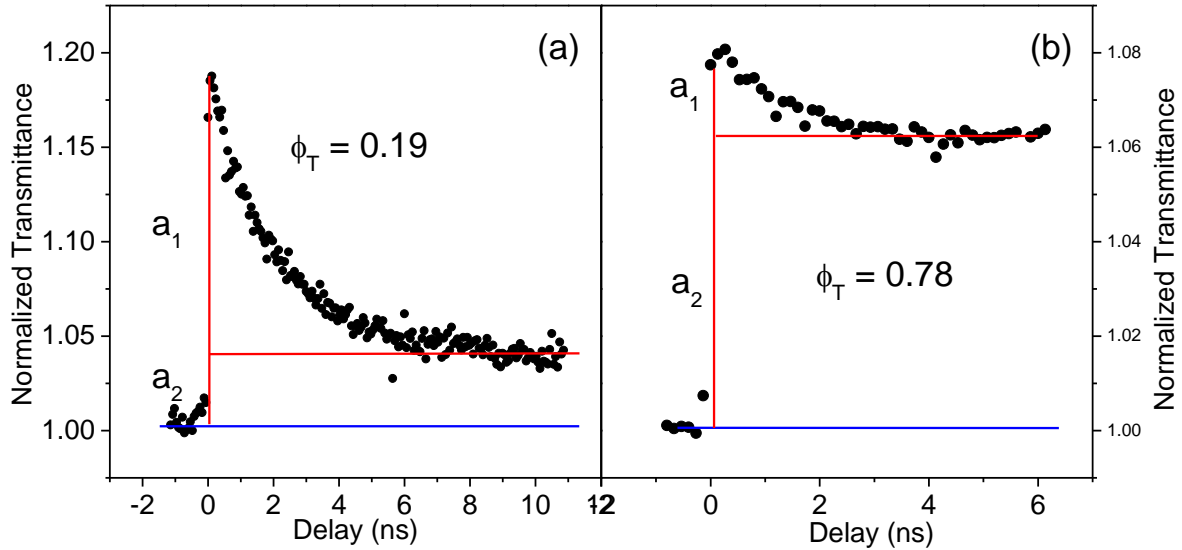


Figure 3.14. Singlet depletion measurement for (a) SiNc at 770nm, $T_L = 0.7$ and $F = 11 \text{ mJ/cm}^2$ ($E = 1 \text{ }\mu\text{J}$, $w_0 = 75 \text{ }\mu\text{m}$) and (b) SD-SO 7517, $T_L = 0.8$ and $F_I = 0.5 \text{ mJ/cm}^2$ ($E = 0.5 \text{ }\mu\text{J}$, $w_0 = 250 \text{ }\mu\text{m}$).

For SiNc the value of $\phi_T = 0.19$ is in good agreement with value ($\phi_T = 0.21$) determined from the double pump-probe method (to be discussed in Chapter 4). On the other hand, for SD-SO 7517 double pump-probe measurements gives $\phi_T = 0.64$ (Chapter 5.). Large difference between value $\phi_T = 0.78$ obtained from the single and value $\phi_T = 0.64$ obtained from double pump-probe methods, indicates that SD-SO 7517 does not fulfill the single pump-probe method's requirements. The singlet depletion technique can give some estimation for ϕ_T but for precise measurements a more accurate technique is required.

3.7.3 White-light Continuum Pump-probe Spectroscopy – Measurements of ESA Spectrum

An ESA spectrum is measured using a pump pulse generated from a femtosecond OPG/OPA and a white light continuum (WLC) probe [46-48]. The WLC pump-probe experimental setup is shown in Figure 3.15. The pump wavelength is usually set close to the peak of linear absorption to create a significant excited state population. The pump beam is modulated with a mechanical chopper at 283 Hz that is synchronized with the output from the laser. The probe signal was recorded using a lock-in amplifier. The WLC was created by focusing 780 nm pulses with a 5cm focal length lens into a 1cm water cell. The spectral range of the WLC was from 380nm to 900nm. The ESA spectrum was measured by changing the wavelength of the probe through the range of interest with narrow band-pass interference filters (~8 - 10nm FWHM) before the sample. In this way there is no need for data correction of the temporal mismatch of the pump and probe due to strong WLC temporal dispersion and, in addition, possible stimulated emission is avoided. For the singlet excited state absorption spectral

measurements the probe was delayed using a 2 ns delay stage while for triplet excited state absorption spectra the delay between pump and probe was fixed and set to 25ns.

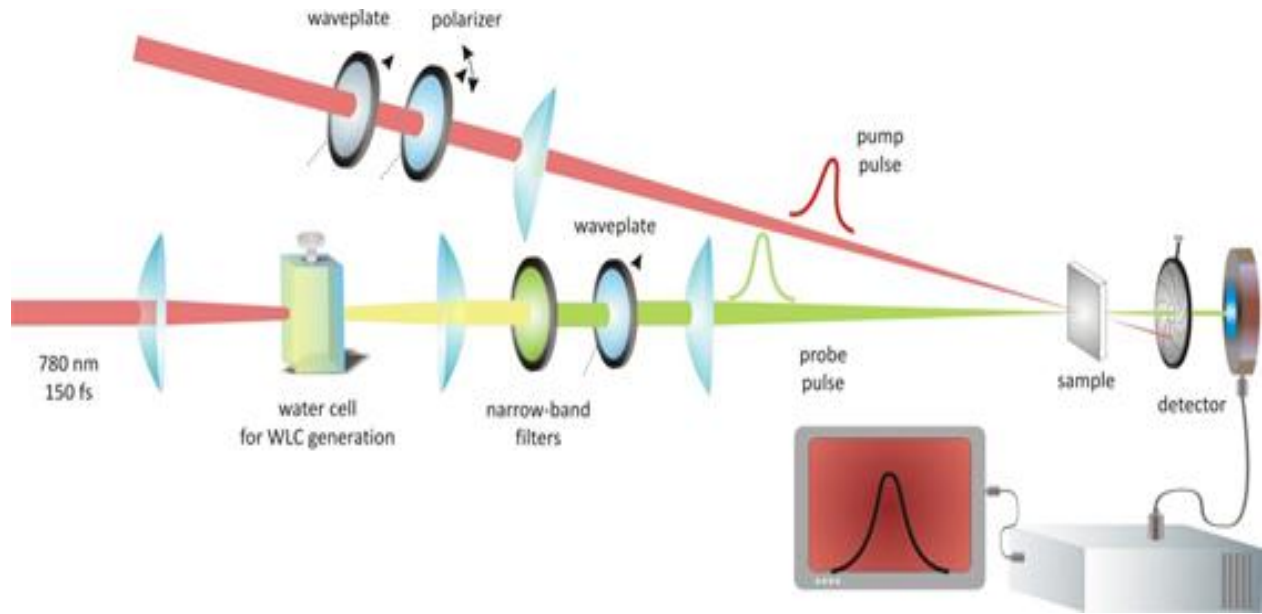


Figure 3.15 White light continuum pump-probe setup

From equation (3.16) the transmittance of the probe at a particular wavelength λ is equal to

$$\begin{aligned}
 T_1(\lambda) &= \exp(-\sigma_{S01}(\lambda) \cdot L \cdot N_{S0} - \sigma_{S,T1n}(\lambda) \cdot L \cdot N_{S,T1}) \\
 &= \exp(-\sigma_{S01}(\lambda) \cdot L \cdot N_{TOT} - \sigma_{S01}(\lambda) \cdot L \cdot N_{S,T1} - \sigma_{S,T1n}(\lambda) \cdot L \cdot N_{S,T1}) \cdot (48)
 \end{aligned}$$

The time dependence was dropped since both $\sigma_{S,T1n}$ and $\sigma_{S,T1n}$ were determined at a specific time delay, again taking $T_L(\lambda) = \exp(-\sigma_{S01}(\lambda) \cdot L \cdot N_{TOT})$

$$\begin{aligned}
 \Delta T(\lambda) &= T_1(\lambda) / T_L(\lambda) = \exp(-(\sigma_{S01}(\lambda) - \sigma_{S,T1n}(\lambda)) \cdot L \cdot N_{S,T1}) \Rightarrow \\
 \ln(\Delta T(\lambda)) &= -(\sigma_{S01}(\lambda) - \sigma_{S,T1n}(\lambda)) \cdot L \cdot N_{S,T1} \quad (49)
 \end{aligned}$$

Measured ESA spectrum in this way represents the difference between $\sigma_{S01}(\lambda)$ and $\sigma_{S,T1n}(\lambda)$ and should be rescaled using absolute cross sections of $\sigma_{S,T1n}$ at the specific wavelength (Λ). Λ is usually set close to the peak of the singlet or triplet ESA spectrum, while $\sigma_{S1n}(\Lambda)$ and $\sigma_{T1n}(\Lambda)$ are determined separately from pump-probe or Z-scan experiments.

Since the wavelength of the pump is fixed, the product $L \cdot N_{S,T1}$ is constant for every λ

$$L \cdot N_{S,T1} = \frac{\ln(\Delta T(\lambda))}{n(\Delta T(\Lambda))} = \frac{(\sigma_{S01}(\lambda) - \sigma_{S,T1n}(\lambda))}{(\sigma_{S01}(\Lambda) - \sigma_{S,T1n}(\Lambda))} \quad (50)$$

The complete ESA spectrum is calibrated using absolute values of $\sigma_{S1n}(\Lambda)$, and $\sigma_{T1n}(\Lambda)$.

$$\sigma_{S,T1n}(\lambda) = \sigma_{S01}(\lambda) - \{\sigma_{S01}(\Lambda) - \sigma_{S,T1n}(\Lambda)\} \times \frac{\ln[\Delta T(\lambda)]}{\ln[\Delta T(\Lambda)]} \quad (51)$$

3.7.4 Double Pump-probe Method

The double pump-probe (DPP) experiment was first introduced by Swatton et. al. in 1997 [49]. The main advantage of this method is that it takes into consideration TT absorption allowing determination of both parameters - the triplet quantum yield and TT absorption cross section - in a single experiment. There have been several reports of DPP measurements of organic compounds [50-52].

The idea of the DPP method is to pump the investigated sample with two strong pulses (usually having the same energies) separated by a certain time delay (usually at least two times longer than the singlet state lifetime) allowing a significant depopulation of the first excited singlet state by IC into the ground state and by ISC to the triplet state (Figure 3.16.). Typically,

although not necessarily, equal wavelengths are used for both pumps and probe to reduce the number of unknown variables in the analysis.

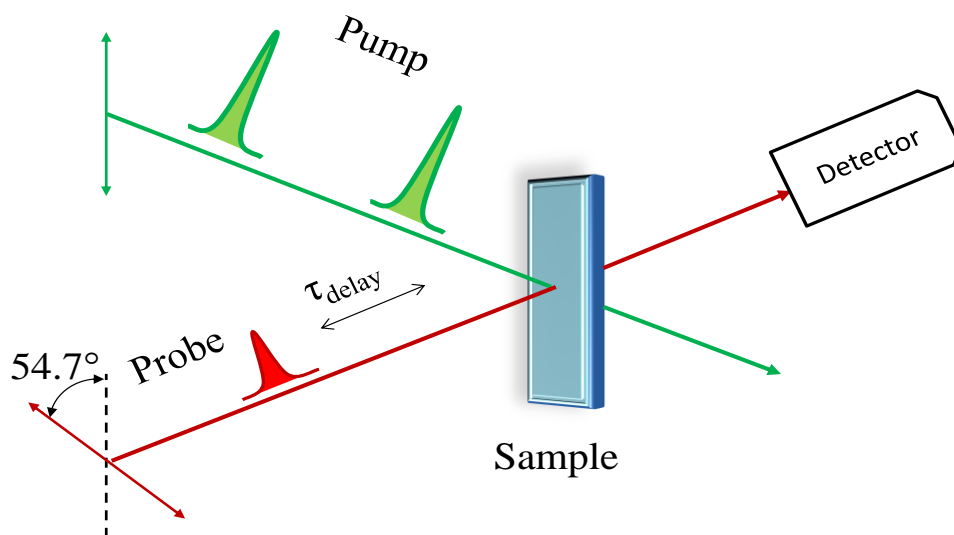


Figure 3.16. Schematic of the double pump-probe experiment.

Solving the set of Equations (3.5) and (3.6) for the first pump, gives the unique solution for the constant κ connecting the triplet yield ϕ_T and TT absorption cross section σ_{TIn} (Equation 3.19). Due to spin-selection rules, the triplet lifetimes are always significantly longer than singlet lifetimes; thus, the second pump encounters a different population distribution than that encountered by the first pump. Specifically, the second pump sees a population in the lowest-lying triplet state and a reduced population in the ground state. Since the second pump interacts with the modified molecular system, and the initial conditions for solving Eqs (3.5) and (3.6) are changed. The second numerical fitting for the transmittance change due to the second pump together with the solution of Equation (3.19), obtained as a result of the first fitting, allows the unique determination of ϕ_T and σ_{TIn} .

3.7.5 Triplet Lifetime Measurements

Since the lifetime of triplet states, τ_T , usually ranges from 10^{-8} to 10^2 s, measuring τ_T by delaying the pulsed probe is not a very practical method. The delay stage in that case should be at least tens of meters. A modified pump-probe setup is used in this case. Usually picosecond or nanosecond laser pulses are used as the excitation source at a wavelength close to the peak of the linear absorption of the investigated molecule and a CW laser is used as the probe. The transmittance of the sample is recorded by a digital oscilloscope Tektronix TDS 680C triggered from the picosecond pump laser. To increase the signal 10mm cells were used while the concentration of the sample in a solution is maximized. Special attention is required to assure that the probe beam does not induce any thermal effects. An example of a triplet state lifetime measurement for molecule SD-SO 7517 (details about these compounds will be given in Chapter 5.) is shown in Figure 3.17.

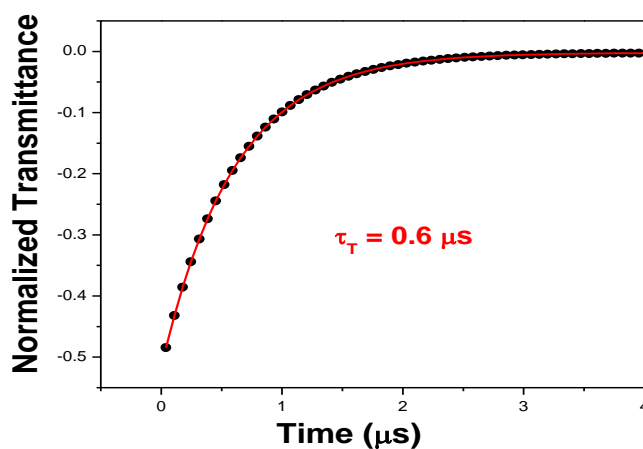


Figure 3.17 Triplet state lifetime measurement of SD-SO 7517 in ACN. Pump: $\lambda = 660\text{nm}$, $\tau_{\text{HW1/e}} = 7$ ps.

CW probe $\lambda = 660\text{nm}$.

3.7.6 Z-scan

Z-scan is a simple, single beam technique for measuring optical nonlinearities. It was developed by *M. Sheik-Bahae et al.* in 1990 [53]. The method is useful for the measurements of both real and imaginary parts of $\chi^{(3)}$ and even higher order of nonlinearities.

A Z-scan setup is shown in Figure 3.18. The method is based on measuring the far field transmittance through the sample as a function of a position, while the sample is moving through the focused beam. If all transmitted light is collected by the detector, we can obtain information about nonlinear absorption (open aperture Z-scan). When a small aperture ($\sim 30\%$) is placed into the beam, information about nonlinear refraction can be obtained (closed aperture Z-scan). Usually, the assumptions are: the sample thickness is much smaller than the Rayleigh range of the beam (thin sample approximation) and a perfect Gaussian beam profile.

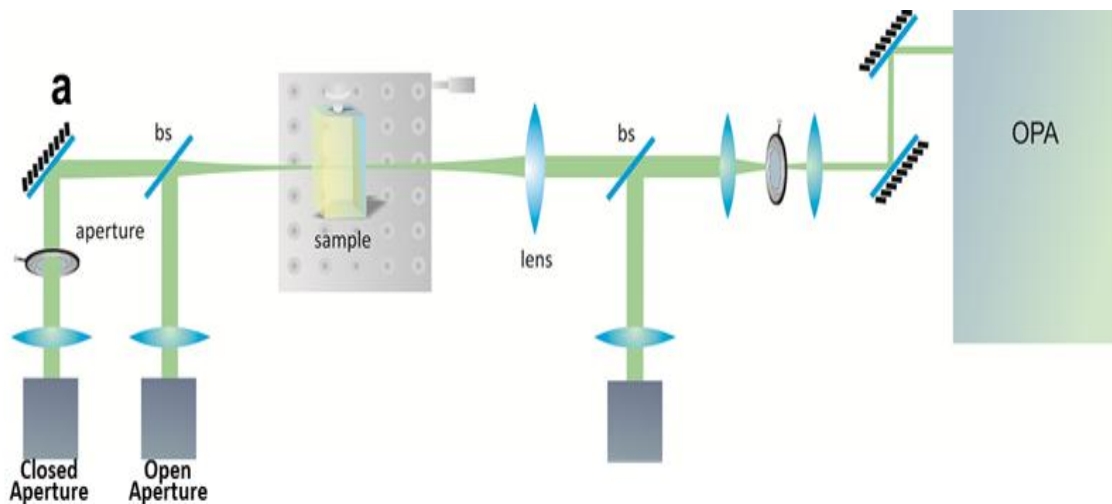


Figure 3.18. Z-scan experimental setup.

Examples of both open and closed aperture Z-scan measurements with picosecond pulses at 532 nm are given in Figure 3.19. Fitting experimental data with the theory, allows determination of the 2PA coefficient for ZnSe (Figure 3.19a) and nonlinear refraction index for CS₂ (Figure 3.19b). ZnSe and CS₂ are very often used as references for setup parameters calibration. Knowing α_2 of ZnSe and n_2 for CS₂ we can determine beam waist w_0 and temporal pulse width $\tau_{\text{HW1/e}}$.

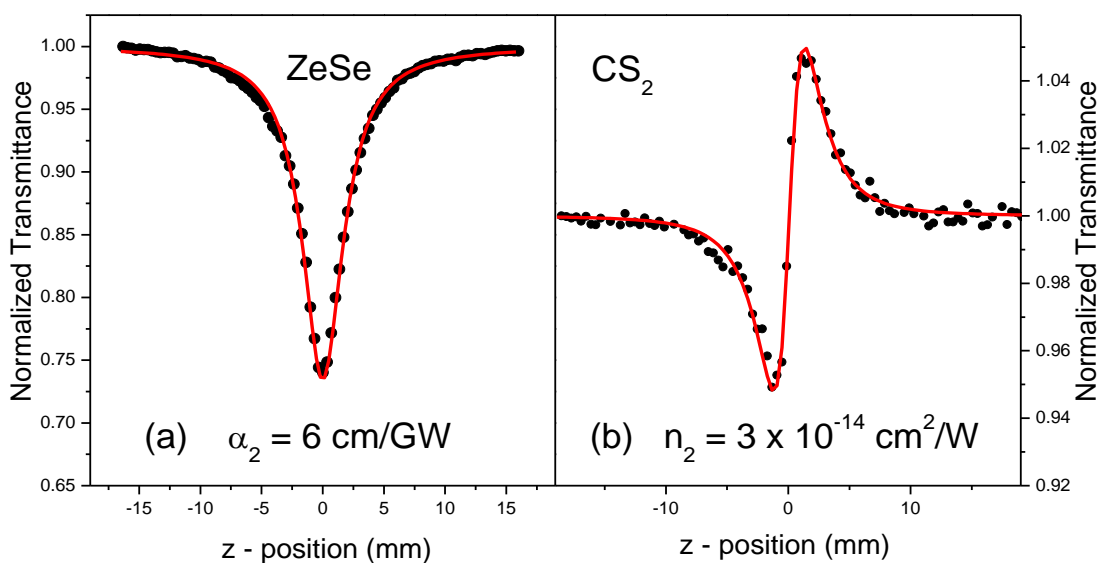


Figure 3.19.(a) Z-scan open aperture measurements for ZnSe at 532nm: $E = 200\text{nJ}$, $\tau_{\text{HW1/e}} = 11\text{ps}$, $w_0 = 16 \mu\text{m}$ and (b) closed aperture measurements for CS₂: $E = 180\text{nJ}$, $\tau_{\text{HW1/e}} = 11\text{ps}$, $w_0 = 16 \mu\text{m}$.

In the region with strong ESA, the Z-scan method allows determination of ESA parameters by solving the set of rate Eqs 28, 29. For molecules with $\phi_T \sim 0$ or with τ_{ISC} significantly shorter than the temporal pulse width, σ_{S1n} can be uniquely determined from Z-scan measurements. In addition, it is also possible to determine the lifetime of the higher excited state τ_{Snl} (lifetime of first singlet state, τ_{S10} , is usually determined through separate pump-probe

measurements). An example of a molecule with $\phi_T \sim 0$ is a squaraine type molecule SD-O 2405 (details about this compound will be given in Chapter 5.). Results for Z-scan measurements of SD-O 2405 are shown in Figure 3.20.

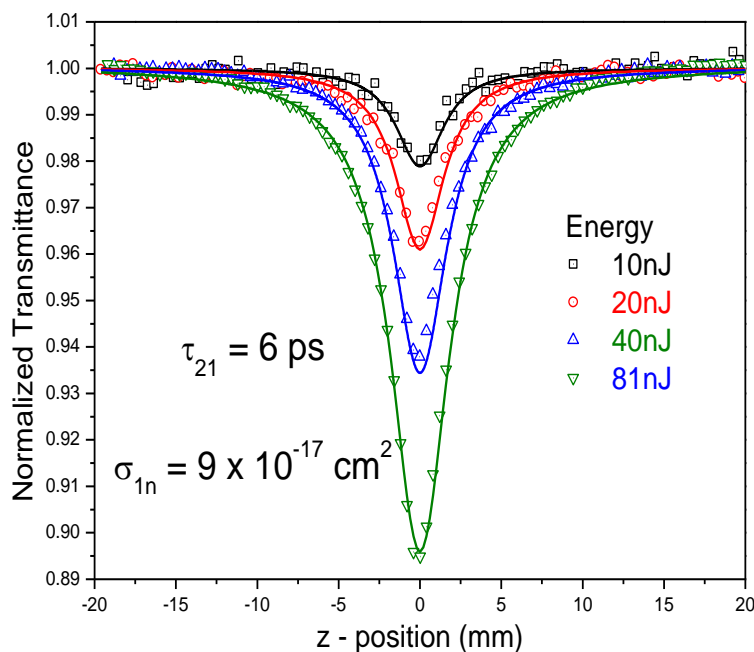


Figure 3.20. Z-scan open aperture measurements for SD-O 2405 in toluene at 460 nm in 1 mm cell for several different energies: $\tau_{\text{HW}1/e} = 8 \text{ ps}$, $w_0 = 16 \mu\text{m}$, $T(\text{lin}) = 0.92$, $\sigma_{\text{S01}} = 1.5 \times 10^{-18} \text{ cm}^2$, $\tau_{\text{S10}} = 2.5 \text{ ns}$.

For molecules with significant ϕ_T , Z-scan measurements with a temporal pulse width shorter or at least comparable with τ_{S10} and τ_{ISC} , it is impossible to uniquely determine all ESA cross-sections and lifetimes together with ϕ_T due to too many unknown parameters. Squaraine SD-S 7508 (details about this molecule will be given in Chapter 5.) is a molecule with $\tau_{\text{S10}} = 4.5 \text{ ps}$ and $\phi_T = 0.98$. τ_{S10} was measured with a femtosecond pump-probe experiment, while ϕ_T was measured with a picosecond DPP experiment. Femtosecond Z-scan experiment (Figure 3.21a) is

used for determination of the singlet state parameters σ_{S1n} and τ_{S1n} . Since $\tau_{S10} = 4.5$ ps is much longer than the pulsewidth of our femtosecond system ($\tau_{HW1/e} = 140$ fs), population of T_1 state can be ignored for femtosecond Z-scan measurement. A picosecond Z-scan experiment (Figure 3.21b) allows additional determination of the triplet state parameters σ_{T1n} and τ_{T1n} . The triplet excited state parameters were additionally confirmed with femtosecond pump-probe measurements at 550 nm (Chapter 5).

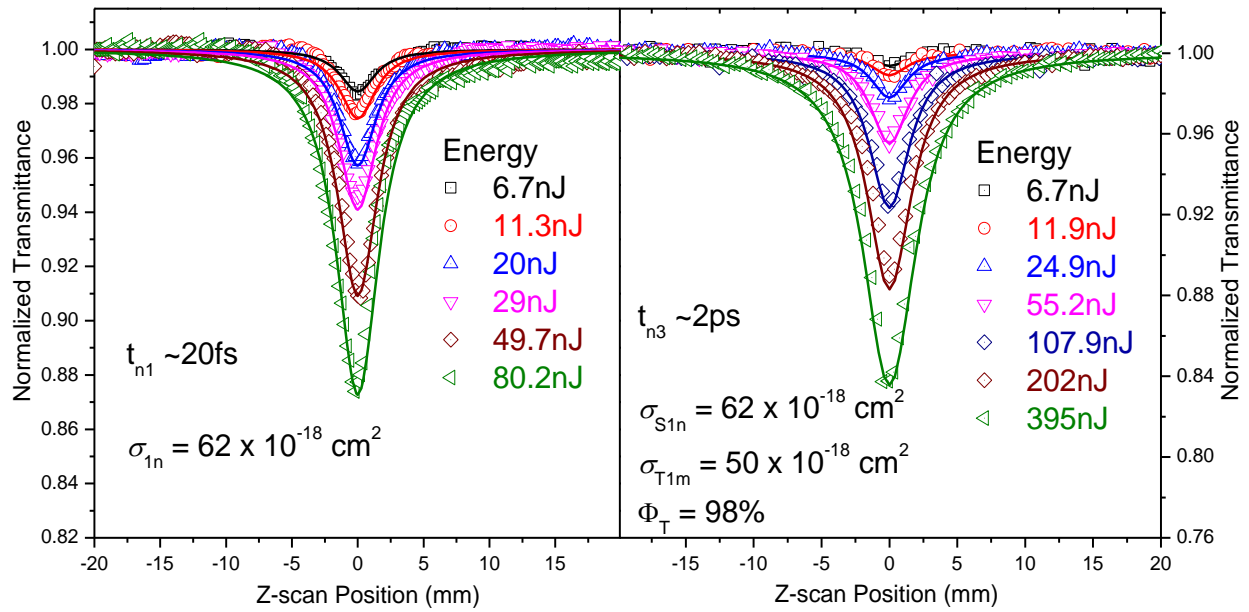


Figure 3.21. (a) Femtosecond open aperture Z-scan measurements for SD-S 7508 in toluene at 550 nm in a 1 mm cell for several different energies: $\tau_{HW1/e} = 140$ fs, $w_0 = 16.7 \mu\text{m}$, $T(\text{lin}) = 0.86$, $\sigma_{S01} = 4.8 \times 10^{-18} \text{ cm}^2$, $\tau_{S10} = 4.5$ ps. (b) Picosecond open aperture Z-scan measurements for SD-S 7508 in toluene at 550 nm: $\tau_{HW1/e} = 8$ ps, $w_0 = 16 \mu\text{m}$, $T(\text{lin}) = 0.93$, $\sigma_{S01} = 4.8 \times 10^{-18} \text{ cm}^2$, $\sigma_{S1n} = 62 \times 10^{-18} \text{ cm}^2$, $\tau_{S10} = 4.5$ ps, $\tau_{S1n} = 20$ fs and $\Phi_T = 0.98$.

3.7.7 Two-photon Excitation Fluorescence (2PF) Spectroscopy

As already mentioned in chapter 2.3 as a consequence of Kasha's rule, independent of the method of excitation, the population always relaxes to the ground state through the fluorescence channel from the lowest singlet excited state S_1 with a constant value of the fluorescence quantum yield Φ_F . As a consequence, the number of emitted photons is always proportional to the absorbed number of photons. When the population in the sample is excited through a 2PA process, scanning the wavelength of excitation and measuring the fluorescence signal for each wavelength allows an accurate determination of the shape of the 2PA spectrum. Since the fluorescence measurement is a relative technique, the 2PA spectrum is usually calibrated using the absolute value of 2PA coefficient obtained from the separate Z-scan measurements at a particular wavelength.

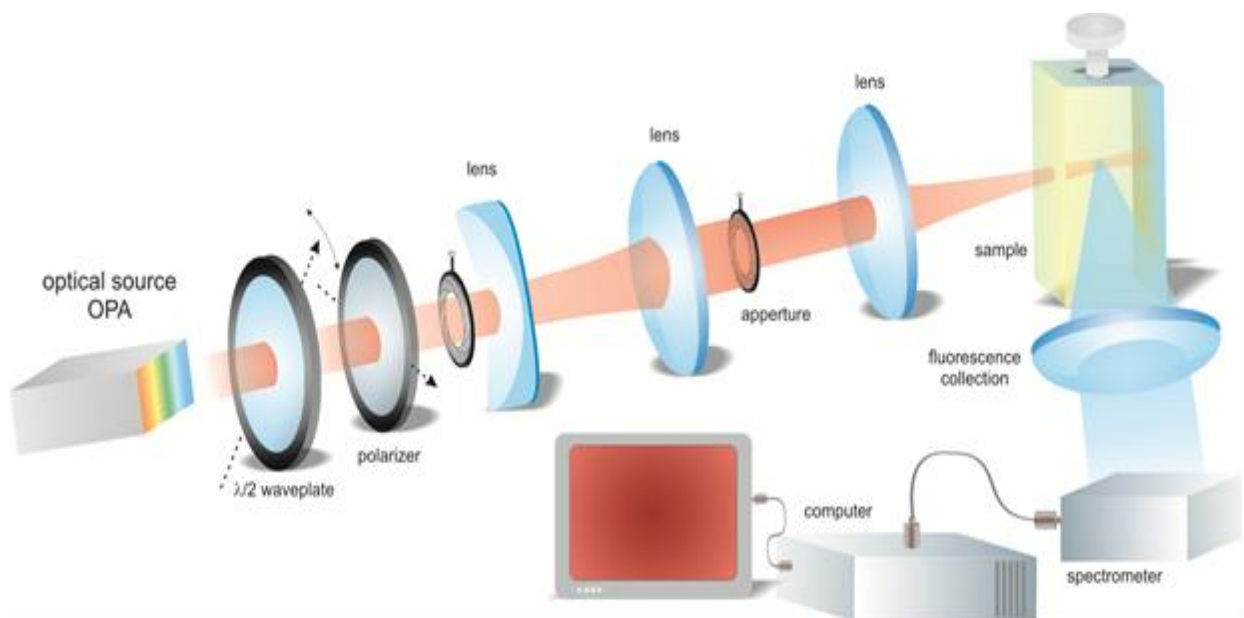


Figure 3.22. Schematics of the two photon fluorescence experimental setup

The 2PF spectrum is measured with the PTI Quantamaster spectrofluorometer. Instead of using a Xenon lamp as the excitation source, the sample is excited with a pulse from the femtosecond OPG/OPA (TOPAS C). The 2PF experimental setup is shown in Figure 3.22. First, the beam is attenuated with a combination of $\lambda/2$ and calcite polarizer and then expanded with a telescope. The aperture after the telescope is used to create a flat top beam which is focused onto the sample. Another lens is used for collection of the fluorescence signal which is detected with a Type R928P photo multiplier tube (PMT).

Although 2PF is the fastest technique for measuring the shape of the 2PA spectrum with high sensitivity, it is applicable only for compounds with a high ϕ_F . Unfortunately, for most of the samples with high ϕ_T and small ϕ_F , measurement of the 2PA spectrum requires the determination of the 2PA coefficient by Z-scan measurements at each wavelength separately.

CHAPTER 4. OPTIMIZATION OF DOUBLE PUMP-PROBE TECHNIQUE

The basic principles of the DPP technique are described in a previous section. Originally this method was used for characterization of SiNc [49]. In the original work the sample was measured with degenerate DPP at 532 nm, into RSA region, where the ground state absorption was very small. To excite a significant part of population, a relatively large fluence (~170 mJ) was used in both pumps.

In all other previous reports, DPP was used for measuring compounds (Porphyrine, Fullerene) with high photochemical stability, while using similar experimental conditions [50-52] as in the original work. However, for characterization of less photochemically stable materials, the DPP measurement has to be performed with both pump intensities significantly reduced, which can limit the method's accuracy. The following discussion will identify and resolve this problem.

Examples of the numerical simulations of DPP dynamics, allowing the decoupling of the two molecular parameters ϕ_T and σ_{Tlm} , for two concentrations and the corresponding fluences that yield the same transmittance change, are shown in Figure 4.1 a and b. The corresponding population dynamics are shown below in Figure 4.1 c and d. Singlet-state parameters of SiNc at 532 nm: $\sigma_{S0l} = 2.8 \times 10^{-18} \text{ cm}^2$ and $\sigma_{S1n} = 32 \times 10^{-18} \text{ cm}^2$ [49, 54, 55] are used in the simulation. At this wavelength, the linear absorption is small, so that $\sigma_{S1n} > \sigma_{S0l}$, corresponding to RSA.

Additionally, based on previous pump-probe measurements of SiNc, it is known that $\kappa = 22 \times 10^{-18} \text{ cm}^2$ (Figure 3.13). For all the curves shown in Figure 4.1, the same value of κ was used, but different combinations of ϕ_T and σ_{T1m} that give this same value of κ . The probe transmittance prior to the second pump is independent of the variations in these combinations, thus indicating that in these experiments, the transmittance changes induced by the first pump unambiguously give κ , but do not uniquely specify ϕ_T or σ_{T1m} . However, after the second pump, the probe transmittance from Equations 3.5 and 3.6 depends on ϕ_T and σ_{T1m} individually.

From the results shown in Figure 4.1, an increase of ϕ_T for the second decrease in transmittance corresponds to a smaller value of σ_{T1m} to keep κ constant. In Figure 4.1a, where the concentration is large and the pump fluence is small, it is seen that the probe transmittance after the second pump pulse is relatively insensitive to changes of ϕ_T , and thus a unique determination of ϕ_T and σ_{T1m} without large errors becomes impossible. This can be understood by observing the population dynamics. In Figure 4.1c, we see that for the conditions of Figure 4.1a only a small fraction of population is transferred to T_1 , therefore ϕ_T cannot be determined with significant accuracy. Altering the measurement conditions by decreasing the concentration and pumping with larger fluences results in a significant population of the triplet states allowing ϕ_T and σ_{T1m} to be uniquely determined, as can be seen in Figure 4.1b and d. Hence, an experiment conducted under the conditions shown in Figure 4.1b should allow unique determination of ϕ_T and σ_{T1m} . As already mentioned, such a large fluence is not always practical due to photo-induced decomposition of some dyes, and may not be available (especially when using an Optical Parametric Generator/Amplifier system) due to insufficient laser output energy, E .

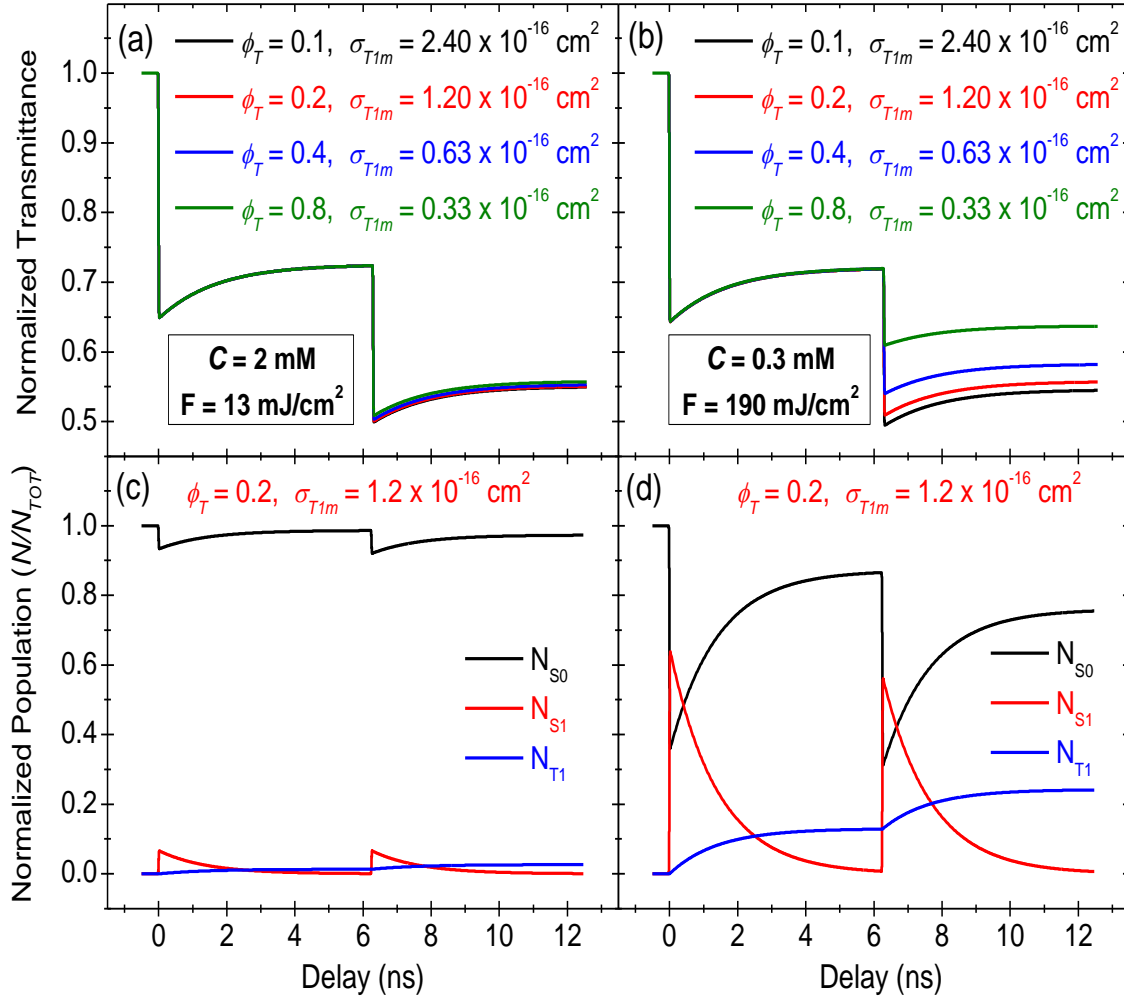


Figure 4.1. (a) and (b) Numerical simulation of DPP dynamics shown as normalized transmittance vs. time delay between pump and probe pulses for SiNc at 532 nm with parameters for different ϕ_T and σ_{T1m} . Using $\kappa = +22 \times 10^{-18} \text{ cm}^2$, $\sigma_{S0I} = 2.8 \times 10^{-18} \text{ cm}^2$, and $\sigma_{S1I} = 32 \times 10^{-18} \text{ cm}^2$, (a) $T_L = 0.6$ ($C = 2 \text{ mM}$) with an input fluence of $F = 13 \text{ mJ/cm}^2$ in each pump and (b) $T_L = 0.95$ ($C = 0.3 \text{ mM}$) with an input fluence of $F = 190 \text{ mJ/cm}^2$ in each pump. (c) and (d) Population dynamics for the ground (N_0), first excited singlet (N_{S1}) and triplet (N_{T1}) states using $\phi_T = 0.2$ and $\sigma_{T1m} = 1.2 \times 10^{-16} \text{ cm}^2$ for the two cases of DPP simulation in (a) and (b), respectively.

The sensitivity of the DPP can be quantified as the change in transmittance after the second pump (ΔT_2) with respect to a change of ϕ_T , i.e. $\Delta T_2/\Delta\phi_T$ as shown schematically in Figure 4.2 a, where the parameters for SiNc at 532 nm were used, keeping κ constant while varying ϕ_T . Insight into the influence of the experimental parameters, such as dye concentration, pump fluences and excitation spectral region, on the accuracy of the DPP is gained. By using a simplified analytical approach with the assumption that $\sigma_{S1n} \ll \sigma_{S0I}$ (otherwise the rate equations have to be solved numerically), only two competing processes are considered, ground-state absorption and TT reabsorption. We can also ignore the population of S_1 for small dye concentrations where the ESA does not deplete the pump. This approximation works reasonably well in regions where $\sigma_{S0I} \gg \sigma_{S1n}$, and for not too high dye concentrations. A similar approach for an analytical solution to the rate and propagation equations was developed in previous papers [56, 57] for optimizing RSA in optical-limiting studies. However, in this work, a simplified analytical solution is developed for both RSA and SA for the DPP.

The equation for the ground-state population density seen by the first pump is:

$$\frac{dN_{S0}}{dt} = -\frac{\sigma_{S0I}N_0I}{\hbar\omega}. \quad (4.1)$$

The population density that stays in the ground state after the first pump is:

$$N_{S0}|_{pump1} = N_{TOT} \exp\left(-\frac{\sigma_{S0I}F_1}{\hbar\omega}\right), \quad (4.2)$$

where F_1 is the fluence of the first pump (e.g. for a Gaussian temporal profile pump $F_1 = \tau_0 I_0 \sqrt{\pi}$)

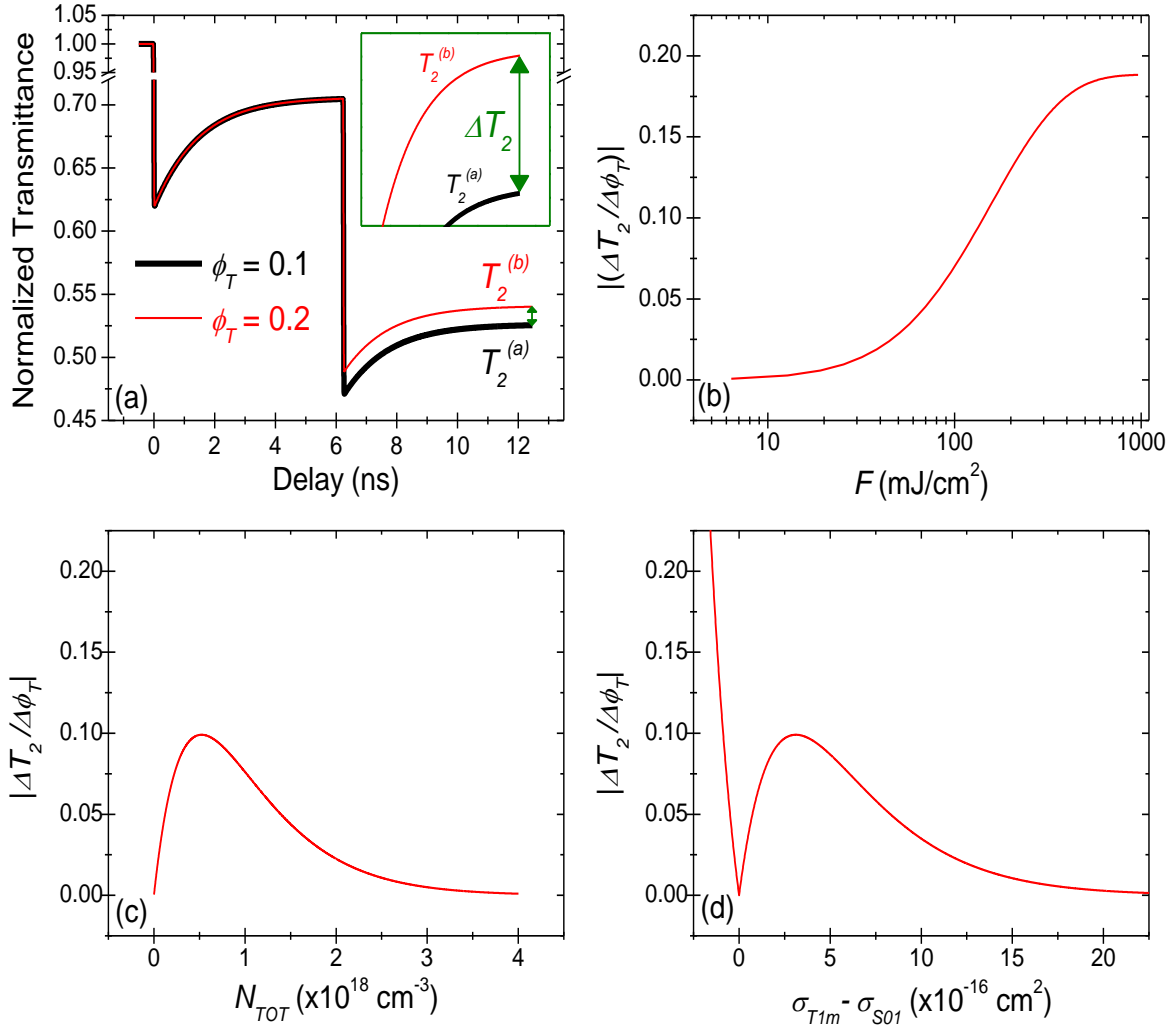


Figure 4.2. Solutions of rate equations (1) and (2): (a) Plot of normalized transmittance vs. delay between pump and probe pulses for the DPP in SiNc indicating changes in transmittance $T_2^{(i)}$ with time as defined in Eq. 5. ΔT_2 is the difference between $T_2^{(b)}$ and $T_2^{(a)}$. The inset shows the expanded region in transmittance between $T_2^{(b)}$ and $T_2^{(a)}$. (b) $|\Delta T_2 / \Delta \phi_T|$ vs. input fluence at a concentration of $C = 0.37$ mM, (c) $\Delta T_2 / \Delta \phi_T$ vs. N_{TOT} with $F = 190$ mJ/cm² in each pump, and (d) $\Delta T_2 / \Delta \phi_T$ vs. the difference in cross sections $\sigma_{T1m} - \sigma_{S01}$ at $C = 0.37$ mM and $F = 190$ mJ/cm² in each pump.

The singlet population density just after the first pump is:

$$N_{S_1} = N_{TOT} - N_{S_0} = N_{TOT} \left[1 - \exp\left(-\frac{\sigma_{S_0 I} F_1}{\hbar \omega}\right) \right]. \quad (4.3)$$

The population density that moves to the triplet state is:

$$N_{T_1} = \phi_T N_{S_1} = \phi_T \left[1 - \exp\left(-\frac{\sigma_{S_0 I} F_1}{\hbar \omega}\right) \right] N_{TOT}. \quad (4.4)$$

The ground-state population density just before the second pump (assuming this time is long compared to τ_S) is:

$$N_{S_0}' = N_{TOT} - N_{T_1} = N_{TOT} \left[1 - \phi_T \left\{ 1 - \exp\left(-\frac{\sigma_{S_0 I} F_1}{\hbar \omega}\right) \right\} \right]. \quad (4.5)$$

The singlet population density just after the second pump is (assuming both pump fluences are the same, $F_1 = F_2$):

$$N_{S_1}' = \left[1 - \exp\left(-\frac{\sigma_{S_0 I} F_1}{\hbar \omega}\right) \right] N_{S_0}'. \quad (4.6)$$

The population density produced by the second pump that moves to the triplet state is:

$$N_{T_1}' = \phi_T N_{S_1}' = \phi_T \left[1 - \exp\left(-\frac{\sigma_{S_0 I} F_1}{\hbar \omega}\right) \right] N_{TOT} \left[1 - \phi_T \left\{ 1 - \exp\left(-\frac{\sigma_{S_0 I} F_1}{\hbar \omega}\right) \right\} \right]. \quad (4.7)$$

Note that in order to decouple ϕ_T and σ_{TIm} it is enough to look at the time delay of zero overlap of the second pump and probe. However, the accuracy of the method at that point also depends on σ_{SIn} . Since in this simplified model we ignore σ_{SIn} , we will look at the transmittance after the second pump, when the state S_1 is significantly depopulated and the influence of σ_{SIn} is minimal:

$$\begin{aligned}
T_2 &= \exp[-\sigma_{S01}N_{S0}'L - \sigma_{T1m}N_{T1}L - \sigma_{T1m}N_{T1}'L] \\
&= \exp[-\sigma_{S01}(N_{TOT} - N_{T1} - N_{T1}')L - \sigma_{T1m}(N_{T1} + N_{T1}')L]. \\
&= \exp[-\sigma_{S01}N_{TOT}L - (\sigma_{T1m} - \sigma_{S01})(N_{T1} + N_{T1}')L]
\end{aligned} \tag{4.8}$$

The normalized transmittance is determined by:

$$T_2^{(i)} = T_2 / T_L = \exp[-(\sigma_{T1m} - \sigma_{S01})(N_{T1} + N_{T1}')L]. \tag{4.9}$$

Again, the linear transmittance is defined as $T_L = \exp(-\sigma_{S01} \cdot L \cdot N_{TOT})$. From Equations (4.4) and (4.7), and by defining the fraction of molecules excited to the first singlet state as; $f = (1 - \exp(-\sigma_{S01}F_1 / \hbar\omega))$, and with $\kappa = \phi_T(\sigma_{T1m} - \sigma_{S01})$ we obtain an analytical solution for the transmittance after the second pump:

$$\begin{aligned}
T_2^{(i)} &= \exp[-(\sigma_{T1m} - \sigma_{S01})\{\phi_T f N_{TOT} + \phi_T f N_{TOT}(1 - \phi_T f)\}L] \\
&= \exp[-\phi_T(\sigma_{T1m} - \sigma_{S01})\phi_T f N_{TOT}(1 + 1 - \phi_T f)L] \\
&= \exp[-\kappa f N_{TOT}(2 - \phi_T f)L]
\end{aligned} \tag{4.10}$$

The DPP accuracy can be defined by the change in transmittance after the second pump (T_2) with a change of ϕ_T :

$$\left| \frac{\Delta T_2^{(i)}}{\Delta \phi_T} \right| = \kappa f^2 N_{TOT} L \exp[-\kappa f N_{TOT}(2 - \phi_T f)L] \tag{4.11}$$

Using these approximations (derivation provided in the Supporting Information), we can write an equation for $T_2^{(i)}$ corresponding to the case of complete S_1 depopulation:

$$T_2^{(i)} = \exp(-\kappa f N_{TOT} [2 - \phi_T f]L), \tag{4.12}$$

where $f = 1 - \exp(-\sigma_{S01}F/\hbar\omega)$ is the fraction of population that is removed from the ground state S_0 with pump excitation and L is the sample length. Differentiating T_2 with respect to ϕ_T gives the DPP accuracy:

$$\left| \frac{\Delta T_2}{\Delta \phi_T} \right| = \kappa f^2 N_{TOT} L \exp(-\kappa f N_{TOT} [2 - \phi_T f] L) . \quad (4.13)$$

The dependence of the DPP accuracy on F and N_{TOT} is shown in Figure 4.2 b and c, again using the parameters for SiNc at 532 nm, corresponding to the dynamics encountered under typical experimental conditions. Figure 4.2 b illustrates increasing accuracy with larger pump fluence. However, photochemical instability of many organic molecules limits the pump fluence. Note, that at $F > 400 \text{ mJ/cm}^2$ this dependence tends to saturate (indicating complete depletion of the ground state); therefore, both of the above factors limit the useful pump fluence. As seen from Figure 4.2 c, the accuracy of the DPP is low at very small concentrations, increases to a maximum, and decreases at larger concentrations, at which only a small fraction of the population moves to the triplet state. Thus, a proper choice of dye concentration is important to increase the sensitivity of the DPP.

Figure 4.2 d shows the interesting dependence of the DPP accuracy on $\sigma_{T1m} - \sigma_{S01}$. When $\sigma_{S01} = \sigma_{T1m}$ the accuracy is zero, corresponding to the case where there is no signal because TT absorption is equal to the ground-state absorption. For small positive values of $\sigma_{T1m} - \sigma_{S01}$, corresponding to RSA, the accuracy increases to a maximum and decreases for larger values. Negative values of $\sigma_{T1m} - \sigma_{S01}$ correspond to SA. Large values of σ_{S01} result in a significant population of $S1$ decaying into the triplet state when ϕ_T is large. However, it is clear that if $\sigma_{S01} \gg \sigma_{T1m}$, i.e. the TT reabsorption can be neglected, the second pump becomes unnecessary,

and the singlet depletion technique is sufficient. Unfortunately, in general it is not known *a priori* if the TT can be neglected. If the excitation pump wavelength corresponds to the SA region, the singlet ground state may be considerably depleted. This will increase the triplet-state population with the use of relatively small pump fluence ($\sim 6 \text{ mJ/cm}^2$) and small dye concentration ($\sim 10 \text{ }\mu\text{M}$, assuming $\varepsilon_{max} \sim 10^5 \text{ M}^{-1} \text{ cm}^{-1}$). This leads to increased accuracy in the determination of ϕ_T and σ_{Tlm} using the DPP. Note that large ϕ_T will lead to larger triplet-state population and, thus, higher accuracy of the DPP. For Figure 4.2 b-d, ϕ_T is chosen to be 0.2.

To demonstrate several possible situations encountered when analyzing triplet dynamics by the DPP, two organic dyes with distinct transient absorption characteristics are studied: (1) a commercially available SiNc (Sigma Aldrich, CAS 92396-88-8; SiNc) and (2) a new sulfur-containing squaraine (labeled as SD-SO 7517);

Picosecond degenerate PP setup is shown in Figure 4.3. The output of the picosecond laser system is first split by a 90:10 beam splitter, **BS**₁, into a pump (black lines) and probe (red lines). The polarization of the pump beams is set using a half-waveplate/polarizer combination, **HWP**₁/**P**₁, that is also used to control the pump energies before being focused by lens (**L**₁) onto the sample and ultimately blocked by aperture **A**. The probe beam is then sent through an additional half-waveplate/polarizer combination, **HWP**₂/**P**₂, to control the probe energy and, most importantly, to set the polarization of the probe at 54.7° (the “magic angle”) with respect to those of the pump. After propagating through a 15 ns delay line, constructed from two corner cubes, **CC**₁ and **CC**₂, and a 0.5 m translation stage, the beam is then sent back to a 50:50 beamsplitter, **BS**₃. A reference 50:50 beamsplitter, **BS**₄, is used to monitor the energy on the sample, and lens, **L**₂, is used to focus the probe within the pumps spot size. The probe is sent

through a final polarizer, P_3 , set at the probe polarization to reduce scattering from the pumps, and onto a signal detector to monitor the transmitted energy using lens, L_3 . Transmittance through the sample is the ratio of energy on the signal detector to the energy on the reference detector.

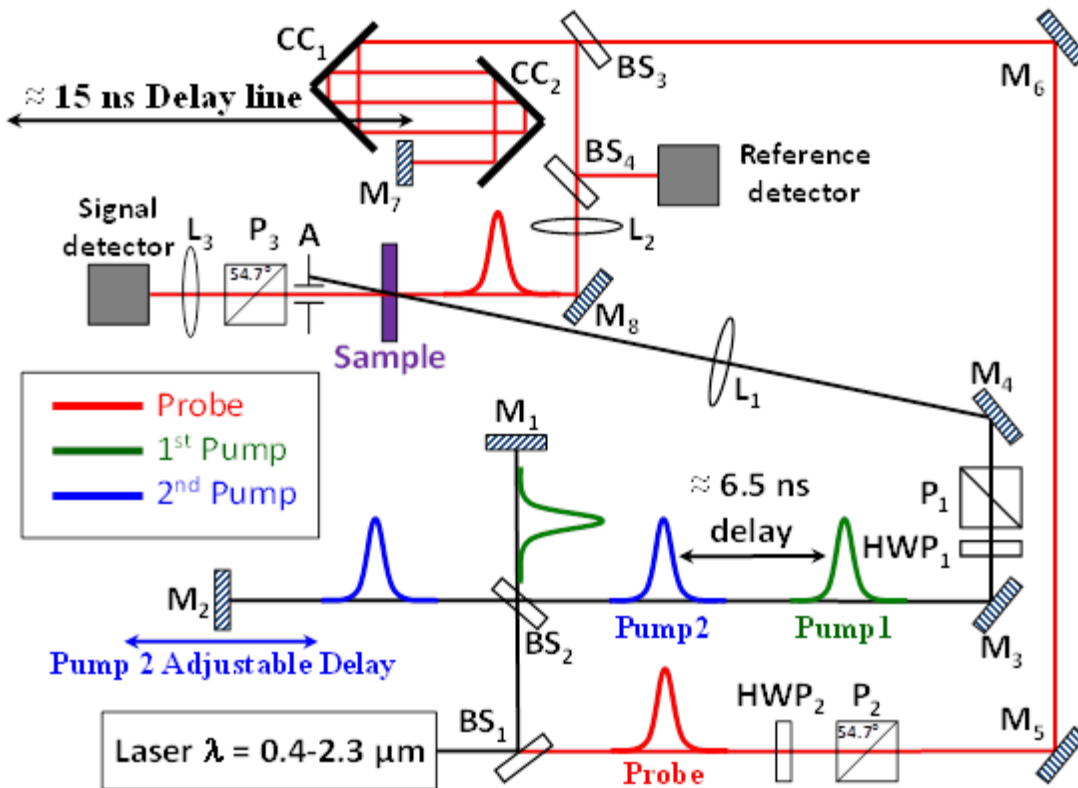


Figure 4.3. The DPP setup for picosecond measurements. Here all wavelengths are the same. Line colors are used to distinguish separate pulses for clarity.

The influence of fluence and concentration in the RSA region can be shown by performing DPP measurements on SiNc samples at 532 nm ($\sigma_{sol} = 2.8 \times 10^{-18} \text{ cm}^2$).

Three SiNc samples with different concentrations were prepared for studies with different pump fluences and in the different spectral regions. For the first sample of SiNc with the largest

concentration, $C = 2.1$ mM, and $F = 11$ mJ/cm² in each pump, the first drop in transmittance is ~25 - 30 %, see Figure 4.4a. To obtain the same change in transmittance for the second SiNc sample with smaller concentration, $C = 0.36$ mM, the pump fluence is increased to $F = 100$ mJ/cm² in each pump, see Figure 4.4b. Fitting the transmission curve for the first pump, the constant κ is determined to be $(22.5 \pm 0.7) \times 10^{-18}$ cm². As shown in the inset of Figure 4.4a, ϕ_T and σ_{TIm} cannot be uniquely determined. The fitting of experimental results for triplet state parameters for the first sample yields a very large error (more than 90%) in separating σ_{TIm} from ϕ_T , showing a major limitation of the DPP. As predicted, the second sample of SiNc, prepared with a smaller concentration and pumped with a larger fluence, allows for a unique determination of $\phi_T = (0.21 \pm 0.04)$ and $\sigma_{TIm} = (1.1 \pm 0.2) \times 10^{-16}$ cm² with significantly reduced errors and is in complete agreement with previously reported values [49, 54, 55]. Note that to use the smaller pump fluences, the wavelength of operation was moved to a region of large linear absorption.

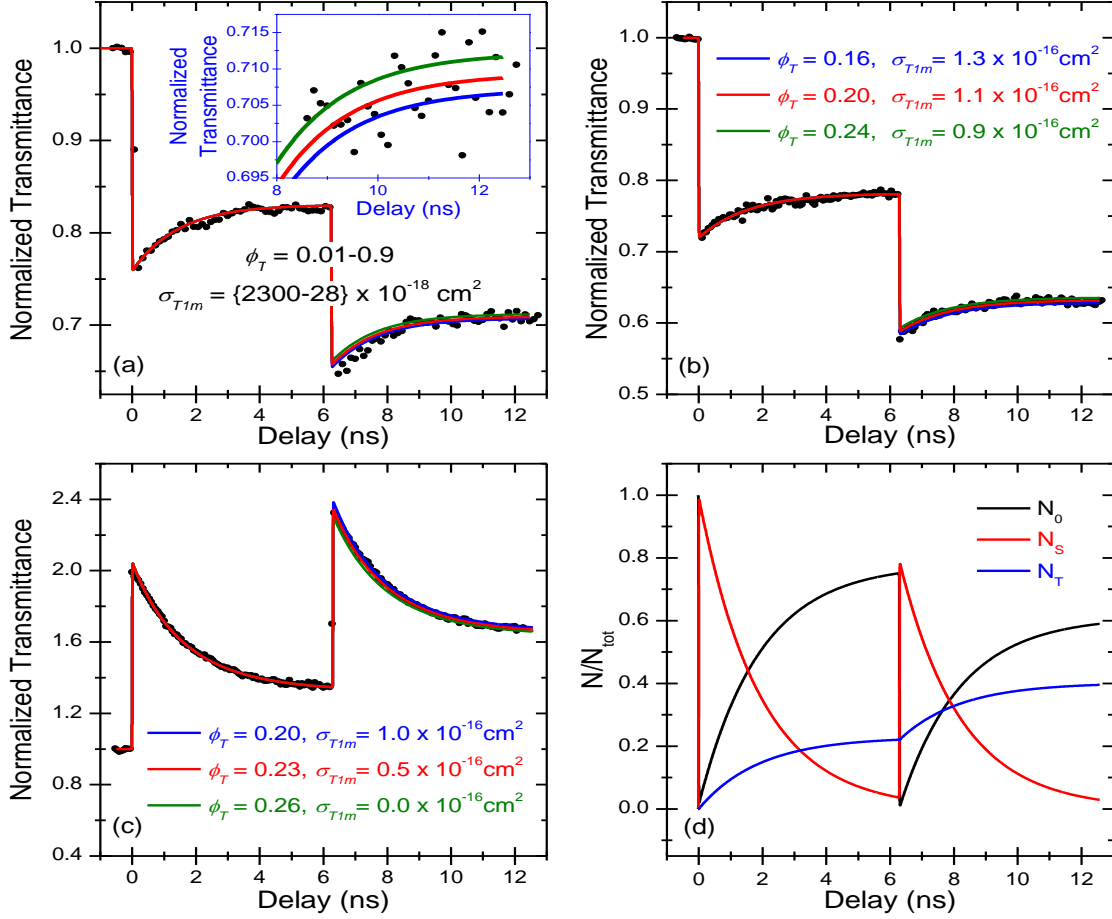


Figure 4.4. Experimental results and theoretical fitting for SiNc: (a) $C = 2.1$ mM ($T_L = 0.7$) and $F = 11$ mJ/cm² ($E = 1$ μJ, $w_0 = 75$ μm) in each pump; (b) $C = 0.36$ mM ($T_L = 0.94$), $F = 100$ mJ/cm² ($E = 15$ μJ, $w_0 = 95$ μm) in each pump. Pumping wavelength is 532 nm; $\sigma_{SiN} = 32 \times 10^{-18}$ cm²; $\tau_S = 1.5$ ns; (c) Experimental results and theoretical fitting for SiNc at 770 nm; $C = 15$ μM ($T_L = 0.3$), $F = 0.84$ mJ/cm² ($E = 0.7$ μJ, $w_0 = 230$ μm) in the first and $F = 0.92$ mJ/cm² ($E = 0.7$ μJ, $w_0 = 220$ μm) in the second pump; $\sigma_{SiN} = (4.0 \pm 0.2) \times 10^{-16}$ cm²; $\tau_S = 1.5$ ns; and (d) population dynamics for case (c). The inset in Figure 4.4a shows three curves that fit the data within the experimental errors indicating low accuracy under these experimental conditions.

The third sample of SiNc was prepared for SA studies, therefore the excitation pump wavelength was tuned to 770 nm, close to the linear absorption peak at 774 nm ($\sigma_{SOI} = 12.5 \times 10^{-16} \text{ cm}^2$; Figure 3.13), see Figure 4.4c. Both the dye concentration and the pump fluences were much smaller for this experiment, with $C = 15 \text{ }\mu\text{M}$, and $F = 0.84 \text{ mJ/cm}^2$ in the first and $F = 0.92 \text{ mJ/cm}^2$ in the second pump. Again constant κ was determined from the first pump and equal: $\kappa = (-2.7 \pm 0.6) \times 10^{-16} \text{ cm}^2$. Fitting the experimental results for the second pump, yields: $\phi_T = (0.23 \pm 0.03)$, which is in agreement with the value obtained from the RSA measurements. The value of the TT cross-section is $\sigma_{TIm} = (0.5 \pm 0.3) \times 10^{-16} \text{ cm}^2$. Figure 4.4d shows population dynamics for SiNc performed in the SA regime. We can see that in this case, even with the smallest pump fluence, the ground state is nearly completely depleted. A larger error in the determination of σ_{TIm} is due to the dominance of linear absorption in this region, $\sigma_{SOI} = 12.5 \times 10^{-16} \text{ cm}^2$, over an order of magnitude larger than σ_{TIm} . However, since ϕ_T is constant for all wavelengths, σ_{TIm} can be determined from a separate pump probe measurement at other wavelengths, once ϕ_T has been determined. A value of $\phi_T = (0.23 \pm 0.03)$, determined from DPP in the SA regime, together with a value of $\kappa = (22.5 \pm 0.7) \times 10^{-18} \text{ cm}^2$, determined from a single pump-probe experiment at 532 nm in the RSA regime, yields a value of σ_{TIm} for 532 nm with reasonable accuracy, $\sigma_{TIm} = (100 \pm 10) \times 10^{-18} \text{ cm}^2$. This shows that accurate results are obtainable with pump fluences that are $10^2 \times$ less than in RSA measurements. When the investigated dyes are not photochemically stable and only exist in small research quantities, significant benefit in determining ϕ_T is gained by moving the DPP to the SA regime.

SD-SO 7517 is example of photochemically unstable molecule. Utilizing DPP in the SA regime, ϕ_T was measured for SD-SO 7517 at two different wavelengths, 640 nm and 660 nm (Figure 4.5) with linear absorption cross sections of 5.1 and $12.1 \times 10^{-16} \text{ cm}^2$, respectively. Excitation wavelengths were chosen to avoid the stimulated emission. As shown in Fig. 7, both experiments give indistinguishable values for $\phi_T = (0.64 \pm 0.03)$, while $\sigma_{Tlm} = (2.4 \pm 0.2) \times 10^{-16} \text{ cm}^2$ at 640 nm and $\sigma_{Tlm} = (4.7 \pm 0.4) \times 10^{-16} \text{ cm}^2$ at 660 nm. At both wavelengths, the values, obtained for σ_{Tlm} , are smaller than the ground state absorption cross section, as expected. These results show that performing the DPP in the SA regime often yields the most accurate determination of ϕ_T . Single pump-probe measurements can now be utilized to determine the wavelength dependence of σ_{Tlm} (after an accurate determination of ϕ_T has been made).

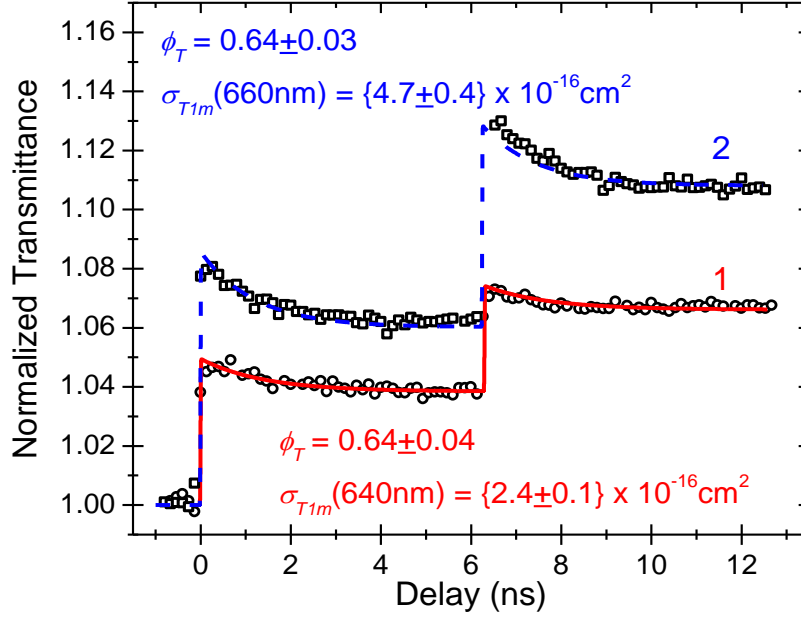


Figure 4.5 DPP experimental results and theoretical fitting for SD 7517: Pump wavelength at (1) 640 nm (red fit); $\sigma_{SOI} = 5.1 \times 10^{-16} \text{ cm}^2$; $\sigma_{SIn} = (2.8 \pm 0.2) \times 10^{-16} \text{ cm}^2$; $C = 6.8 \text{ } \mu\text{M}$ ($T_L = 0.8$); $F = 0.32 \text{ mJ/cm}^2$ ($E = 0.1 \text{ } \mu\text{J}$, $w_0 = 140 \text{ } \mu\text{m}$) in the first and $F = 0.52 \text{ mJ/cm}^2$ ($E = 0.1 \text{ } \mu\text{J}$, $w_0 = 110 \text{ } \mu\text{m}$) in the second pump; and pump wavelength at (2) 660 nm (blue-dash fit); $\sigma_{SOI} = 12.1 \times 10^{-16} \text{ cm}^2$; $\sigma_{SIn} = (5.8 \pm 0.2) \times 10^{-16} \text{ cm}^2$, and $C = 3 \text{ } \mu\text{M}$ ($T_L = 0.8$); $F_1 = 0.5 \text{ mJ/cm}^2$ ($E = 0.5 \text{ } \mu\text{J}$, $w_0 = 250 \text{ } \mu\text{m}$) in the first and $F_2 = 0.55 \text{ mJ/cm}^2$ ($E = 0.5 \text{ } \mu\text{J}$, $w_0 = 240 \text{ } \mu\text{m}$) in the second pump. In both cases $\tau_S = 1.4 \text{ ns}$.

CHAPTER 5. π - CONJUGATED MATERIALS WITH ENHANCED INTERSYSTEM CROSSING RATES

5.1. Polymethine-like molecules

Polymethine dyes (PDs) have been known for more than a century and have found numerous applications as photosensitizers in photography and photodynamic therapy, fluorescent probes in chemistry and biology, active and passive laser media, materials for nonlinear optics and electroluminescence, memory devices, etc.[58-61]. These compounds exhibit large molar absorbance (up to $3 \times 10^5 \text{ M}^{-1}$) and tunable absorption bands in the visible and near-infrared regions important for the development of organic materials with large nonlinearities for nonlinear optical applications. PD's belong to the family of linear π -conjugated materials composed of a molecular chain of alternate single and double covalent bonds and two terminal groups. General structure of PD's is shown in Figure 5.1.

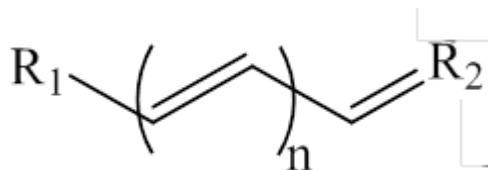


Figure 5.1. General structure of PD molecule; n is length of conjugated chain and R_i is terminal group.

Based on the number of methine ($-\text{CH}=\text{}$) groups in the π -conjugation, linear conjugated compounds can be formally divided into polymethines (containing an odd number of methine groups with alternating single and double bonds) and polyenes (containing an even number of methine groups). These two families of dyes have distinctive electronic structures, and thus differ by their linear and nonlinear optical properties [62-64]. The electronic properties of PDs

can be tailored by changing the length of the conjugation chain and by adding specific electron acceptor (A) or electron donor (D) terminal groups R, thus, forming the following molecular structures: cationic D- π -D, anionic A- π -A, and neutral D- π -A. Additionally, electron acceptor or donor groups may be included into the main π -conjugation chain resulting in the neutral quadrupolar structures, such as D- π -A- π -D or A- π -D- π -A.

Squaraine (or squarylium) dyes (SDs), may be considered as compounds from the polymethine family as they combine polymethine (odd) number of carbon atoms in the chain with an electron acceptor C_4O_2 bridge at the center of the conjugated chromophore [46]. General structure of SD's is shown in Figure 5.2.

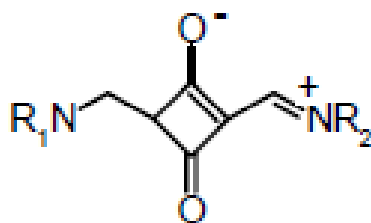


Figure 5.2 General structure of SD molecule; electron acceptor C_4O_2 at the center of the chain and R_1 is terminal group.

PDs are extensively studied and many of their linear and nonlinear properties are well-understood [46, 65-67]. Structure-property relations are developed allowing one not only to predict the main properties of existing compounds but also to synthesize new ones with desirable optical properties. The missing link in this study for PD-like molecules is the clear understanding of singlet-triplet (S-T) conversion processes, which are usually characterized by small triplet quantum yields, ϕ_T , $\sim 10^{-2} - 10^{-4}$ [68-70]. Typically, with nano-, pico- or femtosecond pulse

durations the population of the triplet states is negligibly small and only S-S transitions are needed for the analysis of linear and nonlinear processes. The nature of the vanishingly small intersystem crossing rate, k_{ST} , in polymethine-like molecules has not been systematically interpreted in the literature, and the strategy to design PDs with an increased probability of triplet formation has not been proposed. PD-like molecules with simultaneously large ϕ_T , large 2PA cross sections (δ_{2PA}) and large quantum yield of singlet oxygen generation (ϕ_A) can be potentially useful for application in two-photon photodynamic and optical power limiting requiring strong S-S and triplet-triplet (T-T) excited-state absorption.

The molecular structures of the polymethine-like dyes studied in this work are shown in Figures 5.3-4. They are separated into two groups. The first group (Figure 5.3a-c) reflects attempts to enhance k_{ST} in PDs due to the heavy-atom effect by designing molecules with the heavy-atom substitutions. These molecules contain: Br-atom connected to the π -conjugated chain (labeled as PD 2929) in comparison with the analogous unsubstituted PD 2350; Se-atoms incorporated into the terminal groups (labeled as PD 1852 and PD 4216); and both Se-substituted terminal groups and a Br-atom substitution within the π -conjugated chain (labeled as PD 2972). The second group of compounds (Figure 5.4a-d) correspond to the introduction of atoms with unshared pairs of electrons producing $n \rightarrow \pi^*$ transitions. They are squaraines with oxygen (labeled as SD-O), and with sulfur (labeled as SD-S / SD-SO) atoms in the central acceptor C_4O_2 (or C_4S_2 / C_4SO) fragments. All eight SDs are paired as SD-O 2405 and SD-S 7508; SD-O 2577 and SD-S 7504; SD-O 2243 and SD-S 7507; SD-O 2053 and SD-SO 7517 (containing one sulfur and one oxygen). Each pair of dyes contains the same donor terminal groups, identical

polymethine chain length and differs only by oxygen or sulfur substitution in the central acceptor fragment.

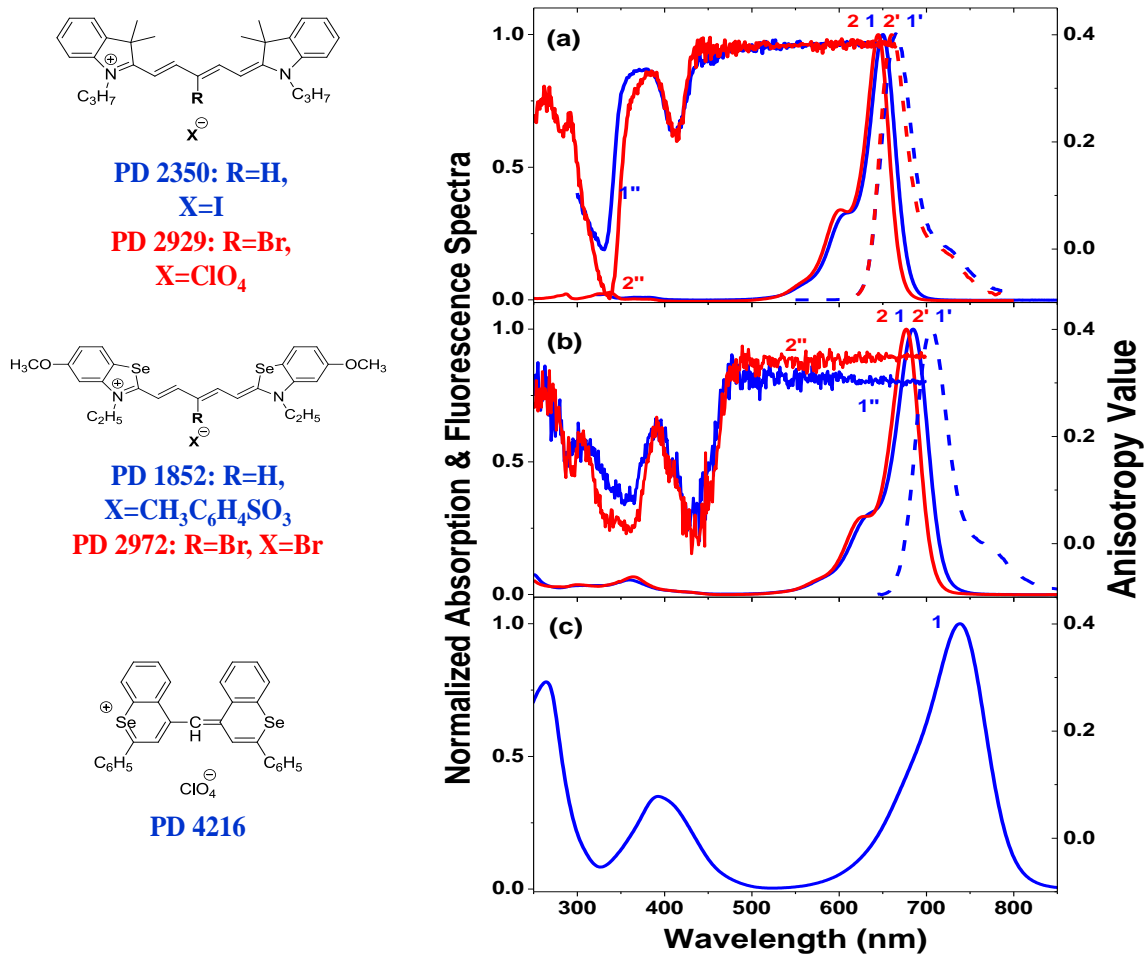


Figure 5.3 Molecular structures, absorption (solid lines 1, 2), fluorescence (dashed lines 1', 2') and anisotropy (1'', 2'') for: (a) PD 2350 (1, 1', and 1'') and PD 2929 (2, 2', and 2''); (b) PD 1852 (1, 1', and 1'') and PD 2972 (2, 2', and 2''); (c) PD 4216 in ACN (1). Absorption and fluorescence spectra are measured in ethanol; anisotropy spectra are measured in glycerol. No fluorescence was detected for PD 4216.

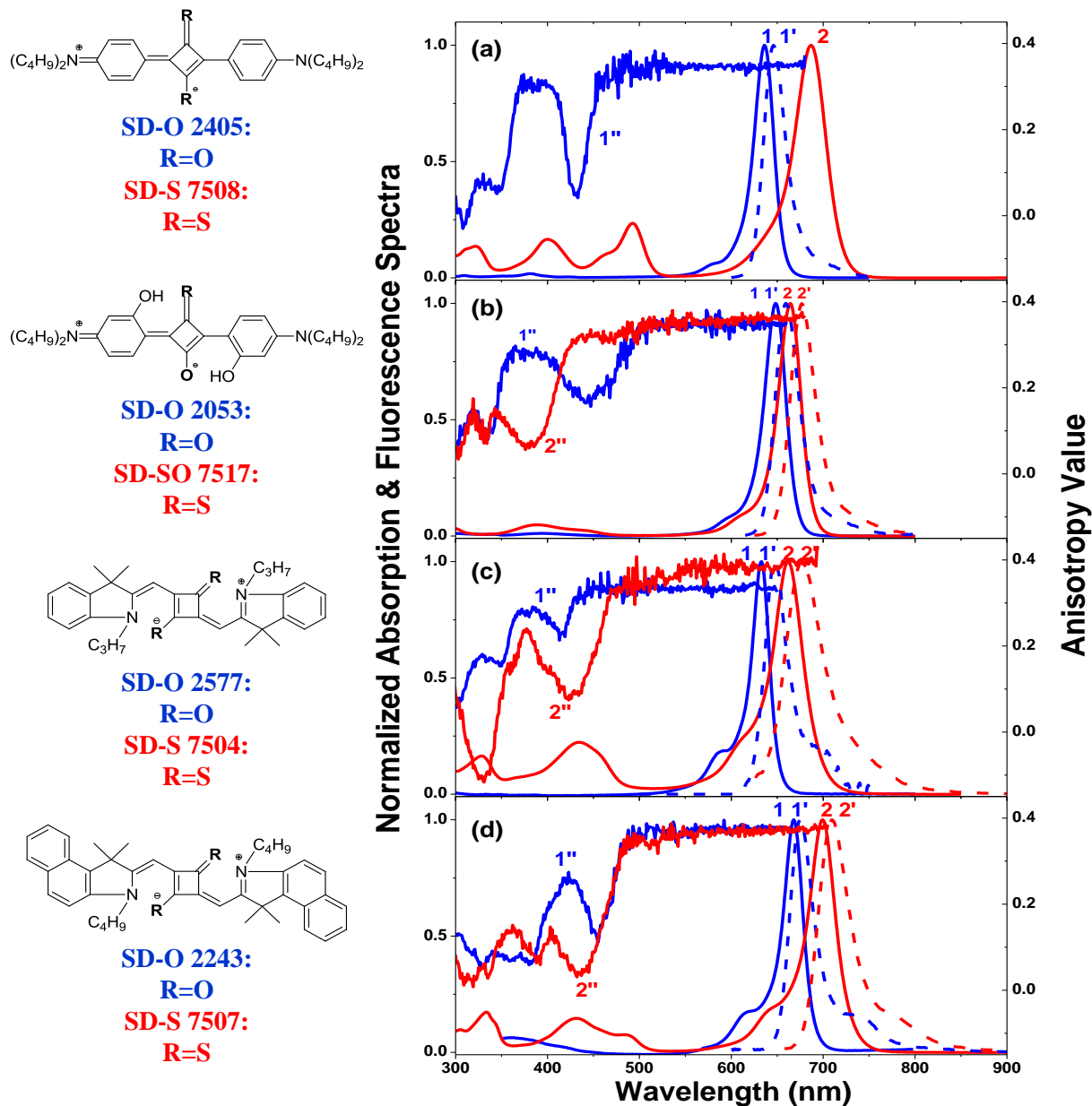


Figure 5.4 Molecular structures, absorption (solid lines 1, 2), fluorescence (dashed lines 1', 2') and anisotropy (1'', 2'') for: (a) SD-O 2405 (1, 1', and 1'') and SD-S 7508 (1) in toluene; (b) SD-O 2053 (1, 1', and 1'') and SD-SO 7517 (2, 2', and 2'') in DCM; (c) SD-O 2577 (1, 1', and 1'') in ethanol and SD-S 7504 (2, 2', and 2'') in toluene; (d) SD-O 2243 (1, 1', and 1'') in DCM and SD-S 7507 (2, 2', and 2'') in toluene. All anisotropy spectra are measured in pTHF. No fluorescence was detected for SD-S 7508.

5.1.1 Linear Experimental Results

The linear absorption spectra of all molecules, recorded by a Varian Cary 500 spectrophotometer, are presented in Figures 5.3-4. The choice of solvents for each dye is based on the solubility of the dyes and includes ethanol (EtOH), toluene (TOL), acetonitrile (ACN), and dichloromethane (DCM). The absorption spectra for all dyes are composed of intense cyanine-like bands attributed to their $\pi\pi^* S_0 \rightarrow S_1$ transitions, and weaker higher-lying $S_0 \rightarrow S_n$ transitions in the visible and ultraviolet regions. The absorption spectra of PDs with and without Br-substitution, shown in Figure 5.3, are similar reflecting that Br-atom placed in the meso-position of the π -conjugated chain does not significantly affect the charge distribution within the chain. The absorption spectrum of PD 4216 is strongly red-shifted even for this short chain length and shows a relatively intense absorption around 400 nm due to the existence of own π -conjugation system in the terminal groups decreasing HOMO/LUMO gap. The main absorption bands for all SD-S dyes, shown in Figure 5.4, are red-shifted (≈ 30 -50 nm) in comparison to their SD-O analogues, and their higher-lying transitions are more intense, which can be explained by the existence of π -conjugation system in the perpendicular S – S chromophore. Note that for SD-SO 7517, of which only one oxygen atom is replaced by sulfur atom, the red-shift of the main absorption band is significantly less, ~ 13 nm with respect to its counterpart SD-O 2053. All SD-S dyes are less photochemically stable than SD-O dyes, which require special care in experimental studies.

The fluorescence spectra of all compounds, corrected for the spectral responsivity of the detection system, are measured by a PTI QuantaMaster spectrofluorimeter and shown in Figures 5.3-4. We note the spectral mirror symmetry between absorption and fluorescence spectra for all

compounds reflecting only a small change in the excited-state geometry upon excitation. Fluorescence quantum yields, ϕ_F , are measured using the standard method of comparison with a known reference dye, Cresyl Violet perchlorate (CAS# 41830-80-2, Sigma Aldrich) in methanol, which has an absorption peak at 594 nm, fluorescence peak at 620 nm, and a fluorescence quantum yield, $\phi_F = 0.54 \pm 0.03$.^[40] No fluorescence ($\phi_F < 0.001$) is observed for SD-S 7508 and PD 4216, however, for different reasons. As to be shown in Section 5.1.2, SD-S 7508 is characterized by near unity ϕ_T , indicating the ISC process as the most effective channel for nonradiative decay of the S₁ state, while the main radiationless path for PD 4216 is internal conversion due to its strongly nonplanar structure.

Excitation anisotropy spectra, shown in Figures 5.3-4, reveal alternating peaks and valleys. The peaks in the excitation anisotropy spectrum indicate a small angle between the absorption and emission transition dipoles, suggesting allowed one-photon absorption (1PA) transitions; while valleys indicate large angles between these two dipoles, suggesting forbidden 1PA transitions, such as transitions between states of the same symmetry. Due to selection rules for symmetrical cyanine-like dyes, these valleys in the anisotropy spectra could indicate the positions of allowed 2PA transitions. Thus, as was shown by us previously, excitation anisotropy spectra can serve as a useful guide to predict the positions of the final states in the 2PA spectra of cyanine-like dyes^[71].

The direct measurements of singlet oxygen, ¹O₂, luminescence at ≈ 1270 nm were performed at room temperature using a PTI QuantaMaster spectrofluorometer with a nitrogen cooled Hamamatsu R5509-73 photomultiplier tube detector. ¹O₂ generation quantum yields (ϕ_Δ)

were measured in comparison with the known dye Acridine in ACN with $\phi_A = 0.82$ [42] at room temperature with air-saturated solution.

The most significant linear properties for the dyes studied are listed in Table 1.

5.1.2 Nonlinear Experimental Results

Nonlinear optical investigations include a broad range of femto- and picosecond pulsewidth measurements with the goal of determining the ISC transitions rates, formation of the excited-state singlet-singlet (S-S) and triplet-triplet (T-T) absorption bands, 2PA bands, singlet and triplet state lifetime dynamics, and ϕ_T .

Single and double pump-probe measurements

For the molecules with small ISC (for example, SD-O molecules), the populations of the triplet states are negligible, and the five-level model can be reduced to a three-level model accounting for the singlet states only. An example of the experimental decay kinetics and its numerical simulation for SD-O 2577 is shown in Figure 5.5a. The measurement is done at pump and probe wavelengths of 532 nm in the reverse saturable absorption (RSA) region where $\sigma_{SIn} \gg \sigma_{SOI}$. Pump-probe dynamics show a complete recovery of the initial transmittance after a few nanoseconds time delay indicating a negligible population of the triplet state. By fitting experimental pump-probe dynamics using simplified Equations 3.5-6, the values of σ_{SIn} and τ_S are determined as: $\sigma_{SIn} = 1.3 \times 10^{-16} \text{ cm}^2$ and $\tau_S = 0.9 \text{ ns}$.

As already mentioned in chapter 3.3 for molecules with significantly large ISC (SD-S molecules) the five-level model cannot be simplified. In this case a classical single pump-probe method cannot simultaneously determine the singlet- and triplet-state absorption parameters and

transition rates and DPP method has to be utilized. A detailed description of the DPP technique and methods for its optimization are described in chapter 4. An example of the experimental DPP decay kinetics and its numerical simulation for SD-S 7504 are shown in Figure 5.5b. This measurement is done at a pump and probe wavelength of 670 nm in the saturable absorption (SA) region, close to the peak of linear absorption where $\sigma_{SIn} \ll \sigma_{S0I}$. The large value of σ_{S0I} ensures that a large fraction of ground-state population is moved to the triplet state which significantly improves the accuracy for determining the triplet quantum yield. By fitting the DPP dynamics, the values of σ_{SIn} , σ_{TIm} , ϕ_T and τ_S are determined as: $\sigma_{SIn} = (2.6 \pm 0.5) \times 10^{-16} \text{ cm}^2$, $\sigma_{TIm} = (2.5 \pm 0.5) \times 10^{-16} \text{ cm}^2$, $\phi_T = (0.75 \pm 0.03)$ and $\tau_S = (0.50 \pm 0.05) \text{ ns}$.

It is important to mention that all triplet yield measurements are performed in air-saturated solutions. The effect of oxygen on ϕ_T and τ_S is also checked by partially removing the oxygen owing to bubbling solutions with nitrogen gas stream for about half an hour. Result show that removing the oxygen from the samples does not significantly affect ϕ_T and τ_S values. There are two reasons for small oxygen influence on ϕ_T and τ_S . First, there is very little probability for effective oxygen quenching of singlet state in this case. As discussed in chapter 2,5 for effective quenching of singlet state energy difference ΔE_{ST} has to be larger than energy difference between ground and first excited state of oxygen. Second, since solubility of molecular oxygen in most organic solvents is relatively low ($\sim 10^{-2} \text{ M}$ at atmospheric pressure) states with decay times shorter than 10 ns will not be effectively quenched in air saturated solutions [10]. The oxygen concentration was not measured before and after bubbling, however, the oxygen concentration after bubbling was decreased significantly thus strongly affecting the triplet-state lifetimes. The main results of single and DPP measurements are given in Table 1.

As seen from Table 1, the largest triplet quantum yields are found for sulfur-containing squaraines, from $\phi_T = 0.46 \pm 0.04$ for SD-S 7507 to $\phi_T = 0.98 \pm 0.02$ for SD-S 7508, and the smallest measurable triplet yield, $\phi_T = 0.05 \pm 0.05$, was found for PD 2929 with Br-substitution in the polymethine chain. PD 2350, without heavy atoms in the chemical structure, and PD 4216, with Se-atoms incorporated into the terminal groups (due to nonplanar dye structure leading to extremely small $\tau_S = 1$ ps), show negligible ISC, and therefore $\phi_T \approx 0$. The same negligible ISC is observed for all oxygen-containing squaraines SD-O 2405, SD-O 2577, SD-O 2243 and SD-O 2053.

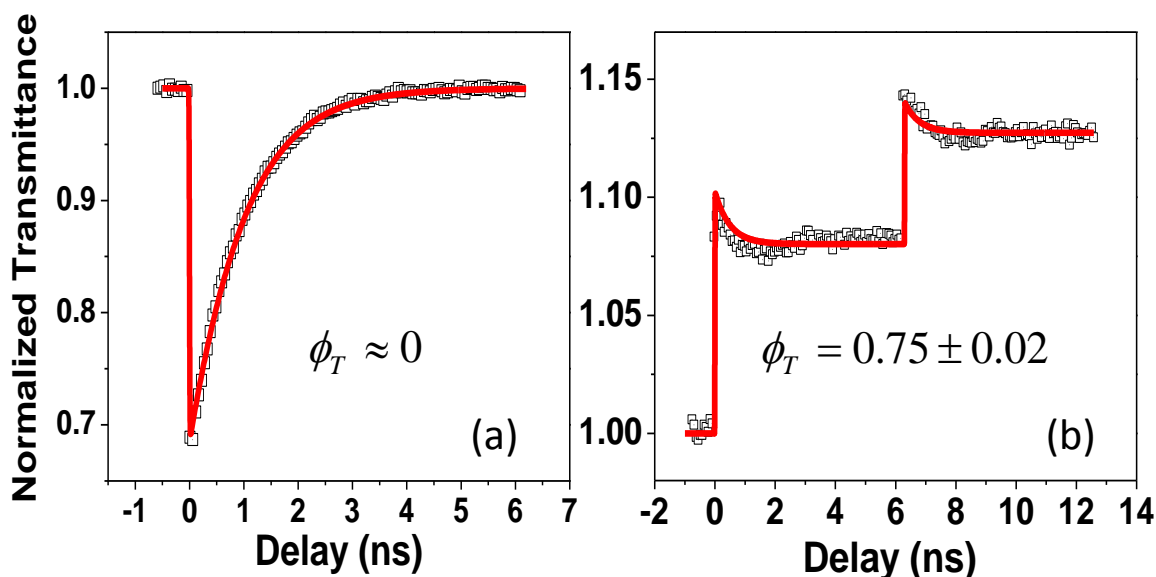


Figure 5.5 (a) Single pump-probe measurements for SD-O 2577 in DCM at 532 nm (linear transmittance 0.7, pump fluence 3.8 mJ/cm^2 , $\sigma_{SOI} = 8.8 \times 10^{-18} \text{ cm}^2$, $\sigma_{SIn} = 1.3 \times 10^{-16} \text{ cm}^2$, $\tau_S = 0.9 \text{ ns}$); (b) DPP measurements for SD-S 7504 in toluene at 670 nm (linear transmittance 0.75, fluence in each pump 0.33 mJ/cm^2 , $\sigma_{SOI} = 5.2 \times 10^{-16} \text{ cm}^2$, $\sigma_{SIn} = (2.6 \pm 0.5) \times 10^{-16} \text{ cm}^2$, $\sigma_{TIn} = (2.5 \pm 0.5) \times 10^{-16} \text{ cm}^2$, $\tau_S = (0.50 \pm 0.05) \text{ ns}$).

ESA measurements

Figure 5.6 a, c, e shows the ESA spectra for three squaraine molecules SD-O 2053, SD-SO 7517 and SD-O 2045, while Figure 5.6 b, d, f presents their decay kinetics measured by degenerate picosecond pump-probe with wavelength set to the RSA region. Oxygen-substituted SDs (i.e. SD-O 2053 and SD-O 2405) show only S - S ESA, and their decay kinetics demonstrate a complete restoration of the ground state population within several nanoseconds (Figure 5.6 b, f). In contrast, the decay kinetics of the oxygen-sulfur substituted SD-SO 7517 shows a non-recovery of the ground state population beyond 4 ns (Figure 5.6 d), indicating a significant population built up in the long-lived triplet state. Figure 5.6 d shows that σ_{S1n} and σ_{T1n} values for SD-SO 7517 at the peaks of S - S and T - T ESA spectra are comparable. The similarity of S - S ESA in two dyes, SD-O 2053 and its analogue SD-SO 7517, is an evidence of the insignificant effect of sulfur substitution on the singlet electronic level structure. Figure 5.7 a represents S - S and T - T ESA spectra for SD-S 7508 ($\Phi_T = 0.98$, $\tau_{ISC} = 4.5$ ps) in toluene, with two distinctive decay kinetics (Figure 5.7 b), measured by femtosecond WLC pump-probe with pump excitation wavelength at 687 nm (i.e. in the linear absorption peak), and two probe wavelengths at 480 nm and 570 nm. The probe kinetics at 480 nm (trace 1 in Figure 5.7 b) firstly shows RSA process (here $\sigma_{S1n} > \sigma_{S01}$) with a fast decay time of ~ 4.5 ps, connected with the rapid depopulation of S_1 state due to ISC to T_1 state. Population of T_1 state leads to T - T ESA with a much slower decay time (> 500 ns, as discussed in Section. 2.2.3) resulting in SA process (here $\sigma_{T1n} < \sigma_{S01}$). In contrast, the probe dynamics at 570 nm (trace 2 in Figure 5.7 b) shows only RSA. Since σ_{S1n} (570 nm) $\approx \sigma_{S01}$ (570 nm), as shown in Figure 5.7 a, the transmittance change connected with S -

S ESA is not observable, and the probe kinetics reflects T-T ESA process only (where $\sigma_{T1n} > \sigma_{S01}$) with much longer lifetime.

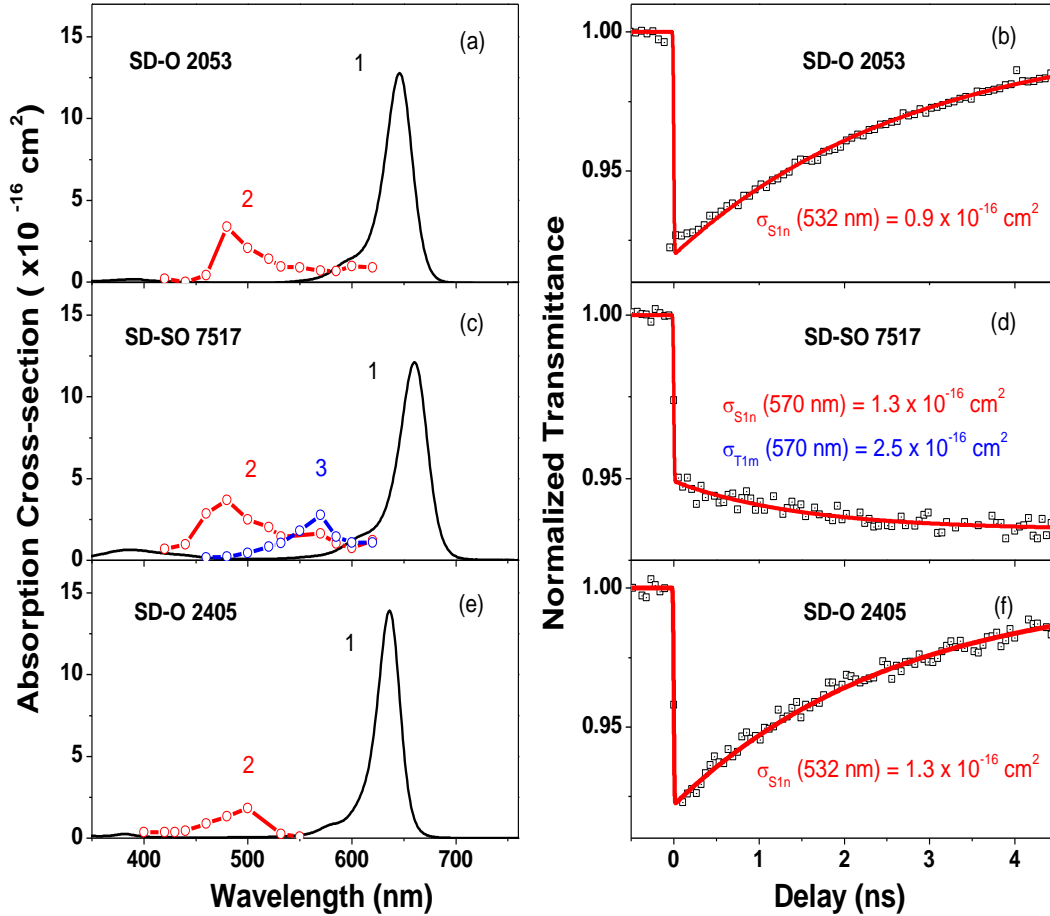


Figure 5.6 Linear absorption (1), S - S (2) and T - T (3) ESA absorption spectra for (a) SD-O 2053; (b) SD-SO 7517; (c) SD-O 2405. Decay kinetics for (d) SD-O 2053 at 532 nm (pump fluence 2.6 mJ/cm², $\sigma_{S01} = 33 \times 10^{-18} \text{ cm}^2$, $\sigma_{S1n} = 0.9 \times 10^{-16} \text{ cm}^2$, $\tau_S = 2.5 \text{ ns}$); (e) SD-SO 7517 at 570 nm (pump fluence 0.5 mJ/cm², $\sigma_{S01} = 23 \times 10^{-18} \text{ cm}^2$, $\sigma_{S1n} = 1.3 \times 10^{-16} \text{ cm}^2$, $\sigma_{T1n} = 2.5 \times 10^{-16} \text{ cm}^2$, $\tau_S = 1.5 \text{ ns}$) (f)

SD-O 2405 at 532 nm (pump fluence 1 mJ/cm², $\sigma_{SOI} = 9.2 \times 10^{-18} \text{ cm}^2$, $\sigma_{SIn} = 1.3 \times 10^{-16} \text{ cm}^2$, $\tau_S = 2.2$ ns); SD-O 2053 and SD-SO 7517 are measured in ACN, and SD-O 2405 is measured in toluene.

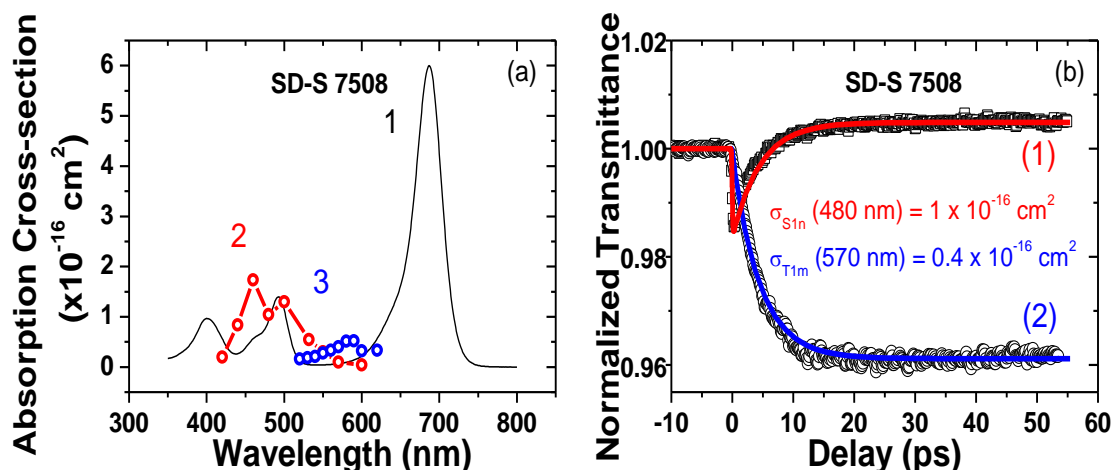


Figure 5.7 Linear absorption (1), S - S (2) and T - T (3) ESA absorption spectra (a) and decay kinetics (b) at 480 nm (pump fluence 0.5 mJ/cm², $\sigma_{SOI} = 90 \times 10^{-18} \text{ cm}^2$, $\sigma_{SIn} = 1 \times 10^{-16} \text{ cm}^2$, $\tau_S = 4.5$ ps) (1) and 570 nm (pump fluence 0.5 mJ/cm², $\sigma_{SOI} = 6.5 \times 10^{-18} \text{ cm}^2$, $\sigma_{TIn} = 0.5 \times 10^{-16} \text{ cm}^2$, $\tau_S = 4.5$ ps) (2) for SD-S 7508 in toluene.

Triplet state lifetime measurements

Triplet-state lifetimes, τ_{T10} , at room temperature are measured with a modified picosecond pump-probe setup, where the pump beam is set at a wavelength close to the linear absorption peak of each investigated dye, and a CW, frequency doubled Nd:YAG laser at 532 nm was used as the probe beam. The transmittance of the sample was recorded by a digital oscilloscope, Tektronix TDS 680C, triggered from the picosecond pump laser. All experimental

data for τ_{T10} are presented in Table 1. It is seen that for most of the molecules in air-saturated solutions, τ_{T10} values are close and vary from 200 to 300 ns.

It is well-known that atmospheric oxygen is an effective quencher of the triplet state,[19]. Therefore, triplet-state lifetime measurements are performed for several sulfur-containing squaraines in two solvents of different polarity, toluene and ACN, before and after oxygen removal using the procedure described in Section.2.2.1. Comparison of decay kinetics for air-saturated and nitrogen-purged toluene and ACN solutions for SD-SO 7517 is shown in Figure 5.8a, b. As seen, SD-S 7517 in both air-saturated solutions shows a single-exponential decay with $\tau_{T10} = 0.2\text{--}0.3 \mu\text{s}$. As expected, oxygen removal leads to an increase of the triplet-state lifetime; however, in different ways depending on solvent polarity. In low polar toluene solution, the single-exponential decay kinetics is changed to double-exponential decay with lifetimes of 0.9 μs and 4.2 μs . In polar ACN solution, triplet-state decay kinetics remain single-exponential with $\tau_{T10} = 0.6 \mu\text{s}$. The double-exponential decay of triplet-state lifetime was also observed for all sulfur-containing squaraines in toluene after oxygen removal (as shown in Table 1), and can be explained by changing the order of the two low lying triplet states of different orbital configuration ($n\pi^*$ and $\pi\pi^*$ nature) in nonpolar solvent. A similar effect was previously observed for aromatic carbonyl compounds.[72] Based on the explanation of Ref. [72], we can assume that the double-exponential kinetics in toluene corresponds to decay from the mixed $n\pi^*$ and $\pi\pi^*$ triplet states, while highly polar ACN, raising the energy of the $\pi\pi^*$ -triplet state with respect to the $n\pi^*$ -triplet state, shows no discernible long-lived component.

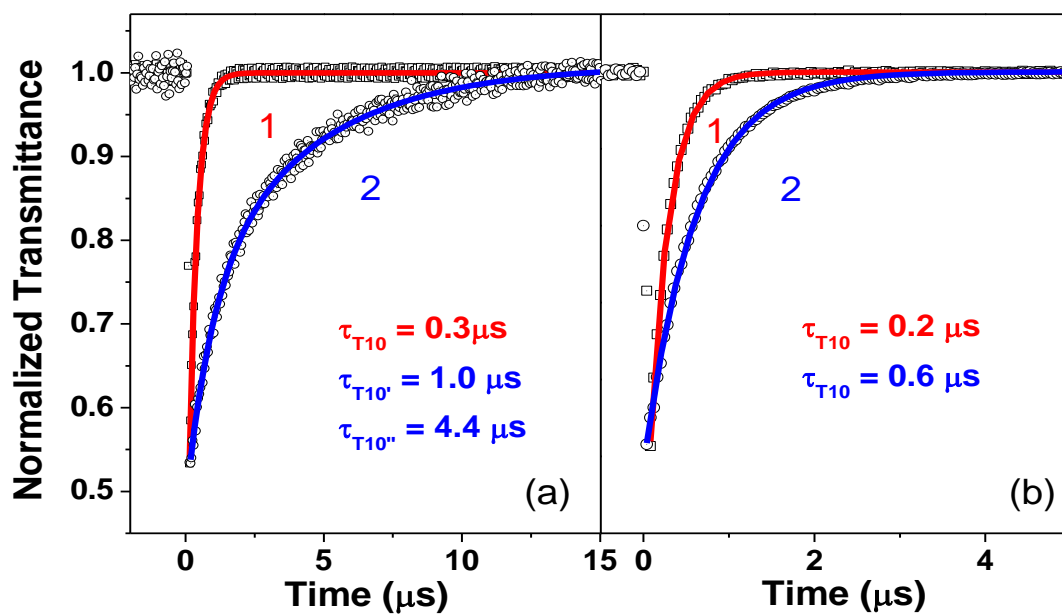


Figure 5.8 Triplet lifetime measurements for SD-S 7517 in (a) toluene and in (b) ACN. Shorter decays (1) correspond to air-saturated solutions, while longer decays (2) correspond to solutions with oxygen removed.

Two-photon absorption measurements

2PA spectra, measured by femtosecond system, are obtained by two well-established methods: two-photon absorption induced fluorescence (2PF) and Z-scan techniques.[53, 73] The 2PF represents an indirect way to measure the 2PA cross sections by comparing the integrated fluorescence signal from the investigated sample to a reference compound (with known 2PA cross section) measured under identical conditions. It can thus be applied to the molecules with relatively large fluorescence quantum yields. The Z-scan, representing a direct way to measure

the 2PA cross sections without the use of reference samples, may be applied to any compound, including nonfluorescent ones. Figure 5.9 shows 2PA spectra of these dyes in toluene solution along with their linear absorption and fluorescence excitation anisotropy spectra. Owing to its large Φ_F , the 2PA spectrum of SD-O 2053 in toluene was measured by 2PF; however, open apertures Z-scans at a few wavelengths were also performed to verify the δ_{2PA} values. The 2PA spectrum of SD-SO 7517 was measured with the open aperture Z-scan in a 1 mm flow cell to avoid photochemical damaging of this dye under strong laser irradiation. The flow rate, controlled by a tube-pump (Masterflex®), was set at ~350 mL/min, which is fast enough to avoid multi-shot excitation of dye molecules. Since 2PA is an instantaneous process, the flowing setup doesn't affect the 2PA signal.

It is seen from Figure 5.9 that both squaraine dyes exhibit similar 2PA spectra. The first 2PA bands are located at the vibrational shoulders of their $S_0 \rightarrow S_1$ transitions with similar $\delta_{2PA} \approx 200$ GM. Note that the “vibronic coupling” band for SD-SO 7517 is slightly red-shifted with respect to SD-O 2053, due to the red-shift of linear absorption peak. The positions of the second 2PA bands with $\delta_{2PA}^{max} = 1200$ GM at 840 nm coincide for both dyes. The third 2PA peaks cannot be resolved due to the presence of the linear absorption edges. The largest $\delta_{2PA} = 1660$ GM (at 760 nm) is observed for SD-SO 7517. This enhancement, as compare to SD-O 2053, can be attributed to the red-shift of the linear absorption peak for SD-SO 7517 leading to a smaller detuning energy and thus to intermediate state resonance enhancement.[74] Based on the previous data [75] and results of the current 2PA measurements, we can conclude that sulfur substitution in squaraine dyes does not significantly affect the energy structure of the singlet $\pi\pi^*$ states.

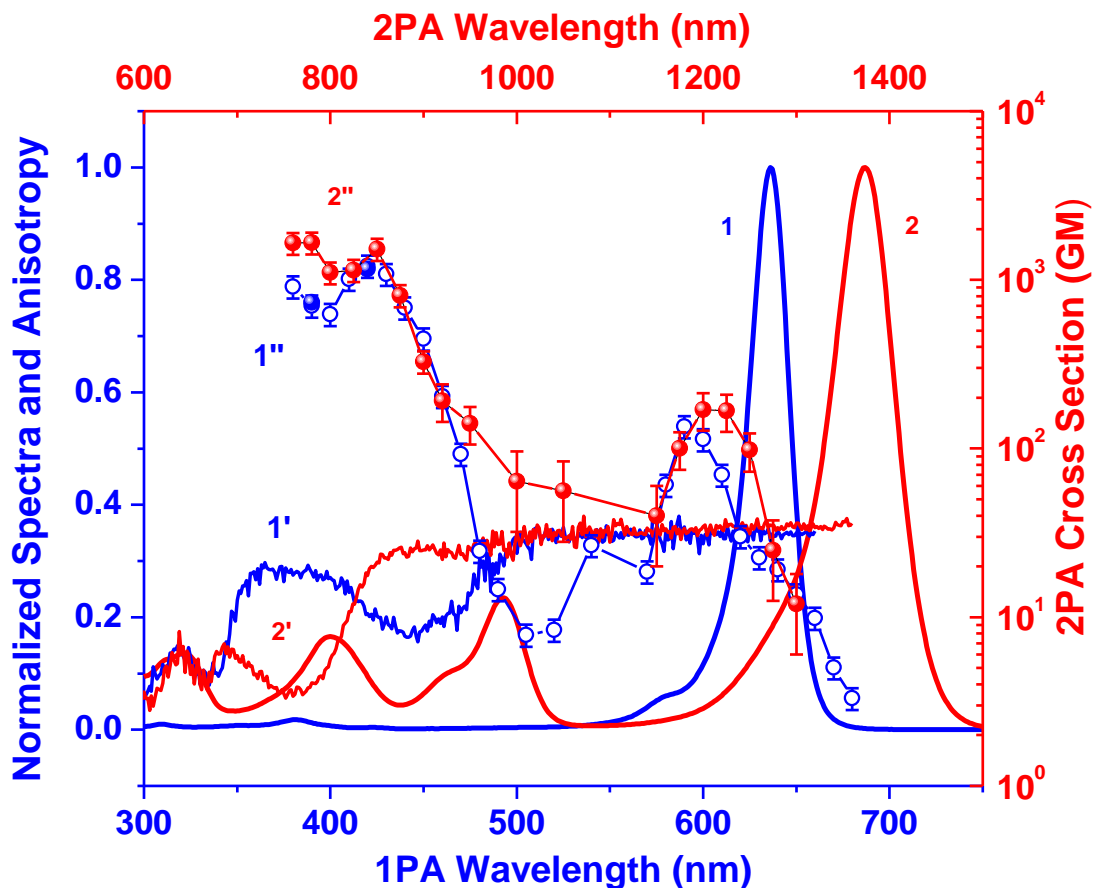


Figure 5.9 Normalized one-photon absorption (1, 2), excitation anisotropy (1', 2'), and two-photon absorption spectra (1'', 2'') for SD-O 2053 (1, 1', 1'') and SD-S 7517 (2, 2', 2''). The two-photon excitation wavelengths and absorption cross sections are shown on the top and right axes, correspondingly. 2PA data shown by solid red circles for SD-S 7517 and solid blue circles for SD-O 2053 are obtained by open-aperture Z-scans. 2PA data shown by blue open circles for SD-O 2053 correspond to 2PF measurements. All spectra are measured in ACN, except excitation anisotropy in pTHF.

Table 1. Photophysical parameters of SD-O, SD-SO and SD-S dyes: $\lambda_{\text{Abs}}^{\text{max}}$ and $\lambda_{\text{Fl}}^{\text{max}}$ are the peak absorption and fluorescence wavelengths; ϵ^{max} is the peak extinction coefficients; Φ_F is fluorescence quantum yield; τ_S is lifetime of lowest singlet excited state; Φ_T and Φ_{Δ} are triplet and singlet oxygen generation quantum yields, respectively; and τ_{T10} is the lifetime of lowest triplet excited state. Two components in τ_{T10} (last column) correspond to double exponential decays observed in toluene. Solvent abbreviations: ethanol (EtOH), toluene (TOL), acetonitrile (ACN) and dichloromethane (DCM).

Dye (Solvent)	$\lambda_{\text{Abs}}^{\text{max}}$ (nm)	$\lambda_{\text{Fl}}^{\text{max}}$ (nm)	ϵ^{max} ($\times 10^5 \text{M}^{-1} \text{cm}^{-1}$)	Φ_F	τ_S Calculated (ns)	τ_S Experiment (ns)	Φ_T	Φ_{Δ}	τ_{T10} (μs) (air saturated solvent)	τ_{T10} (μs) (nitrogen purged solvent)
PD 2350 (EtOH)	646	665	2.36	0.32 \pm 0.03	0.98	0.95 \pm 0.03	0	-	-	-
PD 2929 (EtOH)	645	660	2.67	0.10 \pm 0.01	0.27	0.30 \pm 0.03	0.05 \pm 0.05	Non- detectable	-	-
PD 1852 (EtOH)	685	706	2.05	0.33 \pm 0.03	1.3	1.0 \pm 0.1	0.10 \pm 0.05	Non- detectable	0.29 \pm 0.03	-
PD 2972 (EtOH)	677	692	2.28	0.16 \pm 0.02	0.55	0.50 \pm 0.04	0.09 \pm 0.05	Non- detectable	0.07 \pm 0.01	-
PD4216 (ACN)	738	Non- detectable	0.42	<0.001	-	0.8 \pm 0.3 (ps)	0	-	-	-
SD-O 2405 (TOL)	636	646	3.64	1.0 \pm 0.1	2.3	2.2 \pm 0.2	0	-	-	-
SD-S 7508 (TOL)	687	Non- detectable	1.57	<0.001	-	4.5 \pm 0.5 (ps)	0.98 \pm 0.02	1.0 \pm 0.2	0.24 \pm 0.04	0.6 \pm 0.1 and 3.4 \pm 0.3
SD-O 2577 (DCM)	636	642	3.57	0.27 \pm 0.03	0.7	0.9 \pm 0.1	0	-	-	-
SD-S 7504 (TOL)	678	691	1.59	0.12 \pm 0.01	0.5	0.50 \pm 0.05	0.75 \pm 0.03	0.50 \pm 0.01	0.30 \pm 0.05	0.4 \pm 0.04 and 1.9 \pm 0.2
SD-O 2243 (DCM)	668	675	3.45	0.36 \pm 0.04	1.0	1.3 \pm 0.1	0	-	-	-
SD-S 7507 (TOL)	697	709	1.92	0.25 \pm 0.03	1	1.5 \pm 0.2	0.46 \pm 0.04	0.20 \pm 0.05	0.29 \pm 0.05	0.6 \pm 0.1 and 2.9 \pm 0.3
SD-O 2053 (DCM)	648	660	4.23	0.95 \pm 0.05	2.1	2.3 \pm 0.4	0	-	-	-
SD-SO 7517 (ACN)	661	669	3.16	0.28 \pm 0.03	1.1	1.4 \pm 0.2	0.64 \pm 0.03	0.70 \pm 0.2	0.30 \pm 0.05 (TOL) 0.20 \pm 0.05 (ACN)	1.0 \pm 0.1 and 4.4 \pm 0.4 (TOL) 0.6 \pm 0.1 (ACN)

5.1.3 Quantum-chemical analysis

The electronic structure of the excited states are predicted with the Gaussian 2009 suite of programs.[76] The hybrid exchange-correlation density functional B3LYP[77] is used in combination with 6-31G* basis set.[78] The polarizable continuum model (PCM) in its solvation model density parameterization[79] is used to simulate the solvent effects (ethanol is chosen as the model solvent for PDs and toluene for SDs). Time-dependent density functional theory[80] is used to investigate the electronic structure of the three lowest singlet (S_i) and triplet (T_i) excited states. The excitation energies for these states, along with their dominant configurations are reported in Table 2. Excitation energies for cyanine dyes are known to present a challenge for the TD-DFT method.[81] The physical reasons for this inaccuracy and a remedy to improve the excitation energy predictions was proposed recently [82]. In short, the electronic excitation in cyanine chain results in charge transfer between even and odd atoms of the chain. TD-DFT method in commonly used adiabatic approximation is evaluating the excited state energy in the potential generated by the ground state. This approximation works well when the electron density does not change much upon the excitation, but results in larger than usual errors in cases like cyanine dyes. The improvement in excitation energy can be achieved, however, when the relaxed density of the excited state obtained with standard TD-DFT method is used to generate the potential instead of the ground state density. This can be practically accomplished when the static DFT is used on excited Slater determinant built on the natural orbitals of the excited state, but the orbital optimization is not performed (this is known as frozen density approximation, FD-DFT). The excitation energies in the frozen density approximation, including sum rule spin-contamination correction, are reported as FD-DFT in Table 2. The ground states S_0 and the

lowest singlet excited states S_1 were optimized with B3LYP/6-31G*/PCM and TDA-B3LYP/6-31G*/PCM, respectively, under the assumption of molecular planarity (point group C_{2v} for PD 1852 and PD 2929; point group C_{2h} for SD 2408 and SD 7508). In all S_0 and S_1 states for all four dyes the vibrational analysis revealed two imaginary normal modes, corresponding to out-of-plane vibrational motions (belonging to irreducible representations A_2 and B_1 in the C_{2v} point group; A_u and B_g in the C_{2h} point group). The zero point vibrational energy test [83] is used to inspect whether this apparent non-planarity is physically meaningful. A small step along the imaginary normal mode followed by the new optimization procedure lowered the total energy by less than 0.01 kcal/mol, while the zero point vibrational energy test increased the total energy by over 0.2 kcal/mol in all cases. Therefore, we conclude that their time-averaged dynamic structures (or the largest probabilities of the nuclear densities in quantum terms) for all these molecules in both S_0 and S_1 states are planar.

SOC matrix elements between the first excited singlet and the few lowest triplet states are calculated using the graphical unitary group approach capability in the GAMESS-US computer program (version 11 Aug. 2011).[84] The one-electron approximation to the microscopic Breit-Pauli spin-orbit operator and effective nuclear charges were used.[85] The states for the SOC evaluations are constructed in the basis of single excitations in Kohn-Sham orbitals, with the active space including five HOMOs (HOMO-4, HOMO-3, HOMO-2, HOMO-1, HOMO) and two LUMOs (LUMO and LUMO+1).

It is well established that vibronic interactions can substantially increase the ISC rates, making El-Sayed forbidden transitions nearly as probable as El-Sayed allowed ones.[86] For instance, it is shown that in Porphyrines vibronic spin-orbit terms, resulting from a sharp rise of

the SOC components along the out-of-plane vibrational coordinates, can increase the ISC rate by two orders of magnitude.[87] Here we employ a similar method to investigate non-Franck-Condon effects on SOC matrix elements. For this purpose the planar optimized geometry of the lowest singlet state S_1 is distorted out-of-plane along one of the normal modes. This normal mode is selected as the mode with the largest amplitude of the heaviest atom in the investigated molecule (Se, I, O and S, respectively). The amplitude of this out-of-plane distortion is selected so that the total molecular energy is increased by c. a. 0.6 kcal/mol (kT value at room temperature). The excitation energies and SOC components, obtained in the planar and distorted geometries, are presented in Table 2.

Quantum chemical analysis of PDs with “heavy” atoms

First, experimental results obtained for the series of PDs with the “heavy”-atom substitutions: PDs 2929, 1852, 4216 and 2972 are analyzed. From measurements it follows that Φ_T for Br-substituted PD 2929 is the smallest, not exceeding 0.05. For both Se-substituted PDs 1852 and 2972 Φ_T are similar, 0.10 ± 0.05 , indicating that additional incorporation of Br-atoms into the chain in PD 2972 cannot increase Φ_T and the main effect is connected with “heavy” Se-substitutions. Small values of Φ_T indicate that the fluorescence and internal conversion via singlet states are still dominating the deactivation pathways for PDs. These results have been explained by our quantum-chemical calculations showing that both PD 1852 and PD 2929 have an intense lowest $S_0 \rightarrow S_1$ transition of $\pi\text{-}\pi^*$ nature involving HOMO and LUMO orbitals. As shown in Table 2 for PD 1852, only two triplets (T_1 and T_2) are found to be thermally accessible for ISC deactivation pathways (that is below S_1 in energy as T_1 , or within a few C-C vibrational

quanta above it as T_2). The essential orbitals involved in these transitions (HOMO \rightarrow LUMO and HOMO-1 \rightarrow LUMO) are shown on Figure 5.10. All triplet states for PD 1852 are of $\pi\pi^*$ nature. Therefore, ISC processes between the singlet (S_1) and triplet (T_1 and T_2) states of $\pi\pi^*$ nature are forbidden by El-Sayed rules.[32] The calculated SOC components are indeed small at the planar S_1 geometry. The largest T_2 SOC component is 0.2 cm^{-1} . Out-of-plane distortion, however, results in $\pi\text{-}\sigma^*$ mixing and large (two orders of magnitude) increase in SOC component for T_2 in PD 1852. This state, however, is too high above S_1 (0.5 eV or 12 kcal/mol) to result in a large ISC rate. In PD 2929 this effect is much less pronounced, as HOMO-1 has a node in the center of the molecule at the position of the Br atom (unlike peripheral Se atoms in PD 1852), and ISC cannot efficiently compete with internal channels of relaxation, resulting in negligible triplet quantum yield. Negligibly small SOC elements are found for PD 4216 for all lower-lying triplets. Therefore, we may conclude that 10% triplet quantum yields for Se-substituted PD 1852 and PD 2972 are connected with non-Franck-Condon vibronic enhancement of El-Sayed forbidden ISC channel.







	XY plane	XZ plane
LUMO		
HOMO		
HOMO-1		

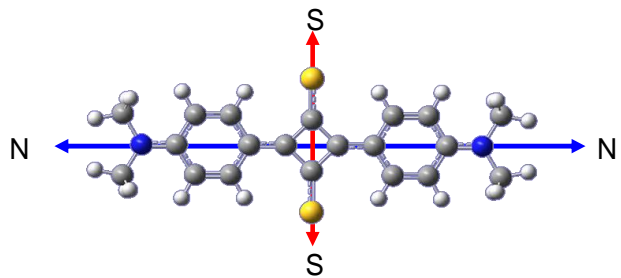
Figure 5.10 Isosurfaces of the essential Kohn-Sham orbitals in in XY and XZ planes for PD 1852.

Quantum chemical analysis of SDs

Now, experimental results for a series of oxygen- and sulfur-substituted squaraines are analyzed. The main difference in the ISC rates between PDs and SDs arises from the nature of their first excited states. As one can see from Figure 5.11, HOMO-1 and HOMO-2 in SD 7508 are of n-type, the same as HOMO-2 in SD 2405 (not shown). These orbitals consist mostly of the n-lone pairs of S (or O) atoms and give rise to the low-lying $n\pi^*$ excited states (S_1 , S_3 , for SD 7508 and S_2 for SD 2405). However, not all El-Sayed allowed transitions have large SOC components according to our calculations, see Table 2. The noteworthy one is $S_1 (n\pi^*) \rightarrow T_3 (\pi\pi^*)$ transition in SD 7508, probably thermally accessible, with SOC component of 1.32 cm^{-1} ,

the largest among all planar S_1 geometries considered here. The vibronic coupling does not enhance this channel appreciably, however, it opens an additional El-Sayed allowed channel $S_1 (n\pi^*) \rightarrow T_1 (\pi\pi^*)$ with SOC component of 2.03 cm^{-1} , favorable due to the small energy splitting between the singlet and triplet states. Calculations show that all squaraine molecules consist of two perpendicular conjugated chromophores: one placed in the horizontal plane between two nitrogen atoms (N–N chromophore), and the second placed in the vertical plane between two sulfur (S–S chromophore) or oxygen (O–O chromophore) atoms, as shown in Figure 5.11 for SD-S 7508. The main distinguishing feature of the vertical chromophore is the existence of unshared electron pairs producing states of $n\pi^*$ nature. Based on the origin of charge distribution within the molecule, four types of MOs are responsible for the lowest electronic transitions as shown in Figure 5.11 for SD-S 7508. The first type, presented by HOMO, and HOMO-3, corresponds to the totally delocalized π -orbitals with the charge spreading to both perpendicular π -conjugated chromophores. The second type of orbitals, presented by HOMO-1 and HOMO-2, correspond to n -type and involve the charge localized at the sulfur atoms as clearly seen in the XZ plane of Figure 5.11. The third and fourth types are π -MOs involving the charge distributed only within the horizontal (N–N) or vertical (S–S) chromophores. Examples are LUMO and LUMO+1, respectively. Calculations show that the electronic transition lowest in energy, corresponds to HOMO-1 \rightarrow LUMO, and is of the $n\pi^*$ nature. This $n\pi^*$ transition, being of very small oscillator strength, is covered by the next intense transition of $\pi\pi^*$ nature, related to HOMO \rightarrow LUMO, which we typically consider as the main $S_0 \rightarrow S_1$ transition. Calculations suggest that by replacing the oxygen atoms in a squaraine ring (SD-O 2405 structure) with sulfur atoms (SD-S 7508 structure) results in an inversion of the lowest $\pi\pi^*$ transition in SD-O 2405

by an $n-\pi^*$ transition in SD-S 7508, so that two ISC channels become available: $S_1 (n\pi^*) \rightarrow T_3 (\pi\pi^*)$, thermally accessible in the planar excited-state geometry and an enhanced of $S_1 (n\pi^*) \rightarrow T_1 (\pi\pi^*)$ transition in the distorted S_1 geometry.



	XY plane	XZ plane
LUMO		
HOMO		
HOMO-1		
HOMO-2		
HOMO-3		
HOMO-4		

Figure 5.11 Molecular schematic of SD-S 7508 showing two perpendicular chromophores, one between nitrogen atoms (blue) and the second between sulfur atoms (yellow). Table presents isosurfaces of Kohn-

Sham orbitals in XY and XZ planes for SD-S 7508.

Table 2. Excitation energies (E_{TD} , eV), leading singlet and triplet configurations, and oscillator strengths (Osc.) predicted with TD-B3LYP/6-31G*/PCM, singlet excitation energies predicted with FD-B3LYP/6-31G*/PCM (E_{FD} , eV), and SOC matrix elements between dominant configurations of each triplet and the lowest singlet S_1 , calculated at the planar optimized S_1 geometry, and out-of-plane distorted S_1 geometry.

	E_{TD} , (eV)	E_{FD} , (eV)	Leading singlet configuration	Osc.		E_{TD} , (eV)	E_{FD} , (eV)	Leading triplet configuration	SOC in planar S_1 (cm^{-1})	SOC in distorted S_1 (cm^{-1})
PD 1852										
S_1	2.18	1.84	HOMO→LUMO	2.61	T_1	1.30	1.24	HOMO→LUMO	0.00	0.00
S_2	2.93	3.08	HOMO-1→LUMO	0.05	T_2	2.42	2.34	HOMO-1→LUMO	0.20	22.1
S_3	3.15	3.01	HOMO-2→LUMO	0.65	T_3	2.82	2.84	HOMO-2→LUMO	0.00	0.00
PD 2929										
S_1	2.33	1.91	HOMO→LUMO	2.92	T_1	1.34	1.39	HOMO→LUMO	0.00	0.02
S_2	3.33	3.03	HOMO-2→LUMO	0.01	T_2	2.45	2.61	HOMO-1→LUMO	0.04	0.38
S_3	3.71	3.76	HOMO-1→LUMO	0.04	T_3	3.13	3.27	HOMO-2→LUMO	0.00	0.00
SD-O 2405										
S_1	2.10	1.77	HOMO→LUMO	3.13	T_1	1.01	1.21	HOMO→LUMO	0.00	0.15
S_2	2.15	3.38	HOMO-2→LUMO	0.00	T_2	2.03	2.33	HOMO-1→LUMO	0.00	5.10
S_3	3.12	3.35	HOMO-1→LUMO	0.00	T_3	2.32	2.50	HOMO-2→LUMO	0.00	0.00
SD-S 7508										
S_1	1.72	1.76	HOMO-1→LUMO	0.00	T_1	1.17	1.29	HOMO→LUMO	0.00	2.03
S_2	1.92	2.11	HOMO→LUMO	1.35	T_2	1.68	1.96	HOMO→LUMO+1	0.00	0.27
S_3	2.15	2.65	HOMO-2→LUMO	0.00	T_3	2.02	2.13	HOMO-4→LUMO	1.32	1.33

5.2. Axially Dendronised Ruthenium(II) Pthalocyanine and Napthalocyanine

Pthalocyanine (Pc) and Napthalocyanine (Nc) compounds belong to the family of macrocyclic conjugated materials structurally closely related to the Porphyrins [88]. Pc's linear spectra typically exhibit two sharp peaks: a Q-band at longer wavelengths (~600 nm) and a B-band (or Soret) at shorter wavelengths (~300 nm). In nonsubstituted Pc's both bands possess $\pi\pi^*$ characteristics [89]. Nc's have a Q-band shifted to longer wavelengths compared to Pc's due to their extended conjugation. The optical window between the Q and B bands is characterized with relatively strong S-S and T-T ESA which makes these materials excellent candidates for optical limiters in the visible optical range.

Heavy atom substitution in the center of Pcs and Nc molecules is commonly used to increase ISC rate. Previous studies showed that the choice of Ruthenium(II) as the central atom increases ϕ_T up to unity with $\tau_{ISC} \sim 5$ ps [90, 91]. In this case, ISC rate is much faster than the value predicted from spin-orbit coupling calculations. According to Ref. [91], such a fast ISC rate is most probably due to a combination of the "heavy-atom" effect and the influence of a low-lying metal to ligand charge-transfer state ($d \rightarrow \pi^*$). However, ultrafast ISC of Ru(II) Pc's and Nc's complexes have still not been completely understood.

Main problem with Pcs and Ncs is the formation of aggregates at high concentrations due to their tendency of π -stacking interaction together with low solubility. Aggregation in concentrated solution usually leads to a significant change of the linear spectrum and the quenching of excited states. The most common solution for the aggregation problem is dendron

attachment to the axial position of the central atom or to the peripheral position of the macrocycle.

Pc and Nc molecules studied in this work include RuPc-G3 and RuNc-G3[92]. Chemical structures of these dyes are shown in Figure 5.12. In both cases Ru(II) is located in the center and is axially substituted with pyridine rings at the focal point of third-generation Fréchet-type G3 dendrons. G3 dendrons substitutions prevents aggregation up to mM concentrated solutions [92].

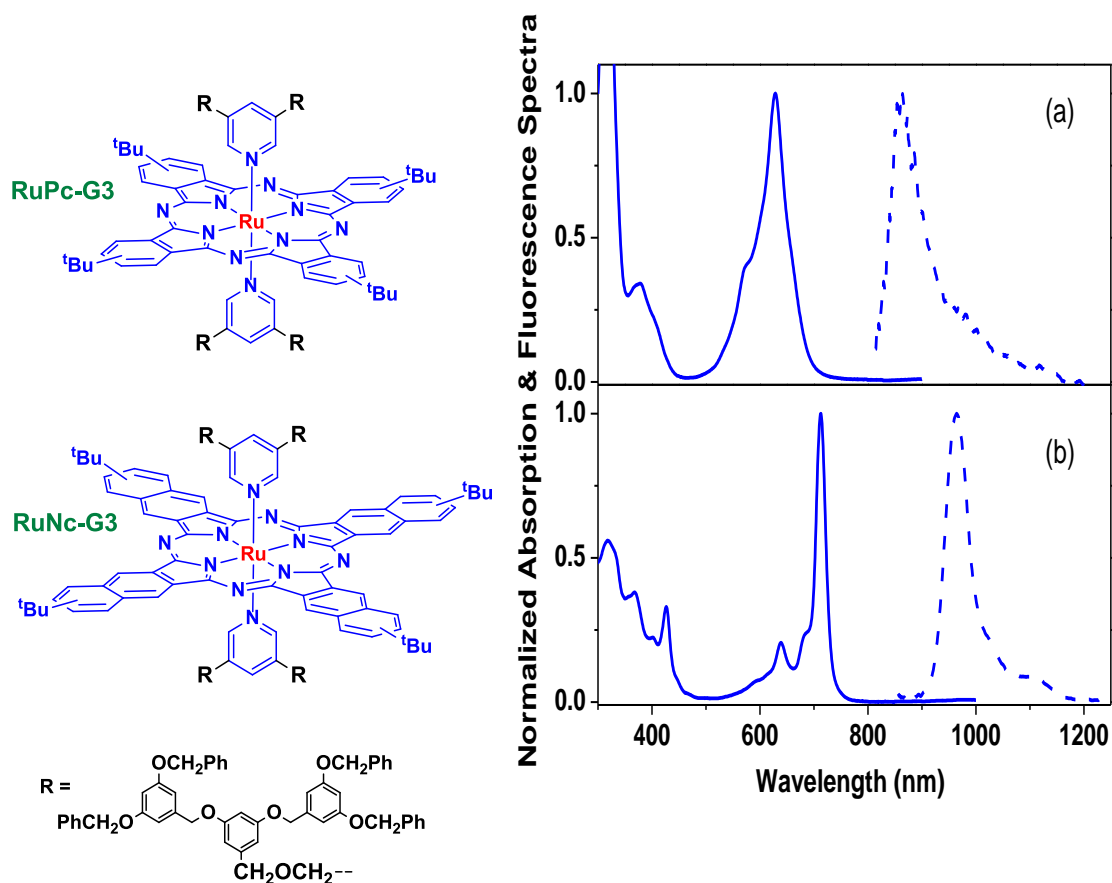


Figure 5.12 Molecular structures, absorption (solid lines) and fluorescence (dashed lines) for: (a) RuPc-G3; (b) RuNc-G3. Absorption and fluorescence spectra are both measured in toluene.

5.2.1 Linear optical properties of Ru Pc and Nc

Figure 5.12 presents the linear absorption spectra of RuPc-G3 and RuNc-G3, recorded by a Varian Cary 500 spectrophotometer, together with the luminescence spectra of both compounds measured by a PTI QuantaMaster spectrofluorimeter. The absorption spectra of both dyes are composed of two intense bands: a B-band at shorter wavelengths and a Q-band at longer wavelengths. As expected, the B-band in both cases is at approximately the same position, while the Q-band of RuNc-G3 is red-shifted by 85 nm comparing to the Q-band of RuPc-G3.

For both molecules luminescence spectra show significantly large Stoke shifts (236 nm for RuPc-G3 and 251 nm for RuNc-G3). Since the lowest triplet state is always placed below the lowest singlet state, a large Stokes shift is usually a characteristic of a phosphorescence emission of RuPc [91, 93]. Due to the long lifetime of the triplet state and the high probability of quenching, phosphorescence emission is usually not detected at room temperature, although there have been several reports of phosphorescence observation at room temperature for highly purified solvents [84-86]. Since both RuPc-G3 and RuNc-G3 are characterized with very small Φ_F ($\ll 1\%$) and almost unity Φ_T (Table 3.), the assumption that the observed luminescence originates from the lowest triplet state seems to be valid. However, the lifetime calculated from fluorescence measurements is very short (~ 10 ps) and agrees with femtosecond pump-probe measurements. Additional measurements are required to determine the nature of observed luminescence.

5.2.2 Nonlinear optical properties of Ru Pc and Nc

Femtosecond double pump-probe measurements

Due to ultrafast ISC, a complete DPP characterization requires femtosecond pulses. Typically, femtosecond sources are avoided for triplet yield studies due to their increased irradiance, compared to picosecond pulses at the same fluence, and typically faster pulse repetition rates, which both may lead to faster photodecomposition. However, a DPP measurement in the SA regime (Chapter 4) allows to use significantly lower pump fluence, reducing the probability of dye photodecomposition.

A setup similar to that shown in Figure 4.3 was used for femtosecond DPP experiment, but the probe pulse was generated by focusing a 780 nm pulse into a 1 cm water cell to create a white-light continuum and a narrow band-pass interference filter (~ 10 nm) was used to select the probe wavelength. Pump pulses were generated from an OPG/A (Light Conversion, TOPAS-800). Spot sizes of both pump beams, measured by knife-edge scans, were ~ 120 μm (HW/ e^2 M), and 20 μm (HW/ e^2 M) for the probe spot size. The probe energy was fixed to ~ 200 pJ ($F \sim 0.032$ mJ/cm²), which is small enough to prevent nonlinear effects induced by the probe. The pump beam was modulated with a mechanical chopper at 283 Hz that was synchronized with the output from the laser. The signal was recorded using a silicon detector and a lock-in amplifier. Experiments were performed at equal pump and probe wavelengths of 620 nm for RuPc-G3 and 710 nm for RuNc-G3, close to the absorption peaks of these molecules, as shown in Figure 5.12. Theoretical fitting was performed using the full set of propagation and rate equations for the five-level system, Figure 3.11 and Eqs. 3.5-3.6. Fitted results for RuNc-G3 are shown in Figure 5.13a with their corresponding population dynamics shown in Figure 5.13b. Scanning with

greater temporal resolution around zero delay of the first pump (shown in the inset of Figure 5.13a), allows a determination of the singlet state parameters using femtosecond pulses.

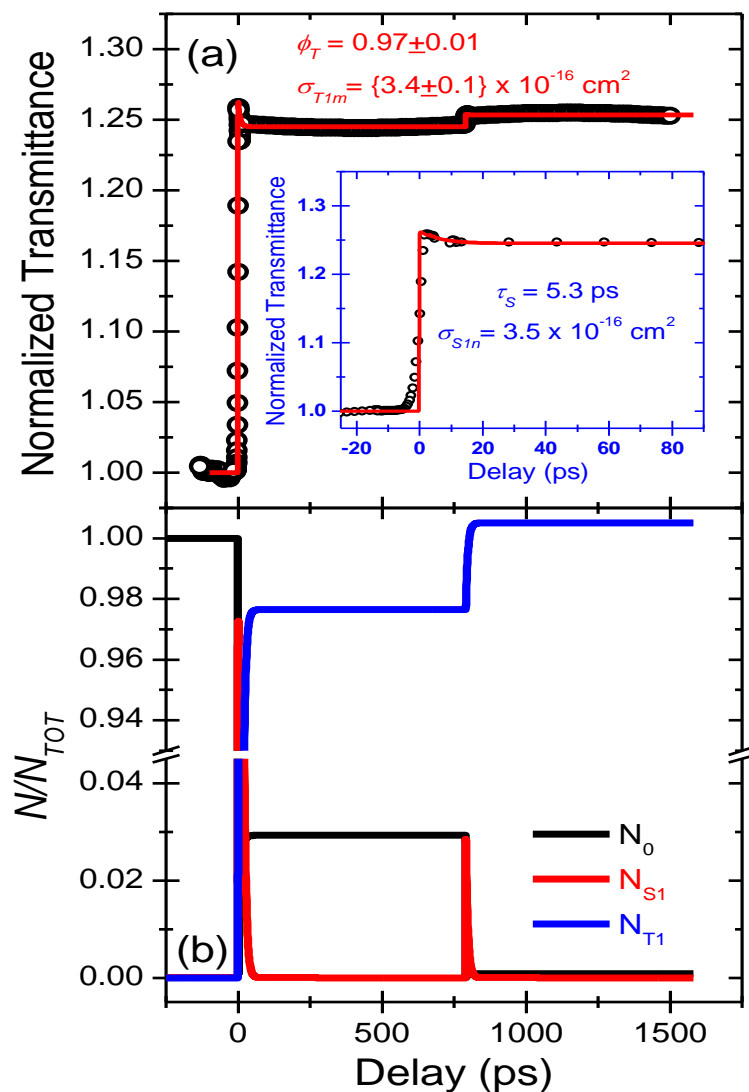


Figure 5.13 (a) DPP and fitting results for RuNc-G3 at a pump of 710 nm ($\sigma_{S0I} = 6.6 \times 10^{-16} \text{ cm}^2$), $C = 12 \text{ } \mu\text{M}$ ($T_L = 0.6$), $F = 3.4 \text{ mJ/cm}^2$ ($E = 0.7 \text{ } \mu\text{J}$, $w_0 = 115 \text{ } \mu\text{m}$) in each pump. The values obtained are: $\phi_T = (0.97 \pm 0.01)$, $\sigma_{S1n} = (3.5 \pm 0.1) \times 10^{-16} \text{ cm}^2$, $\sigma_{T1m} = (3.4 \pm 0.1) \times 10^{-16} \text{ cm}^2$, and $\tau_S = 5.3 \text{ ps}$. Inset: greater temporal resolution scan showing S_1 dynamics for the first pump pulse only. (b) DPP population dynamics for the ground, first excited singlet and triplet states for RuNc-G3 for the conditions in (a).

Figure 5.13a demonstrates an interesting dynamics. There is a small change in transmittance after the first and second pumping pulses. The calculated population dynamics for the ground, first excited singlet and triplet states are shown in Figure 5.13b. It is seen that the fluence of the first pump is large enough to almost completely deplete the ground state. Since ϕ_T is almost unity, all excited state population moves to the triplet state, T_1 , immediately after the first pump, and therefore, the influence of the second pump may be very small. Most important photophysical parameters of RuPc-G3 and RuNc-G3 are collected in Table 3.

ESA measurements

Figure 5.14a and c shows the ESA spectra for RuPc-G3 and RuNc-G3, respectively, while Figure 5.14b and d shows their decay kinetics and determined values of σ_{S1n} and σ_{T1n} measured by non-degenerate femtosecond WLC pump-probe. Pump wavelengths were set close to the peak of the linear absorption (622 nm for RuPc-G3 and 710 nm for RuNc-G3), while probe wavelengths were set in the RSA region (570 nm for RuPc-G3 and 520 nm for RuNc-G3). In both cases S - S and T - T ESA spectra have almost identical shapes and similar cross section values.

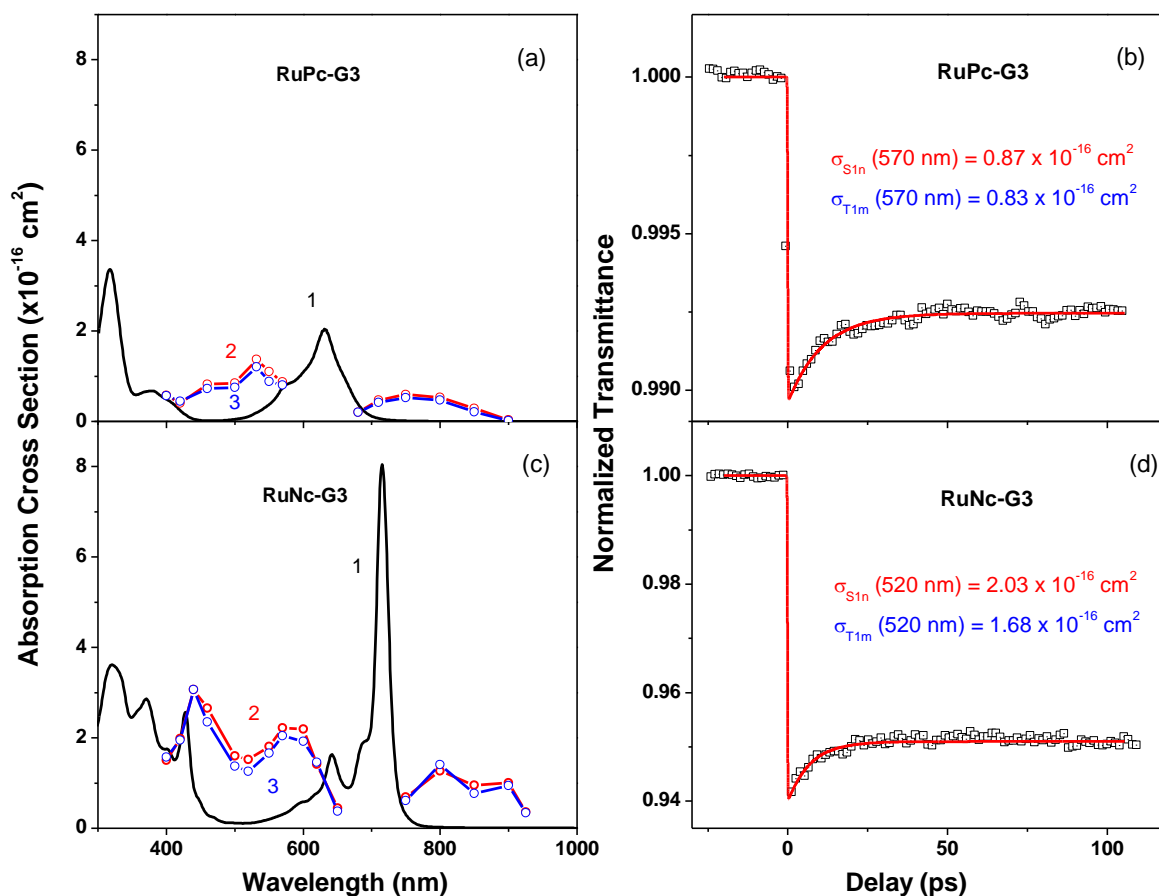


Figure 5.14 Linear absorption (1), S - S (2) and T - T (3) ESA absorption spectra for (a) RuPc-G3 and (b) RuNc-G3. Decay kinetics for (c) RuPc-G3 at 570 nm (pump fluence 2.6 mJ/cm^2 , $\sigma_{S01} = 33 \times 10^{-18} \text{ cm}^2$, $\sigma_{S1n} = 0.9 \times 10^{-16} \text{ cm}^2$, $\tau_S = 2.5 \text{ ns}$); (d) RuNc-G3 at 520 nm (pump fluence 0.5 mJ/cm^2 , $\sigma_{S01} = 23 \times 10^{-18} \text{ cm}^2$, $\sigma_{S1n} = 1.3 \times 10^{-16} \text{ cm}^2$, $\sigma_{T1n} = 2.5 \times 10^{-16} \text{ cm}^2$, $\tau_S = 1.5 \text{ ns}$)

Triplet state lifetime measurements

The experimental setup for triplet lifetime measurements is described in Section 3.3.5. Figure 5.15 presents the triplet state decay kinetics for RuNc-G3 in air-saturated and oxygen-removed (using the procedure described in Section.2.2.1) toluene solutions. As expected, removing oxygen from the solution significantly increases τ_{T10} , however, unlike SD-S molecules, both decays show only single exponential kinetics. Measurements were performed in toluene only because the samples are not soluble in ACN.

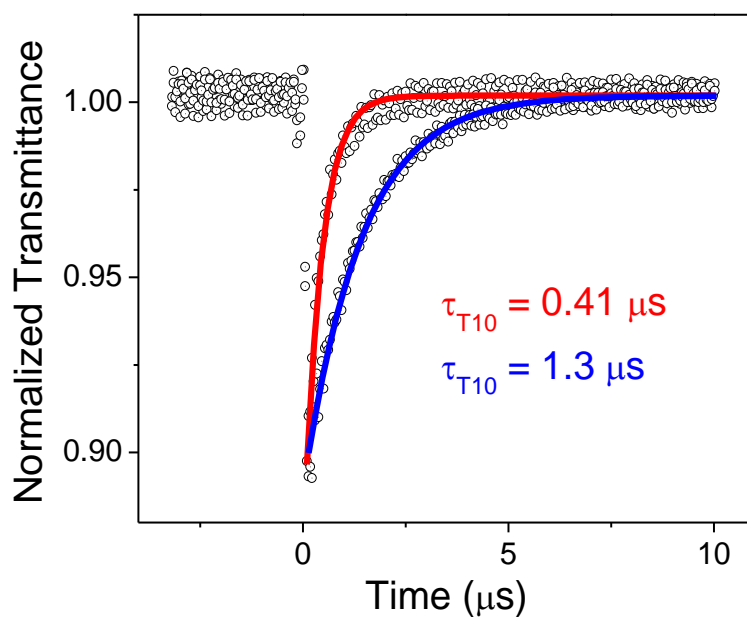


Figure 5.15 Triplet lifetime measurements for RuNc-G3 in toluene. Shorter decays (1) correspond to air-saturated solutions, while longer decays (2) correspond to solutions with oxygen removed.

Table 3. Photophysical parameters of RuPc-G3 and RuNc-G3: $\lambda_{\text{Abs}}^{\text{max}}$ and $\lambda_{\text{Fl}}^{\text{max}}$ are the peak absorption and fluorescence wavelengths; ϵ^{max} is the peak extinction coefficients; Φ_F is fluorescence quantum yield; τ_S is lifetime of lowest singlet excited state; Φ_T is triplet quantum yield, respectively; and τ_{T10} is the lifetime of lowest triplet excited state.

Dye (Solvent)	$\lambda_{\text{Abs}}^{\text{max}}$ (nm)	$\lambda_{\text{FL}}^{\text{max}}$ (nm)	ϵ^{max} ($\times 10^5 \text{ M}^{-1} \text{ cm}^{-1}$)	Φ_F	τ_S Calculated (ps)	τ_S Experiment (ps)	Φ_T	τ_{T10} (air saturated solvent) (μs)	τ_{T10} (nitrogen purged solvent) (μs)
RuPc-G3 (TOL)	628	864	0.5	6×10^{-6}	10	11.0 ± 0.5	0.99 ± 0.01	0.13 ± 0.02	0.20 ± 0.05
RuNc-G3 (TOL)	713	964	2.04	6.5×10^{-3}	7	5.3 ± 0.5	0.97 ± 0.01	0.41 ± 0.02	1.3 ± 0.1

CHAPTER 6. SEMICONDUCTORS

6.1 Optical Properties of Semiconductors

Semiconductors are materials with crystalline structure. Two types of structures are most common in the majority of semiconductors: diamond and zinc-blende. In a diamond lattice all atoms are identical while zinc-blende lattices contain sublattices with different atoms. Semiconductors can be elemental or compound. Elemental semiconductors are single element semiconductors like Si and Ge that belong to group IV of the periodic table. Compound semiconductors are formed of two or more elements. As an example GaAs is a binary III-V compound semiconductor composed from gallium (Ga - group III) and arsenic (As - group V).

The band structure of semiconductors, described with continuous energy bands separated by an energy gap, gives rise to their unique optical properties. The energy band gap, E_g , in semiconductors is usually less than 4 eV. In equilibrium, bands in the electronic ground state of semiconductors are bands filled up to the Fermi level. In intrinsic semiconductors the Fermi level lies between the valence and conduction bands. The highest band below the Fermi level is called the valence band, and the bands above the Fermi level are called conduction bands. Upon excitation, an electron is promoted from the initial occupied state in the valence band to an unoccupied state in the conduction band. This is the so called interband transition that gives rise to the continuous spectrum starting from the lowest photon energy value $\hbar\omega = E_g$. The now empty state in the valence band corresponds to the creation of a positively charged hole. Holes behave as real particles with momentum and kinetic energy. Both electrons and holes are

fermions and obey the Pauli Exclusion Principle. The probability of occupying a specific energy state for fermions is expressed with the Fermi-Dirac distribution function:

$$f(E) = \frac{1}{1 + \exp\left(\frac{E - E_f}{k_B T}\right)}, \quad (2.15)$$

where E_f is the Fermi energy level and k_B is Boltzmann constant. The density of electrons within a certain energy interval is given by the product of this distribution function and the density of states. The density of states is defined as the number of states per unit volume in momentum space.

Based on the relative position of the minimum of the conduction band in E-k space, semiconductors can be direct-gap or indirect-gap. In direct-gap semiconductors, the minimum energy of the conduction band occurs at the same k-value as the maximum energy of the valence band. On the other hand, in indirect-gap semiconductors, the minimum value of the valence conduction band occurs at some other k-value. In indirect-gap materials, the promotion of an electron from the valence to conduction band requires absorption or emission of a phonon due to conservation of momentum, k.

In a simple model, the bands are usually approximated as parabolic in a plot of energy of a carrier versus momentum where m^* is the carrier's effective mass (see Eqs. 2.16). An example of the band structure for the direct band gap material GaAs is shown in Figure 6.1. The E-k relationship for conduction, heavy-hole, light-hole and split-off hole bands is given by:

$$\begin{aligned}
E_c(k) &= E_g + \frac{\hbar^2 k^2}{2m_e^*} \\
E_{hh}(k) &= -\frac{\hbar^2 k^2}{2m_{hh}^*} \\
E_{lh}(k) &= -\frac{\hbar^2 k^2}{2m_{lh}^*} \\
E_{so}(k) &= -\Delta - \frac{\hbar^2 k^2}{2m_{so}^*}
\end{aligned}
\tag{2.16}$$

with the effective masses: m_e^* for electrons, m_{hh}^* for heavy holes, m_{lh}^* for light holes, m_{so}^* for split-off holes.

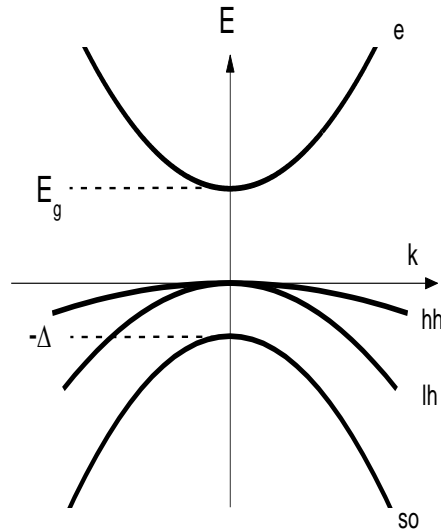


Figure 6.1. Band structure of GaAs with four bands: the electron (e) band, the heavy-hole (hh) band, the light-hole (lh) band and split-off hole (so) band.

After excitation, the electron rapidly relaxes to the lowest unoccupied state in the conduction band by phonon emission. Electrons can return to the valence band through radiative or nonradiative recombination processes.

Very often impurities are introduced in semiconductors to increase the number of positive or negative charge carriers. This is the so called doping process. There are two types of dopants:

donors and acceptors. A donor atom has one more electron than is necessary for a covalent bond and creates an additional impurity state just below the conduction band. The extra electron is very weakly bound to the donor atom and can be easily excited to the conduction band. An acceptor atom has one electron less than is necessary for a covalent bond, and produces an additional impurity state with a hole just above the valence band. An extra hole is very weakly bound to the acceptor atom and can be easily promoted to the valence band.

6.2 Z-scan Measurements of Bound-electronic and Free-carrier Nonlinearities in Semiconductors

In this work the nonlinear optical properties of three different semiconductors are studied: GaAs, InP and InAsP. Their linear spectra measured with a Cary-500 UV-Vis-NIR (170nm to 3300nm) spectrophotometer are shown in Figure 6.2.

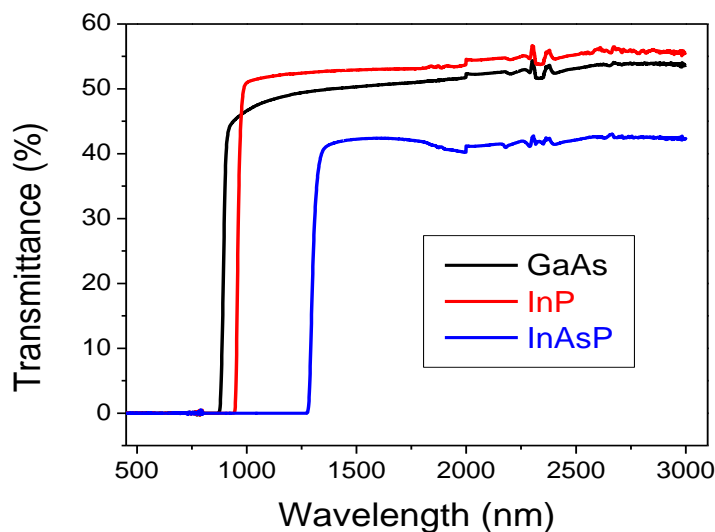


Figure 6.2 Linear spectrum of GaAs, InP and InGaAs.

Table 4. Sample properties of GaAs, InP and InGaAs: bandgap energy, E_g , linear index of refraction, n_0 , and sample thickness, L .

	$E_g/\mu m$	n_0	L/mm
GaAs	0.87	3.36	0.76
InP	0.9	2.91	1
InAsP	1.3	3.07	1.73

In semiconductors the 2PA coefficient, α_2 , is shown to be inversely proportional to the third power of the band gap energy E_g [94, 95]. In the simplified two-parabolic-band model, where only one valence and conduction band are taken into account [95], the dependence of α_2 on the fundamental macroscopic properties of the material is given by:

$$\alpha_2 = K \sqrt{E_p} \cdot \frac{1}{n^2 E_g^3} \cdot F_2 \left(\frac{2\hbar\omega}{E_g} \right) \quad (2.17)$$

where K is a material independent constant experimentally determined to be approximately equal to $3100 \text{ cm/GW}(\text{eV})^{5/2}$, E_p is the Kane energy parameter defined through the Kane momentum P , $E_p = 2P^2 m_e / \hbar^2$, and of the order of 21 eV (22.7 for GaAs, 17 for InP[96]) for many semiconductors [39, 97], E_g is the bandgap energy and n is the refractive index. The F_2 function is given by:

$$F_2(2x) = \frac{(2x-1)^{3/2}}{(2x)^5} \text{ for } 2x > 1 \quad . \quad (2.18)$$

The nonlinear refractive index change can be calculated using a Kramers-Kronig transformation for nondegenerate pump-probe measurements of the 2PA spectrum [98]:

$$\Delta n(\omega_p; \omega_e) = \frac{c}{\pi} \int_0^{\infty} \frac{\Delta a(\Omega; \omega_e)}{\Omega^2 - \omega^2} d\Omega \quad , \quad (2.19)$$

where ω_p and ω_e are the frequencies of the probe and pump respectively. For the degenerate case ($\omega_p = \omega_e$) n_2 (in cm^2/GW) is defined by

$$n_2 = K \frac{\hbar c \sqrt{E_p}}{2n_0^2 E_g^4} G_2 \left(\frac{\hbar \omega}{E_g} \right) \quad . \quad (2.20)$$

The function $G_2(x)$ is given by [39]:

$$G_2(x) = \frac{-2 + 6x - 3x^2 - x^3 - \frac{3}{4}x^4 - \frac{3}{4}x^5 + 2(1-2x)^{3/2} \Theta(1-2x)}{64x^6} \quad (2.21)$$

where $\Theta(y)$ is the Heaviside Step function ($\Theta=0$ for $y < 1$ and $\Theta=1$ for $y \geq 1$). $G_2(x)$ contains contributions from 2PA, Raman and AC-Stark processes [99].

Interband absorption in semiconductors promotes electrons from the valence band to the conduction band creating free carriers. Free carriers can be further excited, absorbing more photons from the incoming pulse and additionally contributing to nonlinear absorption and refraction. In the case of pure 2PA ($\alpha_1 \approx 0$), the free-carrier generation rate is given by

$$\frac{dN}{dt} = \frac{\alpha_2 I^2}{2\hbar\omega} \quad (2.22)$$

where N is the photoexcited charge-carrier density.

In a thin sample and in the slow-varying-amplitude approximation, the wave equation can be separated into propagation equations for irradiance [100]

$$\frac{dI}{dz} = -\alpha_2 I^2 - \sigma_{FC} NI \quad , \quad (2.23)$$

and for the phase change

$$\frac{d\Delta\phi}{dz} = \Delta nk_0 = (n_2 I + \sigma_r N) k_0 \quad . \quad (2.24)$$

where σ_{FC} is the free-carrier absorption cross section and σ_r is the free-carrier refraction cross section.

The free-carrier lifetime in semiconductors is usually much longer than 1ns [101, 102]. Since all the experiments in this chapter are done with femtosecond and picosecond pulses, the loss of carriers due to recombination and diffusion can be ignored. In addition, free-carrier absorption, FCA, can also be ignored for femtosecond pulse experiments.

Nonlinear optical parameters of GaAs, InP and InAsP are measured using open and closed aperture Z-scan with picosecond pulses. The Z-scan setup was described in section 3.7.6. The lenses used are uncoated BaF₂, the mirrors are Au, the beam energy is attenuated with a pair of Au wire-grid polarizers on BaF₂ substrates and the beam splitters are made by depositing thin films of Au on BaF₂ substrates. Three PbS PDA30G amplified photodetectors are used to measure the signal and reference (Figure 3.18). The energy of the laser pulse is measured with a PE9 SH Ophir pyroelectric power meter. The temporal pulse width of the picosecond OPG/A was determined by second-order autocorrelation measurements to be $\tau_{\text{HW1/e}} = (6.6 \pm 0.2)$ ps and is constant through the entire wavelength range from 1000 nm to 1800 nm (Figure 6.3).

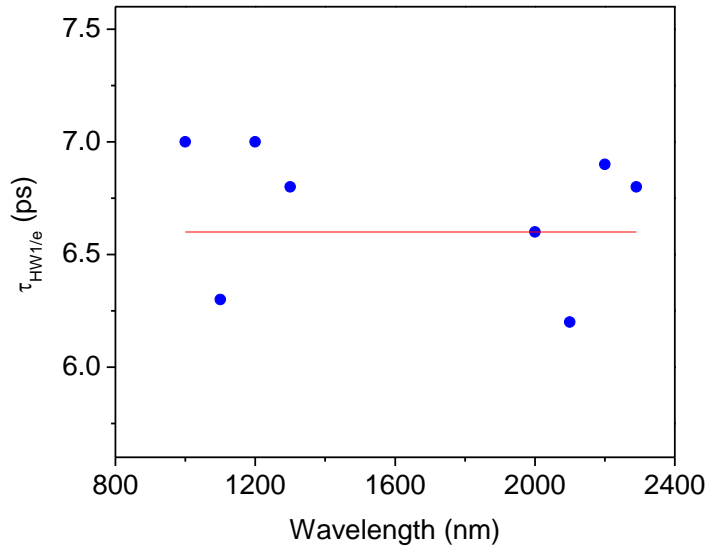


Figure 6.3 Pulse width of picosecond OPG/A.

The beam size is determined (Section 3.7.6) using closed aperture Z-scan measurements of CS₂ at each wavelength. CS₂ is a well-known nonlinear material and has a nonlinear refractive index $n_2 = (3.1 \pm 0.2) \times 10^{-14} \text{ cm}^2/\text{W}$ [53, 103, 104] for measurements done with picosecond pulses longer than 2ps.

The measured spectra of 2PA and FCA of GaAs, InP and InAsP are shown in Figures 6.4, 6.5 and 6.6 respectively. Since the influence of FCA is negligible until relatively high pulse energies, low beam quality and low available energy at certain wavelength regions of the picosecond OPG/A does not allow the determination of σ_{FC} at all wavelengths. 2PA experimental data is compared with values predicted by the theory (Equation 2.17) and in all three cases experimental results are approximately two times larger. This is discussed in more detail in Sec. 6.4.

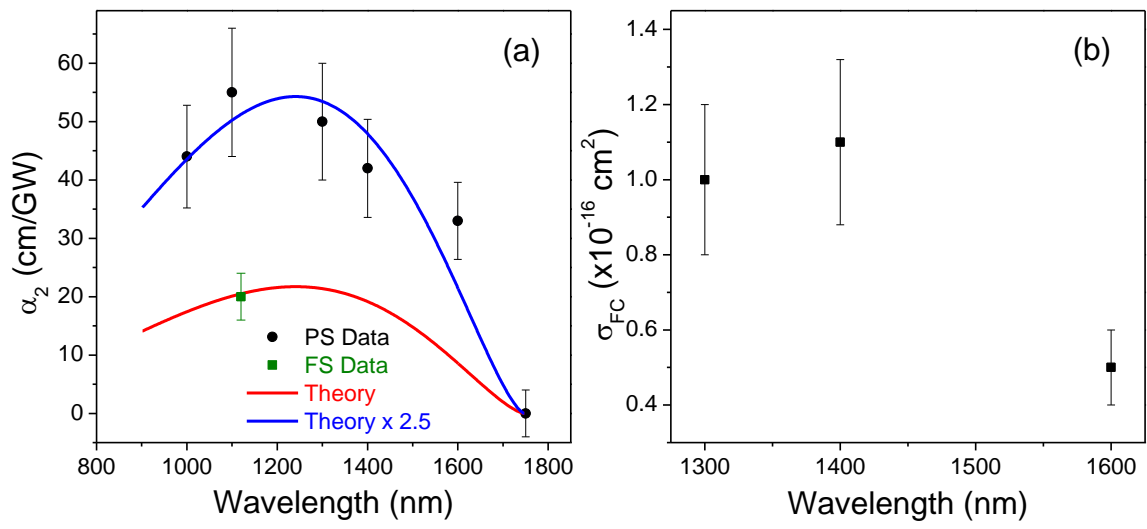


Figure 6.4 (a) Picosecond Z-scan results measured for 2PA in GaAs (black circles) compared to the theory (red solid line) and the same theory scaled by a factor of 2.5 (blue solid line) and (b) free carrier absorption results for GaAs.

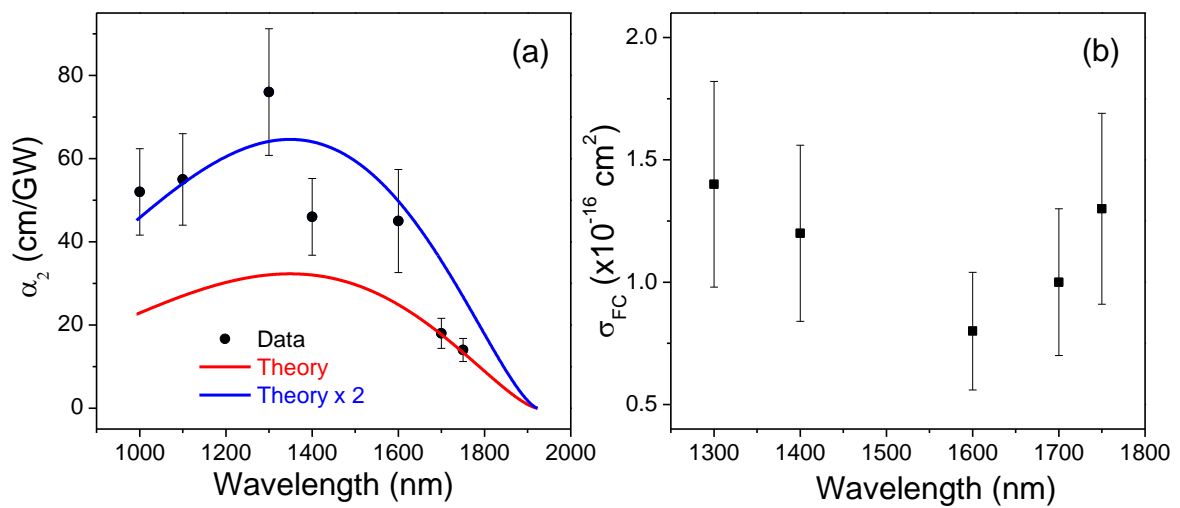


Figure 6.5 (a) Picosecond Z-scan results measured for 2PA in InP (black circles) compared to the theory (red solid line) and the same theory scaled by a factor of 2 (blue solid line) and (b) free-carrier absorption results for InP.

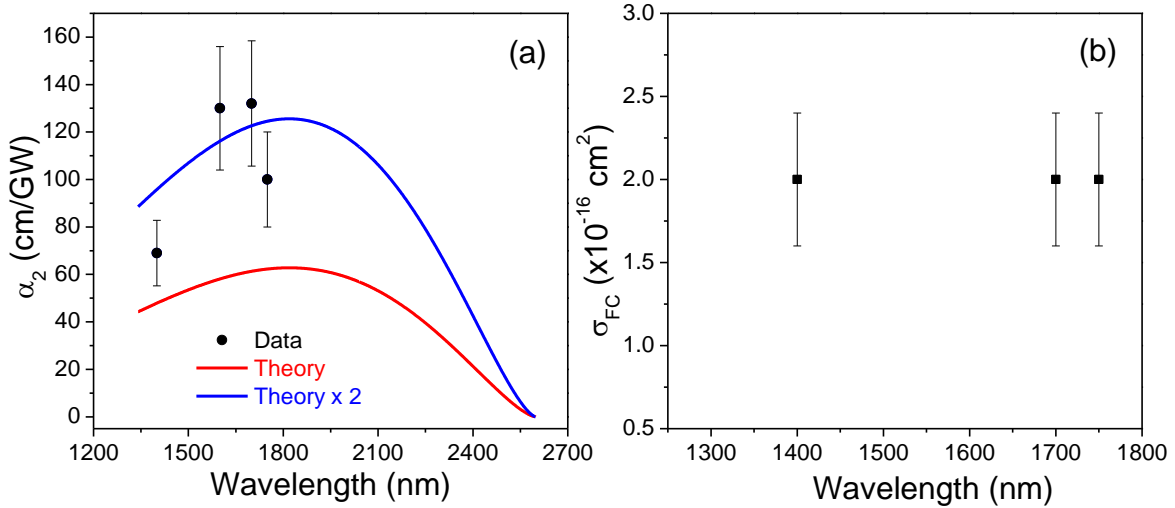


Figure 6.6 (a) Picosecond Z-scan results measured for 2PA in InAsP (black circles) compared to the theory (red solid line) and the same theory scaled by a factor of 2 (blue solid line) and (b) free carrier absorption results for InAsP .

It is important to mention that the theory agrees well with data obtained previously for GaAs [100] and InP [105] and also with femtosecond Z-scan measurements at 1120 nm (green dot in Figure 6.4a). Measured values of σ_{FC} seem to be almost constant through the whole wavelength range and are in reasonable agreement with theoretical prediction from the literature [105].

Nonlinear refraction parameters were obtained from division of closed and open aperture (CA/OA) Z-scan measurements. The measured dispersion of n_2 and σ_r of GaAs, InP and InAsP are shown in Figures 6.7, 6.8 and 6.9 respectively. Values of the measured n_2 are in much better agreement with theory than values of α_2 . For comparison, in addition to picosecond measurements, the n_2 of GaAs was measured with femtosecond Z-scans (green circles in Figure 6.7a.). No free-carrier refraction is observed for GaAs with femtosecond pulses as is expected

since in equation (2.24) due to the large irradiance for femtosecond pulses $n_2 I$ is much larger than $\sigma_r N$.

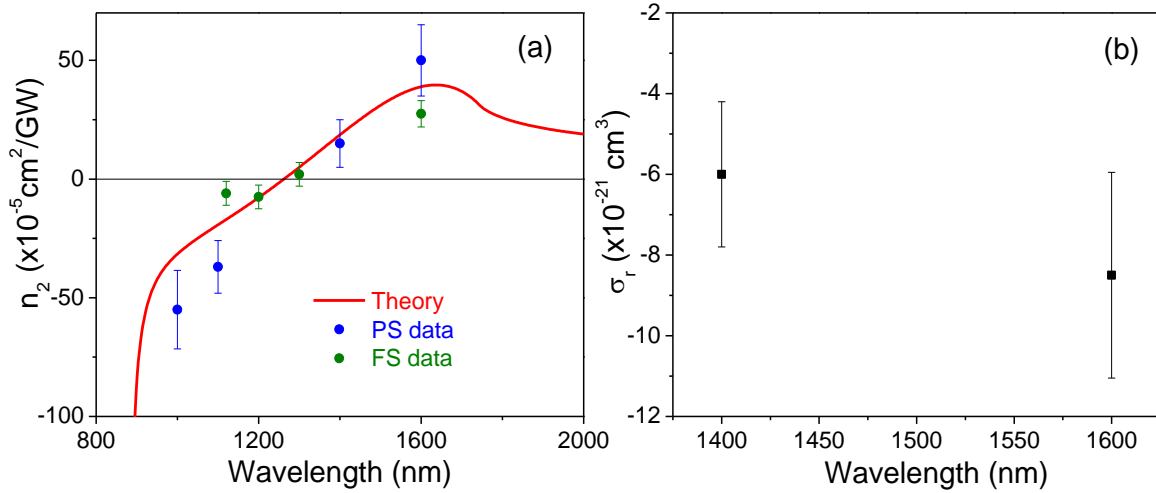


Figure 6.7 (a) n_2 results for GaAs measured with picosecond (blue circles) and femtosecond (green circles) pulses compared to the theory (red solid line) and (b) σ_r spectrum of GaAs.

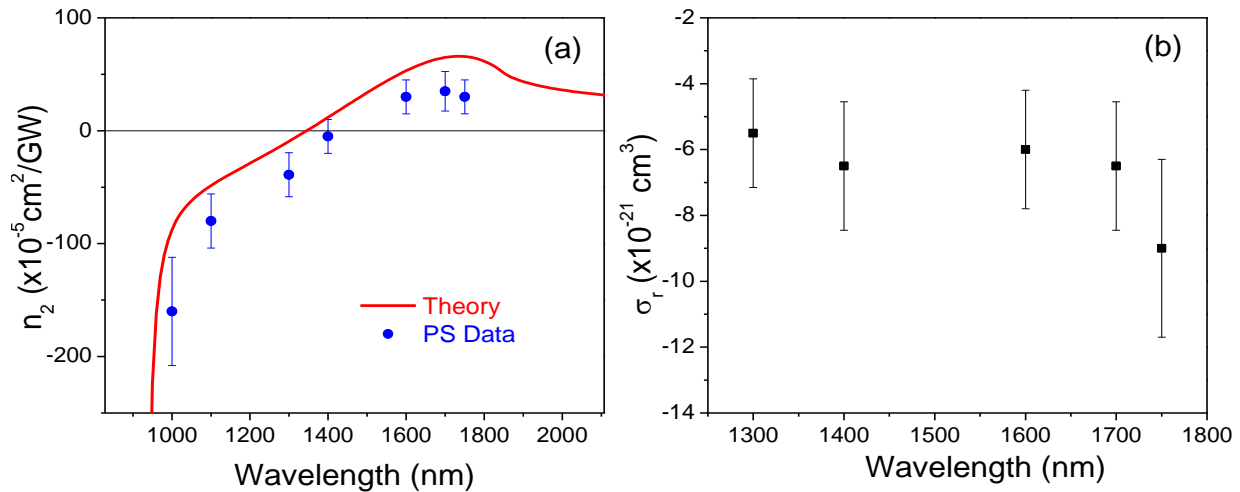


Figure 6.8 (a) n_2 results for InP measured with picosecond (blue circles) pulses compared to the theory (red solid line) and (b) σ_r spectrum of GaAs.

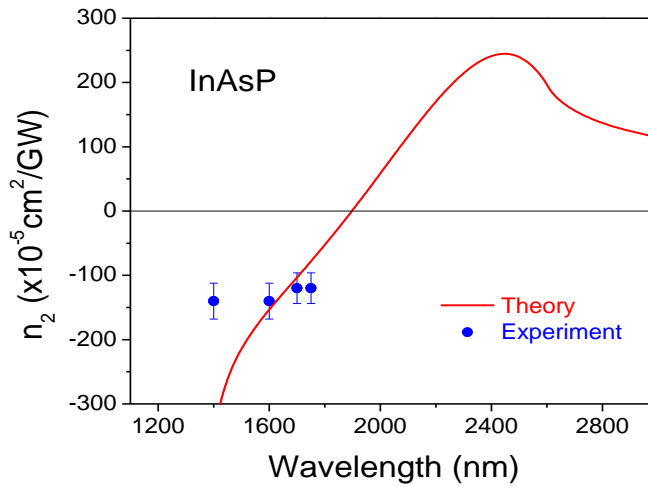


Figure 6.9 (a) n_2 results for InAsP measured with picosecond (blue circles) pulses compared to the theory (red solid line) and (b) σ_r spectrum of InAsP.

In a wavelength region with negligible contributions from free-carrier refraction or where the available laser energy is not high enough to observe free-carrier effects, the CA/OA Z-scan signal has a purely bound electronic contribution. n_2 obtained by fitting the CA/OA signal. Here the nonlinear refractive index is not dependent on the incident irradiance I_0 (Figure 6.10).

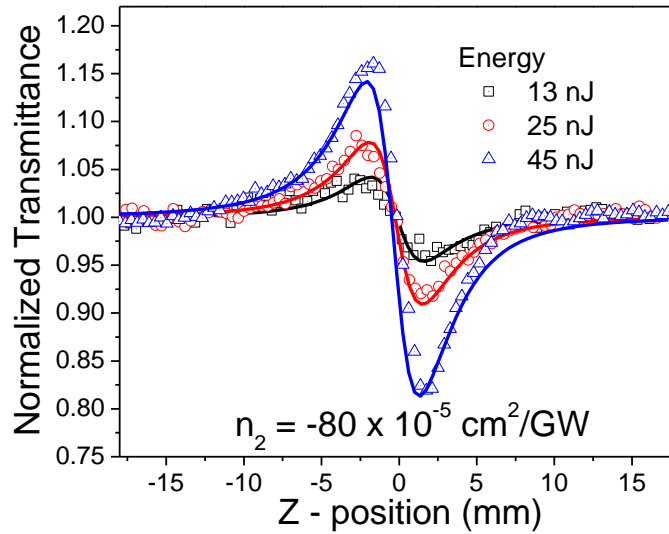


Figure 6.10 CA/OA for picosecond Z-scans of InP at 1100nm. All curves are fit with the same value of $n_2 = -80 \times 10^{-5} \text{ cm}^2/\text{GW}$ indicating no influence of free-carrier refraction.

When a free-carrier refraction influence is present, fitting the CA/OA signal with a purely third-order nonlinear refraction (i.e. treating it as if it were strictly a bound electronic n_2) allows the determination of $\Delta n/I_0$. A plot of $\Delta n/I_0$ versus I_0 then gives a straight line with an intercept that gives the purely electronic n_2 [100]. The slope can determine the free-carrier refraction under the right conditions. Figure 6.11a shows a CA/OA fit with pure electronic n_2 for InP at 1300nm. The dependence of $\Delta n/I_0$ on I_0 is shown in Fig. 6.11b. The fit using the full code including Equations (2.21), (2.22) and (2.23) of CA/OA for InP at 1300nm is given in Figure 6.12.

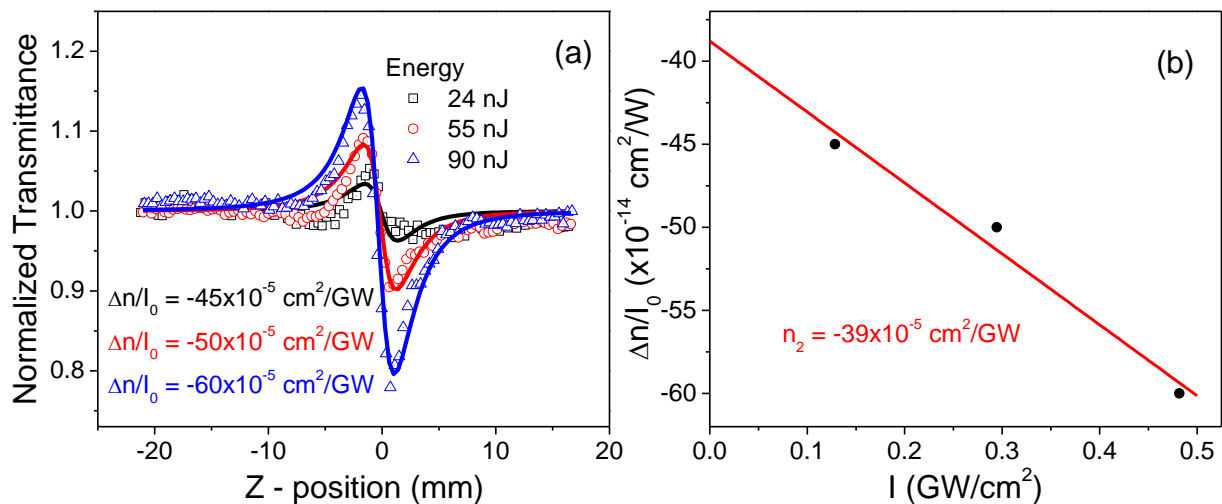


Figure 6.11 (a) CA/OA for picosecond Z-scans of InP at 1300nm fit with a third-order n_2 . (b) Plot of $\Delta n/I_0$ versus I_0 . Intercept gives $n_2 = -39 \times 10^{-5} \text{ cm}^2/\text{GW}$.

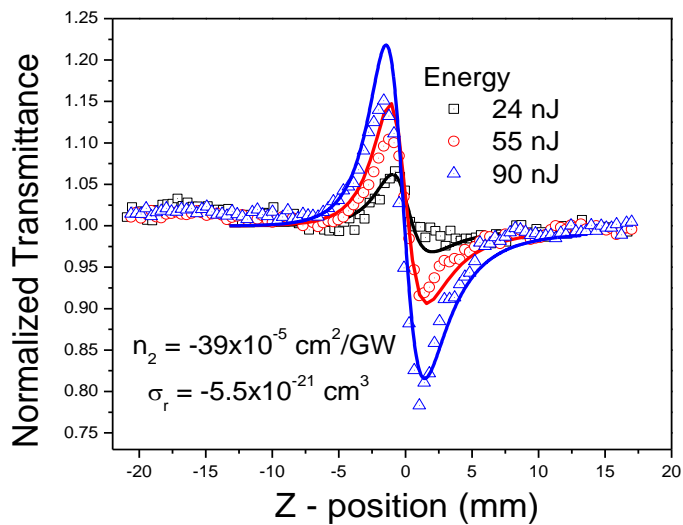


Figure 6.12 CA/OA for picosecond Z-scans of InP at 1300nm fit with full code:

$$n_2 = -39 \times 10^{-5} \text{ cm}^2/\text{GW} \text{ and } \sigma_r = -5.5 \times 10^{-21} \text{ cm}^3.$$

In regions where n_2 and σ_r have opposite signs, the Z-scan curve becomes significantly distorted. Fitting data with a purely third-order n_2 does not give reasonable results and a fit with the full code is required. Figure 6.13 shows Z-scan measurements of InP at 1750nm. The full code fitting gives $n_2 = 30 \times 10^{-5} \text{ cm}^2/\text{GW}$ and $\sigma_r = -9 \times 10^{-21} \text{ cm}^3$. All Z-scan data are shown in Appendix A.

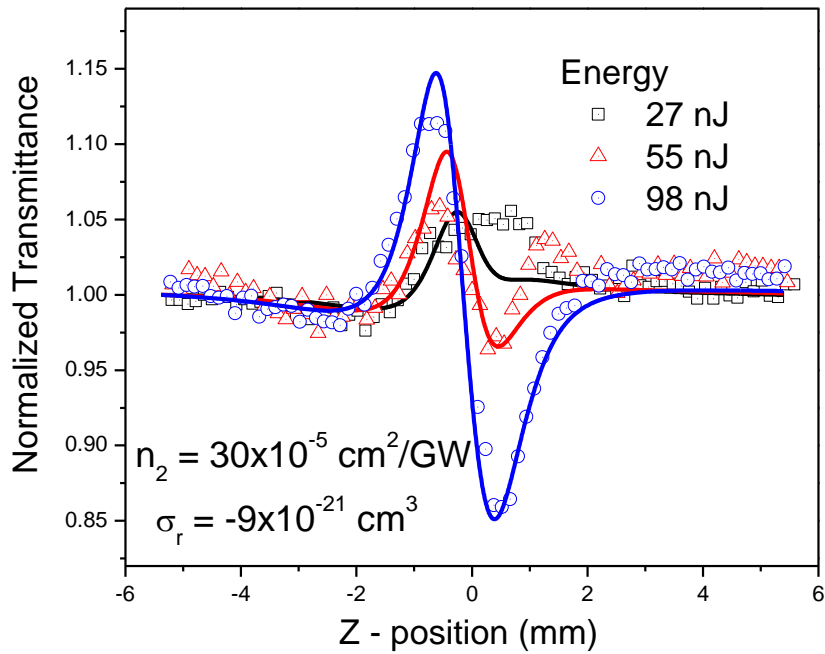


Figure 6.13 CA/OA for picosecond Z- scan of InP at 1750nm fit with full code:

$$n_2 = 30 \times 10^{-5} \text{ cm}^2/\text{GW} \text{ and } \sigma_r = -9 \times 10^{-21} \text{ cm}^3.$$

6.3 Three-Photon Absorption in GaAs

The purpose of the study done in this chapter is to measure the three-photon absorption (3PA) spectrum of GaAs and to compare the results with the theoretical calculations done by Cirloganu [106]. Cirloganu's theory is based on Kane's four-band model [107] including quantum interference between different pathways. Data for three-photon absorption (3PA) in GaAs that was recently published [108] contained only measurements at four wavelengths which is not enough to confirm the theory.

To avoid free-carrier absorption which can dominate 3PA, the spectrum of the 3PA coefficient α_3 of GaAs was first measured by femtosecond Z-scans. Data was taken in a wavelength range where 2PA is not energetically allowed which corresponds to $E_g/3 < \hbar\omega < E_g/2$. For each wavelength, the pulsewidth was measured by second-order autocorrelation. The measured pulse width vs. wavelength is shown in Figure 6.14.

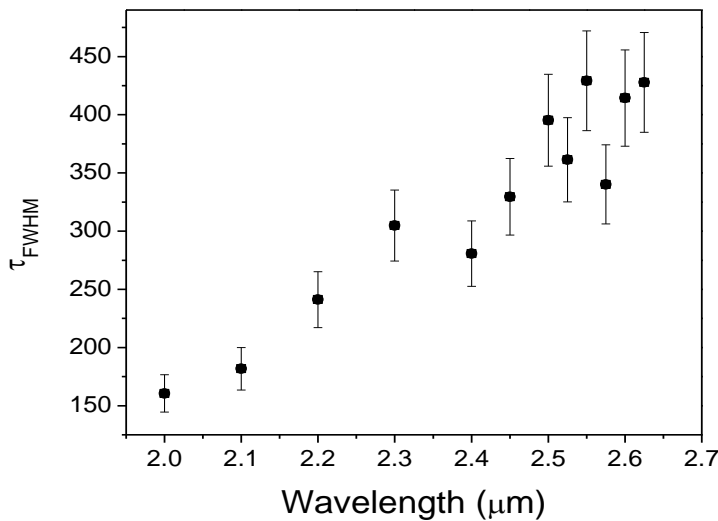


Figure 6.14 Pulse width of femtosecond OPG/A.

Femtosecond Z-scan results are shown in Figure 6.15.

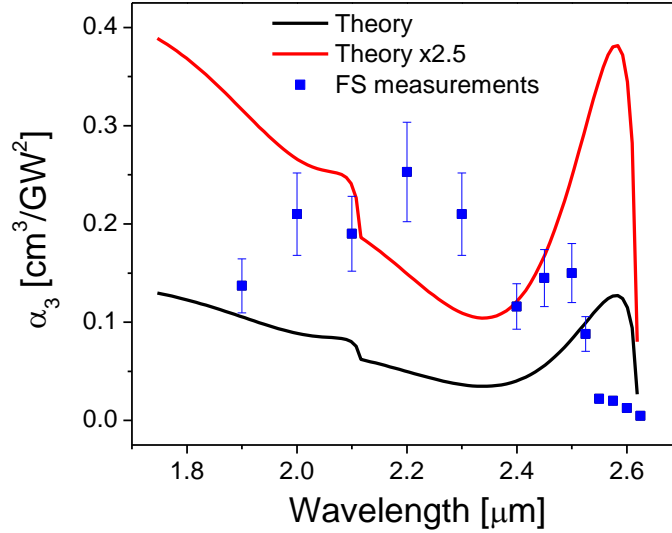


Figure 6.15 Femtosecond Z-scan results measured for 3PA in GaAs (blue squares) compared to the four-band theory (black solid line) and the same theory scaled by a factor of 2.5 (red solid line).

Values of the measured α_3 are in general agreement with data previously published [108] and with the values predicted by theory scaled by factor of 2.5. However, the predicted spectral structure is not observed. Upon measuring the spectra of the pulses used in these experiments, we found that the bandwidth was unusually large. Thus, a possible reason for the discrepancies between theory and experiment is this large pulse bandwidth. The spectrum of the laser was measured with a monochromator and a PbS detector. Transform limited pulses with $\tau_{\text{FWHM}} \sim 500$ fs would have a bandwidth of ~ 25 nm. However, measurements showed that between 2.4 μm and 2.6 μm the bandwidth of the pulses is ~ 100 nm which is 4 times longer than for the transform limited case. For pulses of such a large bandwidth, analysis becomes more complicated since the

assumption that the pulse is monochromatic with a wavelength equal to the spectral peak is no longer valid. In that case nondegenerate absorption has to be additionally considered.

To avoid this problem, the spectrum of α_3 was remeasured with a picosecond laser system since its bandwidth is less than 1 nm in the desired wavelength range. The pulse width of the picosecond DFG was measured using 2PA autocorrelation on a Ge detector. Contrary to the picosecond OPG/A, for which the pulse width remains constant through the entire wavelength range ($\tau_{\text{HW1/e}} \approx 6$ ps), the pulse width of the DFG increases toward longer wavelengths. A plot of the measured pulse width vs. wavelength of the DFG is shown in Figure 6.16.

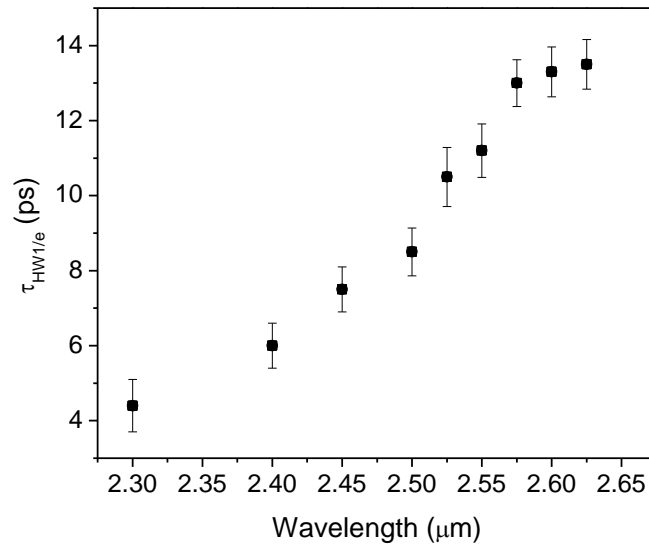


Figure 6.16 Pulse width of picosecond pulses using DFG.

As already mentioned, using picosecond pulses increases the influence of free-carrier absorption. A Z-scan of GaAs at 2300 nm fit with pure 2PA is shown in Figure 6.17a. It is obvious that α_3 depends on the incident irradiance. Figure 6.17b presents plot of $\alpha_{3\text{effective}}$ versus I_0 . An intercept with the y-axis gives the purely electronic α_3 . The same Z-scan data fit with the

full code including free-carrier absorption is shown in Figure 6.18. The value of α_3 obtained using the graphical method (Figure 6.17b) agrees very well with the value obtained using the full code fitting.

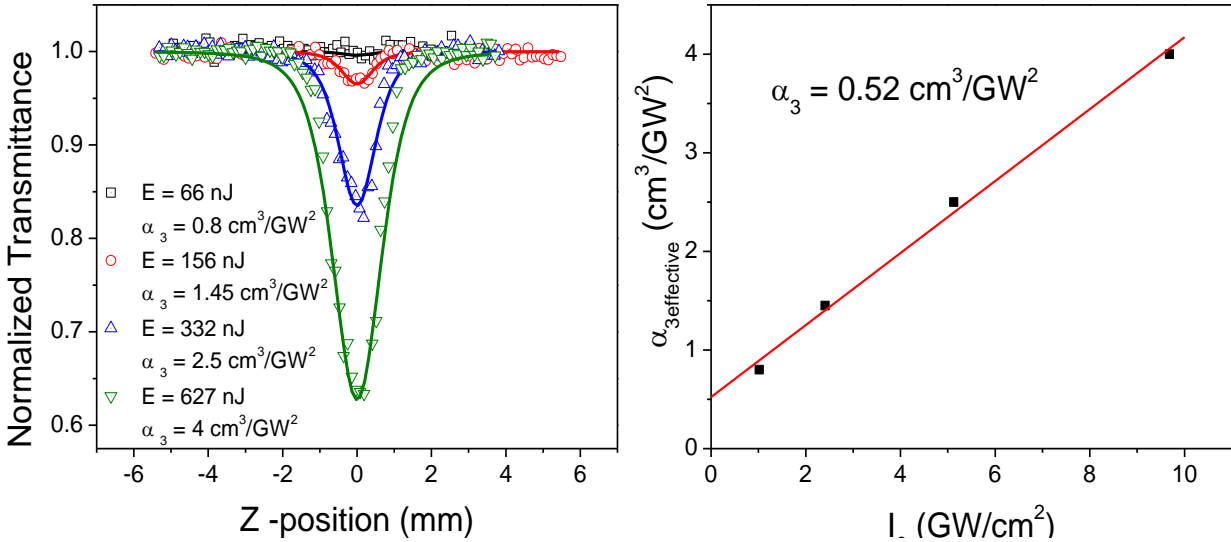


Figure 6.17 (a) Picosecond Z-scan of GaAs at 2300nm - fit with a pure α_3 and

(b) plot of $\alpha_{3\text{effective}}$ versus I_0 , $\alpha_3 = 0.52 \text{ cm}^3/\text{GW}^2$.

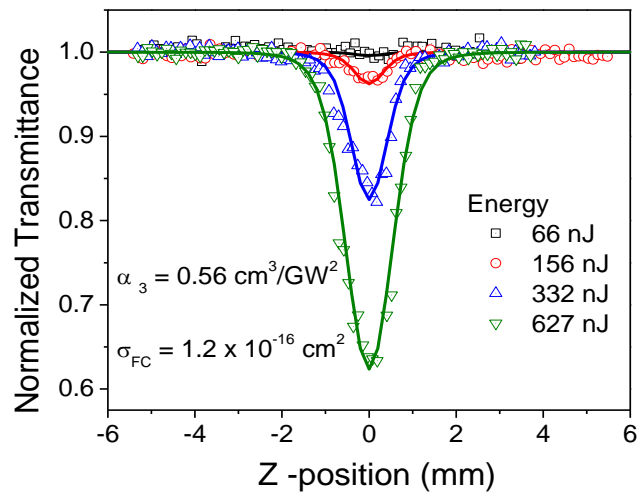


Figure 6.18 Z-scan of GaAs at 2300nm - fit with the full code: $\alpha_3 = 0.52 \text{ cm}^3/\text{GW}^2$, $\sigma_{\text{FC}} = 1.2 \times 10^{-16} \text{ cm}^2$.

The 3PA spectrum of GaAs is shown in Figure 6.19, while the free-carrier absorption spectrum is shown in Figure 6.20a.

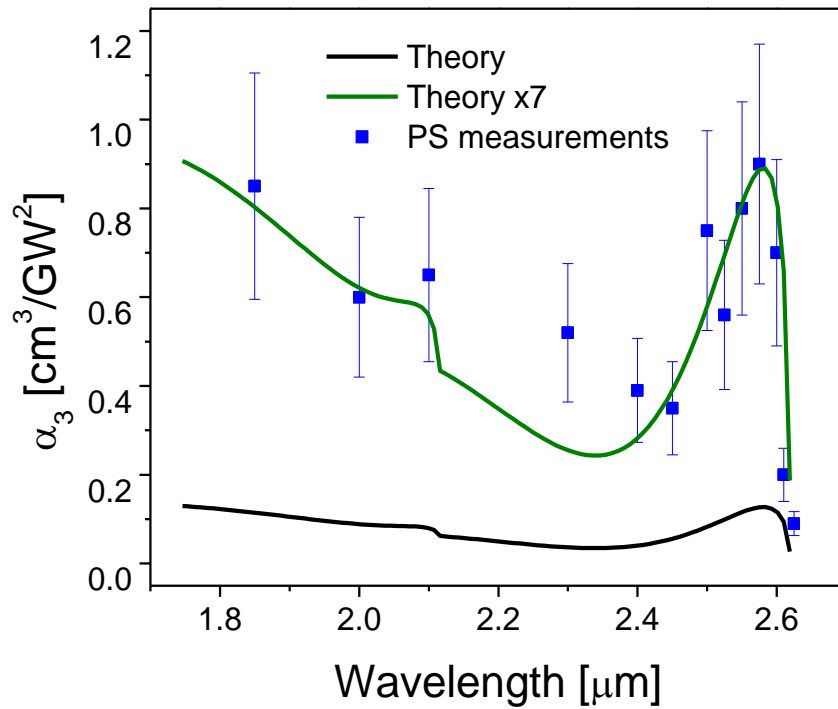


Figure 6.19 Picosecond Z-scan results for 3PA in GaAs (blue squares) compared to the four-band theory (black solid line) and the same theory scaled by a factor of 7 (green solid line).

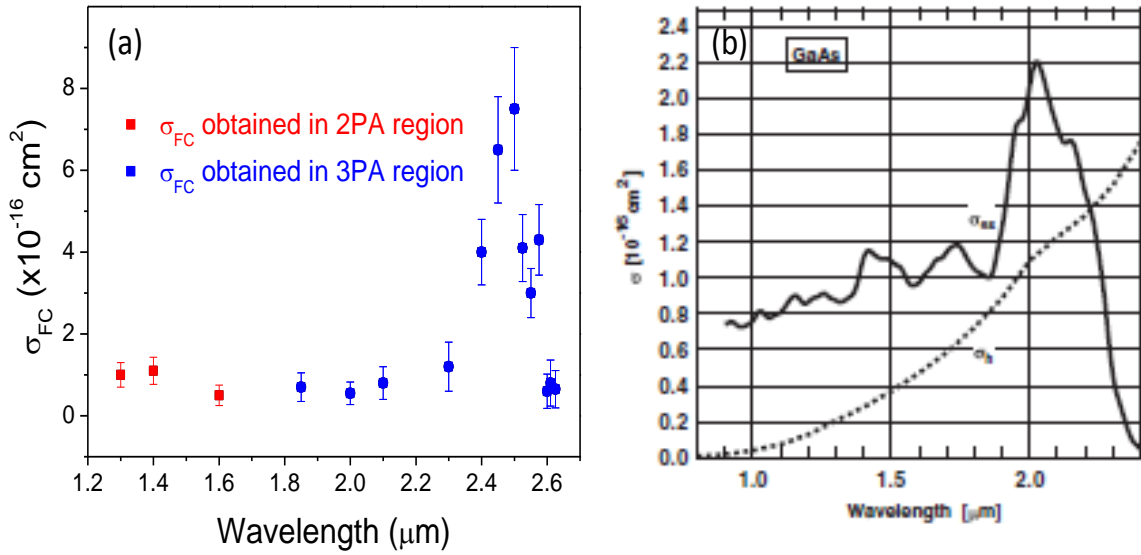


Figure 6.20 FCA of GaAs: (a) experimental results, (b) calculated contributions to FCA from holes and excited electrons.

Although the theory has to be scaled by factor of 7, the spectral structure of 3PA in GaAs is nicely resolved. In addition, the free-carrier absorption spectrum agrees well with theoretical calculations published recently [109] (Figure 6.20b). All 3PA Z-scan data are shown in Appendix B.

6.4 Discussion of picosecond results

The 2PA coefficient, α_2 , problem with “the factor of two” difference between values obtained from Z-scan experiments with our picosecond laser system and theoretical values has been present in our group for a long time. This problem is surprising since the n_2 value of CS_2

agrees with the value reported in the literature [53]. It is important to mention that α_2 measured with the femtosecond system agrees very nicely with the theory.

Before every Z-scan measurement the temporal pulse width is measured by second-order autocorrelation. The laser beam is first split into two beams using a 50/50 beam splitter. One of the beams is delayed with respect to the other using a prism on a movable stage. The two beams are again crossed in a second-harmonic generation (SHG) nonlinear medium, in this case ~ 1 cm thick Potassium Dihydrogen Phosphate (KDP) crystal (Figure 6.21). When the two beams are overlapped in time second harmonic light is generated in crystal. The second harmonic pulse is measured as a function of time delay.

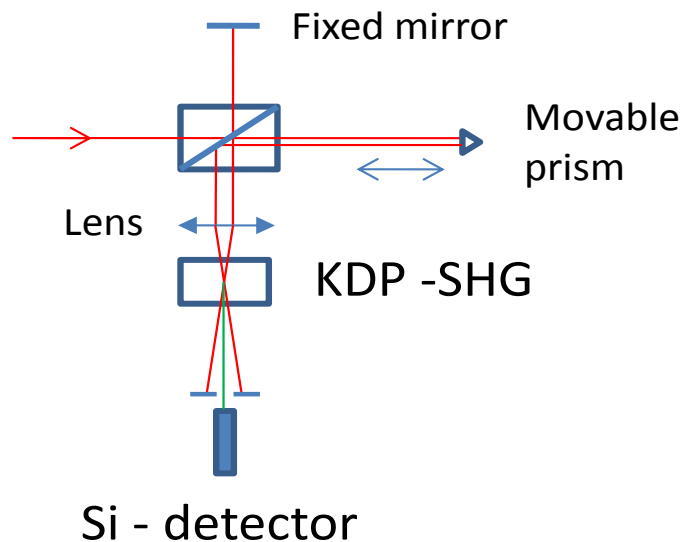


Figure 6.21 Setup 1:Autocorelation setup using KDP crystal.

The autocorrelation signal reveals a shape with two “shoulders” (Figure 6.22). The same shape was often observed in our laboratory for pulses coming from the picosecond OPG/A.

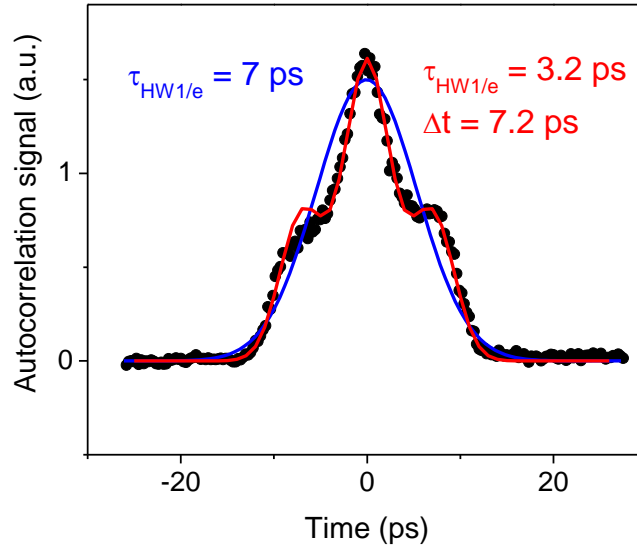


Figure 6.22 Autocorrelation signal of ps idler using KDP crystal fit with a single Gaussian pulse (blue line) and double Gaussian pulse (red line).

This particular shape of autocorrelation suggests the possibility of double pulsing in the system. The autocorrelation trace is fit with both single and double Gaussian pulses. The electric field time dependence of a double Gaussian pulse used for fitting is:

$$\varepsilon(t) = \varepsilon_0 \left(e^{-\left(\frac{t}{\tau}\right)^2} + e^{-\left(\frac{t-\Delta t}{\tau}\right)^2} \right). \quad (2.25)$$

Using a double Gaussian pulse in the fitting of experimental Z-scan data significantly increases the value of α_2 so that the double pulsing seems like a reasonable solution to the “factor of two” problem. To confirm that the shoulders feature is not some autocorrelation setup artifact (Figure 6.22), the pulse width was remeasured at 1000 nm after one month again using Setup 1

and also using Setup 2 shown in Figure 6.23. In the second autocorrelation setup two beams are crossed directly on a GaAs detector. Since the bandgap of GaAs is at 870 nm, the autocorrelation trace represents the 2PA signal measured as a function of time delay. Remeasured autocorrelation signals from both setups are shown in Figure 6.24a and b.

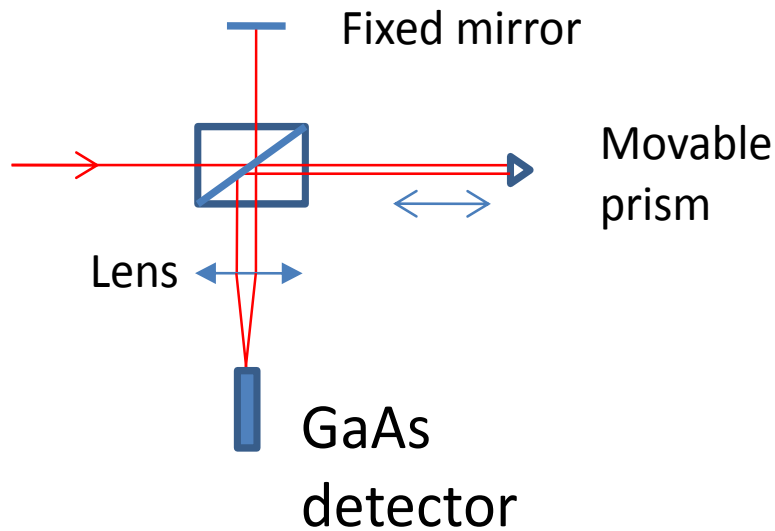


Figure 6.23 Setup2: Autocorrelation setup using 2PA on GaAs detector.

The signal from Setup 1 shows the shoulders again although of a different shape than before, while the signal from Setup 2 shows a very nice autocorrelation trace. It seems that double pulsing is really some artifact of the first autocorrelation setup. Using a much thinner BBO crystal for autocorrelation does not help since the conversion efficiency is too small. The remeasured α_2 of GaAs was again 45cm/GW.

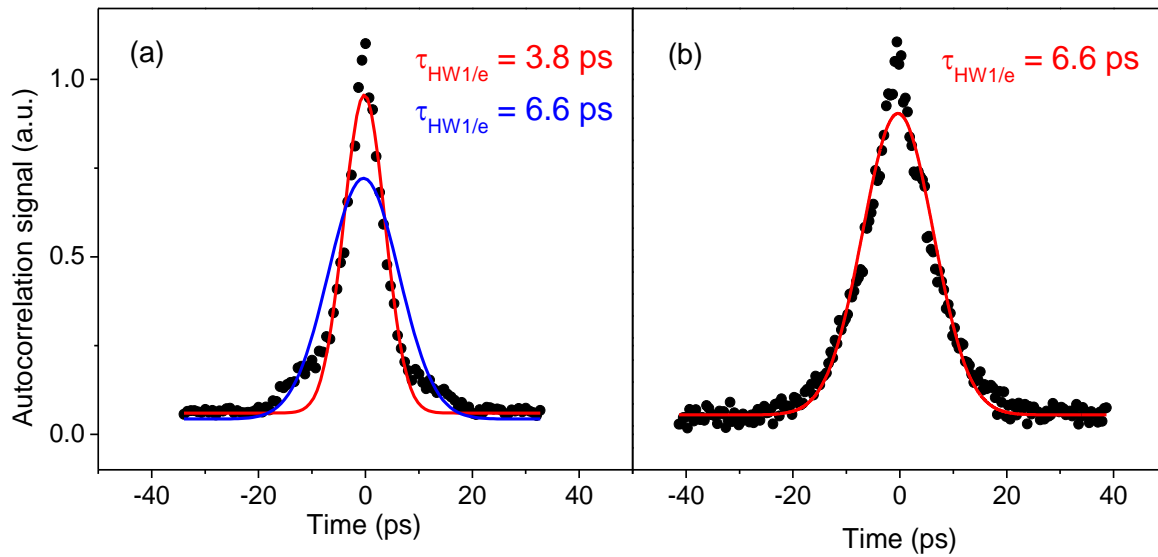


Figure 6.24 Autoceorrelation signal at 1000nm measured on the same day with Setup 1(a) and Setup 2

(b).

In addition, the pulse spectrum was measured with an Optical Spectrum Analyzer (OSA). The pulse spectrum is shown in Figure 6.25. Although the spectral width ($\Delta\lambda_{\text{FWHM}}$) is wider than predicted for a transform limited pulse (0.1 nm), it is still not too broad to cause any significant problem.

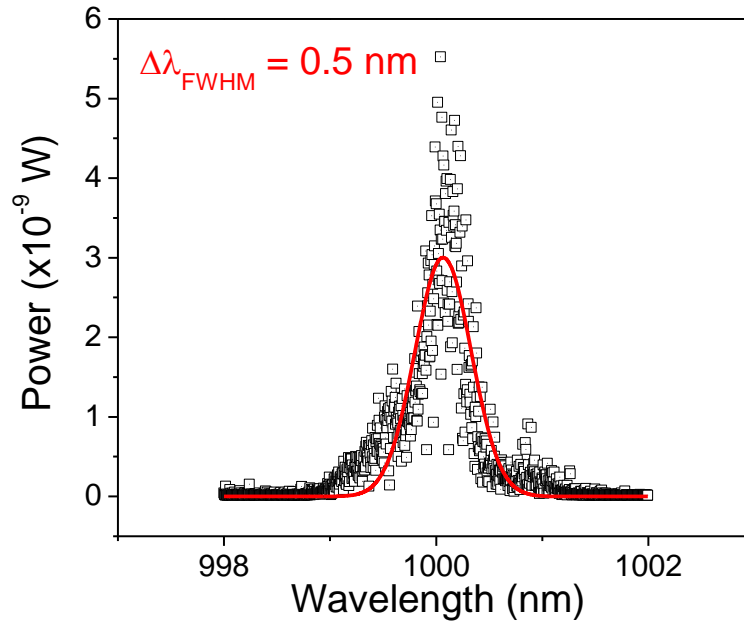


Figure 6.25 Pulse spectrum at 1000nm.

To ensure that “the factor of two” is caused by the OPG/A, autocorrelation and Z-scan experiments are repeated using the 1064 nm fundamental from the laser itself. Again, results were very surprising. An autocorrelation experiment with Setup 1 shows a very nice trace without shoulders. The measured pulse width is in agreement with laser specification (Figure 6.26a). Z-scan measurement of GaAs gives $\alpha_2 = 50$ cm/GW (Figure 6.26b).

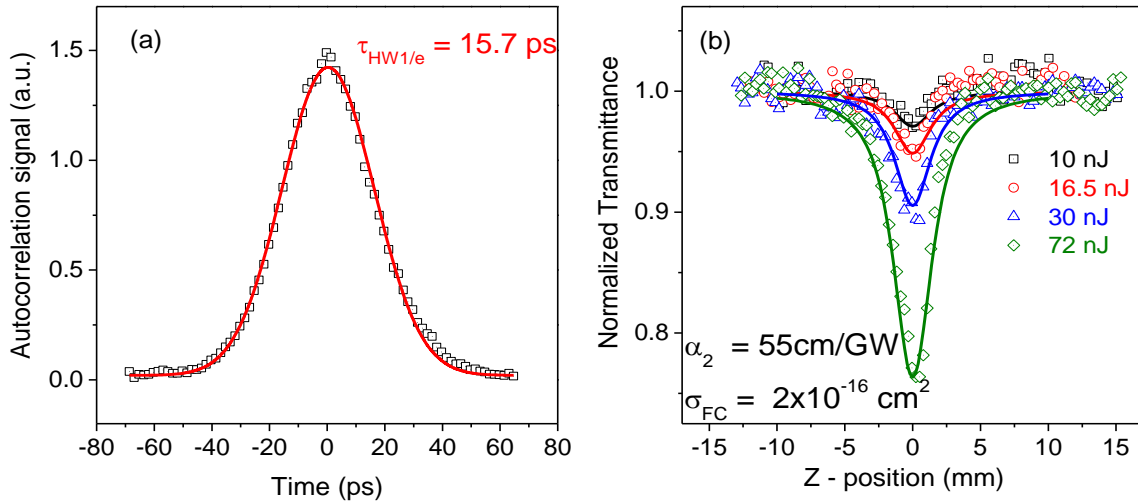


Figure 6.26 (a) Autocorrelation and (b) Z-scan of GaAs using 1064nm from the laser itself

Since the α_2 value of GaAs obtained from Z-scan using 1064 nm from the laser is again two times larger than the theoretical prediction “the Factor of Two” problem is obviously not connected with the OPG/A..

With data available at the moment it is difficult to find an explanation for the “the Factor of Two” problem. From multishot autocorrelation experiments it is impossible to see if there is any modulation present within the pulse. It is surprising that “the Factor of Two” affects only the open aperture Z-scan data. The value of n_2 obtained from closed aperture Z-scans both for CS₂ and for various semiconductors agrees much better with data from the literature and with theoretical values. To see what kind of modulation is actually present on the pulse, experiments like single shot autocorrelation or Frequency-resolved optical gating (FROG)[110] are required. This "factor of two" problem is still under investigation.

CHAPTER 7. CONCLUSION

7.1 Summary

In this dissertation we studied linear and nonlinear optical properties of organic materials and semiconductors. In the organic part, emphasize was on characterization techniques of molecules with enhanced intersystem crossing rate and on different approaches of increasing triplet quantum yield in conjugated molecules. Limitations in the accuracy of the double pump-probe technique (DPP) for independently determining the triplet quantum yield, ϕ_T , and triplet cross-section, σ_{Tlm} have been identified and we have described methods of optimizing the technique in light of these limitations. This optimization is particularly important for dyes that undergo photo-induced decomposition by allowing lower fluences to be used. The limitations are connected primarily with attempts to perform DPP in regions of small linear absorption where materials may exhibit RSA. In the RSA regime, the fraction of ground-state population moved to the triplet state is small at relatively small pump fluence, especially for large dye concentrations, thus leading to low sensitivity and poor accuracy of the DPP. Under these conditions, the values of ϕ_T and σ_{Tlm} cannot be accurately decoupled. To successfully decouple ϕ_T and σ_{Tlm} , a significant fraction of initial ground-state population has to be redistributed to the triplet state. In the RSA regime, where ground-state absorption is small, this can be achieved only by increasing the pump fluence and lowering the dye concentration. This approach is not always practical due to photochemical instability of many organic molecules. Analytical simulations, confirmed by experimental results, show that when the pump wavelength is moved to the SA regime, even a small excitation fluence can significantly depopulate the ground state.

A larger fraction of the ground-state population moved to the triplet state results in greatly improved accuracy in the determination of ϕ_T . Although ϕ_T can be determined accurately in this region, measurements of σ_{TIm} are still inaccurate since κ involves the product of the difference. Precise determination of σ_{TIm} in the RSA region, useful for many applications, requires a separate measurement at the desired wavelength with knowledge of ϕ_T .

With the goal of understanding the efficiency of ISC processes in polymethine-like molecules we investigated both experimentally and theoretically linear and nonlinear spectroscopic properties of a series of PD with Br- and Se- atom substitution, and a series of new squaraine molecules, where one or two oxygen atoms in a squaraine bridge are replaced with sulfur atoms. Using DPP, we determined that “heavy” Br- and Se-atoms substitution in PDs do not significantly enhance singlet-triplet mixing probabilities. These dyes are characterized by small triplet quantum yields ($\phi_T \leq 10\%$) indicating that the internal conversion via singlet states is a dominating deactivation pathway. Our results have been explained by quantum-chemical calculations showing that “heavy” Br- and Se-atoms do not significantly affect the charge distribution within the frontier orbitals, HOMO and LUMO, which are responsible for the main $S_0 \rightarrow S_1$ transitions for these molecular structures. Small, yet measurable, triplet quantum yields are explained by $\pi\text{-}\sigma^*$ mixing in the out-of-plane distorted geometry of S_1 state.

In contrast, the values of ϕ_T and singlet oxygen generation for sulfur-containing SDs reach almost unity. We performed a detailed comparison of a series of sulfur-containing squaraines versus their oxygen-containing analogues. Quantum chemical calculations suggest that replacing the oxygen atoms in a squaraine ring by sulfur atoms leads to an inversion of the energy levels between the lowest $\pi\text{-}\pi^*$ transition (occurring in SD-O molecules) and $n\text{-}\pi^*$

transition (occurring in SD-S molecules), thus significantly reducing the singlet-triplet energy difference, and opening an additional ISC channel connected with non-Franck-Condon vibronic enhancement of the $S_1 (n\pi^*) \rightarrow T_1 (\pi\pi^*)$ transition. Importantly, this inversion, affecting the ISC rate, does not lead to significant changes of the nonlinear optical properties of the molecules; large two-photon absorption cross sections (up to 2000 GM), and large S-S and T-T absorption cross sections (up to $4 \times 10^{-16} \text{ cm}^2$).

Another type of molecule studied is cyclic conjugated compounds; Pthalocyanine (Pc) and Naphthalocyanine (Nc) compounds with Ruthenium(II) as the central atom. Ru(II) Pcs and Ncs are known to have ultrafast ISC rate and ϕ_T close to one. The problem with the formation of aggregates and low solubility in these compounds was resolved by introducing dendron attachment to the axial position of the central atom or to the peripheral position of the macrocycle. Due to ultrafast ISC rate of these molecules, femtosecond DPP was used for determination of ϕ_T . Measured values of ϕ_T reach almost unity indicating no influence of dendron substitutions on the ISC rate.

In the last part of this dissertation the spectral dependence of two-photon absorption, nonlinear refraction, free-carrier absorption and free-carrier refraction are studied using picosecond Z-scans for three different semiconductors: GaAs, InP and InAsP. All 2PA spectra measured follow very nicely the trend of the theory. However, theoretical curves have to be rescaled by factor of two to match experimental data. Theory for GaAs was additionally confirmed with femtosecond Z-scan measurements. The factor of two difference between the picosecond data and the theoretical prediction is not trivial since it is only affecting open aperture Z-scan results. Nonlinear refraction data are in much better agreement with theory and

the data obtained with femtosecond Z-scan measurements. Autocorrelation measurements of the pulse do not clear up the discrepancies. However, autocorrelation measurements are not enough to reveal if any temporal modulation is present in the beam, and additional beam diagnostic measurements are required. Free-carrier absorption and refraction coefficients were previously measured for just one or two wavelengths. The data presented in this study are in relatively good agreement with previously published.

In addition the three-photon absorption spectrum of GaAs is measured using picosecond Z-scans. Although the spectrum was previously measured with femtosecond pulses, spectral structures predicted by theory were not resolved due to the large spectral width of the femtosecond laser. Picosecond data follows very nicely the spectral trend predicted by the theory but it differs from the femtosecond data by an overall the factor of approximately three.

7.2 Future Work

Future work proposed:

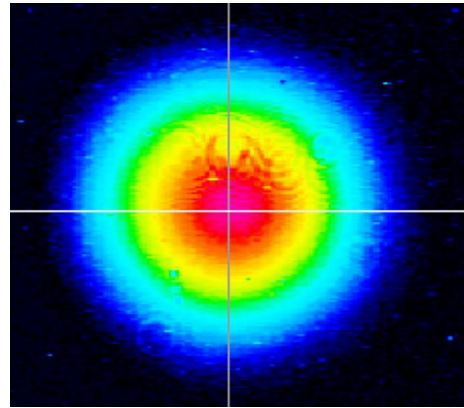
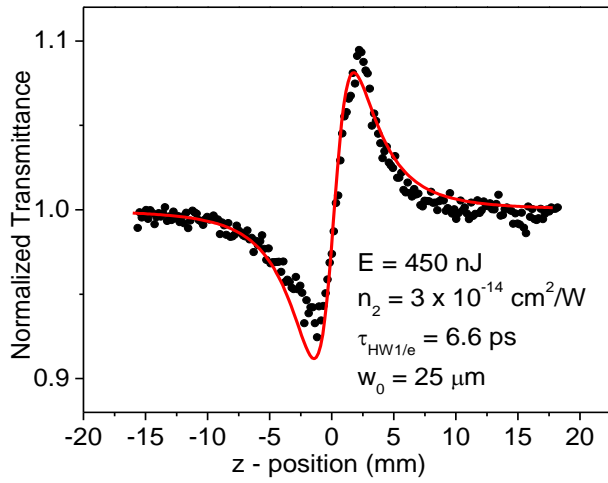
1. Sulfur-squaraine molecules proved to be promising candidates for photodynamic therapy. Next most important step would be to increase their photochemical stability. Additionally, for biomedical applications there are also problems with toxicity and solubility in water that has to be solved.

2. Disagreement between values of 2PA cross section obtained with our picosecond and femtosecond systems is problem present in our group for a long time. Most probable reason is some temporal modulation present in picosecond pulse. Basic autocorrelation experiment is not capable of revealing type modulation present so that additional measurements are required. Single shot autocorrelation experiment would be probably the best approach.

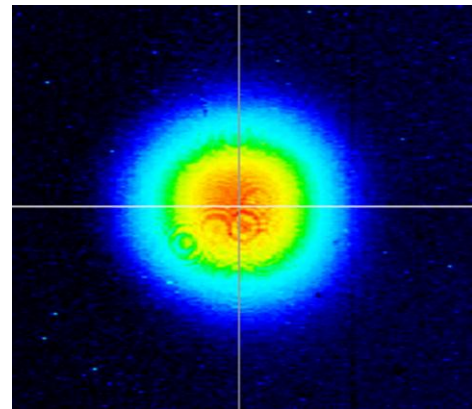
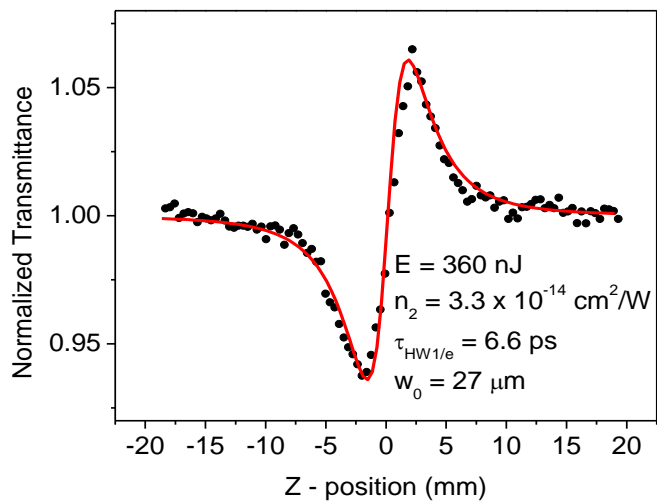
**APENDIX A: PICOSECOND Z-SCAN MEASUREMENTS OF α_2 , σ_{FC} , n_2
AND σ_r .**

CS₂ Beam calibration and beam profile (where available)

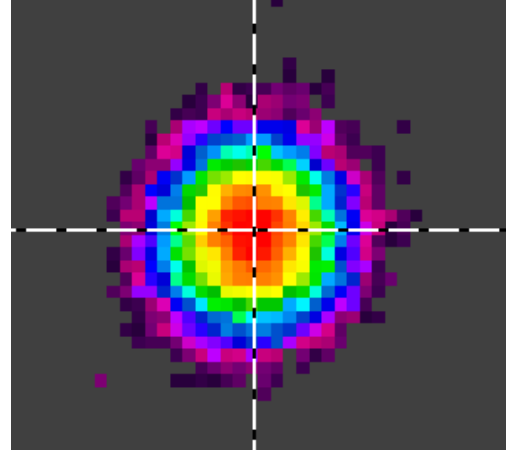
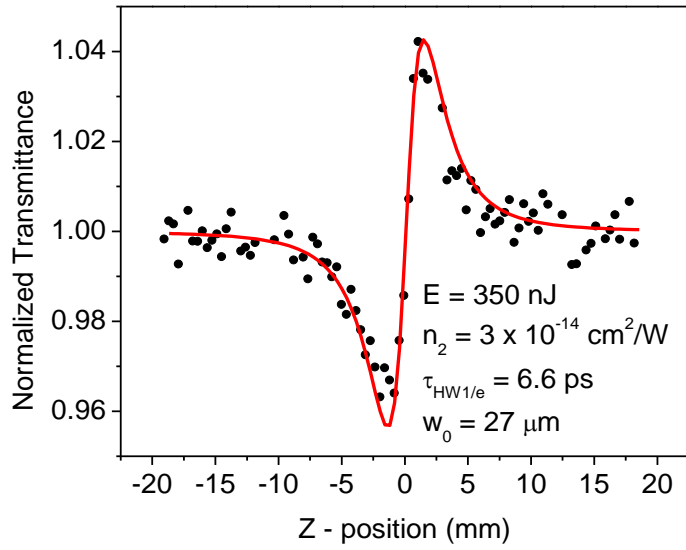
$\lambda = 1000$ nm



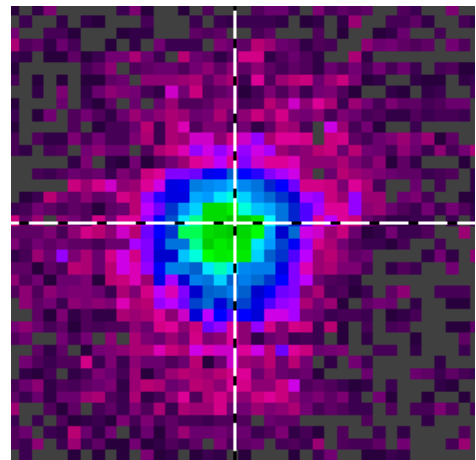
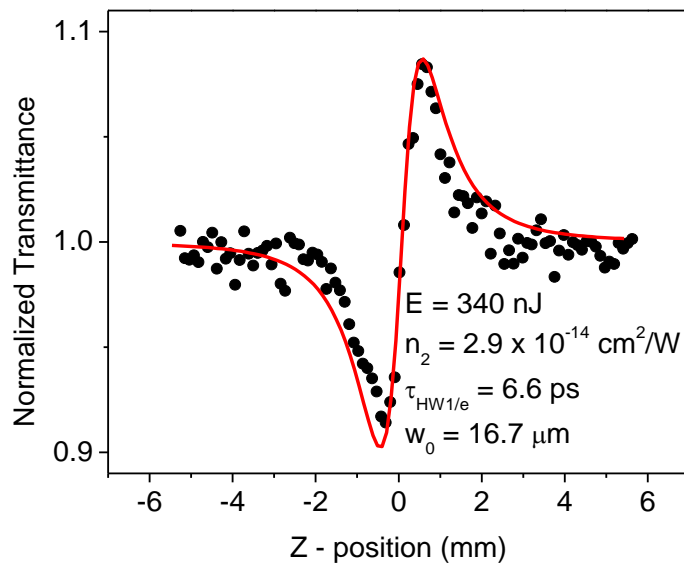
$\lambda = 1100$ nm



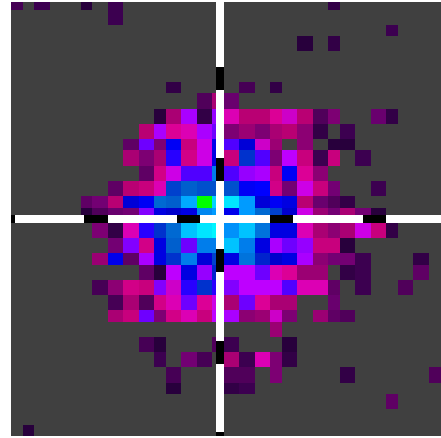
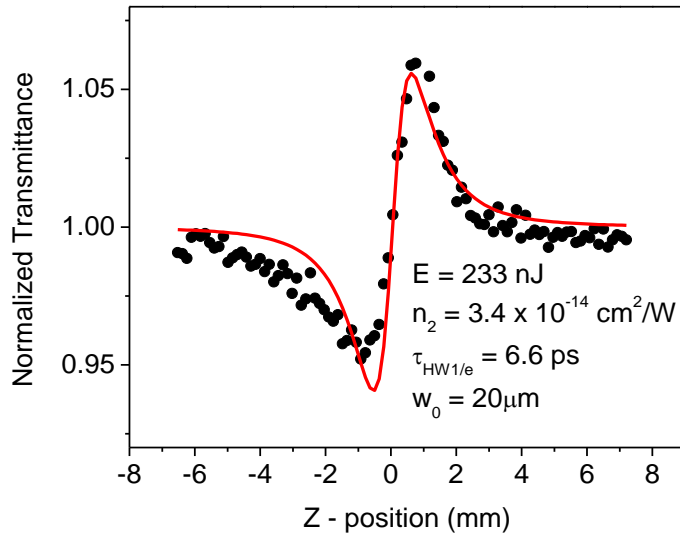
$\lambda = 1300$ nm



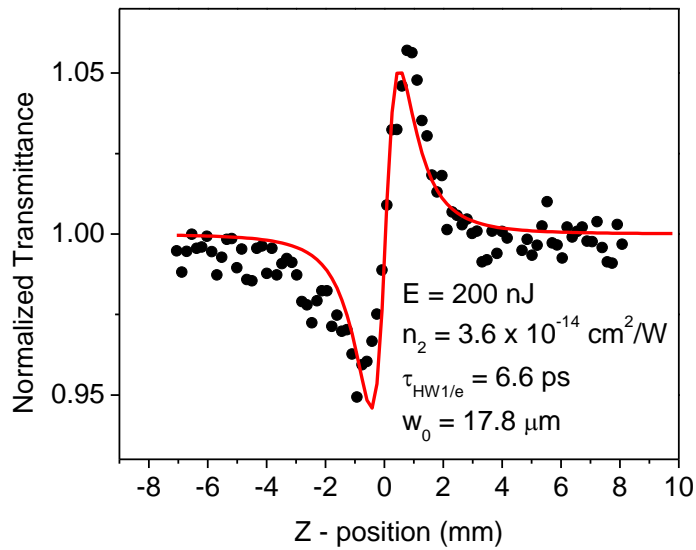
$\lambda = 1400 \text{ nm}$



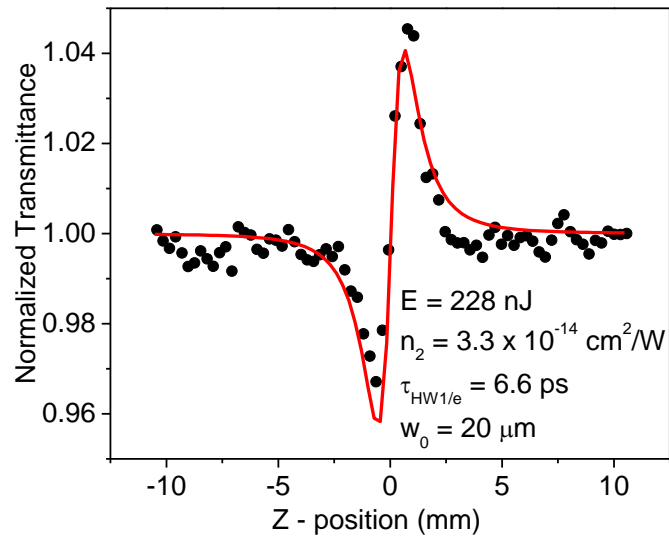
$\lambda = 1600 \text{ nm}$



$\lambda = 1700 \text{ nm}$

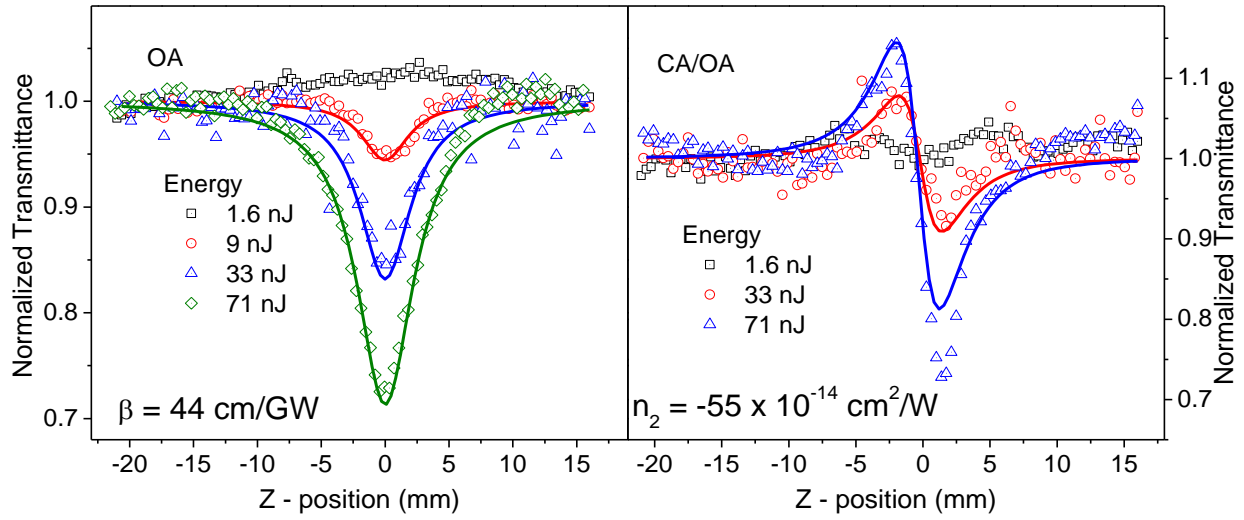


$\lambda = 1750 \text{ nm}$

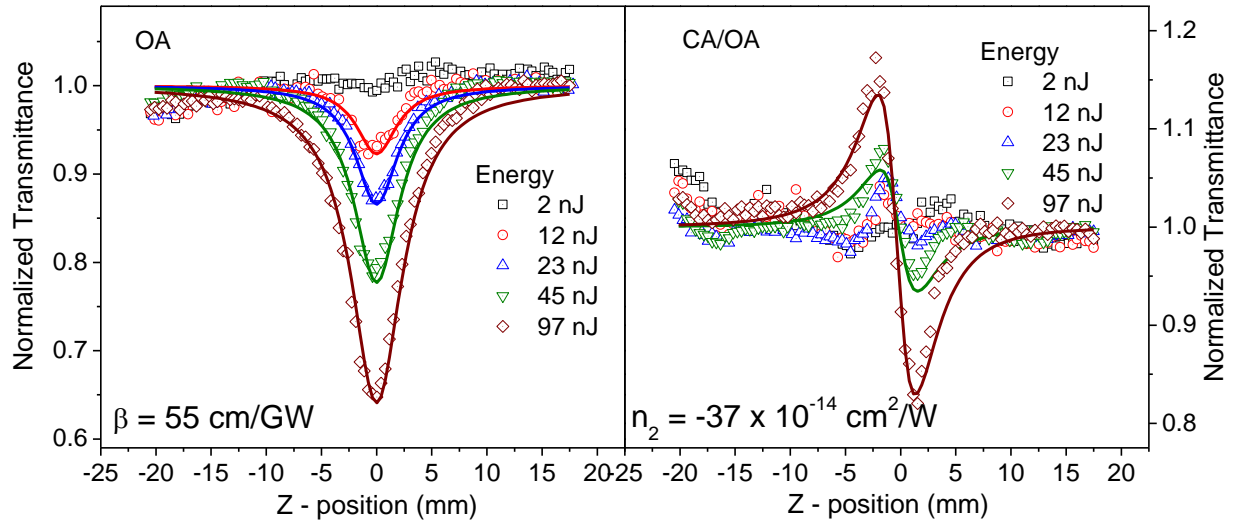


GaAs

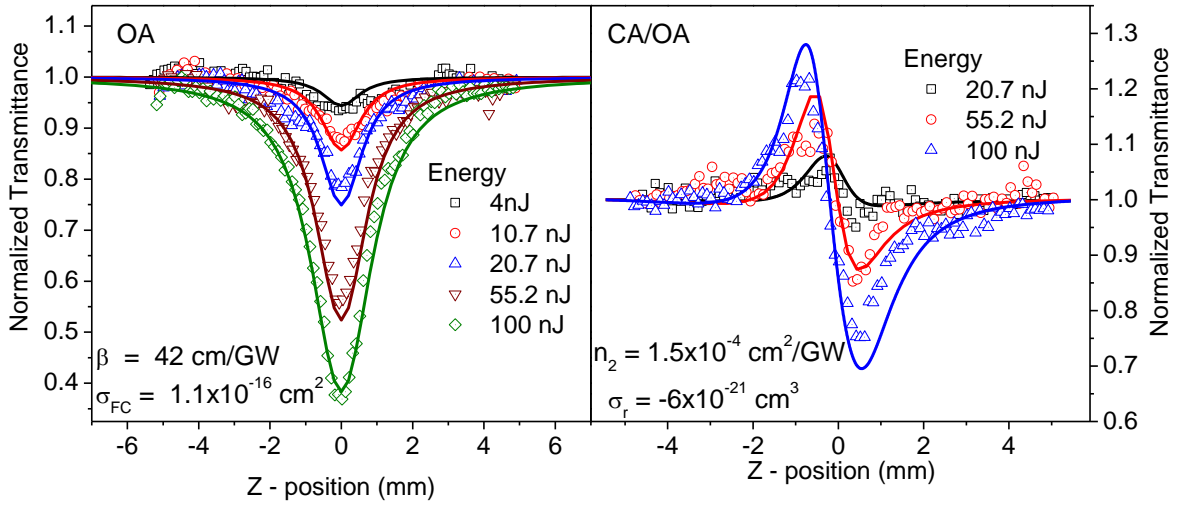
$\lambda = 1000 \text{ nm}$



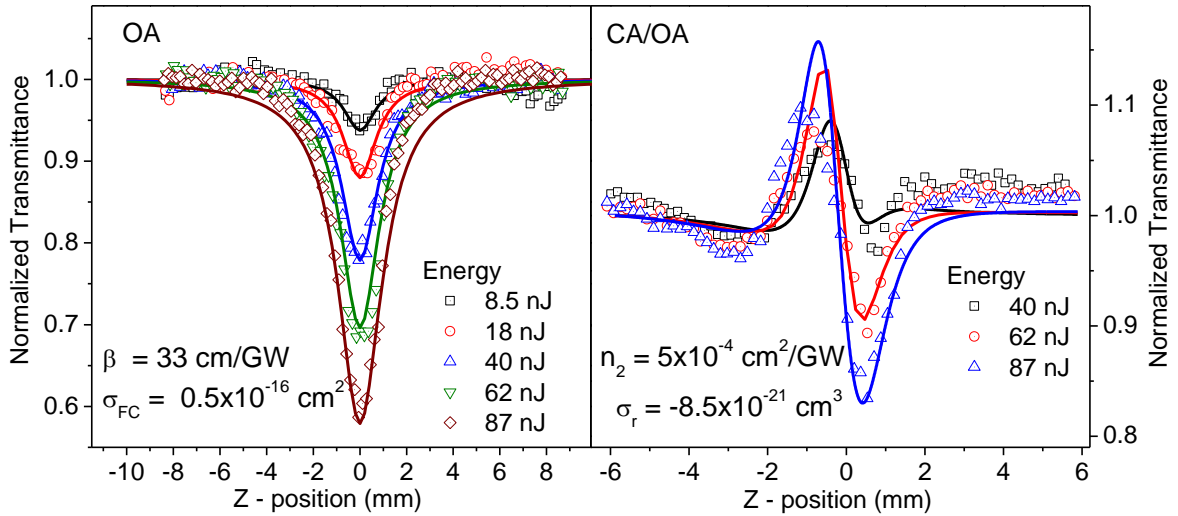
$\lambda = 1100 \text{ nm}$



$\lambda = 1400 \text{ nm}$

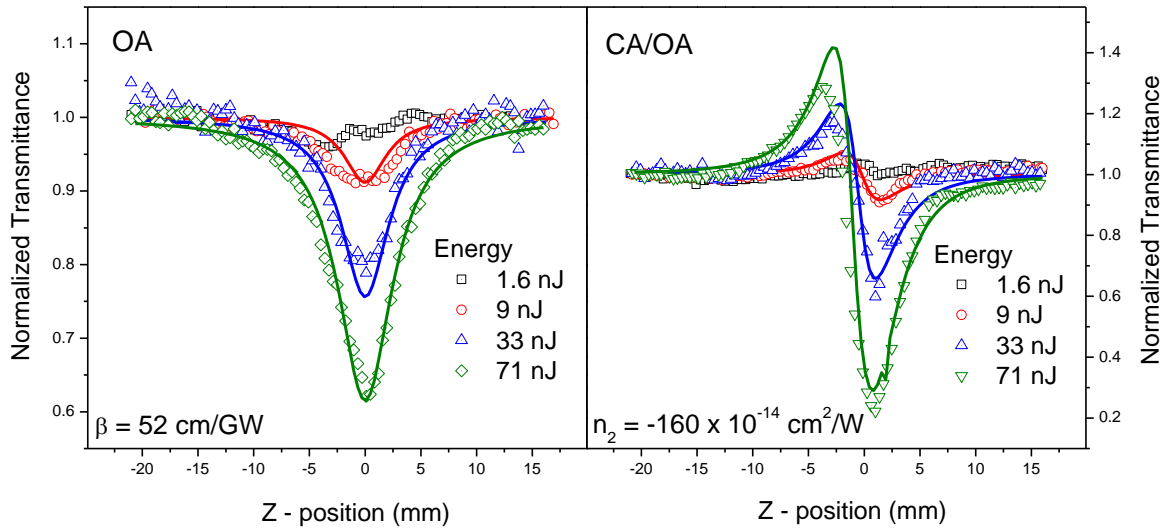


$\lambda = 1600 \text{ nm}$

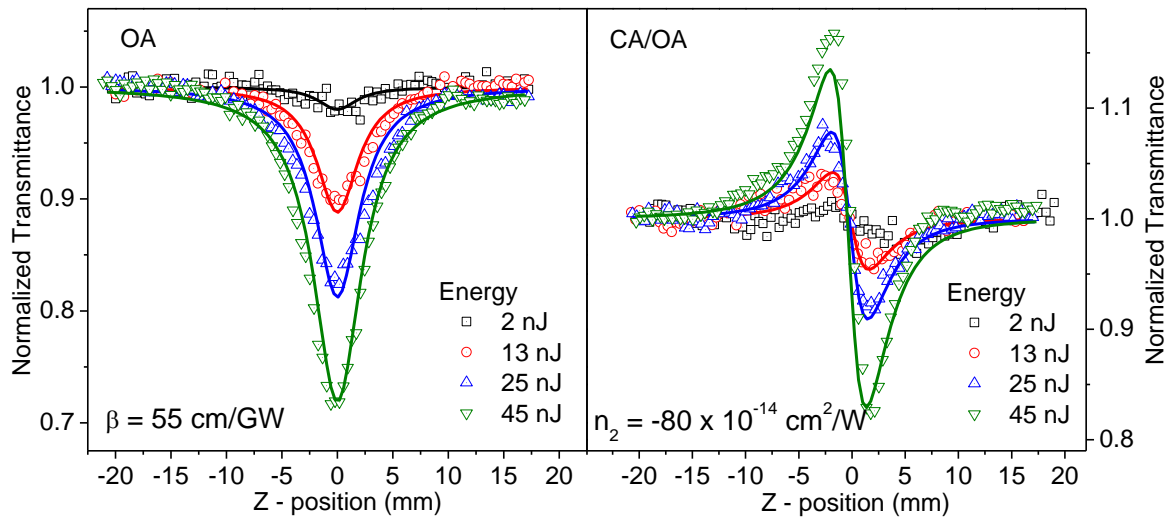


InP

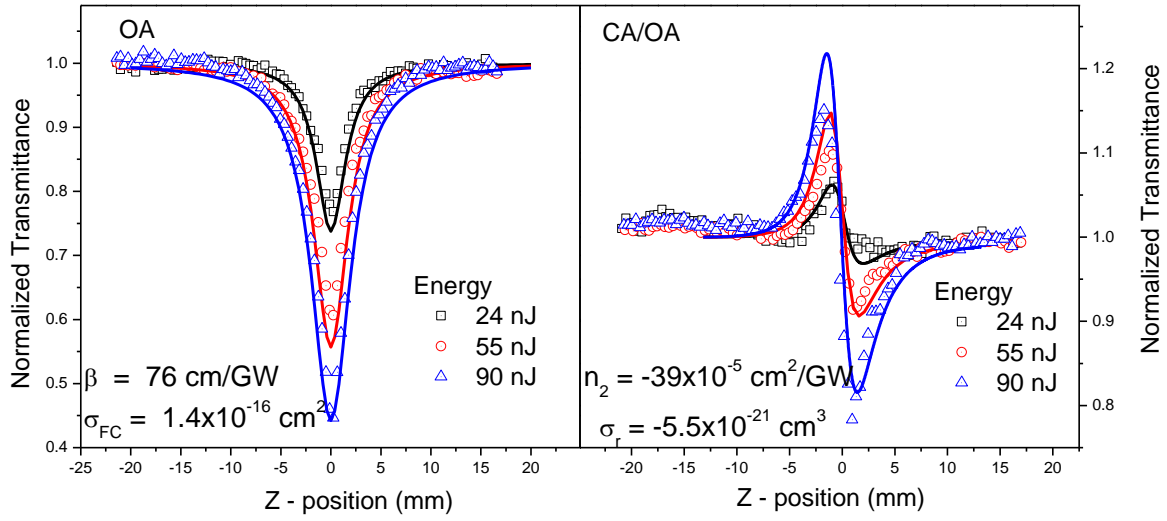
$\lambda = 1000 \text{ nm}$



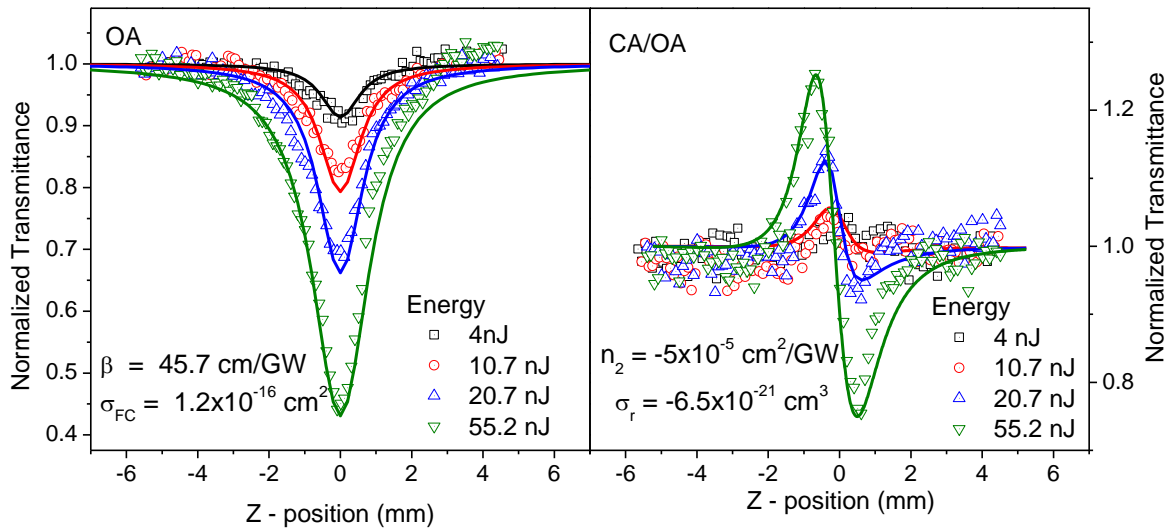
$\lambda = 1100 \text{ nm}$



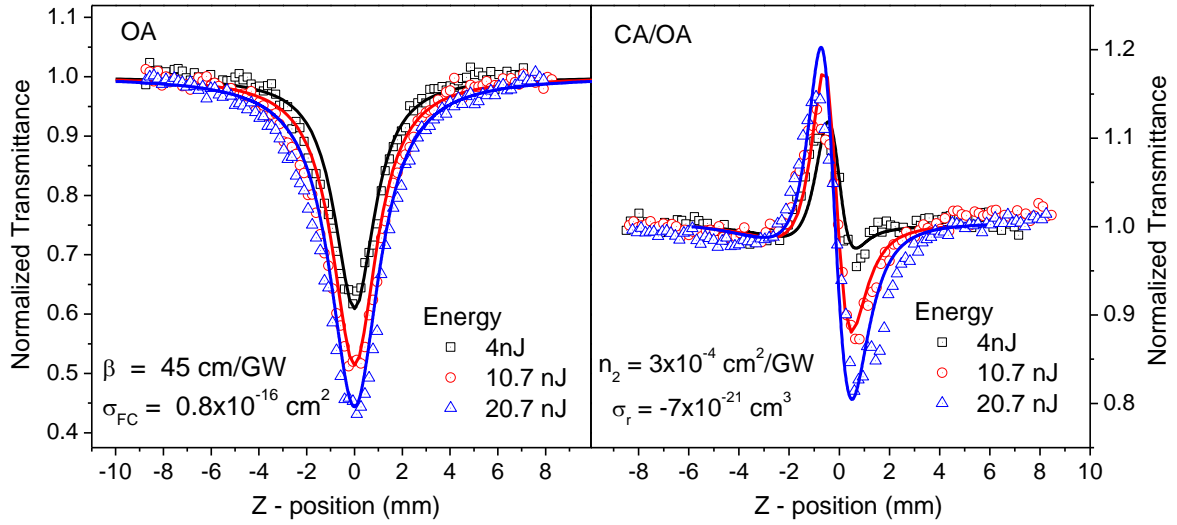
$\lambda = 1300 \text{ nm}$



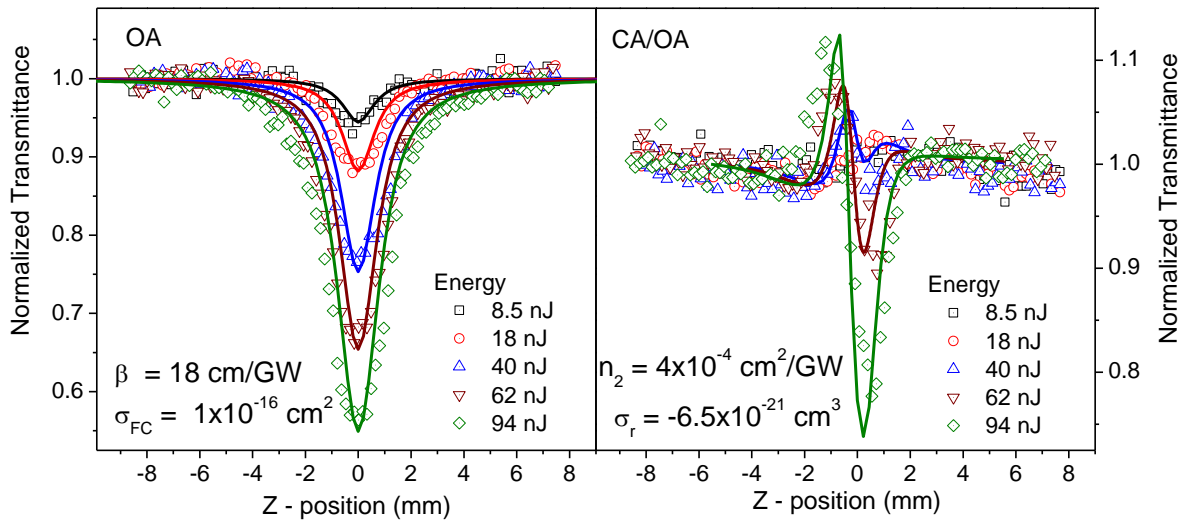
$\lambda = 1400 \text{ nm}$



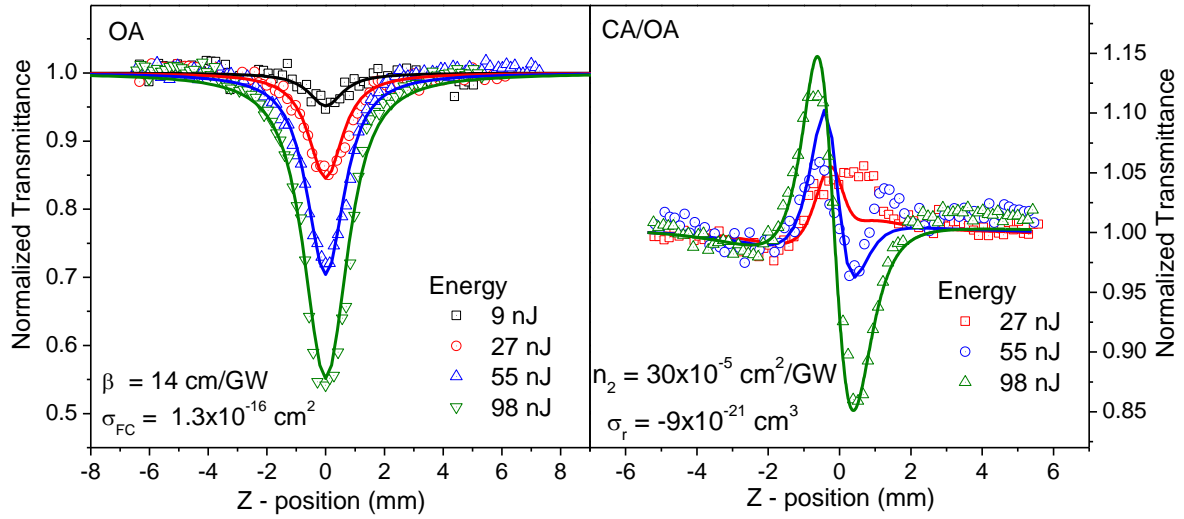
$\lambda = 1600$ nm



$\lambda = 1700$ nm

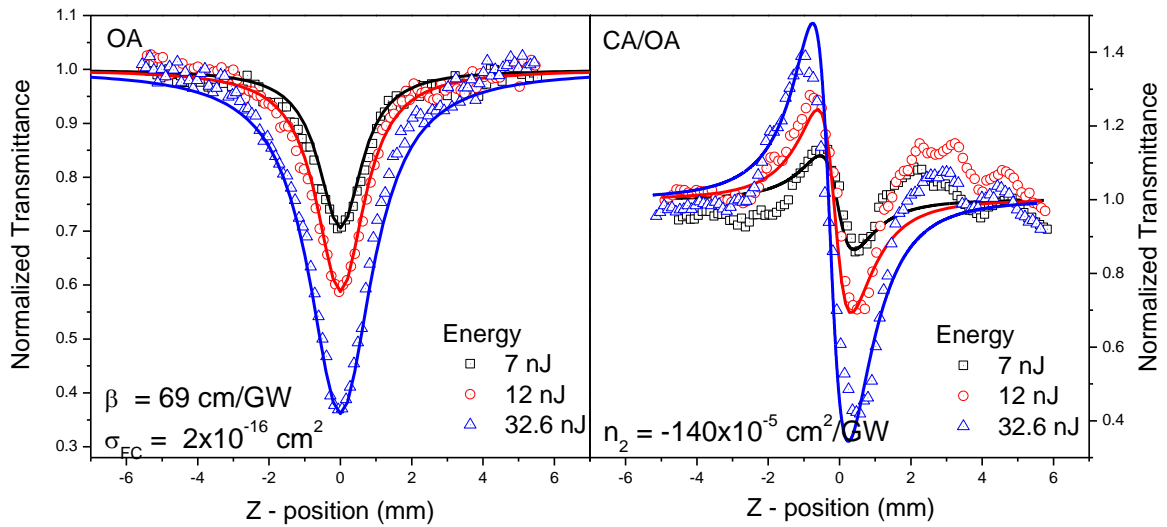


$\lambda = 1750$ nm

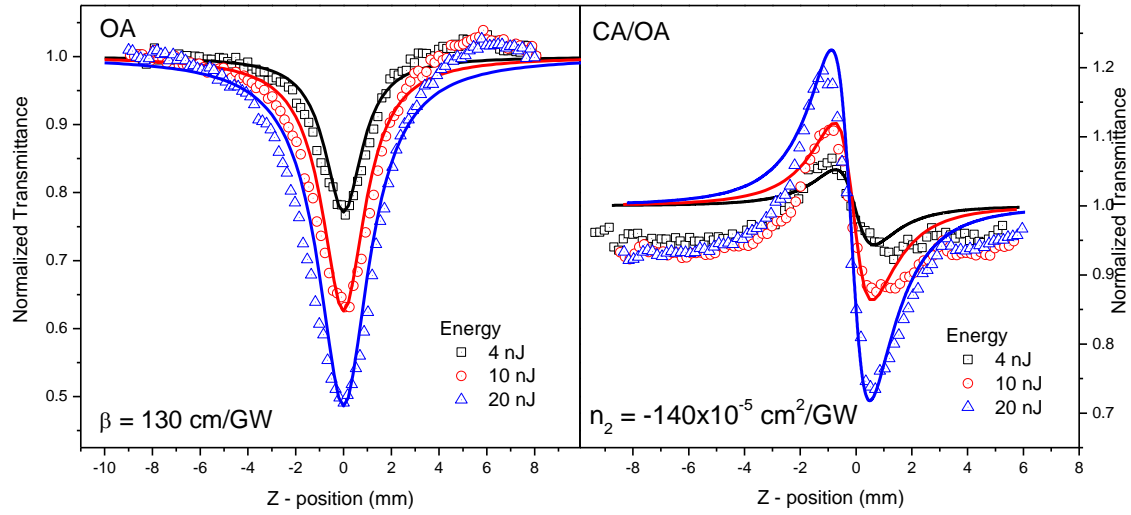


InAsP

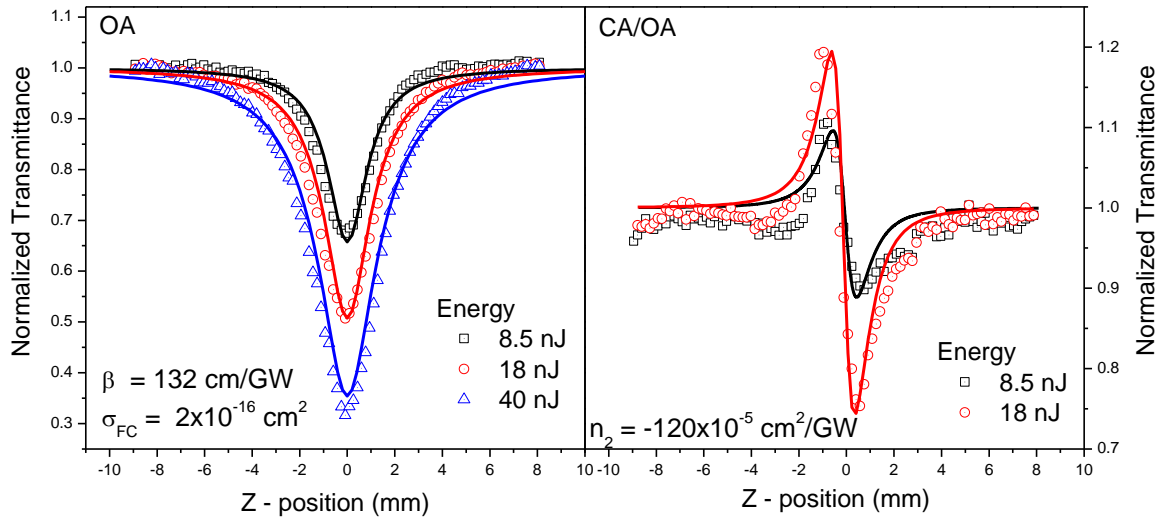
$\lambda = 1400$ nm



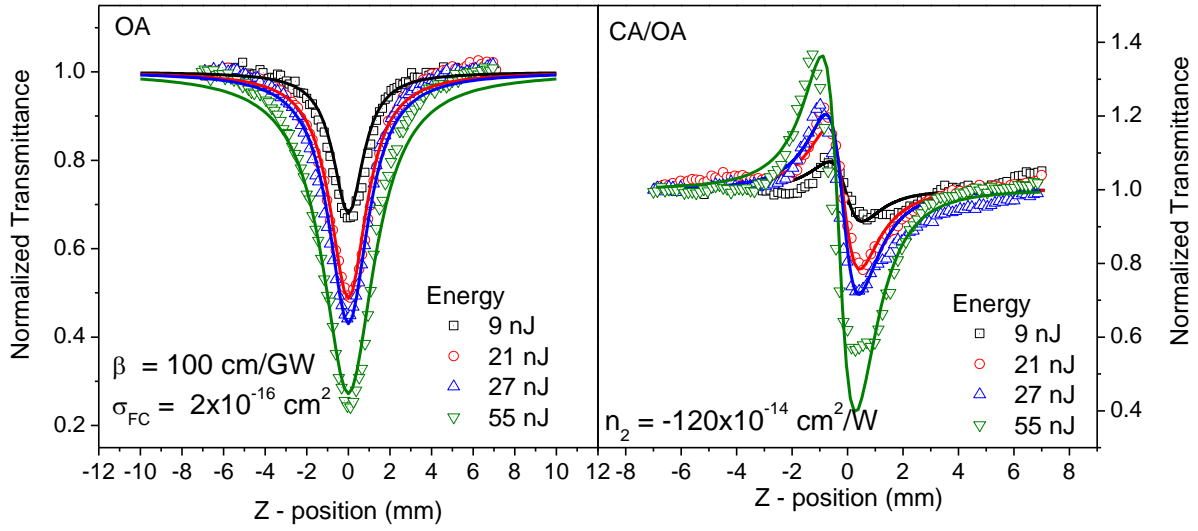
$\lambda = 1600$ nm



$\lambda = 1700$ nm



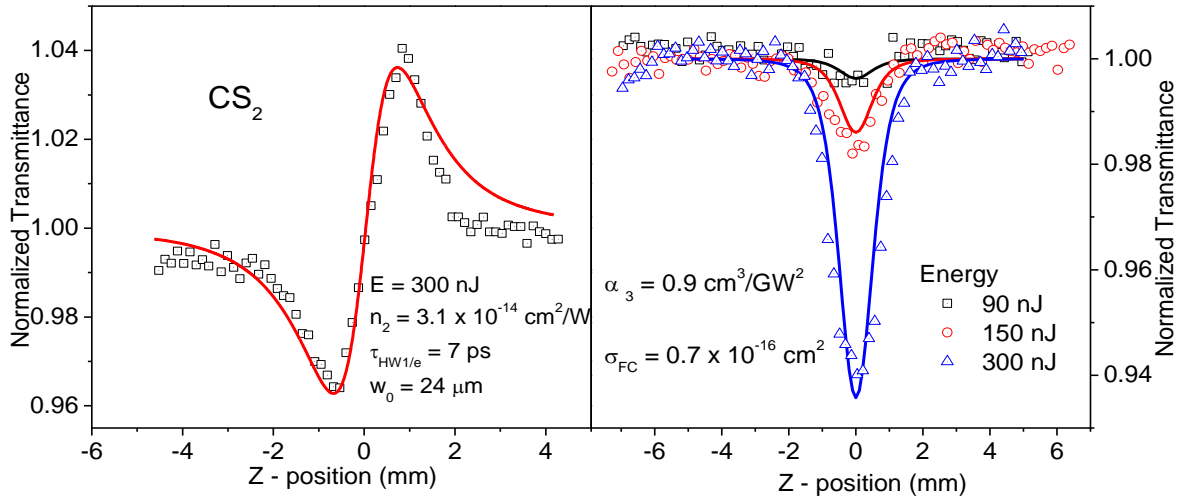
$\lambda = 1750 \text{ nm}$



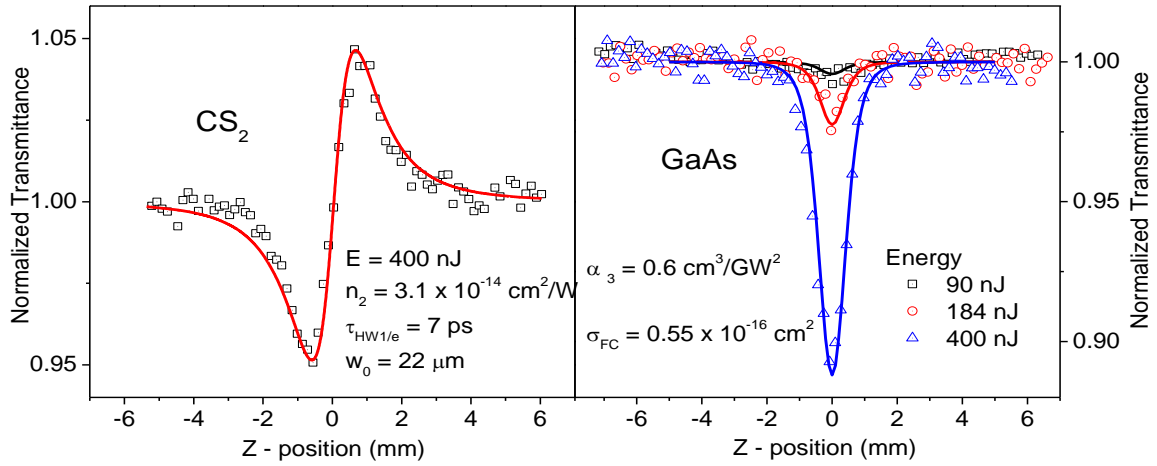
APENDIX B: PICOSECOND Z-SCAN MEASUREMENTS OF 3PA IN GaAs

CS₂ beam calibration and GaAs Open Aperture Z-scan measurement

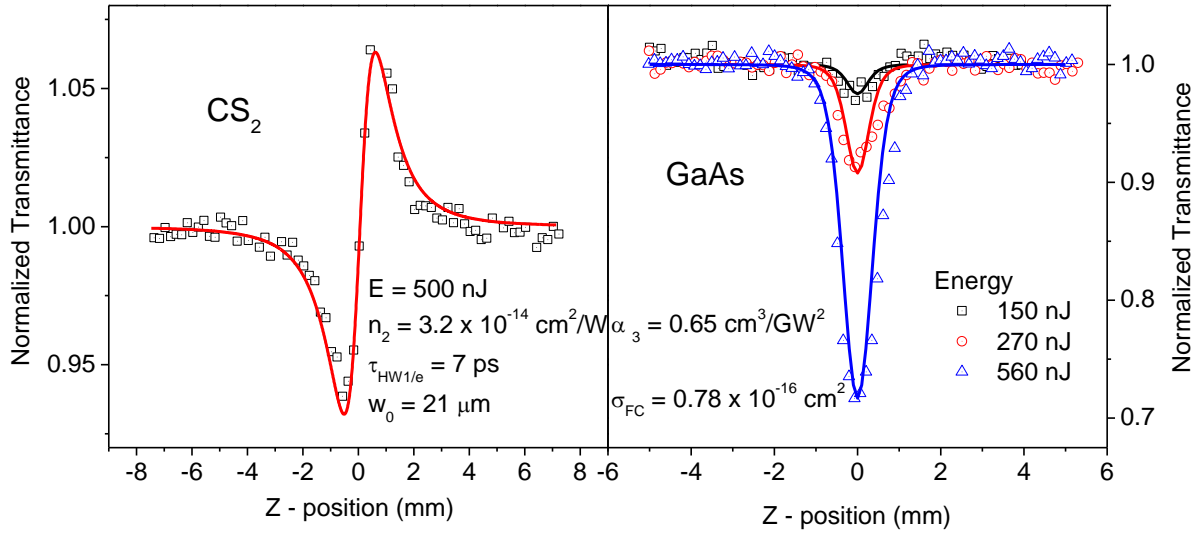
$\lambda = 1850 \text{ nm}$



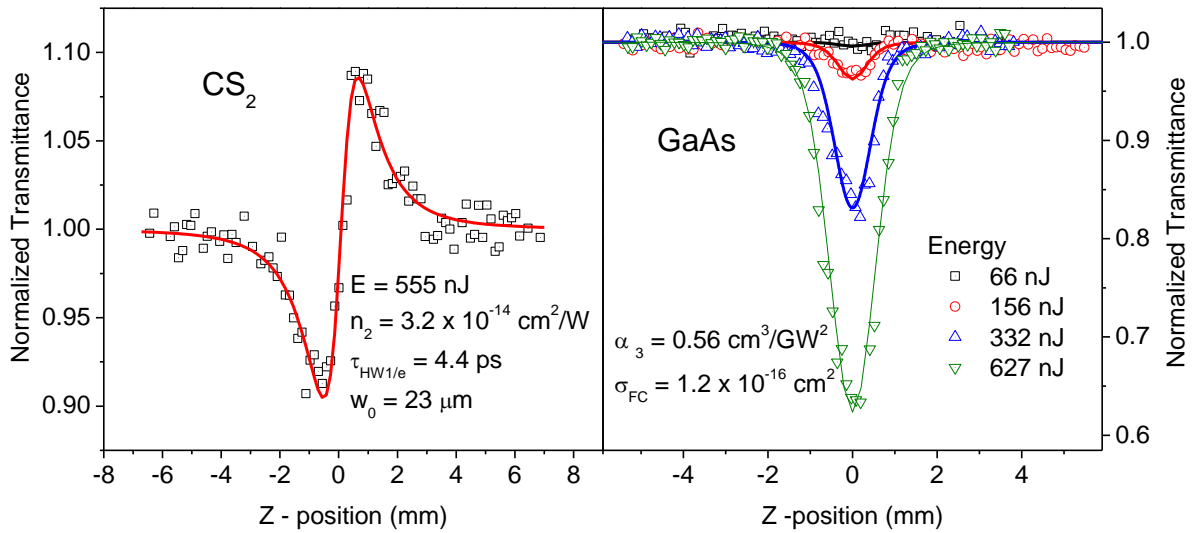
$\lambda = 2000 \text{ nm}$



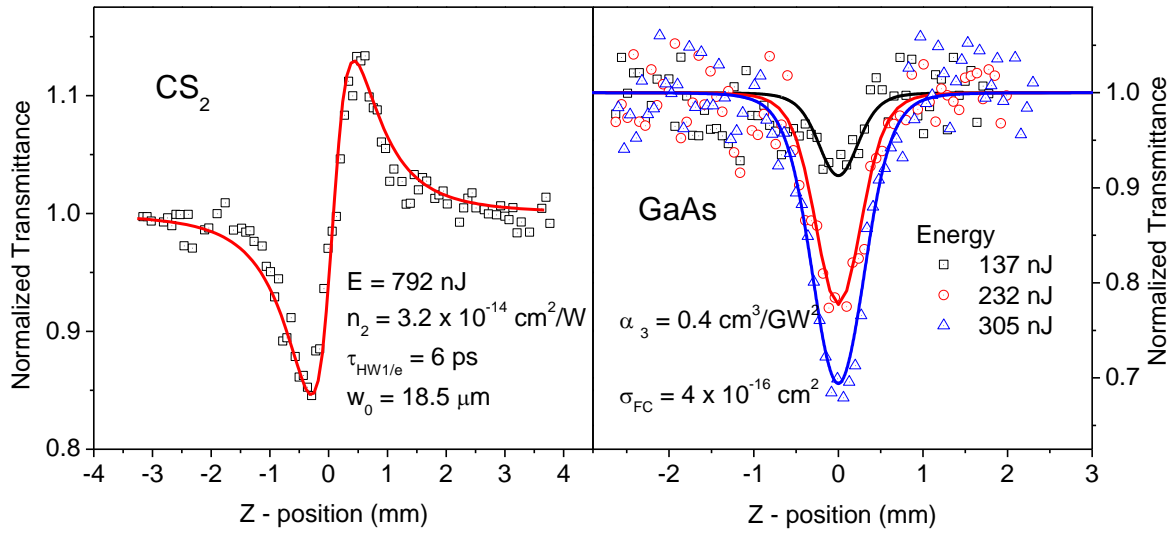
$\lambda = 2100 \text{ nm}$



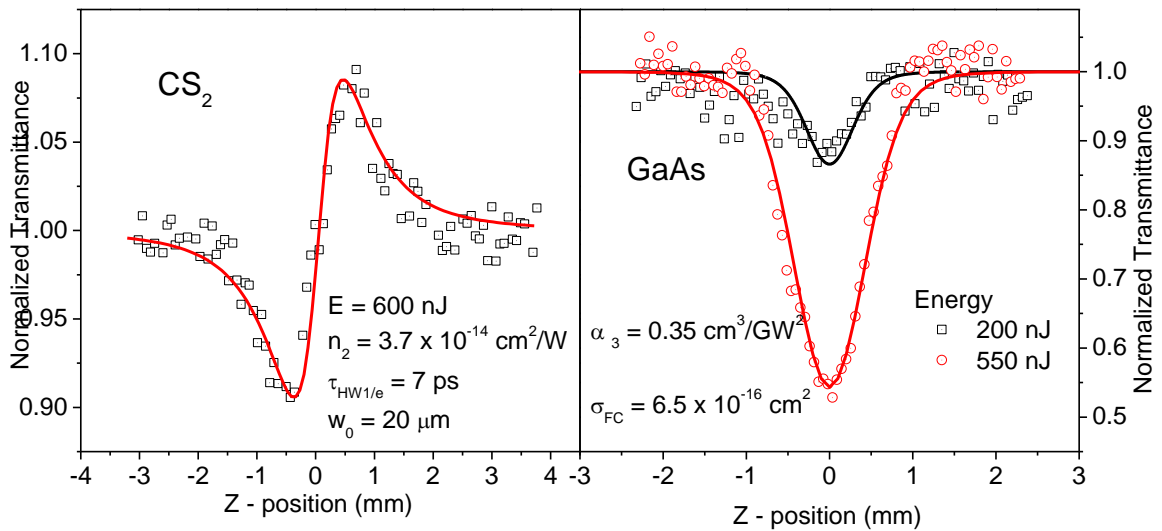
$\lambda = 2300 \text{ nm}$



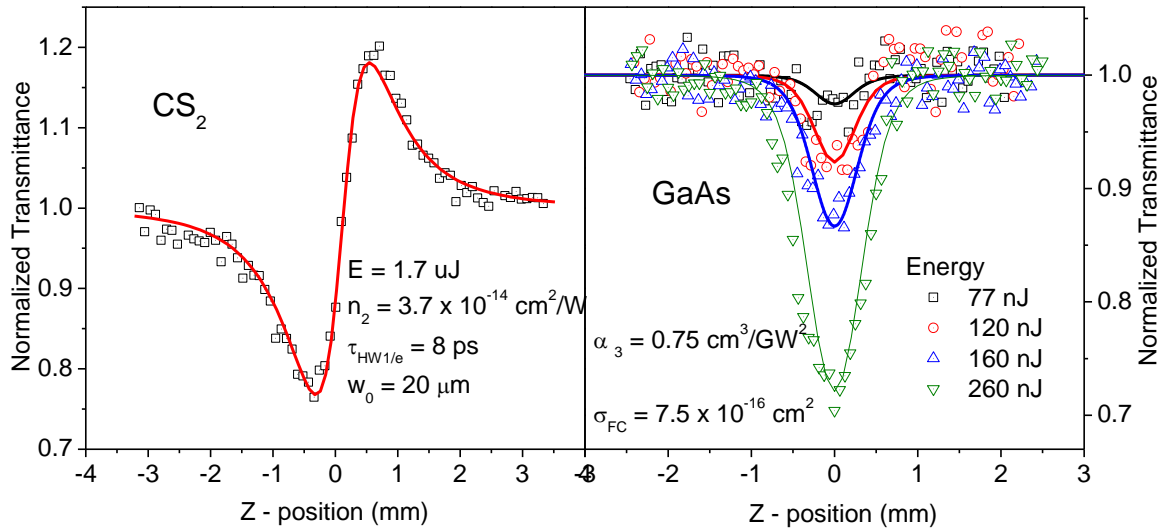
$\lambda = 2400 \text{ nm}$



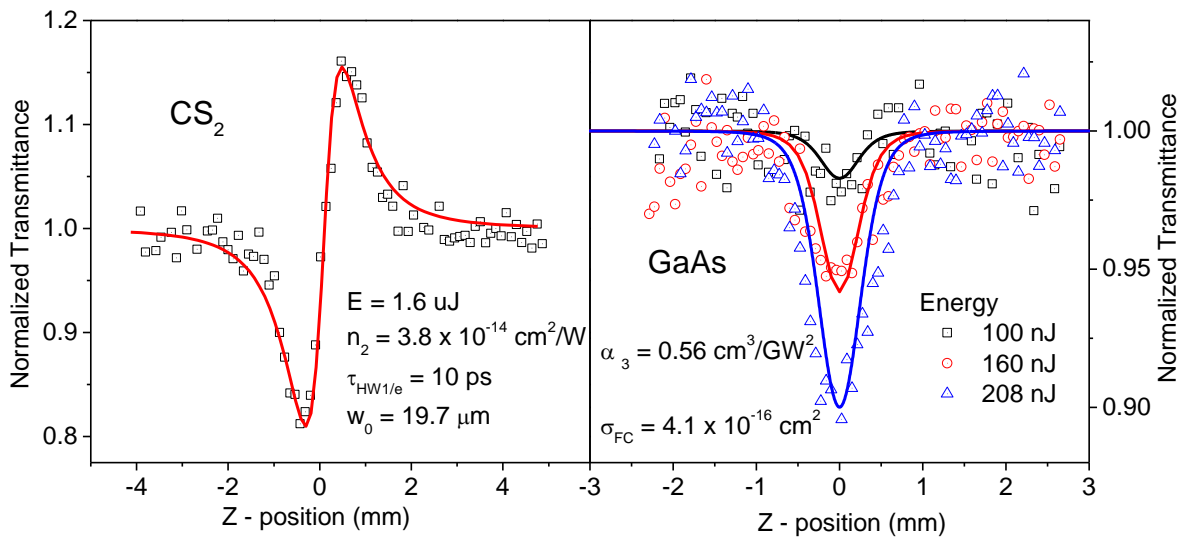
$\lambda = 2450 \text{ nm}$



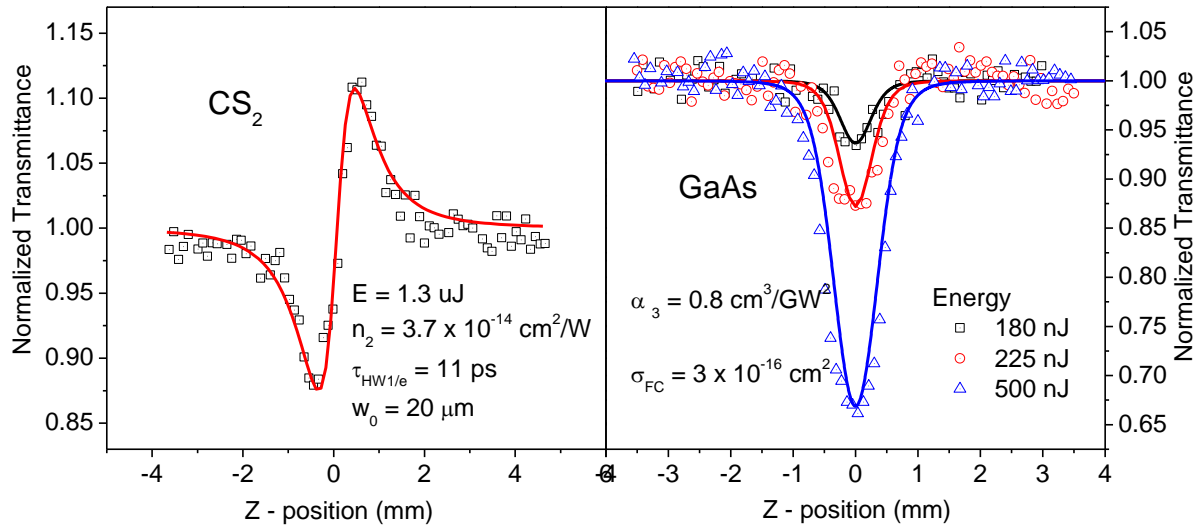
$\lambda = 2500 \text{ nm}$



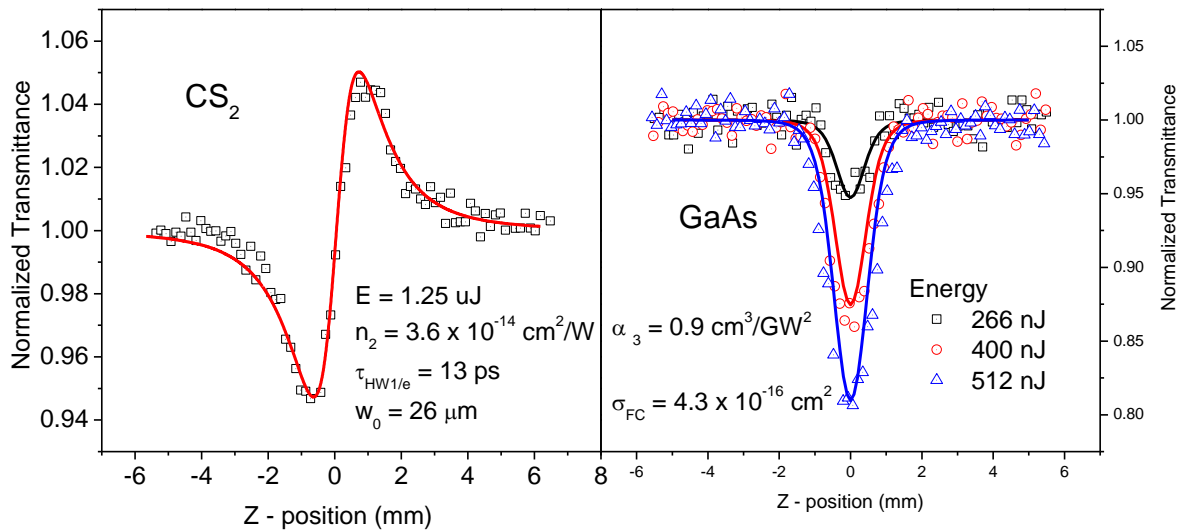
$\lambda = 2525 \text{ nm}$



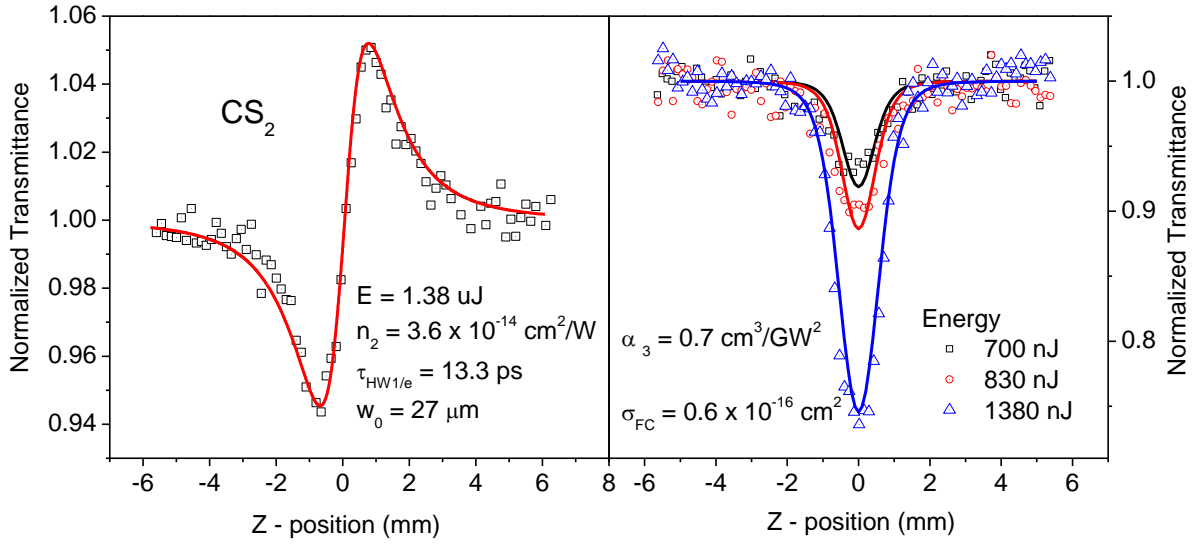
$\lambda = 2550 \text{ nm}$



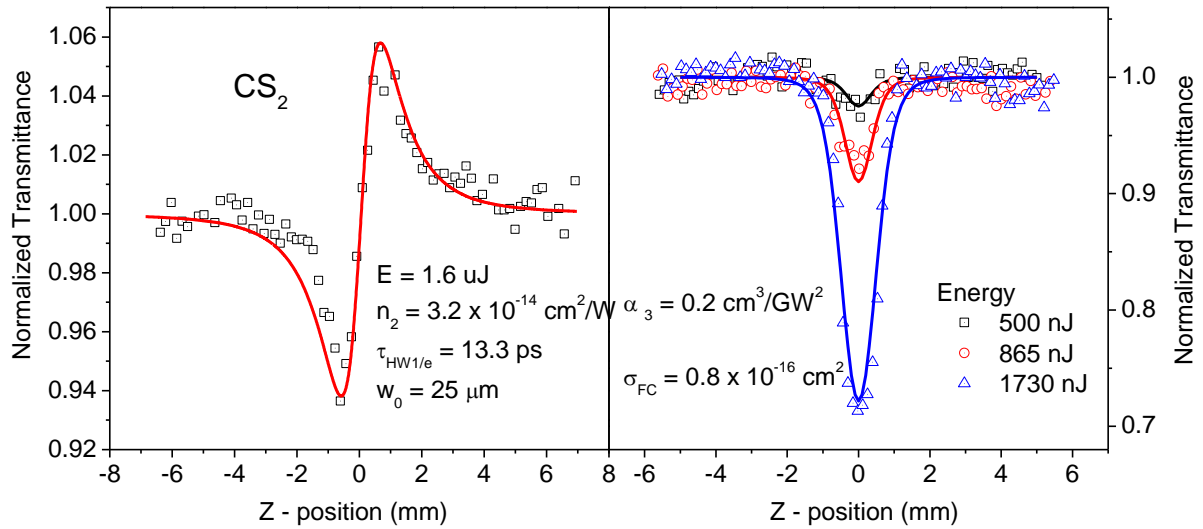
$\lambda = 2575 \text{ nm}$



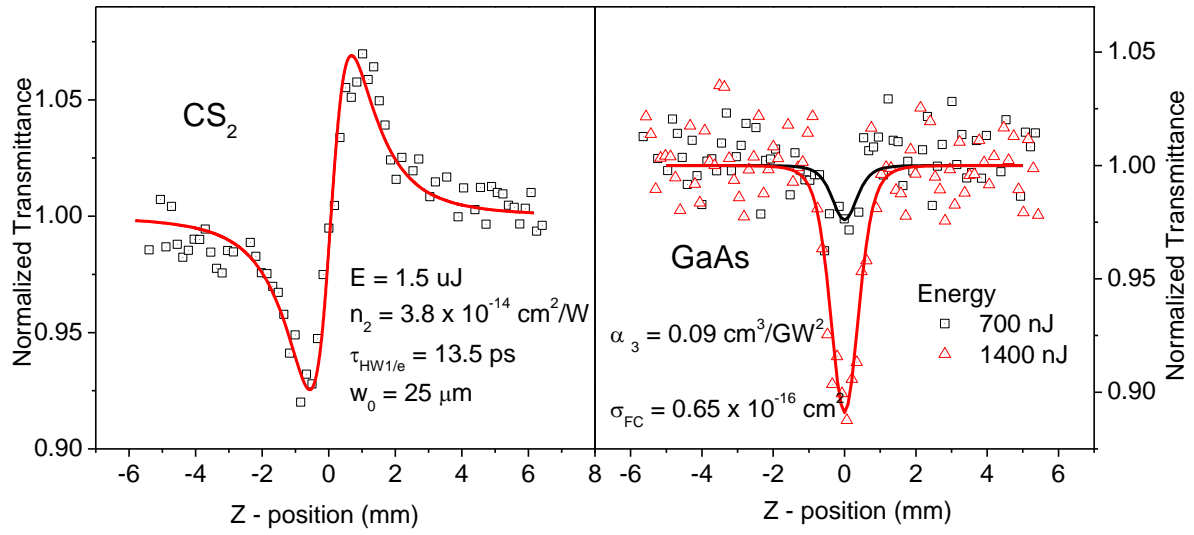
$\lambda = 2600 \text{ nm}$



$\lambda = 2610 \text{ nm}$



$\lambda = 2625 \text{ nm}$



APENDIX C: COPYRIGHT PERMISSION LETTERS



RightsLink®

Home

Account
Info

Help



Title: Optimization of the Double Pump–Probe Technique: Decoupling the Triplet Yield and Cross Section
Author: Davorin Peceli et al.
Publication: The Journal of Physical Chemistry A
Publisher: American Chemical Society
Date: May 1, 2012
Copyright © 2012, American Chemical Society

Logged in as:

Davorin Peceli

LOGOUT

PERMISSION/LICENSE IS GRANTED FOR YOUR ORDER AT NO CHARGE

This type of permission/license, instead of the standard Terms & Conditions, is sent to you because no fee is being charged for your order. Please note the following:

- Permission is granted for your request in both print and electronic formats, and translations.
- If figures and/or tables were requested, they may be adapted or used in part.
- Please print this page for your records and send a copy of it to your publisher/graduate school.
- Appropriate credit for the requested material should be given as follows: "Reprinted (adapted) with permission from (COMPLETE REFERENCE CITATION). Copyright (YEAR) American Chemical Society." Insert appropriate information in place of the capitalized words.
- One-time permission is granted only for the use specified in your request. No additional uses are granted (such as derivative works or other editions). For any other uses, please submit a new request.

BACK

CLOSE WINDOW

Copyright © 2013 [Copyright Clearance Center, Inc.](#) All Rights Reserved. [Privacy statement.](#)
Comments? We would like to hear from you. E-mail us at customercare@copyright.com

Title: Enhanced Intersystem Crossing Rate in Polymethine-Like Molecules: Sulfur-Containing Squaraines versus Oxygen-Containing Analogues

Author: Davorin Peceli, Honghua Hu, Dmitry A. Fishman, Scott Webster, Olga V. Przhonska, Vladimir V. Kurdyukov, Yurii L. Slominsky, Alexey I. Tolmachev, Alexey D. Kachkovski, Andrey O. Gerasov, Artëm E. Masunov, David J. Hagan, and Eric W. Van Stryland

Publication: The Journal of Physical Chemistry A

Publisher: American Chemical Society

Date: Mar 1, 2013

Copyright © 2013, American Chemical Society

Logged in as:

Davorin Peceli

LOGOUT

PERMISSION/LICENSE IS GRANTED FOR YOUR ORDER AT NO CHARGE

This type of permission/license, instead of the standard Terms & Conditions, is sent to you because no fee is being charged for your order. Please note the following:

- Permission is granted for your request in both print and electronic formats, and translations.
- If figures and/or tables were requested, they may be adapted or used in part.
- Please print this page for your records and send a copy of it to your publisher/graduate

school.

- Appropriate credit for the requested material should be given as follows: "Reprinted (adapted) with permission from (COMPLETE REFERENCE CITATION). Copyright (YEAR) American Chemical Society." Insert appropriate information in place of the capitalized words.
- One-time permission is granted only for the use specified in your request. No additional uses are granted (such as derivative works or other editions). For any other uses, please submit a new request.

BACK

CLOSE WINDOW

Copyright © 2013 [Copyright Clearance Center, Inc.](#) All Rights Reserved. [Privacy statement.](#)
Comments? We would like to hear from you. E-mail us at customercare@copyright.com

LIST OF REFERENCES

1. Göppert-Mayer, M., *Über Elementarakte mit zwei Quantensprüngen*. Ann. Phys., 1931. **401**(3): p. 273-294.
2. Maiman, T.H., *Stimulated Optical Radiation in Ruby*. Nature, 1960. **187**(4736): p. 493-494.
3. Franken, P.A., et al., *Generation of Optical Harmonics*. Physical Review Letters, 1961. **7**(4): p. 118-119.
4. Giuliano, C. and L. Hess, *Nonlinear absorption of light: Optical saturation of electronic transitions in organic molecules with high intensity laser radiation*. Quantum Electronics, IEEE Journal of, 1967. **3**(8): p. 358-367.
5. Soffer, B.H. and B.B. McFarland, *FREQUENCY LOCKING AND DYE SPECTRAL HOLE BURNING IN Q-SPOILED LASERS*. Applied Physics Letters, 1966. **8**(7): p. 166-169.
6. Kafalas, P., J.I. Masters, and E.M.E. Murray, *Photosensitive Liquid used as a Nondestructive Passive Q-Switch in a Ruby Laser*. Journal of Applied Physics, 1964. **35**(8): p. 2349-2350.
7. Harter, D.J., M.L. Shand, and Y.B. Band, *Power/energy limiter using reverse saturable absorption*. Journal of Applied Physics, 1984. **56**(3): p. 865-868.
8. Stryland, E.W.V., et al., *Optical limiting with semiconductors*. Journal of the Optical Society of America B: Optical Physics, 1988. **5**(9): p. 1980-1988.
9. Lennard-Jones, J.E., *The electronic structure of some diatomic molecules*. Transactions of the Faraday Society, 1929. **25**(0): p. 668-686.

10. J.N., T., *Modern Molecular Photochemistry*. 1991, Sausalito, California: University Science Book.
11. J.N., T., *Modern Molecular Photochemistry of Organic Molecules*. 2010, Sausalito, California: University Science Book.
12. Fox, M., *Optical Properties of Solids*. 2001, Oxford New York: Oxford University Press.
13. Schäfer, F.P., *Dye Laser*. Topics in Applied Physics. 1973, Berlin: Springer-Verlag.
14. Chidsey, C.E.D., et al., *Effect of Magnetic Fields on the Triplet State Lifetime in Photosynthetic Reaction Centers: Evidence for Thermal Repopulation of the Initial Radical Pair*. Proceedings of the National Academy of Sciences of the United States of America, 1985. **82**(20): p. 6850-6854.
15. McGlynn, S.P., Azumi, T., and Kinoshita, M., *Molecular Spectroscopy of the Triplet State*. 1969: Englewood Cliffs, N.J., Prentice-Hall.
16. Hund, F., *Zur Deutung verwickelter Spektren, insbesondere der Elemente Scandium bis Nickel*. Zeitschrift für Physik, 1925. **33**(1): p. 345-371.
17. Kohl, D.A., *On the Difference in Energy between Singlet and Triplet States*. The Journal of Chemical Physics, 1972. **56**(8): p. 4236-4238.
18. Coyle, J.A.B.a.J.D., *Excited States in Organic Chemistry*. 1975: John Wiley & Sons.
19. Lakowicz, J.R., *Principles of fluorescence microscopy*. 1999, New York: Kluwer Academic.
20. Kasha, M., *Characterization of electronic transitions in complex molecules*. Discussions of the Faraday Society, 1950. **9**(0): p. 14-19.

21. Binsch, G., et al., *On the fluorescence anomaly of azulene*. Chemical Physics Letters, 1967. **1**(4): p. 135-138.
22. Viswanath, G. and M. Kasha, *Confirmation of the Anomalous Fluorescence of Azulene*. The Journal of Chemical Physics, 1956. **24**(3): p. 574-577.
23. Nicolas J. Turro, V.R., J.C. Scaiano, *Modern Molecular Photochemistry of Organic Molecules*. 2010: University Science Books.
24. J.D., B.J.A.a.C., *Excited States in Organic Chemistry*. 1975, London, UK: John Wiley & Sons.
25. Brown, J.M., *Molecular Spectroscopy*. 1998, New York: Oxford University Press.
26. Resnick, R.E.a.R., *Quantum physics of atoms molecules, solids, nuclei, and particles*. 1985: John Wiley & Sons, Inc.
27. Solov'ev, K.N. and E.A. Borisevich, *Intramolecular heavy-atom effect in the photophysics of organic molecules*. Physics-Uspekhi, 2005. **48**(3): p. 231.
28. Lower, S.K. and M.A. El-Sayed, *The Triplet State and Molecular Electronic Processes in Organic Molecules*. Chemical Reviews, 1966. **66**(2): p. 199-241.
29. Englman, R. and J. Jortner, *The energy gap law for radiationless transitions in large molecules*. Molecular Physics, 1970. **18**(2): p. 145-164.
30. Schmidt, K., et al., *Intersystem Crossing Processes in Nonplanar Aromatic Heterocyclic Molecules*. The Journal of Physical Chemistry A, 2007. **111**(42): p. 10490-10499.
31. Beljonne, D., et al., *Spin-Orbit Coupling and Intersystem Crossing in Conjugated Polymers: A Configuration Interaction Description*. The Journal of Physical Chemistry A, 2001. **105**(15): p. 3899-3907.

32. El-Sayed, M.A., *Spin---Orbit Coupling and the Radiationless Processes in Nitrogen Heterocyclics*. The Journal of Chemical Physics, 1963. **38**(12): p. 2834-2838.
33. A.A, K., Jr., *Luminescence and photochemical studies of singlet oxygen photonics*. Journal of Photochemistry and Photobiology A: Chemistry, 2008. **196**(2-3): p. 210-218.
34. Andrasik, S.J., et al., *One- and Two-Photon Singlet Oxygen Generation with New Fluorene-Based Photosensitizers*. ChemPhysChem, 2007. **8**(3): p. 399-404.
35. Schweitzer, C. and R. Schmidt, *Physical mechanisms of generation and deactivation of singlet oxygen*. Chem Rev, 2003. **103**(5): p. 1685-757.
36. DeRosa, M.C. and R.J. Crutchley, *Photosensitized singlet oxygen and its applications*. Coordination Chemistry Reviews, 2002. **233-234**(0): p. 351-371.
37. Belfield, K.D., et al., *Two-Photon Absorption Properties of New Fluorene-Based Singlet Oxygen Photosensitizers*. The Journal of Physical Chemistry C, 2009. **113**(11): p. 4706-4711.
38. McIlroy, S.P., et al., *Two-Photon Photosensitized Production of Singlet Oxygen: Sensitizers with Phenylene-Ethynylene-Based Chromophores*. The Journal of Organic Chemistry, 2005. **70**(4): p. 1134-1146.
39. Boyd, R.W., *Nonlinear Optics*. 2008: Academic Press.
40. Magde, D., et al., *Absolute luminescence yield of cresyl violet. A standard for the red*. The Journal of Physical Chemistry, 1979. **83**(6): p. 696-699.
41. Strickler, S.J. and R.A. Berg, *Relationship between Absorption Intensity and Fluorescence Lifetime of Molecules*. The Journal of Chemical Physics, 1962. **37**(4): p. 814-822.

42. Wilkinson, F., W.P. Helman, and A.B. Ross, *Quantum Yields for the Photosensitized Formation of the Lowest Electronically Excited Singlet State of Molecular Oxygen in Solution*. Journal of Physical and Chemical Reference Data, 1993. **22**(1): p. 113-262.
43. Lessing, H.E. and A. Von Jena, *Separation of rotational diffusion and level kinetics in transient absorption spectroscopy*. Chemical Physics Letters, 1976. **42**(2): p. 213-217.
44. Lament, B., J. Karpiuk, and J. Waluk, *Determination of triplet formation efficiency from kinetic profiles of the ground state recovery*. Photochemical & Photobiological Sciences, 2003. **2**(3): p. 267-272.
45. King, S.M., et al., *Femtosecond ground state recovery: Measuring the intersystem crossing yield of polypyrrolofluorene*. The Journal of Chemical Physics, 2006. **124**(23): p. 234903.
46. Negres, R.A., et al., *The nature of excited-state absorption in polymethine and squarylium molecules*. Selected Topics in Quantum Electronics, IEEE Journal of, 2001. **7**(5): p. 849-863.
47. Padilha, L.A., et al., *Excited state absorption and decay kinetics of near IR polymethine dyes*. Chemical Physics, 2008. **352**(1-3): p. 97-105.
48. Brodeur, A. and S.L. Chin, *Ultrafast white-light continuum generation and self-focusing in transparent condensed media*. J. Opt. Soc. Am. B, 1999. **16**(4): p. 637-650.
49. Swatton, S.N.R., et al., *A time resolved double pump-probe experimental technique to characterize excited-state parameters of organic dyes*. Applied Physics Letters, 1997. **71**(1): p. 10-12.

50. McEwan, K.J.B., G.; Robertson, J. M.; Anderson, H. L., *The Nonlinear Optical Characterization of Meso-Substituted Porphyrin Dyes*. Journal of Nonlinear Optical Physics and Materials, 2000. **9**(04): p. 451-468.
51. Krivokapic, A., et al., *Meso-Tetra-Alkynyl Porphyrins for Optical Limiting—A Survey of Group III and IV Metal Complexes*. Advanced Materials, 2001. **13**(9): p. 652-656.
52. Schell, J., et al., *Reverse saturable absorption in C[₆₀]-doped porous glasses studied by single- and double-pulse pump--probe experiments*. The Journal of Chemical Physics, 1999. **111**(13): p. 5929-5937.
53. Sheik-Bahae, M., et al., *Sensitive measurement of optical nonlinearities using a single beam*. Quantum Electronics, IEEE Journal of, 1990. **26**(4): p. 760-769.
54. Firey, P.A., et al., *Silicon naphthalocyanine triplet state and oxygen. A reversible energy-transfer reaction*. Journal of the American Chemical Society, 1988. **110**(23): p. 7626-7630.
55. Dogariu, A., *Spectral and temporal response of optical nonlinearities*, in *CREOL, The College of Optics and Photonics 1997*, University of Central Florida: Orlando.
56. Xia, T., et al., *Optimization of optical limiting devices based on excited-state absorption*. Appl. Opt., 1997. **36**(18): p. 4110-4122.
57. Kobayakov, A., D.J. Hagan, and E.W. Van Stryland, *Analytical approach to dynamics of reverse saturable absorbers*. J. Opt. Soc. Am. B, 2000. **17**(11): p. 1884-1893.
58. Williams, C.H.G., Trans. R. Soc. Edinburg. **211**.
59. Tyutyulkov, N., *Polymethine dyes structure and properties*. 1991, Sofia, St. Kliment: Ohridski University Press.

60. Spitler, M.T., et al., *Electron Transfer Threshold for Spectral Sensitization of Silver Halides by Monomeric Cyanine Dyes*. The Journal of Physical Chemistry B, 1997. **101**(14): p. 2552-2557.
61. Dempsey, G.T., et al., *Photoswitching Mechanism of Cyanine Dyes*. Journal of the American Chemical Society, 2009. **131**(51): p. 18192-18193.
62. Christie, R.M., *Colour Chemistry*. 2001, Thomas Graham House, Science Park, Milton Road, Cambridge CB4 0WF, UK: The Royal Society of Chemistry.
63. Mishra, A., et al., *Cyanines during the 1990s: A Review*. Chemical Reviews, 2000. **100**(6): p. 1973-2012.
64. Fabian, J., H. Nakazumi, and M. Matsuoka, *Near-infrared absorbing dyes*. Chemical Reviews, 1992. **92**(6): p. 1197-1226.
65. Lepkowicz, R.S., et al., *Nature of the electronic transitions in thiacyanines with a long polymethine chain*. Chemical Physics, 2004. **305**(1-3): p. 259-270.
66. Lim, J.H., et al., *Polymethine and squarylium molecules with large excited-state absorption*. Chemical Physics, 1999. **245**(1-3): p. 79-97.
67. Beverina, L., et al., *Assessment of Water-Soluble π -Extended Squaraines as One- and Two-Photon Singlet Oxygen Photosensitizers: Design, Synthesis, and Characterization*. Journal of the American Chemical Society, 2008. **130**(6): p. 1894-1902.
68. Santos, P.F., et al., *Synthesis and Photochemical Evaluation of Iodinated Squarylium Cyanine Dyes*. Helvetica Chimica Acta, 2005. **88**(5): p. 1135-1143.

69. Salice, P., et al., *Photophysics of Squaraine Dyes: Role of Charge-Transfer in Singlet Oxygen Production and Removal*. The Journal of Physical Chemistry A, 2010. **114**(7): p. 2518-2525.
70. Ogava, K. and Y. Kobuke, *Recent Advances in Two-Photon Photodynamic Therapy. Anti-Cancer Agents in Medicinal Chemistry*, 2008. **8**(3): p. 269-279.
71. O. V. Przhonska, S.W., L. A. Padilha, H. Hu, A. D. Kachkovski, D. J. Hagan, and E. W. Van Stryland, *Two-Photon Absorption in Near-IR Conjugated Molecules: Design Strategy and Structure-Property Relations*. Springer Series on Fluorescence, 2010, ed. O.S. Wolfbeis. Vol. 8. 2010.
72. Rauh, R.D. and P.A. Leermakers, *Solvent effects upon the phosphorescence lifetimes and photoreactivity of butyrophenone*. Journal of the American Chemical Society, 1968. **90**(9): p. 2246-2249.
73. Xu, C. and W.W. Webb, *Measurement of two-photon excitation cross sections of molecular fluorophores with data from 690 to 1050 nm*. J. Opt. Soc. Am. B, 1996. **13**(3): p. 481-491.
74. Hales, J.M., et al., *Resonant enhancement of two-photon absorption in substituted fluorene molecules*. The Journal of Chemical Physics, 2004. **121**(7): p. 3152-3160.
75. Webster, S., et al., *Near-Unity Quantum Yields for Intersystem Crossing and Singlet Oxygen Generation in Polymethine-like Molecules: Design and Experimental Realization*. The Journal of Physical Chemistry Letters, 2010. **1**(15): p. 2354-2360.

76. Frisch M. J., T.G.W., Schlegel H. B., Scuseria G. E., Robb M. A., Cheeseman J. R., Scalmani G., Barone V., Mennucci B., Petersson G. A., et al., *Gaussian 09*, 2009, Gaussian, Inc.: Wallingford CT.
77. Becke, A.D., *Density-functional thermochemistry. III. The role of exact exchange*. The Journal of Chemical Physics, 1993. **98**(7): p. 5648-5652.
78. Rassolov, V.A., et al., *6-31G[^{sup} *] basis set for atoms K through Zn*. The Journal of Chemical Physics, 1998. **109**(4): p. 1223-1229.
79. Marenich, A.V., C.J. Cramer, and D.G. Truhlar, *Universal Solvation Model Based on Solute Electron Density and on a Continuum Model of the Solvent Defined by the Bulk Dielectric Constant and Atomic Surface Tensions*. The Journal of Physical Chemistry B, 2009. **113**(18): p. 6378-6396.
80. Casida, M.E., et al., *Molecular excitation energies to high-lying bound states from time-dependent density-functional response theory: Characterization and correction of the time-dependent local density approximation ionization threshold*. The Journal of Chemical Physics, 1998. **108**(11): p. 4439-4449.
81. Fabian, J., *TDDFT-calculations of Vis/NIR absorbing compounds*. Dyes and Pigments, 2010. **84**(1): p. 36-53.
82. Masunov, A.E., *Theoretical spectroscopy of carbocyanine dyes made accurate by frozen density correction to excitation energies obtained by TD-DFT*. International Journal of Quantum Chemistry, 2010. **110**(15): p. 3095-3100.
83. Masunov, A. and J.J. Dannenberg, *Theoretical Study of Urea. I. Monomers and Dimers*. The Journal of Physical Chemistry A, 1998. **103**(1): p. 178-184.

84. Schmidt, M.W., et al., *General atomic and molecular electronic structure system*. Journal of Computational Chemistry, 1993. **14**(11): p. 1347-1363.
85. Fedorov, D.G., et al., *Spin-orbit coupling in molecules: Chemistry beyond the adiabatic approximation*. International Reviews in Physical Chemistry, 2003. **22**(3): p. 551-592.
86. Marian, C.M., *Spin-orbit coupling and intersystem crossing in molecules*. Wiley Interdisciplinary Reviews: Computational Molecular Science, 2012. **2**(2): p. 187-203.
87. Perun, S., J. Tatchen, and C.M. Marian, *Singlet and Triplet Excited States and Intersystem Crossing in Free-Base Porphyrin: TDDFT and DFT/MRCI Study*. ChemPhysChem, 2008. **9**(2): p. 282-292.
88. Andzelm, J., et al., *Optical Properties of Phthalocyanine and Naphthalocyanine Compounds†*. Journal of Chemical Theory and Computation, 2007. **3**(3): p. 870-877.
89. Rawling, T. and A. McDonagh, *Ruthenium phthalocyanine and naphthalocyanine complexes: Synthesis, properties and applications*. Coordination Chemistry Reviews, 2007. **251**(9–10): p. 1128-1157.
90. Charlesworth, P., et al., *The photophysical properties of a ruthenium-substituted phthalocyanine*. Journal of Photochemistry and Photobiology B: Biology, 1994. **26**(3): p. 277-282.
91. Guez, D., et al., *Photophysical properties of a ruthenium(II) phthalocyanine*. Chemical Physics Letters, 1996. **249**(5–6): p. 309-313.
92. Dasari, R.R., et al., *Synthesis and linear and nonlinear absorption properties of dendronised ruthenium(ii) phthalocyanine and naphthalocyanine*. Chemical Communications (Cambridge, United Kingdom), 2011. **47**(15): p. 4547-4549.

93. Ishii, K., et al., *Control of Photobleaching in Photodynamic Therapy Using the Photodecarbonylation Reaction of Ruthenium Phthalocyanine Complexes via Stepwise Two-Photon Excitation*. The Journal of Physical Chemistry B, 2008. **112**(10): p. 3138-3143.
94. Brandi, H.S. and C.B.d. Araujos, *Multiphonon absorption coefficients in solids: a universal curve*. Journal of Physics C: Solid State Physics, 1983. **16**(30): p. 5929.
95. Wherrett, B.S., *Scaling rules for multiphoton interband absorption in semiconductors*. Journal of the Optical Society of America B: Optical Physics, 1984. **1**(1): p. 67-72.
96. Rosencher, E., *Optoelectronics*. 2002, New York: Cambridge University Press.
97. Cardona, P.Y.Y.a.M., *Fundamentals of Semiconductors: Physics and Material Properties*. 1997: Springer.
98. Hutchings, D.C., et al., *Kramers-Krönig relations in nonlinear optics*. Optical and Quantum Electronics, 1992. **24**(1): p. 1-30.
99. Sheik-Bahae, M., et al., *Dispersion of bound electron nonlinear refraction in solids*. Quantum Electronics, IEEE Journal of, 1991. **27**(6): p. 1296-1309.
100. Said, A.A., et al., *Determination of bound-electronic and free-carrier nonlinearities in ZnSe, GaAs, CdTe, and ZnTe*. Journal of the Optical Society of America B: Optical Physics, 1992. **9**(3): p. 405-414.
101. Weiner, J.S. and P.Y. Yu, *Free carrier lifetime in semi-insulating GaAs from time-resolved band-to-band photoluminescence*. Journal of Applied Physics, 1984. **55**(10): p. 3889-3891.

102. Liu, A. and Y. Rosenwaks, *Excess carriers lifetime in InP single crystals: Radiative versus nonradiative recombination*. Journal of Applied Physics, 1999. **86**(1): p. 430-437.
103. Lepkowicz, R., *Study of the Excited-state Absorption Properties of Polymethine Molecules in CREOL, The College of Optics and Photonics*2004, University of Central Florida: Orlando, Florida.
104. Ross, T.S., *A Picosecond Visible Optical Parametric Oscillator as a Tool for Nonlinear Spectroscopy*, in *CREOL, The College of Optics and Photonics*1998, University of Central Florida: Orlando, Florida.
105. Gonzalez, L.P., et al., *Wavelength dependence of two photon and free carrier absorptions in InP*. Opt. Express, 2009. **17**(11): p. 8741-8748.
106. Cirloganu, C.M., et al., *Three-photon absorption spectra of zinc blende semiconductors: theory and experiment*. Optics Letters, 2008. **33**(22): p. 2626-2628.
107. Kane, E.O., *Band structure of indium antimonide*. Journal of Physics and Chemistry of Solids, 1957. **1**(4): p. 249-261.
108. Hurlbut, W.C., et al. *Multi-Photon Absorption and Nonlinear Refraction of GaAs in the Mid-Infrared*. 2006. Optical Society of America.
109. Krishnamurthy, S., et al., *Temperature- and wavelength-dependent two-photon and free-carrier absorption in GaAs, InP, GaInAs, and InAsP*. Journal of Applied Physics, 2011. **109**(3): p. 033102.
110. R., T., *Frequency resolved optical gating: The measurement of ultrashort laser pulses*. 2000: Kluwer Academic Publishers.